



Vanadium-based Nanomaterials for Energy Storage Applications

Cao, Huili

Publication date:
2021

Document Version
Publisher's PDF, also known as Version of record

[Link back to DTU Orbit](#)

Citation (APA):
Cao, H. (2021). *Vanadium-based Nanomaterials for Energy Storage Applications*. DTU Chemistry.

General rights

Copyright and moral rights for the publications made accessible in the public portal are retained by the authors and/or other copyright owners and it is a condition of accessing publications that users recognise and abide by the legal requirements associated with these rights.

- Users may download and print one copy of any publication from the public portal for the purpose of private study or research.
- You may not further distribute the material or use it for any profit-making activity or commercial gain
- You may freely distribute the URL identifying the publication in the public portal

If you believe that this document breaches copyright please contact us providing details, and we will remove access to the work immediately and investigate your claim.

Vanadium-based Nanomaterials for Energy Storage Applications

Huili Cao

Ph.D. Thesis

Department of Chemistry

Technical University of Denmark

March 2021

**Vanadium-based Nanomaterials for
Energy Storage Applications**

Ph.D. Thesis

March 2021

Huili Cao

hucao@kemi.dtu.dk

Department of Chemistry

Technical University of Denmark

Main supervisor

Assoc. Prof. Susanne Mossin

Department of Chemistry

Technical University of Denmark

Co-supervisor

Prof. Poul Norby

Department of Energy Conversion and Storage

Technical University of Denmark

Preface and Acknowledgments

This dissertation is submitted to Technical University of Denmark (DTU) for the degree of Doctor of Philosophy (Ph.D.). The project was carried out in NanoChemistry group, Department of Chemistry, DTU, under the supervision of Associate Professor Susanne Mossin and Professor Poul Norby. The project financial support is from China Scholarship Council (No.201706220078) and DTU Chemistry.

First and foremost, I would like to express my intensive appreciation to my supervisors Associate Professor Susanne Mossin and Professor Poul Norby for their inspirational guidance and willing to share their expertise in all aspects. I would like to thank Susanne for giving me the chance to communicate with the scientific communities and supporting me in all my ideas. My sincere thanks also goes to Professor Poul for providing the experiment materials, instruments required for the experiment and the guidance for my research. They give me the best possible starting point for fulfilling my PhD project.

Besides my supervisors, I would like to thank the support from NanoChemistry group and Catalysis and Sustainable Chemistry group. In particular Dr. Xinxin Xiao from DTU Chemistry encouraged me and guided me to find a way when I encountered difficulties in my scientific research. Thanks to Professor Jens Ulstrup for sharing his rich experience in electrochemistry and valuable scientific suggestions. I also would like to thank Professor Jingdong Zhang and Dr. Christian Engelbrekt for their help about the electrochemical skills at the beginning of my PhD study.

My sincere thanks also goes to Professor Ulla Gro Nielsen from University of Southern Denmark for the great help during my external stay. I learned quantities of knowledge about solid state nuclear magnetic resonance. I also would like to thank many people at DTU, especially laboratory technicians Bodil Fliis Holten, Joanne Marie Nielsen, David Frej Nielsen, Marie Koefoed, Maria Blanner Bang, Lars Egede Bruhn and John Nissen from building center, PhD coordinator Mette Hansen, IT supporter Burak Yildiz, Bo Sørensen, receptionist Jette Berg Nestén, Monica Esterajher Sønderg for their help during the last three years.

I would like to give a special thanks to my family and friends for their support and understanding during my pursuit of high educations.

March 2021, Kgs. Lyngby

Huili Cao

Contributions during Ph.D. project

This thesis is the main result of my work from 1.1.2018 to 31.3.2021.

The thesis includes the following research publications:

1. **H. Cao***, Z. Zheng, P. Norby, X. Xiao*, S. Mossin*. Electrochemically induced phase transition in $V_3O_7 \cdot H_2O$ nanowires/reduced graphene oxide composites for aqueous zinc-ion batteries. (Submitted)
2. **H. Cao***, Chao Peng, Z. Zheng, Z. Lan, Q. Pan, U. Nielsen, P. Norby, X. Xiao*, S. Mossin*. New Insight into the Effect of the Orientation of Zinc Vanadate on Zinc Ion Storage Performance. (Submitted)
3. **H. Cao***, Z. Zheng, J. Meng, X. Xiao, P. Norby, S. Mossin*. Examining the Effects of Nitrogen-doped Carbon Coating on Zinc Vanadate Nanoflowers Towards High Performance Lithium Anode, *Electrochimica Acta*, 356 (2020) 136791.

During the thesis period, I have also contributed to these publications, which are not included in the thesis work.

Other research publications:

1. **H. Cao**, X. Xiao, X. Wang, J. Liu*, P. Si*. Morphology engineering of self-assembled porous zinc manganate hexagons for lithium ion storage, *Electrochimica Acta*, 330 (2020), 135260.
2. Z. Zheng, Y. Xiao, **H. Cao**, X. Tian, R. Wu, J. Zhang, J. Ulstrup, F. Zhao*. Effect of copper and phosphate on the biosynthesis of palladium nanoparticles by *Shewanella oneidensis* MR-1, *ChemElectroChem*, 7 (2020), 4460.

Academic conference contributions

Oral presentations

1. **H. Cao**, Microwave-assisted fabrication of $V_3O_7 \cdot H_2O$ nanobelts for aqueous zinc-ion battery application, DTU Chemistry PhD symposium 2020, Kgs. Lyngby, Denmark (Best Oral Presentation Award)
2. **H. Cao**, Carbon Coating Effects on Vanadium Oxidation State in Zinc Vanadate and Its Electrochemical Performance. CSC-CRT New Year Seminar 2020, Kgs. Lyngby, Denmark

Poster presentations

1. **H. Cao**, S. Mossin, P. Norby. Yolk-shell-structured porous zinc vanadate@N-doped carbon anode for lithium energy storage. Nordic Battery Conference 2019, Kgs. Lyngby, Denmark.
2. **H. Cao**, S. Mossin, P. Norby, Q. Chi. Shape-controlled synthesis of zinc vanadate and its supercapacitor performance. Sustain Conference 2018, Kgs. Lyngby, Denmark.

Abstract

Rechargeable batteries have been dominating the market for smart and portable electronic devices. To keep pace with the changes in consumer preference, continuous advances in material science research have powered innovation of battery technology and have exceeded the previous limits of battery performance. In the last decades there has been a large interest in application of vanadium-based nanomaterials in both lithium-ion battery (LIB) and zinc ion battery (ZIB) due to a number of favorable properties: They have multiple accessible oxidation states, a rich redox chemistry and the layered structure facilitate ion diffusion. With the pursuit of high-performance electrode materials, a variety of new discoveries have been revealed. This PhD project comprises three main parts; i) the investigation of the carbon coating effects on the oxidation state of the vanadium and the LIB performance; ii) studying the orientation effects on zinc ion storage process; iii) the efficient fabrication of vanadium oxides and discovery of the phase transition during zinc ion storage process.

In the first study, nitrogen-doped carbon coated zinc vanadate nanoflowers with a high specific surface area is fabricated by a facile method consisting of direct precipitation and a subsequent calcination process. By systematic investigations, it is proved that the V^{5+} from $Zn_3(OH)_2(V_2O_7)(H_2O)_2$, the intermediate obtained from precipitation, is largely converted to V^{3+} in ZnV_2O_4 and some of ZnO , accompanied with a vanadium loss of about 9%, leading to increased Zn/V ratio. When applied as anode of LIB, the as-prepared $ZnV_2O_4/ZnO@N$ doped C exhibits a considerable reversible specific capacity of 620 mAh g^{-1} . In-depth electrochemical analysis including testing in a three-electrode system shows that the carbon shell is crucial in maintaining the structural stability and enhancing the capacity of the active material.

The poor electrochemical performance of the carbon coated porous zinc vanadate in ZIB applications encouraged me to further explore the influencing factors on the Zn^{2+} ion energy storage. Two types of zinc pyrovanadate ($Zn_3V_2O_7(OH)_2 \cdot 2H_2O$, $ZnVO$) in nanowires and nanoflakes were studied. They have the same crystal type but different orientations. $ZnVO$ nanowires expose mostly the (001) plane lattice, in contrast to (020) and (110) lattice for $ZnVO$ flakes. Interestingly, nanowires exhibit an excellent specific discharge capacity of 108 mAh g^{-1} , contributed from Faradic and diffusion-controlled

capacity. By comparison, nanoflakes deliver a very poor capacity of 2.2 mAh g^{-1} with only diffusion-controlled capacity. Density functional theory (DFT) reveals significantly different Zn^{2+} ion diffusion rates in ZnVO along different orientations.

The final work builds upon the two previous and considers both the effect of the carbon additive and of the orientation. A $\text{V}_3\text{O}_7 \cdot \text{H}_2\text{O}$ nanobelts/reduced graphene oxide (rGO) composite is synthesized in high yield (85%) by a microwave approach and is shown to expose the (020) plane lattice with a large spacing of 0.85 nm. The growth mechanisms of the highly crystalline nanobelts have been thoroughly investigated, and the governing role of the acid upon the morphology and oxidation state of vanadium has been revealed. When used as the ZIB cathode, the composite delivers a high specific capacity of 410.7 and 385.7 mAh g^{-1} at a current density of 0.5 and 4 A g^{-1} , respectively, with a high retention of the capacity of 93%. Extended cycling results in a gradual irreversible phase transition, *i.e.*, from the original orthorhombic $\text{V}_3\text{O}_7 \cdot \text{H}_2\text{O}$ to a stable hexagonal $\text{Zn}_3(\text{VO}_4)_2(\text{H}_2\text{O})_{2.93}$ phase. This electrochemical route for the phase transition is a new discovery for V_3O_7 materials and provides new insight into the reactions of aqueous ZIBs.

Abstract-Danish

Genopladelige batterier har været dominerede på markedet for smarte og bærbare elektroniske enheder. For at holde trit med ændringerne i forbrugeradfærden har materialeforskning løbende skabt fremskridt og innovation i batteriteknologi og har endda brudt tidligere grænser for batteriydelse. I de sidste årtier har der været stor fokus på vanadiumbaserede nanomaterialer til anvendelse som højkapacitetsbatterielektroder i både lithium-ion-batterier (LIB) og zink-ion-batterier (ZIB). Dette skyldes en række attraktive egenskaber: Vanadium kan antage flere oxidationstrin, der er en rig redoxkemi og de er opbygget af lagdelte krystalstrukturer, der faciliterer diffusion af ioner. I jagten på højtydende elektrodematerialer er der gjort en række nye opdagelser. Dette ph.d. projekt består af tre hovedtemaer: i) undersøgelse af effekten på vanadiums oxidationstrin og materialets ydeevne i LIB ved at overtrække nanomaterialet med en grafen carbonoverflade; ii) studiet af krystalorienterings effekt på zinkionlagringsprocessen; iii) effektiv syntese af vanadiumoxider og opdagelse af en faseovergang i forbindelse med zinkionlagringsprocessen i ZIB.

I den første undersøgelse fremstilles nitrogendopede kulstofbelagte zinkvanadat nanoblomster med et højt specifikt overfladeareal ved en ligetil metode bestående af direkte udfældning og en efterfølgende calcineringsproces. Ved systematiske undersøgelser er det bevist, at V^{5+} fra $Zn_3(OH)_2(V_2O_7)(H_2O)_2$, mellemproduktet opnået ved direkte udfældning, stort set fuldstændigt omdannes til V^{3+} i det endelige materiale som består af ZnV_2O_4 og lidt ZnO , ledsaget af et vanadintab på ca. 9%, hvilket førte til øget Zn/V-forhold. Når materialet anvendes som anoden i lithium-ion-batterier (LIB'er), udviser det en høj reversibel specifik kapacitet på 620 mAh g^{-1} . Grundig elektrokemisk analyse, herunder test i et treelektrodesystem, viser, at carbon overfladebelægningen er afgørende for at opretholde strukturens stabilitet og forbedre kapaciteten af det aktive materiale.

Den ringe elektrokemiske ydeevne for det kulstofbelagte porøse zinkvanadat i ZIB-applikationer tilskyndte mig til at undersøge de påvirkende faktorer på Zn^{2+} ionenergilagring mere dybdegående. To typer zinkpyrovanadat ($Zn_3V_2O_7(OH)_2 \cdot 2H_2O$, $ZnVO$) i nanotråde og nanoflager har den samme krystaltype, men krystallernes

overflade er domineret af forskellige krystalplaner. For ZnVO nanotråde er det (001) planet, mens det er (020) og (110) for ZnVO nanoflager. Af særlig interesse er det, at ZnVO nanotråde udviser en fremragende specifik afladningskapacitet på 108 mAh g^{-1} , med bidrag fra både Faraday og diffusionsstyret kapacitet. Til sammenligning leverer nanoflager en ringe kapacitet på 2.2 mAh g^{-1} som kun skyldes diffusionsstyret kapacitet. Density functional theory (DFT) afslører signifikant forskellige Zn^{2+} ion diffusionshastigheder i ZnVO i de forskellige krystalretninger.

Det sidste arbejde tager både effekten af kulstof og af krystalorienteringen i betragtning. $\text{V}_3\text{O}_7 \cdot \text{H}_2\text{O}$ nanobælter /reduceret grafenoxid (rGO) komposit materiale blev syntetiseret i højt udbytte (85%) ved brug af mikrobølge og har eksponering af (020) planet med en stor gitterafstand på 0.85 nm . Vækstmekanismen for de højkrySTALLINSKE nanobælter er blevet undersøgt grundigt og viser den styrende rolle af den tilsatte syre i forhold til morfologi og oxidationstrin for vanadium. Når materialet bruges som ZIB-katode, kan kompositten levere en høj specifik kapacitet på 410.7 og 385.7 mAh g^{-1} ved en strømtæthed på henholdsvis 0.5 og 4 A g^{-1} med en høj retention af kapacitet på 93%. Cykling over lang tid resulterer i en gradvis faseovergang, fra den oprindelige orthorhombiske $\text{V}_3\text{O}_7 \cdot \text{H}_2\text{O}$ fase til en stabil hexagonal $\text{Zn}_3(\text{VO}_4)_2(\text{H}_2\text{O})_{2.93}$ fase. Dette viser en irreversibel faseovergang via en elektrokemisk rute og dette er en ny opdagelse for disse V_3O_7 -materialer. Denne faseovergang giver et nyt indblik i reaktionerne i vandige ZIB'er.

Acronyms and instructional notes

0-D: zero dimensional

1D: one dimensional

2D: two dimensional

3D: three dimensional

AC: alternative current

AFM: atomic force microscopy

AIB: aluminum-ion battery

A_w: Warburg coefficient

BET: Brunauer-Emmett-Teller

C_{dl}: double-layer capacitance

CE: coulombic efficiency

CMK: ordered mesoporous carbon

CNTs: carbon nanotubes

COFs: covalent organic frameworks

CV: cyclic voltammetry

CVO: calcium vanadate

DMC: dimethyl carbonate

DTU: Technical University of Denmark

EC: ethylene carbonate

EDS, EDX: Energy-dispersive X-ray spectroscopy

EELS: electron energy loss spectroscopy

EIS: electrochemical impedance spectroscopy

E_p: peak potential

EPR: electron paramagnetic resonance

ET: electron transfer

FFT: fast Fourier transform

FTIR: Fourier transform infrared spectroscopy

GDC: galvanostatic charge and discharge

GITT: galvanostatic intermittent titration technique

GO: graphene oxide

HAADF: high-angle annular dark-field

HAc: acetic acid

HRTEM: high-resolution transmission electron microscopy

ICP-OES: inductively coupled plasma-optical emission spectroscopy

IR: ohmic voltage drop

LIB: lithium-ion battery

LTO: lithium titanate

LVO: lithium vanadate

MOFs: metal organic frameworks

OCV: open circuit voltage

PDA: polydopamine

ppm: parts per million

R_{ct}: electron transfer resistance

RE: reference electrode

R_{electrolyte}: electrolyte resistance

rGO: reduced graphene oxide

RT: room temperature

SAED: selected area electron diffraction

SDD: silicon drift detector

SEI: solid electrolyte interphase

SEM: scanning electron microscopy

SHE: standard hydrogen electrode

STEM: scanning transmission electron
microscopy

TEM: transmission electron microscopy

TGA: thermogravimetric analyses

TMOs: transition metal oxides

UV-Vis: ultraviolet–visible spectroscopy

WE: working electrode

XANES: x-ray absorption near edge
structure

XPS: x-ray photoelectron spectroscopy

XRD: X-ray diffraction

ZIB: zinc-ion battery

ZnVair: zinc vanadate obtained in air

ZnVAr: zinc vanadate obtained in argon

ZnVC: carbon coated zinc vanadate

ZnVF: zinc vanadate flowers

ZnVO: zinc vanadate

ZnVS: zinc vanadate precursor

ZnVW: zinc vanadate nanowires

Instructional notes

Acronyms of terms ending in -microscopy, -chemistry, -voltammetry or -spectroscopy, refer to -microscope, -chemical, -voltammogram and -spectrum/spectra, as well. Abbreviations are used in plural form by adding “s”.

Contents

Preface and Acknowledgments	I
Contributions during Ph.D. project	III
Abstract	V
Abstract-Danish	VII
Acronyms and instructional notes	IX
Chapter 1 Background	1
Chapter 2 Battery system	5
2.1 Introduction	5
2.1.1 Principle of LIB	6
2.1.2 Principle of aqueous ZIB	8
Chapter 3 Vanadium-based materials	13
3.1 Vanadium oxides	13
3.1.1 Introduction for vanadium oxides	13
3.1.2 Vanadium oxides in LIB	14
3.1.3 Vanadium oxides in ZIB	24
3.2 Ternary vanadate	29
3.2.1 Introduction for ternary vanadate	29
3.2.2 Ternary vanadate in LIB	30
3.2.3 Ternary vanadate in ZIB	35
3.3 Summary and perspective	39
Chapter 4 Methods and characterization	49
4.1 Methods	49
4.1.1 Precipitation method	49
4.1.2 Microwave method	49
4.1.3 Electrode preparation and battery assemble	50
4.2 Material characterization techniques	51
4.2.1 X-ray diffraction	51
4.2.2 Scanning electron microscopy	51
4.2.3 Transmission electron microscopy	53
4.3 Electrochemical techniques	54
4.3.1 Cyclic voltammetry	54
	XI

4.3.2 Electrochemical impedance spectroscopy	56
4.3.3 Galvanostatic charge and discharge.....	57
4.3.4 Galvanostatic intermittent titration technique	58
Chapter 5 Nitrogen-doped carbon coating on zinc vanadate as lithium anode.....	61
Chapter 6 Zinc vanadate cathode applied in zinc-ion batteries	85
Chapter 7 $V_3O_7 \cdot H_2O$ nanobelts/rGO cathode for zinc-ion batteries	115
Chapter 8 Conclusion and perspectives.....	151
Appendix	155

Chapter 1

Background

The constant occurrence of extreme weather attracts much attention of the mankind to climate change in recent years, and the experts in meteorological science attribute this unusual phenomenon to global warming because of the greenhouse gas emissions. [1] Thus, many countries signed the Paris agreement to ease global warming in 2015 by reducing greenhouse gas emissions and deal with the impacts of climate change. Since non-renewable fossil fuels supply about 80% of the global energy consumption, [2] energy sector innovation is treated as the most possible way to achieve the aims, like promotion of renewable energies to phase out fossil fuel.

To date, numerous countries developed variety of policies to explore the renewable energy and also invested much on the relative projects to meet the targets. [3] In some pioneer counties, solar and wind energy have become the commercial power supply. For example, about 47% of Denmark's total electricity consumption was supplied by wind power in 2019. However, it should be noted that the renewable energy production strongly depends on location and local weather conditions. [4] This uncertainty will lead to an unstable and interrupted power supply. A possible solution to this issue is to optimally combine various renewable energy resources and energy storage system. Among the various type of energy storage system, like supercapacitor, battery, fuel cell, *etc*, battery system has high operating voltage, high energy density, and low maintenance requirements. [5]

Research into battery technologies have been going on for decades, like Ni-Cd batteries, Pb-acid batteries and lithium-ion batteries (LIBs). Since the first commercial LIB entered the market in 1991, it has become the most ubiquitous and the dominant mobile power sources for various applications, such as portable electronic devices and vehicles. [6] With the innovation and engineering in materials and designs during the last three decades, the energy density of LIBs has been increasing over 150 W h kg^{-1} at the cell level, close to the theoretical limits. [7] Though battery technology has attained many breakthroughs, there is an ever-growing demand for better battery performance. Even worse, there are

still many critical challenges that should be overcome to meet the demand of emerging applications, like safety issue, high cost, further improving the energy density and battery life. As a result, the search for suitable electrode material for LIBs and alternative low-cost aqueous multi-ion battery are ongoing studies.

Presently, the most current choices of cathode and anode materials for LIBs are lithium metal oxides (lithium iron phosphate and lithium cobalt oxide) and graphite, respectively, due to their flat working potential, low cost, and abundant material supply. [8] However, the theoretical capacities for these cathode and anode electrode are lower than 200 and 372 mAh g⁻¹, respectively. [9] For further improving power and energy densities of LIB, alloy-type and transition metal oxide anode has been intensively investigated because of its high capacity. The alloying between lithium and electrode materials can reach extremely high capacity up to 1000 mAh g⁻¹. The extensive volume variation of over 300% from the alloying of the electrode hinders the practical applications. However, collapse of the structure, severe electrode pulverization and capacity loss are the result. [10] Additionally, the pure metal substances like Sn metal and V metal are not in their natural forms, resulting in high material processing fee. By comparison, the metal oxide electrodes exhibit high capacity by storing lithium in reversible redox reactions and many of them (e.g. MnO₂, Fe₂O₃, and V₂O₅) can be used as electrode materials in their natural forms (pyrolusite, hematite, and limonite). [11-13] Poor electronic and ionic conductivity of the metal oxides are great challenges. Fortunately, nanotechnology can be introduced to solve the above issue by designing the electrode on the nanoscale to shorten the diffusion distance, provide more electroactive sites and more room to accept the volume change. [14] Additionally, the lithium dendrite formation can be avoided in some metal oxide. [15] Thus, high capacity, low cost and safety make metal oxides-based materials to be promising electrode candidates for next-generation LIBs.

However, the use of toxic organic electrolytes, as well as the high cost of the lithium metal and recycling for LIBs also motivates us to investigate the aqueous rechargeable multivalent-ions batteries as alternatives. These include aluminum-ion batteries (AIBs) and zinc-ion batteries (ZIBs). [16-18] Aqueous electrolytes possess over 100 times higher ionic conductivity than the organic counterparts. [19] Besides, multivalent ions, in principle, enable a very high specific capacity due to the multiple electrons involved. The aluminum ion battery can only be operated in acid solutions (pH < 4) due to precipitation of Al₂O₃ at neutral pH. ZIBs, on the other hand, exhibit unique advantages: i) the aqueous

electrolyte is either pH neutral or mildly acidic with a high ionic conductivity; ii) the zinc anode has a quite negative redox potential (-0.78 V vs. standard hydrogen electrode), leading to a high battery voltage (0.7-2.0 V) [20] and a high theoretical capacity of 820 mAh g⁻¹. [21] Unfortunately, hydrated Zn²⁺ cation has a large radius of 0.43 nm and exhibits sluggish transport kinetics in the active cathode materials, resulting in insufficient rate performance and low coulombic efficiency. [22] It is thus an urgent task to find a suitable cathode material with favorable capacity and stable structure during Zn²⁺ insertion and desorption. To date, the cathode materials of ZIBs can be divided into two categories: tunnel-type and layer-type structures.

Reference

- [1] Balasbaneh, A. T.; Bin Marsono, A. K., *Build. Environ.* **2017**, *124*, 357-368.
- [2] Rempel, A.; Gupta, J., *Energy Res. Soc. Sci.* **2020**, *69*, 101736.
- [3] Karasmanaki, E.; Tsantopoulos, G., *Energy Policy* **2019**, *131*, 111-119.
- [4] Grams, C. M.; Beerli, R.; Pfenninger, S.; Staffell, I.; Wernli, H., *Nat. Clim. Change* **2017**, *7* (8), 557-562.
- [5] Zuo, X.; Zhu, J.; Müller-Buschbaum, P.; Cheng, Y.-J., *Nano Energy* **2017**, *31*, 113-143.
- [6] Wu, T.; Chen, H.; Wang, Q.; Sun, J., *J. Hazard. Mater.* **2018**, *344*, 733-741.
- [7] Palanisamy, M.; Parekh, M. H.; Pol, V. G. *Adv. Funct. Mater.*, **2020**, *30* (46), 2003668.
- [8] Maleki Kheimeh Sari, H.; Li, X., *Adv. Energy Mater.* **2019**, *9* (39), 1901597.
- [9] Goriparti, S.; Miele, E.; De Angelis, F.; Di Fabrizio, E.; Proietti Zaccaria, R.; Capiglia, C., *J. Power Sources* **2014**, *257*, 421-443.
- [10] Zhang, W.-J., *J. Power Sources* **2011**, *196* (1), 13-24.
- [11] Chaudhari, N. K.; Kim, M.-S.; Bae, T.-S.; Yu, J.-S., *Electrochim. Acta* **2013**, *114*, 60-67.
- [12] Gupta, P. K.; Bhandari, A.; Bhattacharya, J.; Ganesh S Pala, R., *J. Power Sources* **2020**, *450*, 227619.
- [13] Weimer, L.; Braun, T.; Hemdt, A. v., *Resour. Policy* **2019**, *64*, 101473.
- [14] Xin, S.; You, Y.; Wang, S.; Gao, H.-C.; Yin, Y.-X.; Guo, Y.-G., *ACS Energy Lett.* **2017**, *2* (6), 1385-1394.
- [15] Chen, L.; Connell, J. G.; Nie, A.; Huang, Z.; Zavadil, K. R.; Klavetter, K. C.; Yuan, Y.; Sharifi-Asl, S.; Shahbazian-Yassar, R.; Libera, J. A.; Mane, A. U.; Elam, J. W., *J. Mater. Chem. A* **2017**, *5* (24), 12297-12309.

-
- [16] Tian, Y.; An, Y.; Wei, C.; Xi, B.; Xiong, S.; Feng, J.; Qian, Y., *ACS Nano* **2019**, *13* (10), 11676-11685.
- [17] Lou, X.; Lin, C.; Luo, Q.; Zhao, J.; Wang, B.; Li, J.; Shao, Q.; Guo, X.; Wang, N.; Guo, Z., *ChemElectroChem* **2017**, *4* (12), 3171-3180.
- [18] Guan, J.; Li, Y.; Guo, Y.; Su, R.; Gao, G.; Song, H.; Yuan, H.; Liang, B.; Guo, Z., *ACS Sustainable Chem. Eng.* **2017**, *5* (1), 1026-1032.
- [19] Tang, B.; Shan, L.; Liang, S.; Zhou, J., *Energy Environ. Sci.* **2019**, *12* (11), 3288-3304.
- [20] Fang, G.; Zhou, J.; Pan, A.; Liang, S., *ACS Energy Lett.* **2018**, *3* (10), 2480-2501.
- [21] Zhao, K.; Wang, C.; Yu, Y.; Yan, M.; Wei, Q.; He, P.; Dong, Y.; Zhang, Z.; Wang, X.; Mai, L., *Adv. Mater. Interfaces* **2018**, *5* (16), 1800848.
- [22] Wei, T.; Li, Q.; Yang, G.; Wang, C., *J. Mater. Chem. A* **2018**, *6* (41), 20402-20410.

Chapter 2

Battery system

2.1 Introduction

In current market, there have been amount of rechargeable batteries in different shapes and sizes, including some coin cells, flexible batteries and megawatt systems to stabilize the electrical distribution network. [1] But batteries all consist of electrolyte, current collectors, a cathode where reduction occurs, and an anode where oxidation takes place along with the electrons transferring to an external circuit via an electronic conductor (discharging mode). The electrochemical reaction can be followed by counting the number of electrons released per unit of time, i.e. I , as shown in the equation 2.1. Battery capacity is measured by counting the amount of charge, normalized to weight, released during discharge or absorbed during charge. For certain material, there is a relationship between the mass of the material and the charge passed in the reaction, described in equation 2.2. Therefore, the theoretical capacity of an electrode is calculated by equation 2.3: [2, 3]

$$I = \frac{dQ}{dt} \quad (2.1)$$

$$m_i = \frac{M_i Q}{nF} \quad (2.2)$$

$$Q_t = \frac{nm_i F}{M_i} \quad (2.3)$$

where ‘ n ’ is the number of electrons involved in the reaction; ‘ m_i ’ is the mass of a specie; ‘ M_i ’ is the molar mass of the specie; ‘ F ’ is Faraday’s constant. It is obvious that the more electrons are involved during the battery reaction, the higher capacity that can be achieved. Metal oxides with high oxidation states can thus exhibit an excellent specific capacity. [4] Actually, the total achieved capacity of a battery is often limited by the electrode (either the anode or cathode) that delivers the smaller capacity, highlighting the importance of matching the capacity of cathode and anode.

The power density of a cell is restricted by the current and voltage. The voltage in a battery is the potential difference between two half-cells. While standard potential U^0 in

each cell is thermodynamically determined at equilibrium. For standard conditions (activities = 1; T = 298 K; P = 1 atmosphere), U^0 is described as following:[5]

$$U^0 = -\frac{\Delta G_r^0}{nF} \tag{2.4}$$

where ‘ ΔG_r^0 ’ is the free energy of a reaction. The reaction will be spontaneous if the ‘ ΔG_r ’ is negative. For a battery system, the reactions during the discharge process are spontaneous. Fig. 2.1 collects standard redox potentials (*vs.* standard hydrogen electrode, SHE) for various chemical substances at 25 °C. [6] It ranks the standard reduction potentials according to their oxidizing and reducing abilities. The strongest reductant in the table is metallic lithium, with the lowest U^0 of about -3.05 V *vs.* SHE. Considering the lightest metal of Li, LIB possesses considerable energy density and power density.

	Half Reaction				Potential	
increasing strength as an oxidizing agent	F_2	+	$2e^-$	\rightleftharpoons	$2F^-$	+2.87 V
	Pb^{4+}	+	$2e^-$	\rightleftharpoons	Pb^{2+}	+1.67 V
	Cl_2	+	$2e^-$	\rightleftharpoons	$2Cl^-$	+1.36 V
	Ag^+	+	$1e^-$	\rightleftharpoons	Ag	+0.80 V
	Fe^{3+}	+	$1e^-$	\rightleftharpoons	Fe^{2+}	+0.77 V
	Cu^{2+}	+	$2e^-$	\rightleftharpoons	Cu	+0.34 V
	$2H^+$	+	$2e^-$	\rightleftharpoons	H_2	0.00 V
	Fe^{3+}	+	$3e^-$	\rightleftharpoons	Fe	-0.04 V
	Pb^{2+}	+	$2e^-$	\rightleftharpoons	Pb	-0.13 V
	Fe^{2+}	+	$2e^-$	\rightleftharpoons	Fe	-0.44 V
	Zn^{2+}	+	$2e^-$	\rightleftharpoons	Zn	-0.76 V
	Al^{3+}	+	$3e^-$	\rightleftharpoons	Al	-1.66 V
	Mg^{2+}	+	$2e^-$	\rightleftharpoons	Mg	-2.36 V
	Li^+	+	$2e^-$	\rightleftharpoons	Li	-3.05 V

Fig. 2.1 Lists of half-cell reactions written as reduction reactions with potentials at standard conditions.

2.1.1 Principle of LIB

LIB, one of the promising energy storage techniques, has been widely applied in some electronics, because of the high energy density and excellent cycling performance. [7] A rechargeable LIB consists of the cathode, anode, separator, electrolyte, and current collectors, see Fig. 2.2, where Al is for the cathode and Cu is for the anode. In the discharge

process, Li^+ ions will be extracted from anode, diffusing through electrolyte, and inserted into cathode. This is accompanied by electrons flowing from anode to cathode through the external circuit, which is a reverse of the charging process. It is also described as a “rocking-chair” battery indicating the lithium ions “rock” forth and back between two electrodes during charge/discharge process.[8] The working principle of the LIB based on intercalation has been widely used since the discovery of intercalation compounds proposed by Goodenough *et al.* [8] Along with the discovery of the highly reversible carbonaceous materials, the first-generation LIB is a layered $\text{Li}_{1-x}\text{CoO}_2$ /graphite Li_xC_6 cell. Detailed redox reactions during discharge process are described as follows: [9]

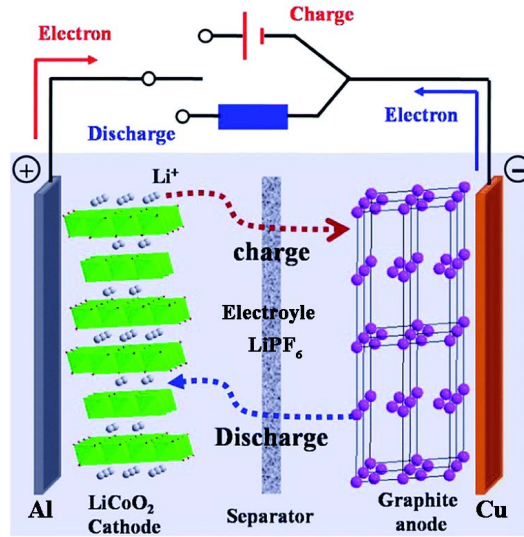
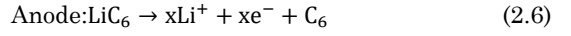
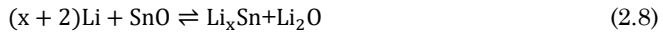


Fig. 2.2 Schematic illustration of LIBs. Reproduced with permission from [9]

In LIBs, the cathode is often lithium intercalated transition metal oxide, hydrogen phosphates and metal phosphates with layered structure due to the flexibility and ability to adapt to the geometry of the guest ion intercalation. [10] Despite the difference in chemical composition, the reaction mechanism can be described as in Equation 2.5. For anodes, the crystalline structure will be more complicated due to the various choices, such as intercalation/deintercalation, conversion, and alloy/de-alloy materials. [11] The

carbon-based materials with layered structure have high stability in thermal and high electronic conductivity sharing the same electrochemical mechanism with that of the above cathodes, and it can be described as the equation 2.6. [12] Materials reacting with lithium according to alloy/de-alloy mechanism consist of silicon oxide, tin oxide, silicon, and zinc *etc.*, showing the reaction example in equation 2.8. [13] The conversion-type electrode materials include metal compounds like phosphides, oxides, nitrides. [14] Take metal oxide as an example, these compounds react with lithium in a redox reaction along with formation of lithium compounds, showing in equation 2.9. In recent researches, the electrodes are generally designed to be composites with mixed mechanisms. [15]



2.1.2 Principle of aqueous ZIB

Unlike LIB, the components of the rechargeable aqueous ZIB are zinc metal anode, Zn^{2+} host-type cathode, and aqueous electrolyte. There are various attractive features: i) near-neutral or slightly acidic electrolyte; ii) highly negative U^0 of zinc compared to other metal based anodes; iii) high abundance of Zn; iv) safety and non-toxicity of aqueous ZIB; v) low requirement to the environment where the battery is assembled in comparison to LIB. [16] Therefore, there is a great potential for the commercialization of ZIB, and it is gaining considerable research attention. [17] To date, there are six main types of cathode materials: Mn-based materials; Prussian blue analogs; V-based materials; polyanion compounds; Chèvre phase compounds; sustainable quinone. [18] Though various cathode materials for ZIB have been studied, the energy storage mechanism of the ZIB is still debatable and ambiguous. Currently, there are four kinds of mechanisms that have been proposed: i) traditional Zn^{2+} ion intercalation process; ii) dual ion insertion in the host materials, like H^+ and Li^+ ; iii) reversible chemical conversion reactions with charge transfer; iv) coordination reactions with organic cathodes (Fig. 2.3). [19]

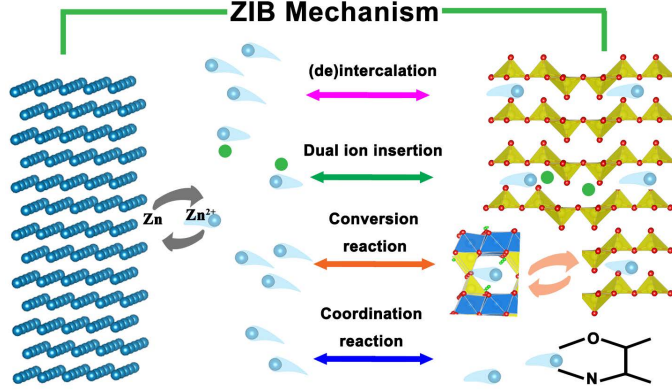
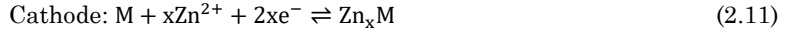


Fig. 2.3 Schematic illustration of ZIBs.

The energy storage mechanism of the reversible Zn^{2+} insertion/extraction in the cathode materials is the most typical one. In the discharge process, the zinc metal anode will be oxidized to release zinc ions, which will intercalate into the cathode to reduce the host materials. The process is summarized as follows: [18]



Where 'M' represents the cathode materials, which often show tunnel-type, layered-type, or open-framework structures, possessing sufficient room for the intercalation of Zn^{2+} . Examples include manganese oxides with various sizes of tunnels, vanadium oxides with layered structures and Prussian blue analogs displaying 3D open-framework structures.

Theoretically, the host materials with large tunnels or large lattice spacing allow a simultaneous insertion of large hydrate zinc ion and other ions (such as H^+) with a high diffusion kinetics. This mechanism has been observed in both manganese oxide and vanadium oxides. For example, the co-insertion of H^+ and Zn^{2+} into MnO_2 cathode, leading to a transition from MnO_2 to $\text{MnO}_2\text{H}_{0.25}\text{Zn}_{0.1}$ to $\text{MnO}_2\text{H}_{0.45}\text{Zn}_{0.2}$. [20] Besides, enriching the electrolyte composition by adding other metal ion salt can also achieve the dual/multi ions co-insertion process.

If the intercalation process is considered as the diffusion-controlled capacity contribution without changing the crystal structure of the host materials, the chemical conversion

reaction mechanism with electron transfer (ET) involved will be attributed to the Faraday's capacity contribution. Hence, ET related conversion reactions exhibit higher capacity than pure intercalation reactions. An example of this kind reaction include both the guest ions inserting into the host material of MnO_2 , and the H^+ reacting with MnO_2 to form a new crystal phase MnOOH to release more electrons. [21] This chemical conversion mechanism is an effective and promising method to design a high-performance ZIB.

The fourth reported mechanism is the using of coordination reactions to store energy. It is observed on the organic polymers including some linkers on metal-organic frameworks (MOFs) and covalent organic frameworks (COFs). Organic polymers as the cathode electrode have abundant functional groups, such as N-H and C=O, which can coordinate with Zn^{2+} to with $\text{C}=\text{O}\cdots\text{Zn}$ interactions. [22] These kinds of interactions are reversible to form and break, accompanied by the storage and release of energy.

Reference

- [1] Kwade, A.; Haselrieder, W.; Leithoff, R.; Modlinger, A.; Dietrich, F.; Droeder, K., *Nat. Energy* **2018**, 3 (4), 290-300.
- [2] Goodenough, J. B.; Park, K.-S., *J. Am. Chem. Soc.* **2013**, 135 (4), 1167-1176.
- [3] Yang, K.; Hu, Y.; Li, L.; Cui, L.; He, L.; Wang, S.; Zhao, J.; Song, Y.-F., *Nano Energy* **2020**, 74, 104851.
- [4] Zhao, Y.; Wang, L. P.; Sougrati, M. T.; Feng, Z.; Leconte, Y.; Fisher, A.; Srinivasan, M.; Xu, Z., *Adv. Energy Mater.* **2017**, 7 (9), 1601424.
- [5] Bonicamp, J. M.; Clark, R. W., *J. Chem. Educ.* **2007**, 84 (4), 731.
- [6] <http://ch302.cm.utexas.edu/echem/echem-cells/selector.php?name=std-red-potentials>
Standard Reduction Potentials
- [7] Lee, J. H.; Yoon, C. S.; Hwang, J.-Y.; Kim, S.-J.; Maglia, F.; Lamp, P.; Myung, S.-T.; Sun, Y.-K., *Energy Environ. Sci.* **2016**, 9 (6), 2152-2158.
- [8] Megahed, S.; Scrosati, B., *J. Power Sources* **1994**, 51 (1), 79-104.
- [9] Xu, G.-L.; Wang, Q.; Fang, J.-C.; Xu, Y.-F.; Li, J.-T.; Huang, L.; Sun, S.-G., *J. Mater. Chem. A* **2014**, 2 (47), 19941-19962.
- [10] Or, T.; Gourley, S. W. D.; Kaliyappan, K.; Yu, A.; Chen, Z., *Carbon Energy* **2020**, 2 (1), 6-43.
- [11] Goriparti, S.; Miele, E.; De Angelis, F.; Di Fabrizio, E.; Proietti Zaccaria, R.; Capiglia, C., *J. Power Sources* **2014**, 257, 421-443.

- [12] Roy, P.; Srivastava, S. K., *J. Mater. Chem. A* **2015**, *3* (6), 2454-2484.
- [13] Liang, S.; Cheng, Y.-J.; Zhu, J.; Xia, Y.; Müller-Buschbaum, P., *Small Method* **2020**, *4* (8), 2000218.
- [14] Lu, Y.; Yu, L.; Lou, X. W., *Chem* **2018**, *4* (5), 972-996.
- [15] Hassan, A. S.; Moyer, K.; Ramachandran, B. R.; Wick, C. D., *J. Phys. Chem. C* **2016**, *120* (4), 2036-2046.
- [16] He, P.; Chen, Q.; Yan, M.; Xu, X.; Zhou, L.; Mai, L.; Nan, C.-W., *EnergyChem* **2019**, *1* (3), 100022.
- [17] Ming, J.; Guo, J.; Xia, C.; Wang, W.; Alshareef, H. N., *Mater. Sci. Eng. R Rep* **2019**, *135*, 58-84.
- [18] Fang, G.; Zhou, J.; Pan, A.; Liang, S., *ACS Energy Lett.* **2018**, *3* (10), 2480-2501.
- [19] Chen, D.; Lu, M.; Cai, D.; Yang, H.; Han, W., *J. Energy Chem.* **2021**, *54*, 712-726.
- [20] Zhao, Q.; Chen, X.; Wang, Z.; Yang, L.; Qin, R.; Yang, J.; Song, Y.; Ding, S.; Weng, M.; Huang, W.; Liu, J.; Zhao, W.; Qian, G.; Yang, K.; Cui, Y.; Chen, H.; Pan, F., *Small* **2019**, *15* (47), 1904545.
- [21] Pan, H.; Shao, Y.; Yan, P.; Cheng, Y.; Han, K. S.; Nie, Z.; Wang, C.; Yang, J.; Li, X.; Bhattacharya, P.; Mueller, K. T.; Liu, J., *Nat. Energy* **2016**, *1* (5), 16039.
- [22] Khayum M, A.; Ghosh, M.; Vijayakumar, V.; Halder, A.; Nurhuda, M.; Kumar, S.; Addicoat, M.; Kurungot, S.; Banerjee, R., *Chem. Sci.* **2019**, *10* (38), 8889-8894.

Chapter 3

Vanadium-based materials

3.1 Vanadium oxides

3.1.1 Introduction for vanadium oxides

Vanadium is widely distributed in the earth crust, but it is never found in a simple vanadium metal substance. It is often combined with other minerals, including vanadinite, carnotite, and mottramite. [1] Pure elemental vanadium is difficult to produce due to the easy contamination by other elements. Instead, vanadium oxides are relatively easy to obtain by melting and precipitation. Vanadium can form various oxides with oxidation states of V^{5+} , V^{4+} , V^{3+} , and V^{2+} . All types of vanadium oxides can be clarified into two categories. They are described as V_nO_{2n-1} and V_nO_{2n+1} family, [2, 3] covering all the reported vanadium oxides including V_3O_7 and V_6O_{11} . The representative oxides for each oxidation state are V_2O_5 , VO_2 , V_2O_3 , and VO with pure oxidation states in each structure. The different oxidation states, d-d transitions and lattice systems lead to unique properties, like the different colors of vanadium ion solution, [4] as shown in Table 3.1.

Table 3.1 The properties list of the four common vanadium oxides

Oxidation state	V^{2+}	V^{3+}	V^{4+}	V^{5+}
Chemical formula	VO	V_2O_3	VO_2	V_2O_5
Lattice system	Octahedral	Trigonal	Monoclinic/ tetragonal	Orthorhombic
Color of ion solution	Violet	Green	Blue	Yellow

The aqueous solution of the ion V^{5+} , V^{4+} , V^{3+} , and V^{2+} are yellow, blue, green and violet, respectively, corresponding to different d-d transitions and optical characteristic wavelengths. Hence, the oxidation state changes can be identified by the colors. There are also some vanadium oxides with different oxidation states of the vanadium, and the crystal structures are also various. It is believed that the mixed oxidation states in the same material can bring a high electron conductivity. Besides, the vanadium oxides are

generally formed with some polyhedra in the crystal to exhibit in tunnel-type or layered-type structures. Therefore, vanadium oxides with mixed oxidation states and fascinating crystal structures make them to be the promising electrode candidates for batteries work in the intercalation mechanism.

3.1.2 Vanadium oxides in LIB

In terms of the battery performances, parameters like capacity and cell potential are crucially related to the intrinsic property of the positive and negative electrode materials. In practice, capacity determines the function time of the battery and high cell potential leads to smaller number of electrons to power the electronics. [5] Fig. 3.1 gives the potential and capacity of the reported electrode materials. For rechargeable LIB in half cell assembled testing with Li metal are generally treated as the reference and counter electrode. It is noted that vanadium-based materials either have a high cell potential (vanadium oxides) or deliver high capacity (vanadate with ternary metal oxides).

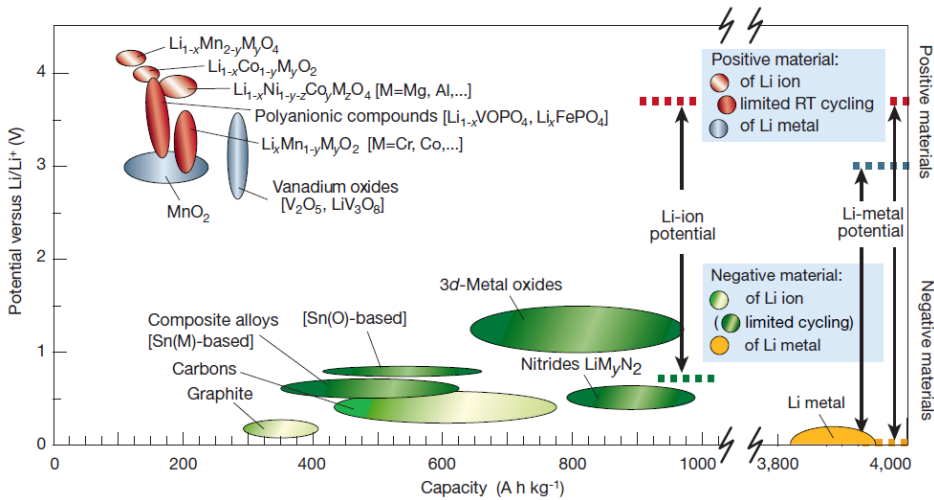


Fig. 3.1 Potential vs. capacity for both anode and cathode materials for rechargeable Li-based cells.
Reproduced with permission from [5]

Vanadium (V) oxide (V₂O₅) is the most common vanadium oxide, displaying a unique layered crystalline structure serving as the insert space of lithium-ion. V₂O₅ is cheap, and easy to synthesize. It also has high theoretical capacity of 443 mAh g⁻¹, indicating 1 mol V₂O₅ accommodating 3 mol of Li⁺ insertion and extraction. [6] Nevertheless, it also provides a wide working potential window of about 3.5 V vs. Li/Li⁺, endowing it as a

promising positive electrode candidate for LIB. Fig. 3.2 presents the V_2O_5 crystal structure that is often investigated as the electrode in LIB. Its crystalline structure in the 3D sketch with three axes, with an orthorhombic phase with lattice parameters of $a = 11.4985 \text{ \AA}$, $b = 3.5502 \text{ \AA}$, and $c = 4.3432 \text{ \AA}$. It is obvious that the V_2O_5 is constructed by a series of VO_5 pyramids forming the layered structure. The oxygen atoms in the pyramids are bonded with two or three vanadium atoms, and the V-O bond interaction in the adjacent layer is weak. [7] Li^+ has an ionic radius of about 0.76 \AA [8], and supposedly to intercalate perpendicularly into the c-axis with the layered character of the host materials maintained. And the Li^+ insertion leads to a series of phase transformations even irreversible changes, which may make the energy storage performance decay. It highlights that the repeatable charge and discharge process requires stable structure. The low electronic and ionic conductivity of V_2O_5 also limit its performance. Besides, the toxicity of V_2O_5 to humans should also be taken seriously. Inhalation and exposure to the materials will lead to damage to the respiratory system and the skin. Herein, caution is needed when dealing with V_2O_5 .

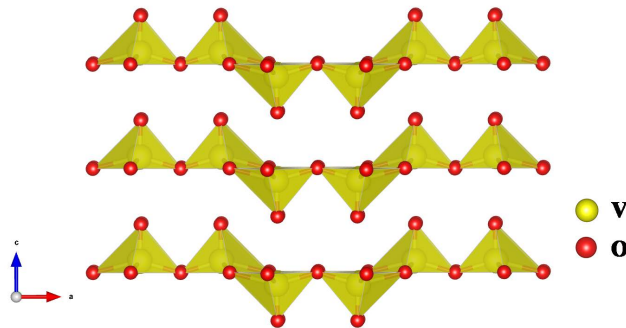


Fig. 3.2 The crystalline structure of the V_2O_5 .

For the reaction mechanism of the V_2O_5 , several phases of $\text{Li}_x\text{V}_2\text{O}_5$ can be obtained from $\epsilon\text{-Li}_{0.5}\text{V}_2\text{O}_5$, $\delta\text{-LiV}_2\text{O}_5$, and $\gamma\text{-Li}_2\text{V}_2\text{O}_5$ and finally to the $\omega\text{-Li}_3\text{V}_2\text{O}_5$ phase with 3 units of Li^+ intercalations with increased puckering in the crystal phase layers.[9] The corresponding phase transformation process is shown in Fig. 3.3. However, the rock-salt $\omega\text{-Li}_3\text{V}_2\text{O}_5$ phase formation is irreversible because amount of lithium cannot deintercalate from the structure, leading to a decay in battery capacity. In the initial lithium intercalation process, $\alpha\text{-Li}_x\text{V}_2\text{O}_5$ ($x < 0.1$), $\epsilon\text{-Li}_x\text{V}_2\text{O}_5$ ($0.35 < x < 0.7$), and the $\delta\text{-LiV}_2\text{O}_5$ ($0.9 < x < 1$) have small energy differences, making it difficult to distinguish the transition process in electrochemical method. [10] Additionally the transition voltage plateaus are very close

at 3.4 and 3.2 V for α to ϵ and ϵ to δ respectively, and the intercalation process maintains the V_2O_5 skeleton without alteration of the matrix. When more than one Li is intercalated, an irreversible structure will be formed, leading to the transition from δ - LiV_2O_5 to γ - $Li_2V_2O_5$ with a potential plateau shown at 2.3 V. The double chain of the V_2O_5 framework will be slightly puckered with the pyramids alternating up and down individually and tilting the apical oxygen atoms on two pyramids closer to each other. With increased cycling, the amount of γ - LiV_2O_5 increases as well. This formation process also depends on some parameters, like crystalline morphology and discharge depth. When the V_2O_5 is deeply discharged lower than 2 V, the deintercalation reaction is severely hindered due to the formation of ω - $Li_3V_2O_5$ phase. Accordingly, to avoid the irreversible reactions, the potential range of the V_2O_5 is generally set at 2-4 V involving intermediates with stable morphology which supports reversible intercalation/deintercalation. In this case, there are 2 units of Li^+ involved with a capacity of 294 mAh g^{-1} .

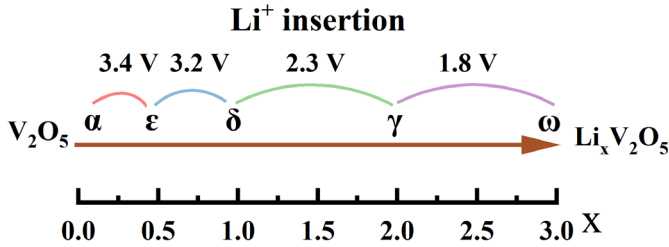


Fig. 3.3 Schematic illustrating the different amount of Li inserted in V_2O_5 .

Apart from V_2O_5 , the metastable VO_2 with a vanadium oxidation state of +4 is investigated as the cathode materials as well. It is made of a double-shear derivative structure with distorted VO_6 octahedra sharing both corner and edge, as shown in Fig. 3.4a. The monoclinic phase constants are $a = 9.06 \text{ \AA}$, $b = 5.772 \text{ \AA}$, $c = 4.520$, $\alpha = 89.99^\circ$, $\gamma = 91.4^\circ$, $\beta = 89.83^\circ$. VO_2 has perovskite-like cavities with four capped faces, allowing the Li^+ diffusion parallel to the $[010]$ crystal orientation. The edge-sharing in the expansion direction prevents V-O bond cleavage, creating a relatively stable structure.[11] There are also some other vanadium oxides with mixed oxidation states of vanadium confirmed to be the promising cathode materials for LIBs. For example, the structure of V_3O_7 is described as layers, consisting of VO_6 octahedra and VO_5 trigonal bipyramids with mixed vanadium oxidation states of V^{4+} and V^{5+} in a ratio of 1:2. With the insertion of crystal

water in the layer, $\text{V}_3\text{O}_7 \cdot \text{H}_2\text{O}$ exhibits high capacity retention, due to the large lattice spacing. Its crystal structure is shown in Fig. 3.4b, with an orthorhombic crystalline phase ($a = 16.930 \text{ \AA}$, $b = 9.359 \text{ \AA}$, $c = 3.644 \text{ \AA}$, $\alpha = \gamma = \beta = 90^\circ$). V_6O_{13} as another mixed-valence oxide (V^{5+} and V^{4+} : the mol rate 1:2) is studied as the electrode materials, composed of single and double vanadium oxide layers. Fig. 3.4c represents the 3D crystal structure of the V_6O_{13} with monoclinic phase ($a = 11.922 \text{ \AA}$, $b = 3.68 \text{ \AA}$, $c = 10.138 \text{ \AA}$, $\alpha = \gamma = 90^\circ$, $\beta = 100.87^\circ$). The adjacent layers provide the active sites for lithium intercalation. With all of the vanadium reducing to V^{3+} , there will be 8 units of Li^+ involving in the redox reaction of per unit, suggesting a high capacity of 417 mAh g^{-1} . The energy storage mechanism is in agreement with the Li-ion intercalation process, but the phase transition process during the intercalation process is still ambiguous.

To pursue an excellent electrochemical performance of the vanadium oxides, various strategies have been reported, such as morphologies engineering, size controlling to nanoscale, synthesizing composites and doping with other ions.

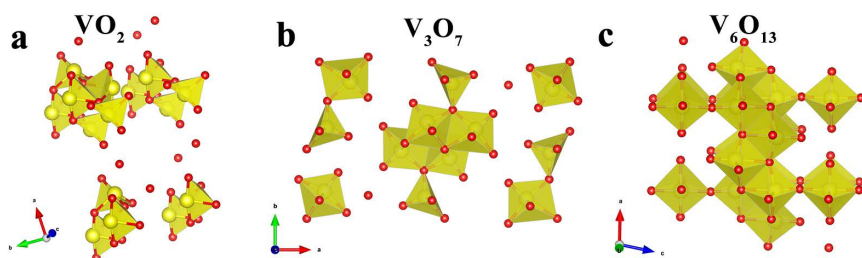


Fig. 3.4 Crystalline structure of VO_2 , V_3O_7 and V_6O_{13} .

3.1.2.1 Morphologies Engineering

The morphologies of the pure vanadium oxide nanomaterials used as the cathode electrode of LIB vary from 0- to 3-dimensional. To date, many researchers are committed to designing the electrode materials with fancy morphologies, such as core-shell, porous, and nanoscale. It cannot be neglected that the morphology effect on the electrochemical performance is also sensitive to the lithiation mode, determined by the potential window difference. If one Li^+ is transferred per V_2O_5 unit, the potential window is typically 2.5-4V, and the two Li^+ transfer mode needs the potential window of 2-4 V. For a much broader potential window like 1.5-4 V, there will be three electrons/ Li^+ transferred during the intercalation process. Table 3.2 summarizes the V_2O_5 cathode materials in different morphologies from 0D to 3D. As listed, the V_2O_5 materials with three electrons

transferred typically exhibit much high capacity but low capacity retention, due to the irreversible reactions. Zhai and coworkers [12] synthesized centimeter-long V_2O_5 nanowires by the hydrothermal method. When used in the three-electron transfer mode, the initial discharge capacity can reach up to 351 mAh g^{-1} , but it declines to 175 mAh g^{-1} already after 20 cycles, leading to capacity retention of 43%. Herein, ω phase formation is an irreversible reaction process. Two-electron transfer mode is the most typical mechanism with a capacity of 294 mAh g^{-1} . Although the morphology of V_2O_5 varies, its reversible capacity exhibited in all morphologies is over 200 mAh g^{-1} but less than 300 mAh g^{-1} along with relatively high capacity retention. The V_2O_5 with one electron transferred delivers low capacity due to the theoretical capacity of 147 mAh g^{-1} , but with excellent cyclic stability even at a high current density. Thus, the morphology effect on the energy storage performance should be investigated in the same insertion mode. For example, Wang *et al.* [13] fabricated V_2O_5 in porous nanotubes, nanofibers, and nanobelts morphologies in 1-D by electrospinning techniques and subsequent annealing. The morphology can be tailored by adjusting the annealing temperature: 400°C for porous nanotubes, 500°C for hierarchical nanofibers, and 600°C for single-crystalline nanobelts. When used as the cathode electrode of LIB, porous nanotubes show an initially discharge capacity of 114.1 mAh g^{-1} due to the porous structure providing efficient electron transfer, short Li^+ diffusion distance, exposing a high area of the active sites. But the porous structure shows limited stability, which is more obvious for two-electron transfer mode. In comparison, the solid single crystal nanobelt exhibits superior cyclic-capacity retention in the same insertion mode. The authors explained that it is because of the crystal orientation of the V_2O_5 . If the intercalation plane is perpendicular to the long propagation axis, significant stress can be withstood without disintegration, leading to an excellent tolerance of the intercalation process.

Table 3.2 The summary of V_2O_5 cathode electrode for LIB in various morphologies.

Morphology	Synthesis method	Reversible capacity [mAh g ⁻¹]	Cycle	Current density [mA g ⁻¹]	Voltage Window [V]	Capacity retention [%]	Ref.
0-D nanoparticle (150 nm)	Template	229	50	300	2-4	92	[14]
0-D nanoparticle (1-5 nm)	Sol-gel	244	50	300	2.1-4	83	[15]

1-D nanotubes (560 nm)	Electrospun	95	250	2000	2.5-4	80.5	[13]
1-D nanobelts (5-50 nm)	Stirring treatment	242	50	60	2-4	86	[16]
1-D nanorod (100-200 nm)	Thermal decomposition	240	30	147	2-4	90.2	[17]
1-D nanowires (80-120 nm)	hydrothermal	175	20	50	1.5-4	43	[12]
2-D microflakes (2 μ m)	hydrothermal	210	50	44	1.5-3.8	60	[18]
2-D thin film (3-30 nm)	Deposition	142	50	50	2.6-4	100	[19]
2-D nanosheets (60-80 nm)	Ultrasonication	206	100	500	2-4	78	[20]
2-D nanosheets (2.1-3.8 nm)	Liquid exfoliation	250	300	294	2-4	93.8	[21]
3-D hollow microsphere (300 nm)	Precipitation at room-temperature	200	100	2400	2-4	89.7	[22]
3-D flower structure (microscale)	Hydrothermal	210	100	29	1.75-4	84	[23]
3-D hierarchical starfish-like (100-300 nm)	Sol-gel	214	60	200	1.5-4	46	[24]
3-D yolk-shelled microsphere (1 μ m)	Solvothermal	227	50	300	2-4	89	[25]
3-D yolk-shell (1 μ m)	Hydrolytically	218	100	300	2-4	79.3	[26]
3-D octahedrons (2 μ m)	Hydrothermal	96	500	2000	2.4-4	98.5	[27]

Fig. 3.5 shows the representative vanadium (V) oxides (V_2O_5) morphologies applied in LIB cathodes. Besides V_2O_5 , other types of vanadium oxides (VO_x) also can be applied in LIB as the cathode electrodes. Due to the complicated crystal structure and fabrication process, a few research groups are focusing on fabricating pure VO_x as LIB cathode electrodes. Three representative examples are summarized: VO_2 , V_3O_7 , and V_6O_{13} . Mai *et al.* [28] fabricated hybrid VO_2 composite in 1-D morphology of nano-scrolls, nanobelts, and nanowires by a hydrothermal process. By investigating the stability of the VO_2 in different potential windows, the energy storage mechanism is proposed to be the same as that in V_2O_5 . In a potential window of 1.5-4V, 1D hybrid VO_2 delivers 248 mAh g^{-1} , which dramatically decreases 52% after 100 cycles. While in a voltage range of 2-3 V, the capacity retention can reach 85% (134 mAh g^{-1}), which can be explained by irreversible reactions occurring at low voltages due to disorder and destruction of the layered structure, ultimately leading to the capacity fading. In comparison, the nanowire-assembled 3-D hollow microspheres [29] in the same potential range exhibit 90% capacity retention (about 175 mAh g^{-1}) because the 3D morphology provides higher specific surface area. As for V_3O_7 and V_6O_{13} , the voltage potential window is confined into a range of 1.5-4 V generally with low capacity retention and the morphology is 1D nanowire and nanorod.

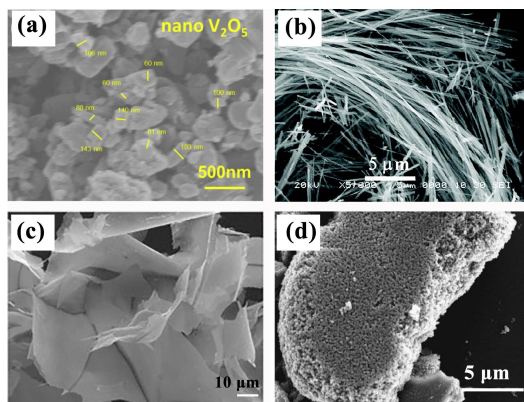


Fig. 3.5 Example of V_2O_5 electrode materials in a) 0-D nanoparticles; [14] b) 1-D nanowires; [18] (c) 2-D nanosheets; [20] and d) 3-D porous architecture. [30] Reproduced with permission from [14, 18, 20 and 30]

To summarize, although the lithium-ion insertion mode can affect the electrochemical performance, the morphology effects are also verified. Innovative architectures are promoted by many researcher groups, such as porous structure with high specific surface area, but lack of stability for some of these materials needs to be considered. Making full

use of the architectures and combining them with the intercalation mechanism will help to design the practically useful cathode materials.

3.1.2.2 Composite materials

Preparing V_2O_5 composites is another common strategy to get excellent electrochemical performance, and this include various carbonaceous materials, conductive polymers, sulfide or phosphate, and other metal oxides. The synergistic effects between two different components can enhance the lithiation and intercalation process. Table 3.3 lists some representative examples of V_2O_5 -based composite electrodes. Carbon and carbonaceous materials are good additives because of their high abundance distribution, excellent electron conductivity, environmentally friendliness, and mechanical stability. There are different kinds of carbonaceous materials available, like reduced graphene oxide (rGO) or graphene, carbon nanotubes (CNTs) and graphite. The introduction of carbonaceous materials and conductive polymers (polyaniline and pyrrole) can be considered together. They can enhance the electrode performance of pure V_2O_5 by providing more active sites, improving the electron conductivity, and stabilizing the structure. For example, Mohammad and coworkers [31] fabricated V_2O_5 /mesoporous carbon by synthesizing the mesoporous carbon template first and then using an ultrasonically assisted method. The obtained composites have a high specific surface area of $77.2 \text{ m}^2 \text{ g}^{-1}$, and exhibits an excellent reversible capacity of 291, 265, and 247 mA g^{-1} at a current density of 100, 250, and 500 mA g^{-1} respectively when used as the cathode electrode of LIB. In comparison, V_2O_5 nanoparticles only show a capacity of 275, 235, and 182 mA g^{-1} at the same current densities. The capacity of the composite decays significantly during cycling testing but it's still higher than for the pure V_2O_5 nanoparticles. The authors suggested that the better performance of the $\text{V}_2\text{O}_5/\text{C}$ nanoparticle is due to the fast transport channels for Li^+ in the porous composite materials.

Carbonaceous additive in $\text{V}_3\text{O}_7 \cdot \text{H}_2\text{O}$ have been thoroughly investigated as well. Zhang *et al.* [32] synthesized $\text{V}_3\text{O}_7 \cdot \text{H}_2\text{O}@\text{C}$ core-shell structured composites by a hydrothermal process, where the carbon is derived from glucose. By changing the amount of glucose, the thickness of the coating layer can be controlled. When used as a cathode electrode of LIB, it delivers a reversible capacity of 151.2 Ah g^{-1} after 45 cycles at the potential window of 1.5-4 V. While the $\text{V}_3\text{O}_7 \cdot \text{H}_2\text{O}$ pure nanobelts only exhibit 100 mAh g^{-1} after 30 cycles, indicating an effective coating process. There are also some other strategies to produce

composites. For example, Zhang *et al.* [33] designed a $V_3O_7 \cdot H_2O$ electrode with carbon materials of multiwall CNTs and graphene-like sheets in 3D porous network. The graphite sheets link the CNTs into porous networks. Then a modified Hummer's method is applied to the carbon network to create active groups on the surface to attract metal ions. After a facile hydrothermal method, $V_3O_7 \cdot H_2O$ arched carbon composites are achieved.

Table 3.3 The summary of the V_2O_5 composite cathode electrode for LIB.

Component	Synthesis method	Reversible capacity [mAh g ⁻¹]	Cycle	Current density [mA g ⁻¹]	Voltage Window [V]	Capacity retention [%]	Ref.
V_2O_5 /C nanoparticle	Ultrasonically assisted method	163	100	500	2-4	59	[31]
V_2O_5 @C nanoparticle	Capillary-induction	296	50	1000	2-4	99	[34]
V_2O_5 /polyaniline	Electrochemical method	263	60	300	1.5-4	–	[35]
V_2O_5 /pyrrole	Sol-gel	225.4	50	30	1.8-4	91	[36]
V_2O_5 /multi-wall carbon nanotube	Hydrothermal	133	200	300	2-4	78	[37]
V_2O_5 /graphene	Solvothermal	153	100	100	2-4	60.3	[38]
V_2O_5 nanosheet/rGO	Solvothermal	102	160	600	2-4	52	[39]
FeF_3 / V_2O_5 nanoparticle	Liquid-phase method	209	30	30	2-4.5	83.5	[40]
V_2O_5 -NiO film	Laser reactive deposition	340	500	150 (0.5 C)	1-4	61	[41]
V_2O_5 - SnO_2 microtube	Sol-gel	165	50	100	2-4	44	[42]
$LiVOPO_4$ @ V_2O_5 core-shell nanosphere	Hydrothermal	135	200	30	3-4.5	90	[43]

Some transition metal compounds are also applied to form V_2O_5 -based composites. Among the listed examples, introducing transition metal compounds can lead to either special

morphologies or wide potential windows. Li *et al.* [42] synthesized $\text{V}_2\text{O}_5/\text{SnO}_2$ microtube composites by a sol-gel method employing natural cellulose microfiber as a template. Different concentrations of Sn^{2+} is used to obtain different loading of SnO_2 in the final product. The initial discharge capacity of SnO_2 -12.1 %- V_2O_5 composite reaches 375 mAh g^{-1} , much higher than the theoretical capacity of V_2O_5 (294 mAh g^{-1}), suggesting a significant capacity contribution from SnO_2 . Zhang *et al.* [43] obtained an orthorhombic LiVOPO_4 core with a tetragonal V_2O_5 shell via a hydrothermal route followed by surface oxidation treatment. Used as cathode of LIB, its potential can be up to 4.5 V. The reversible capacity delivered is much higher than other V_2O_5 with one electron transfer mode.

3.1.2.3 Doping materials

Foreign element doping into the electrode materials can produce some defects or replacing some of the metal ions in the host crystal structures, which is considered the most prevailing and effective way to improve the electrochemical performances. The electronic structure of V also can be modified. The intrinsic conductivity and lithium-ion diffusion coefficient during the intercalation process can be improved. There are some doping examples summarized in Table 3.4, showing outstanding capacity retention. Li and coworkers [44] prepared Sn-doped V_2O_5 microspheres by microwave-assisted solvothermal synthesis. The addition of Sn^{4+} ion makes the a - and c -axes of the V_2O_5 crystal structure slightly expand and the b -axis compressed. The doped ion stays between the VO_5 layers and forms a SnO_6 octahedron with the oxygen atoms in the structure.[45] Used as a cathode in LIB, Sn-doped V_2O_5 microspheres exhibit a capacity of 212 mAh g^{-1} , and the charge transfer resistance ($185 \text{ }\Omega$) is lower than for pure V_2O_5 ($263 \text{ }\Omega$). Nanostructured Mn-doped V_2O_5 is another example of doping by replacing the V ion. The effect of the doping method on the electrochemical performance of the V_2O_5 cathode is obvious when testing rate performance. The as-prepared Mn-doped V_2O_5 by Zeng et al [46] delivers the discharge capacities of 251, 214, and 171 mAh g^{-1} at 300, 600, 1500 mA g^{-1} , respectively, which are about 16% higher than the pure V_2O_5 .

Table 3.4 The summary of guest ion doped V_2O_5 cathode for LIB.

Component	Synthesis method	Specific capacity [mAh g^{-1}]	Cycle	Current density [mA g^{-1}]	Voltage window [V]	Capacity retention [%]	Ref.
Sn- V_2O_5	Microwave-	212	50	200	2-4	82	[44]

	assisted						
Cu-V ₂ O ₅	Solid-state chemical	258.7	50	300	2-4	89.5	[47]
Mg-V ₂ O ₅	Magnetron reactive sputtering	473	1	150 $\mu\text{A cm}^{-2}$	1.5-4	—	[48]
Ce-V ₂ O ₅	Solid-state chemical	239	50	150	2-4	85.1	[49]
Mn-V ₂ O ₅	Microwave reactions	201	50	300	2-4	80	[46]
Co-V ₂ O ₅	Hydrothermal method	395	50	30	2-4	69	[50]

Other representative examples of cation ion-doped vanadium oxides are listed as follows. W-doped VO₂ nanosheets in 3D networks fabricated by hydrothermal route [51] have a very fast Li⁺ diffusion coefficient ($2.62 \times 10^{-14} \text{ cm}^2 \text{ s}^{-1}$), about 5 times higher than the pure VO₂ electrode ($4.94 \times 10^{-15} \text{ cm}^2 \text{ s}^{-1}$). The 3D-flower-like Al/Na co-doped V₆O₁₃ cathodes [52] obtained by a hydrothermal method show a lower electron transfer resistance (268.6 Ω) than the pure V₆O₁₃ (465.1 Ω). Co-doped V₂O₃ nanospheres [53] exhibit an excellent reversible capacity of 923.9 mAh g⁻¹ after 800 cycles, in comparison to 328.2 mAh g⁻¹ of the pure V₂O₃. The above examples prove that cation doping can effectively enhance the electrochemical performance.

3.1.3 Vanadium oxides in ZIB

Unlike Li based electrode, Zn electrode is air- and water stable, which is considered to be the promising anode of ZIB. Finding a suitable cathode electrode for practical applications, remains as a challenge for aqueous ZIB. The limitation is the low capacity and the poor structure stability during the guest ion storage process. It is not surprising that most of the research literature on aqueous ZIB are focusing on exploring and designing cathode materials. The high discharge voltage and high specific capacity are the two main requirements for the cathode materials. The relationship between the operating potential and specific capacity is summarized in Fig. 3.6. Vanadium oxides have become important cathode materials in the ZIB due to their low cost, high abundant resource, and the many accessible oxidation states of vanadium. The vanadium oxides and vanadate have a relatively low average operating voltage (about 0.8 V) compared to other candidates but they have a high capacity.

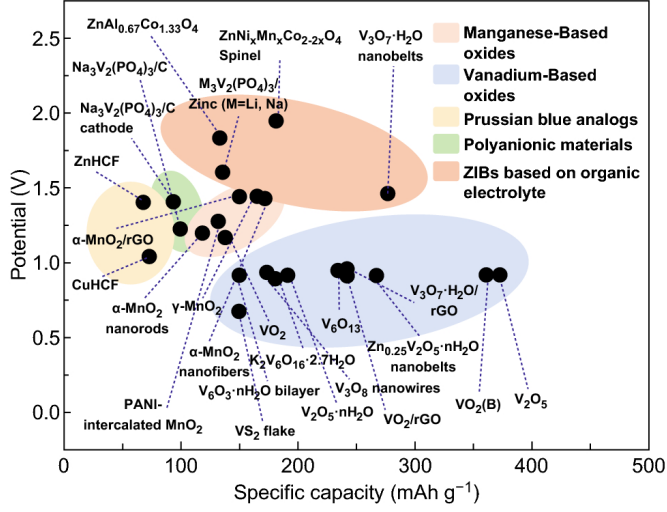


Fig. 3.6 Operating potential vs. capacity for various cathode materials. *Reproduced with permission from [54]*

Layered vanadium oxides are the most studied vanadium-based materials as cathode materials for ZIB. The stable crystal structure and diversity of vanadium are their key advantages. Generally, the V-O coordination polyhedra in vanadium oxides can be assembled into larger different units as is also known from the polyoxometallates. The common polyhedra in vanadium oxides are octahedra in distorted and regular form, tetrahedra, trigonal bipyramid, and pyramid. With the insertion of the Zn^{2+} ion in the crystal structure, the VO_x polyhedra share the corner or edge with other polyhedra to stabilize the framework while the oxidation state can change from V^{5+} to V^{4+} or even V^{3+} to fit the extra cation. Take the simplest and lowest-molecular-weight of V_2O_5 as an example, Zn^{2+} inserts into its layers by sharing the oxygen atoms from vanadium polyhedra to form fourfold coordination environment around Zn^{2+} . The reactions are summarized as follows: [55]



The number of Zn^{2+} inserted into the vanadium oxides depends on the natural properties of the materials, such as the size, conductivity and morphology. One unit of Zn^{2+} inserted into V_2O_5 results in 295 mAh g^{-1} , when vanadium is reduced from V^{5+} to V^{4+} , this is generally treated as the reference when comparing the capacity of vanadium oxides,

because V_2O_5 has the highest oxidation state and lowest molecular weight per unit of vanadium.

Table 3.5 gives a comparison between the Zn^{2+} and Li^+ charge carrier ions. It is noted that Zn^{2+} possess a similar ionic radius as Li^+ . However, the radii of the hydrated Zn^{2+} ion is about 4.3 Å, which leads to sluggish transport kinetics in the active cathode materials, and results in higher requirements for the material design. The typical cathode materials with tunnel-type and layer-type structures are expected to have large lattice spacing, which provide rich active sites to increase the contact area between the electrolyte and electrode, resulting in fast mass diffusion and reaction. [56] For example, the orthorhombic V_2O_5 crystal structure is constructed by single layered VO_5 pyramids, where the interlayer spacing is about 5.77 Å. It allows the guest Zn^{2+} to be easily transported during intercalation process. But the layered structure of V_2O_5 is interestingly unstable with the insertion of many Zn^{2+} ions, reaching a rapid capacity decline. The issue also occurs on other vanadium oxides. Thus, the design of vanadium oxides with stable structures is in high demand. Strategies are summarized in the following sections.

Table 3.5 Comparison of Zn^{2+} and Li^+ charge carrier ions.

Charge carriers	Zn^{2+}	Li^+
Electrode potential vs. SHE (V)	-0.76	-3.04
Specific gravimetric capacity (mAh g^{-1})	820	3862
Relative atom mass	65.38	6.941
Ionic radii (Å)	0.74	0.76
Specific volumetric capacity (mAh cm^{-3})	5855	2066

3.1.3.1 Insertion of other molecules or cations

The sluggish ion diffusion kinetics and collapse of the lattice structure are main issues for the aqueous battery system, causing serious electrostatic repulsion between the guest ions and the host lattice. Introducing other molecules or ions into the interlayers of the vanadium oxides has been adopted, which can enlarge the lattice spacing or change the structure type from a layered structure to a stable tunnel framework.

H_2O is one of the most commonly used pre-intercalation molecules in an aqueous battery system, exhibiting the potential to achieve low cost and fast diffusion properties. The guest molecule is intercalating into the vanadium oxide crystal structure layers during

the synthetic process to form structural water, leading to a large $[\text{VO}_x]_n$ interlayer d-spacing by weakening the van der Waals force between the layers. Therefore, the presence of water in the crystal structure can effectively reduce the electrostatic interaction between the V-O polyhedra and the Zn^{2+} ions. The abundant structural water also facilitates the Zn^{2+} ion diffusion in the structure forming hydrogen bonds. Lai *et al.* [57] have developed $\text{V}_6\text{O}_{13} \cdot n\text{H}_2\text{O}$ hollow micro-flowers by a hydrothermal process. As a control experiment, dehydrated V_6O_{13} has also been prepared by calcinating the material in Ar at 400 °C. Used as a cathode electrode of ZIB, $\text{V}_6\text{O}_{13} \cdot n\text{H}_2\text{O}$ delivers a high capacity of 292 mAh g⁻¹ after 1000 cycles at 5 A g⁻¹, in comparison to 151 mAh g⁻¹ of the dehydrated V_6O_{13} .

Pre-intercalation of cations into vanadium oxides interlayers can also significantly enhance the electrochemical performance by increasing the structural stability, ion diffusion kinetics, and electron conductivity. Cations can be Li^+ , [58] Na^+ , [59] Fe^{2+} , [60] Zn^{2+} , [61] and Ca^{2+} . [62] Taking Na^+ as an example, layered-type V_2O_5 will transform into a tunnel-type with the insertion of Na^+ . [59] The VO_6 octahedra in V_2O_5 are connected into a two-dimensional $[\text{V}_4\text{O}_{12}]_n$ layers linked by sharing oxygen atoms. VO_5 square pyramids serve as the linkers between the layers to form the new 3D tunnel-type crystal structure. The Na^+ ion is located between the $[\text{V}_4\text{O}_{12}]_n$ layers acting as “pillars” to increase the tunnel structure stability during Zn^{2+} insertion and extraction. Another example is NH_4^+ , a typical cation applied to expand the interlayer space. The intercalated NH_4^+ ion shares the same function as structural water by forming a hydrogen bond between the top and bottom layers of the V_2O_5 . [63] As a result, the interlayer distance of the NH_4^+ preintercalated $\text{V}_2\text{O}_5 \cdot n\text{H}_2\text{O}$ is about 10.9 Å, larger than that of the pure V_2O_5 with 5.77 Å.

Although the chemical intercalation of guest molecules or cations has been successful, it will also lead to some issues. For example, if there are too many water molecules, the van der Waals' force between the layers are weakened as well, leading to an unstable structure. Besides, guest ions will block the Zn^{2+} transfer channel to hinder the intercalation process. Therefore, optimizing the amount of water and guest ions is very important to achieve a favorable structure and fast kinetics simultaneously.

3.1.3.2 Conductive additives

Combining vanadium oxides with highly conductive materials is a useful way to reduce internal resistance and ameliorate charge transfer efficiency, consequently achieving enhanced electrochemical performance.

For example, carbon black is generally mechanically mixed with active material and binder to prepare the slurry for battery assembly. However, the carbon black is commonly in a nanoparticle morphology and the mechanical mixing process leads to poor contact between the carbon and active materials. Moreover, the volume variations in the vanadium oxides during the Zn^{2+} ion insertion and desertion process will further disturb the contact. Therefore, carbon black added during the battery assembly process will not be considered the best or most effective alternative. It will not be discussed further in this chapter.

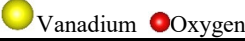
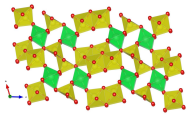
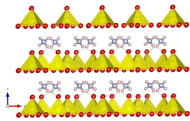
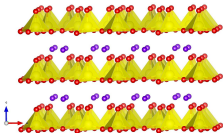
In terms of the other carbonaceous additives, CNTs, rGO, and conductive polymers are popular choices to be introduced into vanadium oxides electrodes. Yin and coworkers [64] have proposed two-dimensional CNT paper/ V_2O_5 composites as the cathode of ZIB, delivering a specific capacity of 312 mAh g^{-1} . When increasing the current density by 10-fold, capacity retention is 75% due to the random stacking arrangement of the scaffold CNT, offering great electrolyte infiltration from all directions. Graphene nanosheets with a large specific surface area are highly flexible and can support a wide range of active materials. Zang *et al.* [65] have compared the performance of the V_2O_5 active materials arched on graphene nanosheets composites (about 300 mAh g^{-1} after 5000 cycles at 2 A g^{-1}) and pure V_2O_5 active materials (about 50 mAh g^{-1}). They explain the excellent performance of the composites is mainly due to the large surface area and the fast electron transfer channels provided by the high conductivity of the graphene nanosheets. Besides, the heteroatom-doping (like P-, N-, and S-) on the carbonaceous additives can further improve the electron conductivity of the vanadium oxide composites. Another important additive is conducting polymer, which can not only provide high electronic conductivity but also serve as a protective interface to vanadium oxides. Xu *et al.* [66] proposed the poly(3, 4-ethylene dioxythiophene) coated V_2O_5 composites as a Zn-ion energy storage material with a high specific capacity of 360 mAh g^{-1} . The polymer shell is likely to increase the Zn^{2+} transport kinetics and prevent the structural collapse during cycling.

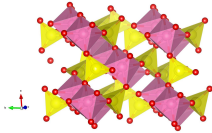
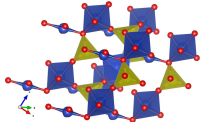
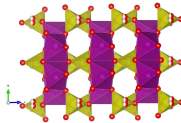
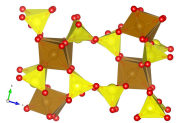
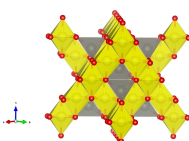
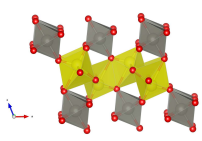
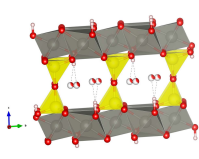
3.2 Ternary vanadate

3.2.1 Introduction for ternary vanadate

Ternary vanadate compounds ($M_xV_yO_z$, $M = NH_4^+$, Li, Ni, Cu, Co, Mn, Fe, Zn) attract considerable attention as intercalation-type electrode materials for both LIB and aqueous ZIB, due to the low cost, wide availability, stable lattice structure, and high theoretical capacity. The ternary vanadate has both the vanadium and other oxides synergistic features such as multiple oxidation states and superior electrochemical conductivity. The oxidation state of M takes values from +3 to +1, and vanadium from +5 to +2. Similar to V_2O_5 , vanadate compounds consist of various VO_x polyhedra, which are linked together to form different crystal structures. Here, I summarize some representative compounds in Table 3.6. It is challenging to directly correlate the crystal structures of the materials with their electrochemical properties due to other effects such as morphology and crystal orientations. Therefore, the detailed energy storage mechanism difference is summarized below. The effect of crystal water on vanadate-based materials structure is generally regarded as enlarging the layer spacing and is rarely discussed in literature. Herein, I classify the vanadate with and without crystal water as the same crystal structure type.

Table 3.6 The summary of the crystal system, crystal structure, and cell parameters of the various $M_xV_yO_z$.

Material	Crystal system	Crystal structure	Unit cell parameters	Ref.
				
LiV_3O_8	Monoclinic		$6.68 \times 3.60 \times 12.03$ $90 \times 107.83 \times 90$	[67]
$(NH_4)_2V_3O_8$	Tetragonal		$8.89 \times 8.89 \times 5.58$ $90 \times 90 \times 90$	[68]
$Ni_3V_2O_8$	Orthorhombic		$5.94 \times 11.42 \times 8.24$ $90 \times 90 \times 90$	[69]

CoV ₂ O ₆	Monoclinic		9.25×3.50×6.62 90×111.62×90	[70]
Cu ₃ V ₂ O ₈	Triclinic		5.20×5.35×6.50 69.22×88.69×68.08	[71]
Mn ₂ V ₂ O ₇	Monoclinic		6.18×8.72×4.96 90×103.6×90	[72]
Fe ₂ V ₄ O ₁₃	Monoclinic		8.31×9.40×14.57 90×102.23×90	[73]
ZnV ₂ O ₄	Cubic		8.41×8.41×8.41 90×90×90	[74]
ZnV ₂ O ₆	Monoclinic		9.26×3.52×6.59 90×111.37×90	[75]
Zn ₃ (OH) ₂ (V ₂ O ₇)(H ₂ O) ₂	Hexagonal		6.05×6.05×7.19 90×90×120	[76]

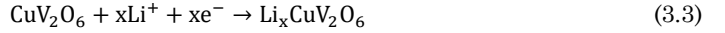
3.2.2 Ternary vanadate in LIB

3.2.2.1 Mechanism in ternary vanadate

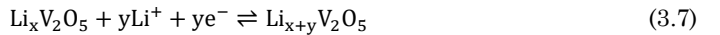
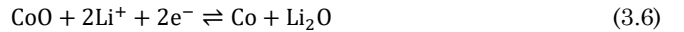
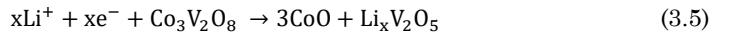
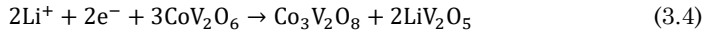
The electrochemical active voltage region of vanadate is 0-3 V (*vs.* Li/Li⁺). During the Li⁺ insertion process, the uptake of lithium ions is accompanied by the reduction of metal ions (*i.e.* M²⁺→M⁰, or even M⁰→LiM, as well as the reduction of vanadium V⁵⁺, V⁴⁺→V³⁺, V²⁺) to

maintain the overall charge balance. A previous study reveals that the ternary vanadium oxides in general exhibits an irreversible reaction during the first lithium insertion process to form M_xO_y and $Li_xV_yO_z$ composites. In the following lithiation/delithiation process, the reversible reactions occur for M_xO_y and $Li_xV_yO_z$ individually, along with the oxidation state changes. The lithiation mechanism in ternary vanadate is still unknown, however, due to the different formation of lithium vanadate phases in the discharge process.

Ternary vanadate materials are proposed to undergo an intercalation process accompanied by phase transition during the energy storage process. In 2003, Morcrette *et al.* [77] reported a new layered electrode material of copper vanadate $Cu_{2.33}V_4O_{11}$, which reversibly reacts with Li through a displacement reaction. The following energy storage mechanism is based on this principle. The α - CuV_2O_6 nanowires fabricated by Ma *et al.* [78] in 2008 are used for the anode of LIB. The Cu extrusion mechanism (eq 3.3) is proposed to explain the accommodation of lithium in copper vanadate.



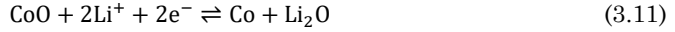
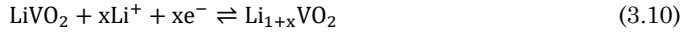
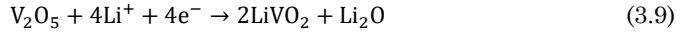
As a result of several years of research, it has been proven that the first discharge process of the vanadate is an irreversible decomposition, and the vanadium in vanadate undergoes the same mechanism as that in V_2O_5 , with the formation of $Li_xV_2O_5$ phases, including δ - LiV_2O_5 , γ - $Li_2V_2O_5$ or even ω - $Li_3V_2O_5$ phases. Taking CoV_2O_6 as an example, Ni and co-workers [79] have investigated the Li^+ ion insertion mechanism by ex-situ XRD. The $Co_3V_2O_8$ phase appears with upon discharge to about 2 V. The metallic Co shows up at about 0.02 V. Therefore, the possible electrochemical reactions for CoV_2O_6 is summarized as follows:



The same $Li_xV_2O_5$ phase is observed during the lithiation process of $Co_3V_2O_8$, [80] $Mn_2V_2O_7$ [81], and NiV_3O_8 [82] electrode with Li^+ insertion. Soundharrajan *et al.* [83] and Yang *et al.* [80] applied ex-situ XRD and TEM to elucidate the electrochemical lithium

storage mechanism of the $\text{Co}_3\text{V}_2\text{O}_8$ anode. The decomposition of the active materials is confirmed by the absence of the $\text{Co}_3\text{V}_2\text{O}_8$ phase and the generation of $\delta\text{-LiV}_2\text{O}_5$ and Li_2O . The observations of amorphous $\text{Li}_x\text{V}_2\text{O}_5$ and crystal Co further proves the above lithiation mechanism. Sambandam and co-workers [84] proposed a novel anode of $\beta\text{-Mn}_2\text{V}_2\text{O}_7$ for LIB. The (002) plane of $\gamma\text{-Li}_x\text{V}_2\text{O}_5$ and (221) plane of metallic Mn are observed in a discharged state.

On the other hand, some researchers have proposed formation of a new type of lithium vanadate rather than the $\text{Li}_x\text{V}_2\text{O}_5$ phase in the ternary vanadate. For example, Luo *et al.* [85] fabricated the hierarchical $\text{Co}_2\text{V}_2\text{O}_7$ nanosheets by using graphene oxide (GO) as the template. In-situ XRD is applied to investigate the lithiation process in the materials. The authors proposed that $\text{Co}_2\text{V}_2\text{O}_7$ is first decomposing to form CoO and V_2O_5 at 0.4 V. Upon further lithiation, the new peaks at 2 theta of 21.5° , 43° , and 51.5° appear, which is assigned to (111), (311) and (400) planes of LiVO_2 , respectively. Finally, Co is obtained from CoO and Li_xVO_2 from LiVO_2 . The reactions are summarized as follows:



Zhu *et al.* [86] also proposed a novel Co_2VO_4 anode for LIBs, and the Li^+ storage mechanism is assumed in multiple steps with the formation of LiVO_2 on the basis of XRD evidence. Hu *et al.* [87] fabricated pure single-crystalline $\varepsilon\text{-Cu}_{0.95}\text{V}_2\text{O}_5$ by a solvothermal route for LIBs, which can react electrochemically with 2.64 units of Li in reversible fashion with the generation of LiVO_2 observed by XRD. Zhu and co-workers [88] have used ZnV_2O_4 as Li insertion electrode. The authors prove that the lithiation phase for vanadium is $\text{Li}_x\text{V}_2\text{O}_4$ ($\text{Li}_2\text{V}_2\text{O}_4$ or LiV_2O_4) by both XRD and SEAD. Besides the one type of lithium vanadate formation, Yin and co-workers [89] synthesized the hollow precursor-derived $\text{Zn}_3\text{V}_2\text{O}_8$ nanocages for anode material of LIB. Ex-situ XRD, XPS and TEM confirm the presence of both $\text{Li}_x\text{V}_2\text{O}_5$ and LiVO_2 , with the insertion of Li^+ ion.

In terms of the M in $\text{M}_x\text{V}_y\text{O}_z$, the most generally accepted energy storage mechanism is the formation of metallic M. However, there is still an exception: Zn. Jo *et al.* [90] synthesized carbon-coated $\text{Zn}_3\text{V}_2\text{O}_8$ nanoflower as LIB anode material. According to the

in situ XRD, simultaneous conversion of zinc vanadate to lithium vanadate and lithium vanadate to lithium ion to lithium oxide occurs above 0.8V according to the in situ XRD:



It is noted that the produced zinc undergoes an alloying reaction with lithium, suggesting the zinc has the same alloy/de-alloy mechanism as ZnO for the lithiation process. The alloying reactions also occur on other types of zinc vanadate, like ZnV_2O_4 [88], $\text{Zn}_3\text{V}_3\text{O}_8$, [91], and $\text{Zn}_3\text{V}_2\text{O}_7(\text{OH})_2 \cdot 2\text{H}_2\text{O}$. [92]

In summary, the vanadate-based materials undergo decomposition in the first discharge process and form lithium vanadate and metallic metal or metal alloy with Li. After that, reversible reactions take place like Li^+ intercalation in lithium vanadate and redox reaction of metal oxides to pure metallic metal or metal alloys.

3.2.2.2 Electrochemical performance of ternary vanadate for LIB

Benefiting from the multiple oxidation states of the vanadium, ternary metal oxides show impressive physical-chemical properties and complex electrochemical process, which attract great attention as anode materials for LIB. Typical vanadates are $\text{M}_3\text{V}_2\text{O}_8$, MV_2O_6 , $\text{M}_3\text{V}_3\text{O}_8$, MV_2O_4 ($\text{M} = \text{Co}, \text{Cu}, \text{Mn}, \text{Zn}, \text{Ni}, \text{Fe}$). Table 3.7 depicts the LIB performance of various vanadate-based materials in different morphologies from the literature. Due to the capacity contributed by the redox reaction contributed, vanadates with the highest oxidation state of vanadium show the highest reversible capacity. Based on the above energy storage mechanism described in section 3.2.2.1, $\text{M}_3\text{V}_2\text{O}_8$ ($\text{M} = \text{Co}, \text{Cu}, \text{Mn}, \text{Ni}, \text{Fe}$) with M^{2+} and V^{5+} involve a maximum of 12 units of electron transferred during Li^+ intercalation process in the first discharge cycle, suggesting a reversible capacity of 762 mAh g^{-1} in the first cycle regardless of irreversible reactions such as the formation of solid electrolyte interface (SEI) film. In the following cycles, one vanadium in $\text{M}_3\text{V}_2\text{O}_4$ is limited to V^{4+} as the highest oxidation state, suggesting the maximum number units of electron transferred decreases to 11 with a theoretical capacity of 746 mAh g^{-1} . In comparison, the alloying reaction in zinc vanadate makes the $\text{Zn}_3\text{V}_2\text{O}_8$ achieve the highest reversible capacity in both the initial cycle (946 mAh g^{-1} with a maximum of 15 units of electron) and the following cycles (883 mAh g^{-1}).

In practice, the electrochemical performance measured may differ from the theoretical value. It is noted that the reversible capacity after many cycles can still maintain a high value, which can be even higher than the theoretical capacity. For example, Lv *et al.* [93] fabricated amorphous $\text{Ni}_3\text{V}_2\text{O}_8$ wires encapsulated in crystalline tubular nanostructures obtained by electrospinning followed by calcination to introduce oxygen vacancy defects. The loose amorphous nanowires possess a specific surface area of $20.05 \text{ m}^2 \text{ g}^{-1}$ along with a dominant pore size of 7 nm. Used as an anode electrode of LIB, it can deliver a high capacity of 962 mAh g^{-1} even after 300 cycles at a current density of 300 mA g^{-1} . The authors suggest that the excellent performance is due to the fast electrode kinetics due to the amorphous structure and porous morphology alleviating the volume expansion, and oxygen vacancies facilitating the ion diffusion in the structure. Nie and co-workers [94] designed a grass-like $\text{Zn}_3\text{V}_3\text{O}_8$ nanobelts array coated on three-dimensional carbon fiber cloth by a hydrothermal process with a subsequent heat treatment. The mass loading on the carbon cloth is about 1.3 mg cm^{-2} , 10 wt% of the composite. The as-prepared electrode delivers the highest capacity of 1723 mAh g^{-1} reported so far in vanadate-base materials and the capacity retention after 30 cycles is still 95%. The authors demonstrate that the outstanding cyclic stability is attributed to the nanobelt structure and providing the fast electron and Li^+ diffusion in and out of the electrolyte and materials. The contribution of the carbon fiber to the capacity cannot be neglected.

Table 3.7 The summary of the vanadate-based electrode applied in LIB.

Anode	Synthesis method	Reversible capacity [mAh g^{-1}]	Cycle	Current density [mA g^{-1}]	Initial capacity [mAh g^{-1}]	Ref.
Porous $\text{Zn}_3\text{V}_2\text{O}_8$ nanospheres/graphite	Liquid reflux and calcination	648	100	800	1415	[95]
Hollow hexagonal prismatic pencil $\text{Co}_3\text{V}_2\text{O}_8 \cdot n\text{H}_2\text{O}$	Hydrothermal synthesis	847	255	500	1224	[96]
Amorphous $\text{Ni}_3\text{V}_2\text{O}_8$ wire	Electrospinning and calcination	962	300	300	1312	[93]
$\text{Cu}_3\text{V}_2\text{O}_8$ nanoparticles	Co-precipitation	773	50	50	1157	[97]
MnV_2O_6 nanobelts	Hydrothermal	468.1	50	100	875.8	[98]

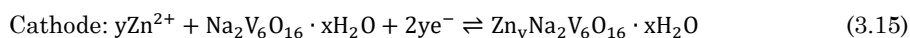
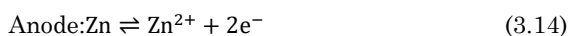
Single-phase NiV_2O_6	Sol-gel	750	400	800	1210	[99]
Microporous CoV_2O_6 nanosheet	Template and calcination	623	500	500	1067	[100]
$\text{Zn}_3\text{V}_3\text{O}_8$ /carbon fiber composites	Hydrothermal	1723	30	100	1798	[94]
Spinel-based CoV_2O_4 nanoparticles	Solvothermal	953	100	100	545	[101]
Spinel-based $\text{Co}_{0.25}\text{Mn}_{0.75}\text{V}_2\text{O}_4$ nanoparticles	Solvothermal	971	100	100	591	[101]
Porous ZnV_2O_4 nanowires	Hydrothermal	473	100	5000	584	[102]

Therefore, choosing suitable electrode materials and designing reasonable morphologies are both important for battery applications. The excellent electrochemical performance can be achieved by designing the crystal structure such as forming amorphous or creating defects on the vanadate, fabricating the porous morphologies, and adding additives to obtain composites.

3.2.3 Ternary vanadate in ZIB

3.2.3.1 Reaction mechanism in ternary vanadate

There are various V-O types of coordination polyhedra present in the unknown ternary vanadate materials due to the different oxidation states. These polyhedra can bind to each other in different ways to form various types of vanadates, and further create the tunnel-type and layer-type structures, allowing reversible Zn^{2+} intercalation and deintercalation. Based on the available literature, the most common reaction mechanisms of ZIB in vanadate-based materials can be classified into the insertion and extraction of Zn^{2+} , see Fig. 3.7. It demonstrates that the insertion of Zn^{2+} results in a reversible structure evolution from $\text{M}_x\text{V}_y\text{O}_z$ to $\text{Zn}_i\text{M}_x\text{V}_y\text{O}_z$ both in tunnel-type and layer-type. The guest Zn^{2+} is located in the interlayers or tunnels of the structures. Taking the layered $\text{Na}_2\text{V}_6\text{O}_{10} \cdot x\text{H}_2\text{O}$ as an example, the half-cell reaction can be described as follows: [103]



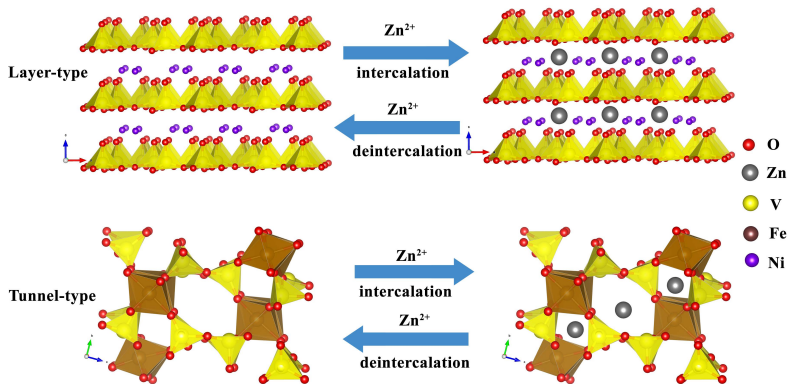
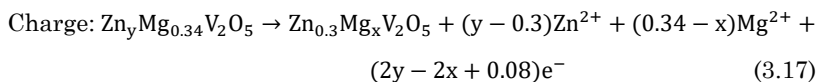
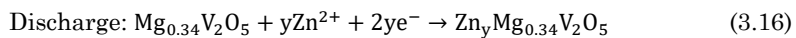


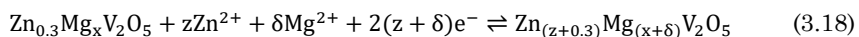
Fig. 3.7 Typical examples of vanadate-based electrodes based on Zn^{2+} insertion/extraction mechanism in both layer-type and tunnel-type materials.

Apart from the typical Zn^{2+} intercalation energy storage mechanism, some new mechanisms have also been proposed. For example, the replacement and co-intercalation mechanisms have also been confirmed the vanadate $\text{Mg}_{0.34}\text{V}_2\text{O}_5$ by multiple characterizations. [104] The first discharge process obeys the typical Zn^{2+} intercalation reaction mechanism, but most of Mg is deintercalated and further displaced by Zn^{2+} ion to form $\text{Zn}_{0.3}\text{Mg}_x\text{V}_2\text{O}_5$ after the charging process. In subsequent cycles, Zn^{2+} and Mg^{2+} achieve co-intercalation reactions, described as follows:

The first cycle on the cathode:



The subsequent cycles:



$$y < 1.66; x < 0.34; z < 1.4; \delta < 0.34$$

Despite the rapid development of ZIB, most of the researchers in the field rely on trial and error for the development of new cathode materials with high capacity and rate performance, without sufficient understanding of the fundamental mechanisms. The energy storage mechanism of different cathode materials, and the work reported here will reflect this approach to the research.

3.2.3.2 Electrochemical performance of the vanadate

The introduction of different cations, to form vanadates result in more attractive electrochemical performance compared to the pristine vanadium oxides by improving the structural stability and the size of the ion diffusion channel. There are four main categories reported for vanadates applied in ZIB: alkali vanadates, alkaline earth vanadates, transition metal vanadates, and ammonium vanadates. More details are given below.

Alkali vanadates including lithium vanadate, sodium vanadate, and potassium vanadate, have been applied in Li and Na ion storage systems for decades, but they are still new in the ZIB field. Muhammad *et al.* [58] initially reported an intercalated cathode of the layered LiV_3O_8 (LVO) for ZIB with a storage capacity of 173 mAh g^{-1} at 133 mA g^{-1} in 2017. The *ex-situ* X-ray absorption near edge structure (XANES) and *in situ* synchrotron XRD reveal the Zn^{2+} storage mechanism in LVO: the oxidation state of vanadium provides electron transfer and intercalation of the guest ion occurs in the (100) plane with formation of a metastable ZnLiV_3O_8 phase. This observation makes alkali vanadate promising for application as ZIB cathode material and offers opportunities for the use of electrochemically induced metastable materials for energy storage applications. Consequently, Yang *et al.* [105] proposed an effective strategy by chemically intercalating Li^+ ion into V_2O_5 to synthesize $\text{Li}_x\text{V}_2\text{O}_5$ as ZIB cathode materials, demonstrating an excellent cycling performance (232 mAh g^{-1} at 5 A g^{-1} after 500 cycles). Meanwhile, sodium and potassium vanadate are also reported to have outstanding Zn^{2+} storage capability via the same intercalation mechanism. For example, Hu *et al.* [103] fabricated a highly durable ZIB system with $\text{Na}_2\text{V}_6\text{O}_{16} \cdot 1.63\text{H}_2\text{O}$ nanowire as the cathode, delivering a high capacity of 352 mAh g^{-1} at 50 mA g^{-1} . Balaji *et al.* [106] proposed 1D nanorods of the layered $\text{K}_2\text{V}_6\text{O}_{16} \cdot 2.7\text{H}_2\text{O}$ as the ZIB cathode, showing a capacity of 296 mAh g^{-1} over 100 cycles at 200 mA g^{-1} .

Alkaline earth vanadates are another type of vanadates with inserted metal ions of Mg, Ca, Ba, *etc.* Recent studies reveal that the alkaline earth vanadates can also provide a superior electrochemical performance towards Zn^{2+} storage sharing the same intercalation mechanism as of alkaline vanadates. For example, the layered $\text{Mg}_x\text{V}_2\text{O}_5 \cdot n\text{H}_2\text{O}$ reported by Ming *et al.* [104] has a much large interlayer spacing of 13.4 \AA (against 11.07 \AA for Li^+), due to the larger radius of Mg^{2+} 4.3 \AA compared to that of Li^+

(3.8 Å). Thus, the obtained $\text{Mg}_x\text{V}_2\text{O}_5 \cdot n\text{H}_2\text{O}$ presents a high capacity of 353 mAh g⁻¹ at 100 mA g⁻¹. *Ex situ* XRD and XPS are applied to confirm the reversible (de)intercalation of Zn^{2+} ion in the (100) plane, along with the reduction of the vanadium from V^{5+} to V^{3+} . Xia *et al.* [62] demonstrate a double-layered $\text{Ca}_{0.25}\text{V}_2\text{O}_5 \cdot n\text{H}_2\text{O}$ (CVO) for ZIB cathode materials, displaying a high capacity of 340 mAh g⁻¹ at ca. 600 mA g⁻¹. The excellent performance is attributed to the large CaO_7 polyhedra in CVO expanding the size of the cavity between V_4O_{10} layers and high electrical conductivity of the CVO.

Common transition metal ions (Zn, Mn, Cu, Co, Ni, etc.) can react with vanadium oxides to form transition metal vanadate that are also relevant as cathode materials for ZIB. Due to the various structures, compositions, and properties, this type of vanadate has a large number of family members, and can exhibit a surprising performance as energy storage materials and reveal new mechanisms. For example, Liu *et al.* [107] proposed a typical spinel ZnV_2O_4 as the cathode electrode of ZIB, delivering a high reversible capacity of 312 mAh g⁻¹ at 10 C. In contrast to other vanadate materials, the oxidation state of vanadium in ZnV_2O_4 of V^{3+} is very low. Thus, it will be oxidized to V^{4+} in the first charge process by the extraction of Zn^{2+} to form the Zn-poor $\text{Zn}_x\text{V}_2\text{O}_4$ phase to allow the Zn^{2+} intercalation process in the following cycles. A triclinic CuV_2O_6 cathode is reported with an impressively high specific capacity of 427 mAh g⁻¹ at 0.1 A g⁻¹. [108] This super excellent performance is assigned to the divalent cation replacement between Cu^{2+} and Zn^{2+} which is less destructive for the structure.

Ammonium ions can offer the same function as metal ions to form ammonium vanadates, such as $(\text{NH}_4)_2\text{V}_{10}\text{O}_{25}$, [109] $(\text{NH}_4)_2\text{V}_3\text{O}_8$ [110] and $\text{NH}_4\text{V}_4\text{O}_{10}$, [111] all of which have a layered structure allowing Zn^{2+} storage. Compared to the metal vanadates, ammonium vanadates have low density and molecular weight, leading to high gravimetric and volumetric capacities. Besides, the network of $\text{N-H} \cdots \text{O}$ hydrogen bonds between the ammonium ion and vanadium-oxide layer creates a stable structure that can result in a great cycling performance. For example, Tang and co-workers [112] proposed an $\text{NH}_4\text{V}_4\text{O}_{10}$ compound with a large interplanar spacing (9.8 Å) showing a stable discharge capacity of 255.5 mAh g⁻¹ for 1000 cycles at 10 A g⁻¹. The capacity is achieved by embedding Zn^{2+} ion into the layered $\text{NH}_4\text{V}_4\text{O}_{10}$ to form $\text{Zn}_x\text{NH}_4\text{V}_4\text{O}_{10}$ and a new phase $\text{Zn}_3\text{V}_2\text{O}_7(\text{OH})_2 \cdot 2\text{H}_2\text{O}$.

To provide concise information about the materials and performance, a comprehensive summary of more vanadate-based cathode materials reported recently is displayed in Table 3.8. As elucidated, vanadate materials usually manifest high capacity and excellent long-term cycling stability. However, the vanadate usually shows a low operation voltage (less than 2 V), which will seriously limit their commercial applications.

Table 3.8 Brief summary of the electrochemical performance for the vanadate-based cathode.

Cathode	Reversible capacity [mAh g ⁻¹]	Cycle	Current density [mA g ⁻¹]	Potential range [V]	Ref.
LiV ₃ O ₈ nanorods	200	4000	5000	0.2-1.6	[30]
NaV ₃ O ₈ ·1.5H ₂ O nanobelts	150	1000	4000	0.3-1.3	[113]
K ₂ V ₈ O ₂₁ flakes	247	50	300	0.2-1.4	[114]
KV ₃ O ₈ ·0.75H ₂ O nanobelts/carbon nanotubes	379	10000	5000	0.2-1.3	[115]
MgV ₂ O ₄ flowers	129	500	4000	0.2-1.4	[116]
CaV ₆ O ₁₆ ·3H ₂ O nanowires	170	300	500	0.2-1.6	[117]
BaV ₆ O ₁₆ ·3H ₂ O nanobelts	129	2000	5000	0.3-1.4	[118]
H ₁₁ Al ₂ V ₆ O _{23.2} microspheres	141	7000	5000	0.4-1.8	[119]
Zn ₂ V ₂ O ₇ nanowires	138	1000	4000	0.4-1.4	[120]
AgVO ₃ nanowires	95	1000	2000	0.4-1.3	[121]
CuV ₂ O ₆ nanowires	143	1200	5000	0.2-1.4	[122]
(NH ₄) ₂ V ₄ O ₉ sheets	125	2000	5000	0.3-1.3	[123]

3.3 Summary and perspective

This chapter mainly introduces the applications and energy storage mechanism differences of vanadium-based materials including vanadium oxides and ternary vanadates in LIBs and ZIBs. The chemical diversity, structural diversity and tenability of the vanadium-based materials provide great advantages including excellent theoretical capacity and super capability to allow large cation ions insertion/desertion. Although the

bulk materials have some intrinsic drawbacks like poor electrical conductivity, poor cycling stability and slow ion diffusion coefficients, researchers have proposed some feasible strategies to overcome the above defects: i) designing micro or nano-structure materials; ii) fabricating composites; iii) producing defects in crystal structures; iv) developing a new type of vanadium-based materials. Based on the above solutions, the electrochemical performances of the vanadium-based materials have been greatly improved in recent years and the capacities are also much higher than the commercial batteries.

Despite the impressive progress in the battery system, vanadium-based materials are still far from commercial devices. Moreover, the detailed intrinsic electrochemical reaction mechanisms in LIB and ZIB is still under debate. Thus, such efforts still need to be made to promote the development of battery research:

- 1) The methods of synthesizing these compounds are complicated and expensive, including the template and hydrothermal process. Simple and controllable methods are needed.
- 2) Morphology and structure type are generally considered to be important factors affecting the energy storage process. However, how they affect the intercalation process is barely discussed, as well as the formation mechanisms for the morphology and crystal structure. Therefore, further study also should concentrate on these parts.
- 3) Vanadium-based materials generally exhibit a low operating voltage for ZIB, which should be improved further to achieve commercial applications.
- 4) The complicated chemical components of the vanadium-based materials might exhibit novel reaction mechanisms, such as a replacement mechanism, compared to other materials in both LIB and ZIB. Thus, it is necessary to explore the detailed information for the reaction and make full use of the observation to reach a satisfying electrochemical performance.
- 5) Recyclability of the battery still needs to be considered during the pursuit of the high-performance electrode materials, especially for the ones with toxicity and safety issues.

Reference

- [1] Moskalyk, R. R.; Alfantazi, A. M., *Miner. Eng.* **2003**, *16* (9), 793-805.
- [2] Allred, J. M.; Cava, R. J., *J. Solid State Chem.* **2013**, *198*, 10-17.

- [3] Yuan, N.; Li, J.; Lin, C., *Adv. Sens. Appl. II* **2001**, 4596.
- [4] Yue, Y.; Liang, H., *Adv. Energy Mater.* **2017**, *7* (17), 1602545.
- [5] Tarascon, J. M.; Armand, M., *Nature* **2001**, *414* (6861), 359-367.
- [6] Yin, B.; Liu, Z.; Wang, Y.; Ji, X.; Huan, Y.; Dong, D.; Hu, X.; Wei, T., *ACS Appl. Mater. Interfaces* **2020**, *12* (41), 45961-45967.
- [7] Song, H.; Zhang, C.; Liu, Y.; Liu, C.; Nan, X.; Cao, G., *J. Power Sources* **2015**, *294*, 1-7.
- [8] Shizuka, K.; Kobayashi, T.; Okahara, K.; Okamoto, K.; Kanzaki, S.; Kanno, R., *J. Power Sources* **2005**, *146* (1), 589-593.
- [9] Chan, C. K.; Peng, H.; Twisten, R. D.; Jarausch, K.; Zhang, X. F.; Cui, Y., *Nano Lett.* **2007**, *7* (2), 490-495.
- [10] Pecquenard, B.; Gourier, D.; Baffier, N., *Solid State Ionics* **1995**, *78* (3), 287-303.
- [11] Nethravathi, C.; Viswanath, B.; Michael, J.; Rajamath, M., *Carbon* **2012**, *50* (13), 4839-4846.
- [12] Zhai, T.; Liu, H.; Li, H.; Fang, X.; Liao, M.; Li, L.; Zhou, H.; Koide, Y.; Bando, Y.; Golberg, D., *Adv. Mater.* **2010**, *22* (23), 2547-2552.
- [13] Wang, H.-g.; Ma, D.-l.; Huang, Y.; Zhang, X.-b., *Chem. Eur. J* **2012**, *18* (29), 8987-8993.
- [14] Zhu, K.; Meng, Y.; Qiu, H.; Gao, Y.; Wang, C.; Du, F.; Wei, Y.; Chen, G.; Wang, C.; Chen, G., *J. Alloys Compd.* **2015**, *650*, 370-373.
- [15] Kim, T.; Shin, J.; You, T.-S.; Lee, H.; Kim, J., *Electrochim. Acta* **2015**, *164*, 227-234.
- [16] Rui, X.; Tang, Y.; Malyi, O. I.; Gusak, A.; Zhang, Y.; Niu, Z.; Tan, H. T.; Persson, C.; Chen, X.; Chen, Z.; Yan, Q., *Nano Energy* **2016**, *22*, 583-593.
- [17] Pan, A.; Zhang, J.-G.; Nie, Z.; Cao, G.; Arey, B. W.; Li, G.; Liang, S.-q.; Liu, J., *J. Mater. Chem.* **2010**, *20* (41), 9193-9199.
- [18] Chou, S.-L.; Wang, J.-Z.; Sun, J.-Z.; Wexler, D.; Forsyth, M.; Liu, H.-K.; MacFarlane, D. R.; Dou, S.-X., *Chem. Mater.* **2008**, *20* (22), 7044-7051.
- [19] Chen, X.; Pomerantseva, E.; Banerjee, P.; Gregorczyk, K.; Ghodssi, R.; Rubloff, G., *Chem. Mater.* **2012**, *24* (7), 1255-1261.
- [20] Li, Y.; Yao, J.; Uchaker, E.; Yang, J.; Huang, Y.; Zhang, M.; Cao, G., *Adv. Energy Mater.* **2013**, *3* (9), 1171-1175.
- [21] Rui, X.; Lu, Z.; Yu, H.; Yang, D.; Hng, H. H.; Lim, T. M.; Yan, Q., *Nanoscale* **2013**, *5* (2), 556-560.

-
- [22] Shao, J.; Li, X.; Wan, Z.; Zhang, L.; Ding, Y.; Zhang, L.; Qu, Q.; Zheng, H., *ACS Appl. Mater. Interfaces* **2013**, *5* (16), 7671-7675.
- [23] Kumar, P.; Hu, L.-H., *J. Alloys Compd.* **2016**, *655*, 79-85.
- [24] Liang, X.; Gao, G.; Wu, G.; Yang, H., *Electrochim. Acta* **2016**, *188*, 625-635.
- [25] Pan, A.; Wu, H. B.; Yu, L.; Lou, X. W., *Angew. Chem. Int. Ed.* **2013**, *52* (8), 2226-2230.
- [26] Pang, H.; Cheng, P.; Yang, H.; Lu, J.; Guo, C. X.; Ning, G.; Li, C. M., *Chem. Commun. (Cambridge, U. K.)* **2013**, *49* (15), 1536-1538.
- [27] Rahman, M. M.; Sadek, A. Z.; Sultana, I.; Srikanth, M.; Dai, X. J.; Field, M. R.; McCulloch, D. G.; Ponraj, S. B.; Chen, Y., *Nano Research* **2015**, *8* (11), 3591-3603.
- [28] Mai, L.; Wei, Q.; An, Q.; Tian, X.; Zhao, Y.; Xu, X.; Xu, L.; Chang, L.; Zhang, Q., *Adv. Mater.* **2013**, *25* (21), 2969-2973.
- [29] Niu, C.; Meng, J.; Han, C.; Zhao, K.; Yan, M.; Mai, L., *Nano Lett.* **2014**, *14* (5), 2873-2878.
- [30] Li, Q.; Chen, D.; Tan, H.; Zhang, X.; Rui, X.; Yu, Y., *J. Energy Chem.* **2020**, *40*, 15-21.
- [31] Ihsan, M.; Meng, Q.; Li, L.; Li, D.; Wang, H.; Seng, K. H.; Chen, Z.; Kennedy, S. J.; Guo, Z.; Liu, H.-K., *Electrochim. Acta* **2015**, *173*, 172-177.
- [32] Zhang, Y.; Zhou, M.; Fan, M.; Huang, C.; Chen, C.; Cao, Y.; Li, H.; Liu, X., *Curr. Appl. Phys.* **2011**, *11* (5), 1159-1163.
- [33] Zhang, X.; Yu, M.; Zhao, S.; Li, F.; Hu, X.; Guo, S.; Lu, X.; Tong, Y., *Part. Part. Syst. Charact.* **2016**, *33* (8), 531-537.
- [34] Zhang, X.-F.; Wang, K.-X.; Wei, X.; Chen, J.-S., *Chem. Mater.* **2011**, *23* (24), 5290-5292.
- [35] Park, K.-I.; Song, H.-M.; Kim, Y.; Mho, S.-i.; Cho, W. I.; Yeo, I.-H., *Electrochim. Acta* **2010**, *55* (27), 8023-8029.
- [36] Ren, X.; Shi, C.; Zhang, P.; Jiang, Y.; Liu, J.; Zhang, Q., *Mater. Sci. Eng. B* **2012**, *177* (12), 929-934.
- [37] Partheeban, T.; Kesavan, T.; Vivekanantha, M.; Sasidharan, M., *Appl. Surf. Sci.* **2019**, *493*, 1106-1114.
- [38] Chen, D.; Yi, R.; Chen, S.; Xu, T.; Gordin, M. L.; Lv, D.; Wang, D., *Mater. Sci. Eng. B* **2014**, *185*, 7-12.
- [39] Cheng, J.; Wang, B.; Xin, H. L.; Yang, G.; Cai, H.; Nie, F.; Huang, H., *J. Mater. Chem. A* **2013**, *1* (36), 10814-10820.

- [40] Wu, W.; Wang, Y.; Wang, X.; Chen, Q.; Wang, X.; Yang, S.; Liu, X.; Guo, J.; Yang, Z., *J. Alloys Compd.* **2009**, *486* (1), 93-96.
- [41] Liu, H.-R.; Chu, Y.-Q.; Fu, Z.-W.; Qin, Q.-Z., *J. Power Sources* **2003**, *124* (1), 163-169.
- [42] Li, X.; Ji, Y.; Huang, J.-S.; Li, J.; Huang, J., *ChemistrySelect* **2017**, *2* (26), 7987-7995.
- [43] Zheng, J.-c.; Han, Y.-d.; Sun, D.; Zhang, B.; Cairns, E. J., *Energy Storage Mater.* **2017**, *7*, 48-55.
- [44] Li, Z.; Zhang, C.; Liu, C.; Fu, H.; Nan, X.; Wang, K.; Li, X.; Ma, W.; Lu, X.; Cao, G., *Electrochim. Acta* **2016**, *222*, 1831-1838.
- [45] Li, Y.; Yao, J.; Uchaker, E.; Zhang, M.; Tian, J.; Liu, X.; Cao, G., *J. Phys. Chem. C* **2013**, *117* (45), 23507-23514.
- [46] Zeng, H.; Liu, D.; Zhang, Y.; See, K. A.; Jun, Y.-S.; Wu, G.; Gerbec, J. A.; Ji, X.; Stucky, G. D., *Chem. Mater.* **2015**, *27* (21), 7331-7336.
- [47] Zhang, H.; Rong, Y.; Jia, W.; Chai, H.; Cao, Y., *J. Alloys Compd.* **2019**, *802*, 139-145.
- [48] Panagopoulou, M.; Vernardou, D.; Koudoumas, E.; Katsarakis, N.; Tsoukalas, D.; Raptis, Y. S., *J. Phys. Chem. C* **2017**, *121* (1), 70-79.
- [49] Chen, P.; Zheng, G.; Guo, G.; Wang, Z.; Tang, J.; Li, S.; Wen, Z.; Ji, S.; Sun, J., *J. Alloys Compd.* **2019**, *784*, 574-583.
- [50] Ji, Y.; Fang, D.; Wang, C.; Zhou, Z.; Luo, Z.; Huang, J.; Yi, J., *J. Alloys Compd.* **2018**, *742*, 567-576.
- [51] Gu, L.; Wang, J.; Ding, J.; Li, B.; Yang, S., *Electrochim. Acta* **2019**, *295*, 393-400.
- [52] Lv, T.-t.; Zou, Z.-g.; Li, Y.-w.; Li, S.-y.; Zhang, Y.-j., *J. Electroanal. Chem.* **2018**, *829*, 42-50.
- [53] Zhang, S.; Zhang, L.; Xu, G.; Zhang, X.; Zhao, A., *CrystEngComm* **2020**, *22* (10), 1705-1711.
- [54] Xu, W.; Wang, Y., *Nano-Micro Lett.* **2019**, *11* (1), 90.
- [55] Chen, H.; Chen, L.; Meng, J.; Yang, Z.; Wu, J.; Rong, Y.; Deng, L.; Shi, Y., *J. Power Sources* **2020**, *474*, 228569.
- [56] Cao, Z.; Chu, H.; Zhang, H.; Ge, Y.; Clemente, R.; Dong, P.; Wang, L.; Shen, J.; Ye, M.; Ajayan, P. M., *J. Mater. Chem. A* **2019**, *7* (44), 25262-25267.
- [57] Lai, J.; Zhu, H.; Zhu, X.; Koritala, H.; Wang, Y., *ACS Appl. Energy Mater.* **2019**, *2* (3), 1988-1996.

-
- [58] Alfuruqi, M. H.; Mathew, V.; Song, J.; Kim, S.; Islam, S.; Pham, D. T.; Jo, J.; Kim, S.; Baboo, J. P.; Xiu, Z.; Lee, K.-S.; Sun, Y.-K.; Kim, J., *Chem. Mater.* **2017**, *29* (4), 1684-1694.
- [59] He, P.; Zhang, G.; Liao, X.; Yan, M.; Xu, X.; An, Q.; Liu, J.; Mai, L., *Adv. Energy Mater.* **2018**, *8* (10), 1702463.
- [60] Yang, Y.; Tang, Y.; Liang, S.; Wu, Z.; Fang, G.; Cao, X.; Wang, C.; Lin, T.; Pan, A.; Zhou, J., *Nano Energy* **2019**, *61*, 617-625.
- [61] Yan, M.; He, P.; Chen, Y.; Wang, S.; Wei, Q.; Zhao, K.; Xu, X.; An, Q.; Shuang, Y.; Shao, Y.; Mueller, K. T.; Mai, L.; Liu, J.; Yang, J., *Adv. Mater.* **2018**, *30* (1), 1703725.
- [62] Xia, C.; Guo, J.; Li, P.; Zhang, X.; Alshareef, H. N., *Angew. Chem. Int. Ed.* **2018**, *57* (15), 3943-3948.
- [63] Zhao, H.; Fu, Q.; Yang, D.; Sarapulova, A.; Pang, Q.; Meng, Y.; Wei, L.; Ehrenberg, H.; Wei, Y.; Wang, C.; Chen, G., *ACS Nano* **2020**, *14* (9), 11809-11820.
- [64] Yin, B.; Zhang, S.; Ke, K.; Xiong, T.; Wang, Y.; Lim, B. K. D.; Lee, W. S. V.; Wang, Z.; Xue, J., *Nanoscale* **2019**, *11* (42), 19723-19728.
- [65] Zhang, X.; Tang, Y.; He, P.; Zhang, Z.; Chen, T., *Carbon* **2021**, *172*, 207-213.
- [66] Xu, D.; Wang, H.; Li, F.; Guan, Z.; Wang, R.; He, B.; Gong, Y.; Hu, X., *Adv. Mater. Interfaces* **2019**, *6* (2), 1801506.
- [67] Wadsley, A., *Acta Crystallogr.* **1957**, *10* (4), 261-267.
- [68] Theobald, F. R.; Theobald, J.-G.; Vadrine, J. C.; Clad, R.; Renard, J., *J. Phys. Chem. Solids* **1984**, *45* (6), 581-587.
- [69] Sauerbrei, E. E.; Faggiani, R.; Calvo, C., *Acta Crystallogr. B* **1973**, *29* (10), 2304-2306.
- [70] Markkula, M.; Arevalo-Lopez, A. M.; Paul Attfield, J., *J. Solid State Chem.* **2012**, *192*, 390-393.
- [71] Coing-Boyat, J., *Acta Crystallogr. B* **1982**, *38* (5), 1546-1548.
- [72] Liao, J. H.; Leroux, F.; Piffard, Y.; Guyomard, D.; Payen, C., *J. Solid State Chem.* **1996**, *121* (1), 214-224.
- [73] Wang, X.; Heier, K. R.; Stern, C. L.; Poeppelmeier, K. R., *Inorg. Chem.* **1998**, *37* (26), 6921-6927.
- [74] Ebbinghaus, S. G.; Hanss, J.; Klemm, M.; Horn, S., *J. Alloys Compd.* **2004**, *370* (1), 75-79.
- [75] Andreotti, G. D.; Calestani, G.; Montenero, A., *Cryst. Mater.* **1984**, *168* (1-4), 53.

- [76] Zavalij, P. Y.; Zhang, F.; Whittingham, M. S., *Acta Crystallogr. C* **1997**, *53* (12), 1738-1739.
- [77] Morcrette, M.; Rozier, P.; Dupont, L.; Mugnier, E.; Sannier, L.; Galy, J.; Tarascon, J. M., *Nat. Mater.* **2003**, *2* (11), 755-761.
- [78] Ma, H.; Zhang, S.; Ji, W.; Tao, Z.; Chen, J., *J. Am. Chem. Soc.* **2008**, *130* (15), 5361-5367.
- [79] Ni, S.; Ma, J.; Zhang, J.; Yang, X.; Zhang, L., *J. Power Sources* **2015**, *282*, 65-69.
- [80] Yang, G.; Cui, H.; Yang, G.; Wang, C., *ACS Nano* **2014**, *8* (5), 4474-4487.
- [81] Xia, D.; Xu, S.; Wang, W.; Wang, D.; Wu, M.; Gong, F., *Chem. Commun. (Cambridge, U. K.)* **2020**, *56* (58), 8043-8046.
- [82] Ni, S.; Ma, J.; Zhang, J.; Yang, X.; Zhang, L., *Chem. Commun. (Cambridge, U. K.)* **2015**, *51* (27), 5880-5882.
- [83] Soundharrajan, V.; Sambandam, B.; Song, J.; Kim, S.; Jo, J.; Duong, P. T.; Kim, S.; Mathew, V.; Kim, J., *J. Colloid Interface Sci.* **2017**, *501*, 133-141.
- [84] Sambandam, B.; Soundharrajan, V.; Song, J.; Kim, S.; Jo, J.; Duong, P. T.; Kim, S.; Mathew, V.; Kim, J., *J. Power Sources* **2017**, *350*, 80-86.
- [85] Luo, Y.; Xu, X.; Zhang, Y.; Chen, C.-Y.; Zhou, L.; Yan, M.; Wei, Q.; Tian, X.; Mai, L., *ACS Appl. Mater. Interfaces* **2016**, *8* (4), 2812-2818.
- [86] Zhu, C.; Liu, Z.; Wang, J.; Pu, J.; Wu, W.; Zhou, Q.; Zhang, H., *Small* **2017**, *13* (34), 1701260.
- [87] Hu, W.; Zhang, X.-b.; Cheng, Y.-l.; Wu, Y.-m.; Wang, L.-m., *Chem. Commun. (Cambridge, U. K.)* **2011**, *47* (18), 5250-5252.
- [88] Zhu, X.; Jiang, X.; Xiao, L.; Ai, X.; Yang, H.; Cao, Y., *Curr. Appl. Phys.* **2015**, *15* (4), 435-440.
- [89] Yin, Z.; Qin, J.; Wang, W.; Cao, M., *Nano Energy* **2017**, *31*, 367-376.
- [90] Jo, J. H.; Choi, J. U.; Kim, H. J.; Yashiro, H.; Myung, S.-T., *ACS Sustainable Chem. Eng.* **2020**, *8* (4), 1908-1915.
- [91] He, J.; Liu, X.; Chen, X.; Zheng, H.; Feng, C., *J. Alloys Compd.* **2018**, *741*, 315-322.
- [92] Yan, H.; Luo, Y.; Xu, X.; He, L.; Tan, J.; Li, Z.; Hong, X.; He, P.; Mai, L., *ACS Appl. Mater. Interfaces* **2017**, *9* (33), 27707-27714.
- [93] Lv, C.; Sun, J.; Chen, G.; Yan, C.; Chen, D., *Nano Energy* **2017**, *33*, 138-145.
- [94] Nie, R.; Fang, G.; Zhou, J.; Guo, J.; Tang, Y.; Liu, S.; Cai, Y.; Hao, P.; Liang, S., *Electrochim. Acta* **2017**, *246*, 97-105.

-
- [95] Bie, C.; Pei, J.; Wang, J.; Hua, K.; Chen, D.; Chen, G., *Electrochim. Acta* **2017**, *248*, 140-149.
- [96] Wu, F.; Xiong, S.; Qian, Y.; Yu, S.-H., *Angew. Chem. Int. Ed.* **2015**, *54* (37), 10787-10791.
- [97] Li, M.; Gao, Y.; Chen, N.; Meng, X.; Wang, C.; Zhang, Y.; Zhang, D.; Wei, Y.; Du, F.; Chen, G., *Chem. Eur. J* **2016**, *22* (32), 11405-11412.
- [98] Zhang, S.; Hu, R.; Liu, L.; Wang, D., *Mater. Lett.* **2014**, *124*, 57-60.
- [99] Zhou, Z.; Zhang, J.; Chen, S.; Yao, H.; Zhao, Y.; Kuang, Q.; Fan, Q.; Dong, Y., *Electrochim. Acta* **2020**, *359*, 136979.
- [100] Zhang, L.; Zhao, K.; Luo, Y.; Dong, Y.; Xu, W.; Yan, M.; Ren, W.; Zhou, L.; Qu, L.; Mai, L., *ACS Appl. Mater. Interfaces* **2016**, *8* (11), 7139-7146.
- [101] Muruganantham, R.; Lu, J.-S.; Maggay, I. V. B.; Chang, B. K.; Wang, P. K.; Liu, W.-R., *Surf. Coat. Technol.* **2020**, *389*, 125602.
- [102] De Juan-Corpuz, L. M. Z.; Nguyen, M. T.; Corpuz, R. D.; Yonezawa, T.; Rosero-Navarro, N. C.; Tadanaga, K.; Tokunaga, T.; Kheawhom, S., *ACS Appl. Nano Mater.* **2019**, *2* (7), 4247-4256.
- [103] Hu, P.; Zhu, T.; Wang, X.; Wei, X.; Yan, M.; Li, J.; Luo, W.; Yang, W.; Zhang, W.; Zhou, L.; Zhou, Z.; Mai, L., *Nano Lett.* **2018**, *18* (3), 1758-1763.
- [104] Ming, F.; Liang, H.; Lei, Y.; Kandambeth, S.; Eddaoudi, M.; Alshareef, H. N., *ACS Energy Lett.* **2018**, *3* (10), 2602-2609.
- [105] Yang, Y.; Tang, Y.; Fang, G.; Shan, L.; Guo, J.; Zhang, W.; Wang, C.; Wang, L.; Zhou, J.; Liang, S., *Energy Environ. Sci.* **2018**, *11* (11), 3157-3162.
- [106] Sambandam, B.; Soundharrajan, V.; Kim, S.; Alfaruqi, M. H.; Jo, J.; Kim, S.; Mathew, V.; Sun, Y.-k.; Kim, J., *J. Mater. Chem. A* **2018**, *6* (32), 15530-15539.
- [107] Liu, Y.; Li, C.; Xu, J.; Ou, M.; Fang, C.; Sun, S.; Qiu, Y.; Peng, J.; Lu, G.; Li, Q.; Han, J.; Huang, Y., *Nano Energy* **2020**, *67*, 104211.
- [108] Liu, Y.; Li, Q.; Ma, K.; Yang, G.; Wang, C., *ACS Nano* **2019**, *13* (10), 12081-12089.
- [109] Wei, T.; Li, Q.; Yang, G.; Wang, C., *J. Mater. Chem. A* **2018**, *6* (41), 20402-20410.
- [110] Jiang, H.; Zhang, Y.; Xu, L.; Gao, Z.; Zheng, J.; Wang, Q.; Meng, C.; Wang, J., *Chem. Eng. J.* **2020**, *382*, 122844.
- [111] Yang, G.; Wei, T.; Wang, C., *ACS Appl. Mater. Interfaces* **2018**, *10* (41), 35079-35089.
- [112] Tang, B.; Zhou, J.; Fang, G.; Liu, F.; Zhu, C.; Wang, C.; Pan, A.; Liang, S., *J. Mater. Chem. A* **2019**, *7* (3), 940-945.

- [113]Wan, F.; Zhang, L.; Dai, X.; Wang, X.; Niu, Z.; Chen, J., *Nat. Commun.* **2018**, *9* (1), 1656.
- [114]Tang, B.; Fang, G.; Zhou, J.; Wang, L.; Lei, Y.; Wang, C.; Lin, T.; Tang, Y.; Liang, S., *Nano Energy* **2018**, *51*, 579-587.
- [115]Wan, F.; Huang, S.; Cao, H.; Niu, Z., *ACS Nano* **2020**, *14* (6), 6752-6760.
- [116]Tang, W.; Lan, B.; Tang, C.; An, Q.; Chen, L.; Zhang, W.; Zuo, C.; Dong, S.; Luo, P., *ACS Sustainable Chem. Eng.* **2020**, *8* (9), 3681-3688.
- [117]Liu, X.; Zhang, H.; Geiger, D.; Han, J.; Varzi, A.; Kaiser, U.; Moretti, A.; Passerini, S., *Chem. Commun. (Cambridge, U. K.)* **2019**, *55* (16), 2265-2268.
- [118]Wang, X.; Xi, B.; Ma, X.; Feng, Z.; Jia, Y.; Feng, J.; Qian, Y.; Xiong, S., *Nano Lett.* **2020**, *20* (4), 2899-2906.
- [119]Wei, T.; Liu, Y.; Yang, G.; Wang, C., *Energy Storage Mater.* **2020**, *30*, 130-137.
- [120]Sambandam, B.; Soundharrajan, V.; Kim, S.; Alfaruqi, M. H.; Jo, J.; Kim, S.; Mathew, V.; Sun, Y.-k.; Kim, J., *J. Mater. Chem. A* **2018**, *6* (9), 3850-3856.
- [121]Liu, H.; Wang, J.-G.; Sun, H.; Li, Y.; Yang, J.; Wei, C.; Kang, F., *J. Colloid Interface Sci.* **2020**, *560*, 659-666.
- [122]Yu, X.; Hu, F.; Cui, F.; Zhao, J.; Guan, C.; Zhu, K., *Dalton Trans.* **2020**, *49* (4), 1048-1055.
- [123]Zhang, Y.; Jiang, H.; Xu, L.; Gao, Z.; Meng, C., *ACS Appl. Energy Mater.* **2019**, *2* (11), 7861-7869.

Chapter 4

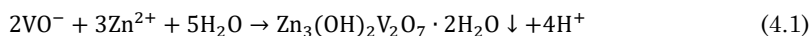
Methods and characterization

4.1 Methods

4.1.1 Precipitation method

Precipitation occurs when anions react with cations to form an insoluble ionic solid in solution. For some common ionic solids, the solubility rules are generally used to determine the possibility of the reaction occurring. The prediction of the precipitation reaction helps researchers to design the reactions to fabricate materials. Factors, such as pH, time, pressure, temperature, surfactant and solution concentration, can affect the precipitation reaction in terms of thermodynamics, kinetics and thus the structure and yield of the reactant/product.

In this PhD project, the zinc vanadate flower was obtained by precipitation. Zinc cation is from $\text{Zn}(\text{CH}_3\text{COO})_2 \cdot 2\text{H}_2\text{O}$ solution and vanadium anion from NH_4VO_3 solution. The carbon coated zinc vanadate precursor is fabricated with starch as surfactant to restrict the size of the product and stabilize the morphology. The formation of the solid zinc vanadate precursor can be described as follows:



After that, the solid precursor is coated by polydopamine (PDA) in a dopamine solution. By calcining the precursor and PDA coated precursor in Ar and air, respectively, various samples will be obtained. The detailed fabrication process is described in Chapter 5 and 6.

4.1.2 Microwave method

Microwave method has drawn much attention for synthesis of inorganic nanomaterials due to high heating rates, fast fabrication and high-energy efficiency. It is based on supplying energy directly to ions or polar solvent molecules. [1] This technique results in

fast crystallization and uniform nucleation to provide products with small particle sizes and a narrow particle size distribution. In comparison to conventional heating processes using hydrothermal method, the microwave method also has a greater reproducibility and the stirring can be maintained during the reactions. [2] Besides, the temperature and pressure profiles can be collected during the fabrication process as a function of time and this enhances the understanding of the reaction process.

In this PhD project, the zinc vanadate nanowires and the vanadium oxide ($V_3O_7 \cdot H_2O$) nanobelts were obtained with a Biotage® Microwave Reactor. The reaction parameters were monitored during the reaction. Zinc vanadate nanowires are obtained by heating the solution of NH_4VO_3 , $Zn(NO_3)_2 \cdot 6H_2O$ and glycine at 100 °C for 6 h. While the vanadium oxides are employing $VOSO_4 \cdot xH_2O$ as the vanadium source, reacting at 180 °C for 2 h by using non-oxidizing acid to control pH. GO was obtained by a modified Hummers method.[3] The details for the fabrication process for a representative synthesis are in Chapter 6 and Chapter 7.

4.1.3 Electrode preparation and battery assemble

The working electrodes for both LIB and ZIB were prepared as follows. The active material, carbon black and polyvinylidene fluoride were mixed to form a slurry in 1-methyl-2-pyrrolidinone with a weight ratio of 8:1:1 and 7:2:1 for LIB and ZIB, respectively. After that, the slurry was coated on current collector of copper foil (LIB anode) and steel mesh (ZIB cathode) electrode with a geometrical area of 1.77 cm², and then dried in a vacuum oven at 120 °C for 12 h.

The tested coin cells were CR2032 type bought from Hohsen in Japan and glass microfibers were used as the separator. LIBs were assembled in an argon glove box with 1 M $LiPF_6$ in ethylene carbonate/dimethyl carbonate (EC:DMC = 1:1 by volume) as the electrolyte and Li foil as the counter-/reference electrode. ZIBs were assembled in air with a metallic zinc foil as the anode and 3 M $Zn(CF_3SO_3)_2$ as the electrolyte.

4.2 Material characterization techniques

4.2.1 X-ray diffraction

When electromagnetic radiation with a wavelength which is comparable to the interatomic distances interacts with an ordered crystal without the exchange of energy, diffraction occurs and the wave will be reflected and only propagate in specific directions. In all, there are three common incident beams that can have wavelengths of around 1 Å, which is typical for interatomic distances in matter: X-ray, electrons and neutrons. Among these, the X-ray is most widely used for identification of the crystalline materials, like X-ray diffraction (XRD). In a crystalline structure, the scattered X-rays undergo constructive and destructive interference, shown in Fig. 4.1. The reflections from the planes obey the Bragg's law:

$$2d\sin\theta = n\lambda \quad (4.2)$$

where 'n' is a positive integer, 'λ' is the wavelength of the incident X-ray, 'd' is the spacing of the crystal planes and 'θ' is the incidence and reflection angle. The X-rays incident on the crystal at an angle θ will produce coherent diffraction at specific angles. When the travelled distance difference (2d sinθ) is equal to an integral number of the wavelength (nλ), signal is detected. Otherwise, the emergent beams are no longer in phase, and cancel each other, so that no reflected intensity will be observed. The intensity of the diffracted beams is related to the type and position of the atoms, while the width of the peak depends on the size and degree of the crystallite's perfection.

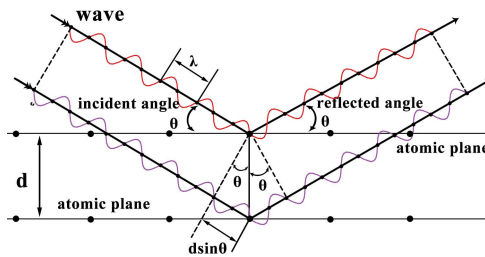


Fig. 4.1 Bragg's law.

4.2.2 Scanning electron microscopy

The scanning electron microscope (SEM) is a kind of electron microscope by using electron beam to interact with atoms from the specimen to reflect the surface information of the

sample, including the morphology and composition. The microscope is typically operated at a vacuum atmosphere (ca. 10^{-12} bar). The electron beam is produced from the electron gun of a tungsten wire with a sharp tip, which is applied in this project. The electrons then will be accelerated by the high voltage drop (0.2 to 40 keV) between the cathode of the electron gun and the anode. Accelerated electrons are then focused by the condenser and objective lens to form an electron probe, which will be controlled to scan the surface of the specimen in a raster scan pattern. The position of the beam combined with the intensity of the electron signal is used to produce an image. When the focused beam hits the sample, various signals can be obtained, shown in Fig. 4.2, such as secondary electron and X-rays. Secondary electrons are generated by ionization, which are collected by Everhart-Thornley detector to present the standard SEM images. To obtain high quality images, several parameters need to be considered, such as accelerating voltage, spot size, and working distance. In this project, AFEG 250 Analytical ESEM was used for investigating the morphology of the zinc vanadate and vanadium oxide materials.

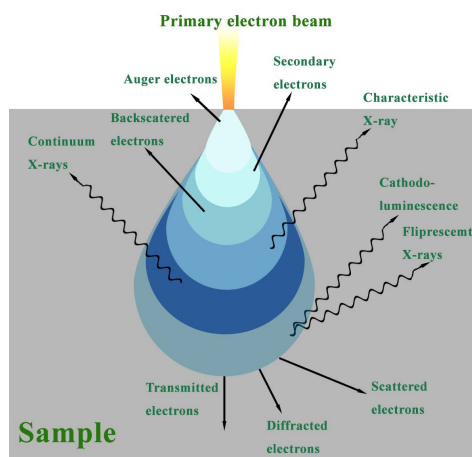


Fig. 4.2 Schematic of electron beam interaction.

An atom contains ground state electrons in discrete energy levels, such as K, L and M shells, see Fig. 4.3. When an incident beam electron excites an electron in a low-energy shell (inner shell), the electron from high-energy shell (outer shell) will fill the hole and release the energy difference to form an Energy-dispersive X-ray spectrum. The method is called EDX, or EDS. Each element has its own unique energy shell structure resulting in a characteristic X-ray. Hence, EDS is often used to determine the presence of the chemical elements and their relative percentage in the sample, which is often integrated

into SEM and STEM. The EDS detector in this project is a silicon drift detector (SDD), having short processing time and allowing very high throughput.

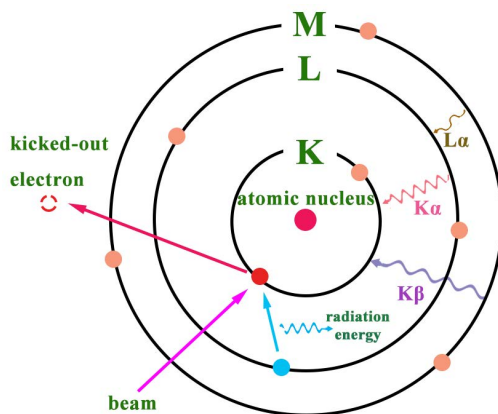


Fig. 4.3 A brief principle of EDS.

4.2.3 Transmission electron microscopy

Transmission electron microscopy (TEM) is a microscopy method where a parallel electron beam with high energy is transmitted through a thin specimen to generate images. The electrons are generated by the electron gun by thermionic emission from lanthanum hexaboride (LaB_6) rods or tungsten filaments which is connected to a high voltage source (200 kV), and then directed by lenses to form a parallel electron beam. [4] There are two basic operations of the TEM: diffraction and image mode (Fig. 4.4), controlled by adjusting the intermediate lens. TEM collects transmitted electrons for imaging. Thus, the sample thickness is generally less than 100 nm. Scanning transmission electron microscopy (STEM) mode can be achieved in the same instrument by changing the electron beam from a parallel to a focused one as a probe to scan samples. STEM is very useful for EDS mapping and electron energy loss spectroscopy (EELS). In this project, TEM images were tested on a FEI Tenai T20 with an operating voltage of 200 kV. The high-angle annular dark-field scanning transmission electron microscopy (HAADF-STEM) images and EELS were obtained with a FEI Titan Analytical 80-300ST TEM at 300 kV.

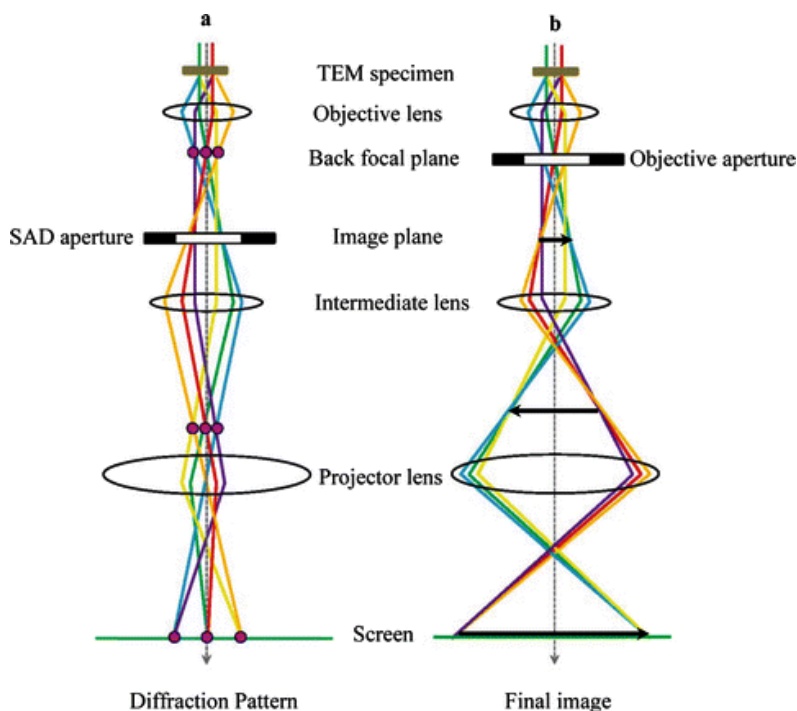


Fig. 4.4 The two basic operation modes of the TEM imaging system. Diffraction mode (a) and image mode. *Reproduced with permission from [5]*

4.3 Electrochemical techniques

4.3.1 Cyclic voltammetry

Cyclic voltammetry (CV) is generally applied to investigate the kinetics and reversibility of an electrochemical redox reaction, and to determine the intermediates during the redox reaction and the stability of reaction products. A potential is applied over, the working electrode in periodical sweep between low potential (E_{low}) and high potential (E_{high}), see Fig. 4.5a. At the same time the current responds are collected versus applied potential to give CV curves see Fig. 4.5b. The positive wave indicates that there is an oxidation reaction occurring oxidizing R to O. The important parameters include anodic potential (E_p^a) and anodic peak current (I_p^a). In reverse direction, the reduction reaction occurs from O to R, including the parameters of cathodic potential (E_p^c) and cathodic current (I_p^c).

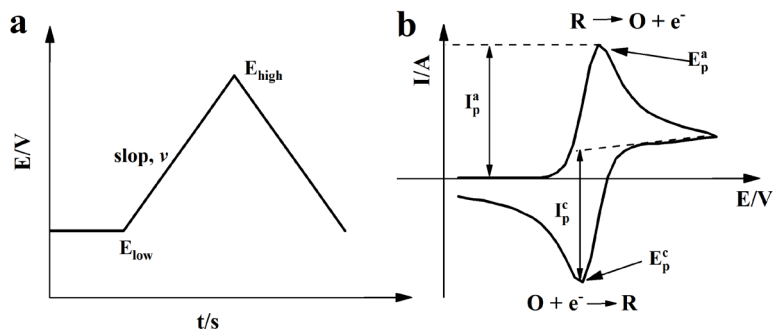


Fig. 4.5 Profiles of potential versus time for CV (a), and a typical reversible cyclic voltammogram (b).

An overall electrode reaction, $O + ne^- \rightleftharpoons R$ consists of a series of steps, see Fig. 4.6, including electron transfer at the electrode surface and adsorption (diffusion). In an ideal reversible one electron transfer reaction, the difference between the two peak potentials, ΔE , is 56.5 mV. The relationship between the number of electron transfer and ΔE can be described by the following equation: [6]

$$\Delta E = E_{pa} - E_{pc} = \frac{56.5 \text{ mV}}{n} \quad (4.3)$$

However, the typical experimental values of the potential difference are greater than the theoretical one, due to the polarization over-potential and the electron transfer rate. The current is governed by the rates of the diffusion and electron transfer steps. The rate of the slowest step defines the rate of the whole electrochemical reaction. If diffusion is the slowest step the electrochemical reaction is called reversible. The peak current (i_p) will obey the Randles-Ševčík equation: [7]

$$i_p = 0.4463nAcF\left(\frac{nADFv}{RT}\right)^{\frac{1}{2}} \quad (4.4)$$

where 'n' is the number of transferred electrons, 'A' is the geometrical area of the electrode, 'c' the concentration of analyte, 'F' is Faraday's constant, 'D' is the diffusion coefficient of the species, 'R' is the gas constant and 'T' is the temperature. For irreversible reactions (where the electron transfer step is the slowest one), the peak current is smaller, and the potential difference is greater than the reversible reaction. In this PhD project, LIB coin cells were tested in a potential range of 0.02-3.0 V at scan rate of 0.1 mV s⁻¹. ZIB coin cells were examined in a range of 0.2-1.8 V at scan a range from 0.1-0.8 mV s⁻¹.

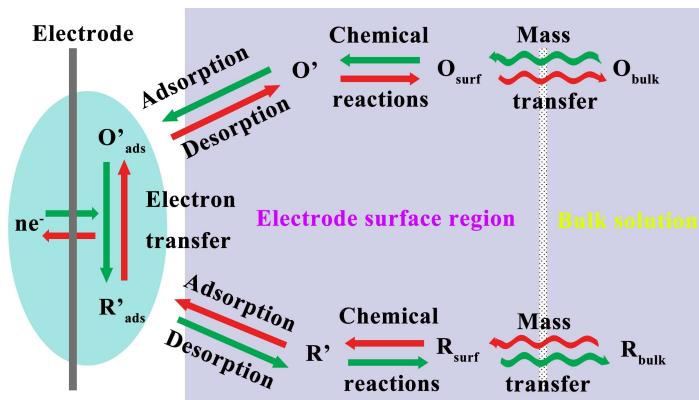


Fig. 4.6 Pathway of a general electrode reaction.

4.3.2 Electrochemical impedance spectroscopy

Electrochemical impedance spectroscopy (EIS) is a perturbative characterization of the dynamics of an electrochemical process, which is generally employed to investigate the diffusion coefficient of the metal ions in electrode materials. The electrochemical impedance is measured under an AC potential with a small excitation signal, leading to a pseudo-linear AC current response, like Fig. 4.7a. The sinusoidal current has a phase-shift to the sinusoidal potential, and the electric impedance of the electrode based on Ohm's Law is described in the following equation: [8]

$$Z = |Z|e^{-j\Phi} \quad (4.5)$$

where ' $|Z|$ ' is the modulus of the applied potential divided by the current response, ' j ' is the imaginary number and ' Φ ' is the phase shift. When the electrochemical system exhibits pure capacitor, Φ equals to $\pi/2$. While the pure resistor behavior has Φ equals 0.

Due to the complex behaviors, the electrode generally contains more than one element, including electrolyte resistance ($R_{\text{electrolyte}}$), electron transfer resistance (R_{ct}), and capacitance (C_{dl}) in series and parallel configurations, see Fig. 4.7b. Faradic currents will go the way of R_{ct} , and non-faradaic currents go the way of C_{dl} . Since the diffusion behavior on the surface of the working electrode cannot be neglected, Warburg impedance is also introduced into the circuit, which models semi-infinite linear diffusion. In this PhD project, this versatile element is employed to calculate the metal ion diffusion coefficient for both LIB and ZIB system.

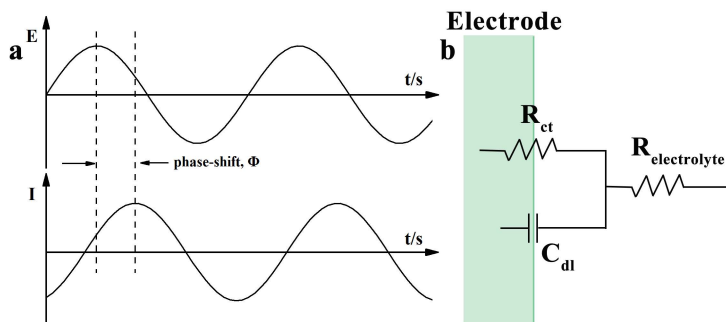


Fig. 4.7 Simusoidal current response in a linear system (a), and the impedance behavior on the surface of an electrode (b).

4.3.3 Galvanostatic charge and discharge

Galvanostatic charge and discharge (GDC) is a standard technique to study the electrochemical performance and cycle-life of a battery. The battery is conducted under a constant current until reaching a set potential, and then employed a reverse constant current, see Fig. 4.8a. A repetitive loop of charging and discharging is called a cycle. The corresponding plots of potential *vs.* time are the GCD curves, see Fig. 4.8b. The specific capacity is the amount of electric charge per gram of the active materials, which can be calculated according to the GCD curves and Equation 4.6. The unit of the specific capacity is ampere-hour per gram (Ah g^{-1}), where $1\text{Ah} = 3600$ coulombs. There are some plateaus observed along the potential plots in the GCD curves, see Fig. 4.8b. These occurs at the redox potential of the active materials and are due to the metal ion intercalation and de-intercalation process. The plateaus are very obvious at lower current density, and the phase transition occurs at the same time scale. At higher current density, the time during a charge or discharge is not long enough to complete inserting or deserting from the electrode, leading to a polarization of the battery. Coulombic efficiency (CE) is another important parameter, describing the charge efficiency, which is ratio of the total charge extracted from the battery to the total charge into the battery over one cycle, see Equation 4.7.

$$Q = \frac{I \cdot t}{3600 \cdot m} \quad (4.6)$$

$$\epsilon_{\text{coulombic}} = \frac{Q_{\text{discharge}}}{Q_{\text{charge}}} \quad (4.7)$$

In this project, GCD testing of the cell was evaluated at various current densities on either a Metrohm Autolab potentiostat or a Biologic Science Instrument VMP3.

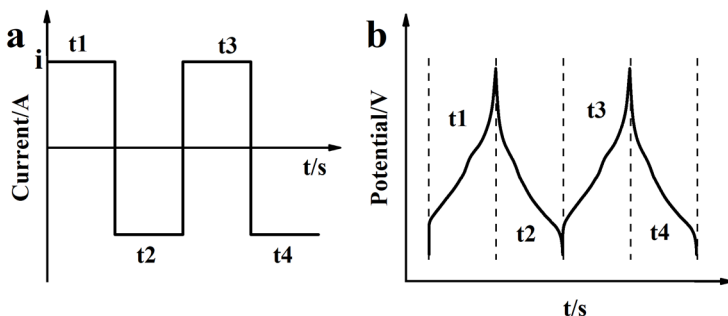


Fig. 4.8 Cyclic chronopotentiometry plots.

4.3.4 Galvanostatic intermittent titration technique

Galvanostatic intermittent titration technique (GITT) measures the changes in cell voltage under period with and without current. When a constant current is applied to the electrode material, the metal ion will be inserted into and desorbed from the host material during charging and discharging process. By using current step, the amount of charge injected or withdrawn in each step can be controlled. Due to the metal ion concentration gradient forming from the surface to the bulk of the active material during the period with constant current, the voltage will be changed to reach a steady state when interrupting the current. By calculating the rate of change in average metal ion concentration, the diffusion coefficient of the metal ion can be determined.

Fig. 4.9 illustrates constant current and its response of this current during charge and discharge process. In this PhD project, the measurements were performed on an Autolab potentiostat at current density of 60 mA g⁻¹ for 30 min and a relaxation duration of 120 min. Zn²⁺ diffusion coefficient (D, cm² s⁻¹) in vanadium oxide and graphene oxide composite materials can be obtained via:[9]

$$D = \frac{4L^2}{\pi t} \left(\frac{\Delta E_s}{\Delta E_t} \right)^2 \quad (4.8)$$

where 't' is the time (s) for an applied galvanostatic current; 'L' is the diffusion length of Zn²⁺ (cm), calculated by the electrode thickness of the coating layer; 'ΔE_s' and 'ΔE_t' are the quasi-equilibrium potential and the change of cell potential during the current pulse, respectively.

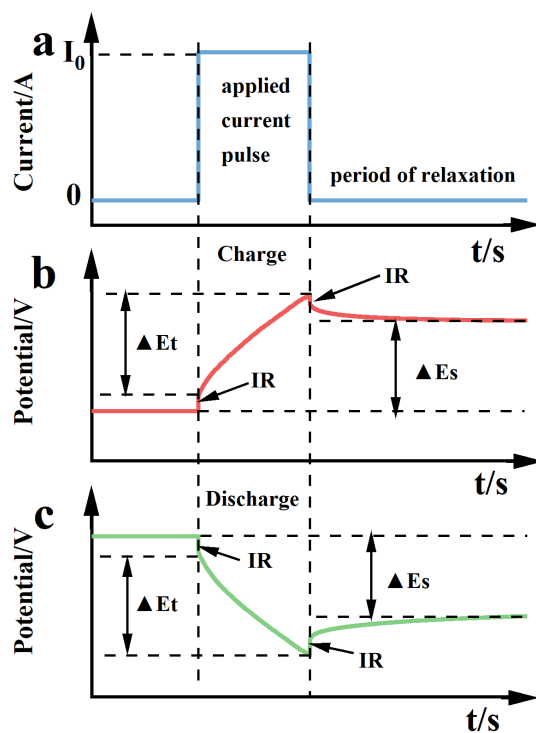


Fig. 4.9 Current as a function of time in an individual current step and the potential as a function of time when a current is applied. The Ohmic voltage drop (IR) is the instantaneous change in voltage immediately after onset and interruption of a current.

References

- [1] Morsali, A.; Hashemi, L., *Adv. Inorg. Chem.* **2020**; 76, pp 33-72.
- [2] Tawfik, A. S.; Shafquat, M.; Arunima, N.; Brij, B., *Advanced Nanomaterials for Water Engineering, Treatment, and Hydraulics* **2017**, chapter 3, 40-57.
- [3] Zhang, M.; Hou, C.; Halder, A.; Ulstrup, J.; Chi, Q., *Biosens. Bioelectron.* **2017**, 89, 570-577.
- [4] Williams, D. B.; Carter, C. B., The Instrument. In *Transmission Electron Microscopy: A Textbook for Materials Science* **2009**, chapter 9, 141-171.
- [5] Deepak, F. L.; Anumol, E. A.; Li, J., *Metal Nanoparticles and Clusters* **2018**, chapter 7, 219-287.
- [6] Nicholson, R. S.; Shain, I., *Anal. Chem.* **1964**, 36 (4), 706-723.
- [7] Paixão, T. R. L. C., *ChemElectroChem* **2020**, 7 (16), 3414-3415.
- [8] Ramos, P. M.; Fonseca da Silva, M.; Cruz Serra, A., *Measurement* **2004**, 35 (1), 89-96.
- [9] Yan, H.; Ru, Q.; Gao, P.; Shi, Z.; Gao, Y.; Chen, F.; Chi-Chun Ling, F.; Wei, L., *Appl. Surf. Sci.* **2020**, 534, 147608.

Chapter 5

Nitrogen-doped carbon coating on zinc vanadate as lithium anode

As described in the introduction, transition metal oxides are highly appealing candidates for application as LIBs anode materials and have been widely investigated. Among these, zinc vanadates with both conversion-type and alloying materials deliver a high theoretical capacity. To further improve its electrochemical performance, carbon coating at the nanoscale is introduced to stabilize the crystal structure during the Li^+ ion intercalation process and thus to achieve a long cycling life, as well as by improving the ionic and electronic conductivities. Similar to other metal oxides, however, the vanadium in zinc vanadate experience partial reduction in the carbon coating process. Knowledge of the oxidation state is important for the estimation of the number of electrons that can be transferred. More interestingly, the coating process can also result in a change in the ratio between the metals due to loss of vanadium during the annealing of zinc vanadate. This effect is not widely recognized. Therefore, I designed an experiment to systematically investigate the effect of the carbon coating on the oxidation states of the vanadium and the changes of the zinc to vanadium ratio as described in the following published publication, Paper I. Furthermore, the effects on the Li^+ ion storage are well studied by comparing the zinc vanadate without carbon coating. I conceived and performed all experiments described in the paper except the EPR analysis. The analysis and writing of the paper were also performed by me with suggestions and proof reading by the other authors.

This chapter is a published article: H. Cao, Z. Zheng, J. Meng, X. Xiao, P. Norby, S. Mossin, Examining the effects of nitrogen-doped carbon coating on zinc vanadate nanoflowers towards high performance lithium anode, *Electrochemical Acta*, 356 (2020) 136791. <https://doi.org/10.1016/j.electacta.2020.136791>.

This published article is given below and with reproduced here with the permission of *Electrochimica Acta* which is an Elsevier journal:



Examining the effects of nitrogen-doped carbon coating on zinc vanadate nanoflowers towards high performance lithium anode

Huili Cao^{a,*}, Zhiyong Zheng^a, Jie Meng^a, Xinxin Xiao^a, Poul Norby^b, Susanne Mossin^{a,*}

^a Department of Chemistry, Technical University of Denmark, 2800 Kgs. Lyngby, Denmark

^b Department of Energy Conversion and Storage, Technical University of Denmark, 2800 Kgs. Lyngby, Denmark

ARTICLE INFO

Article history:

Received 5 June 2020

Revised 15 July 2020

Accepted 15 July 2020

Available online 20 July 2020

Keywords:

Nitrogen-doped carbon

Oxidation state

Zinc vanadate

Anode

Lithium-ion battery

ABSTRACT

Coating transition metal oxides with nitrogen-doped carbon is an efficient way to enhance lithium-ion battery performance by improving the conductivity and stability of the electrodes. So far, little attention has been paid to how the calcination process affects bimetallic oxides, such as zinc vanadate, with regards to the oxidation state of the metal, the zinc/vanadium ratio and the specific surface area. In this work, we report nitrogen-doped carbon coated zinc vanadate nanoflowers (particle size: 10 nm; coating layer thickness: 20 nm) with a high specific surface area ($115 \text{ m}^2 \text{ g}^{-1}$) through a facile method. High-angle annular dark-field scanning transmission electron microscopy, X-ray diffraction and electron paramagnetic resonance spectroscopy reveal that V^{5+} from the precipitated $\text{Zn}_3(\text{OH})_2(\text{V}_2\text{O}_7) \cdot (\text{H}_2\text{O})_2$ is largely converted to V^{3+} in ZnV_2O_4 . A vanadium loss of about 9% during calcination lead to increased Zn/V ratio and formation of ZnO. When applied as anode in a lithium-ion battery, the as-prepared $\text{ZnV}_2\text{O}_4/\text{ZnO}/\text{N}$ doped C exhibits a considerable reversible specific capacity of 620 mAh g^{-1} at a current density of 0.1 A g^{-1} after 50 cycles, very close to the theoretical capacity (651 mAh g^{-1}) and considerably higher than the non-coated counterpart (306 mAh g^{-1}). The material is stable during extended cycling (200 cycles at 0.5 A g^{-1}). In-depth electrochemical analysis including three-electrode system testing shows that the carbon shell is crucial in maintaining the structure stability and enhancing the capacity of the active material.

© 2020 Elsevier Ltd. All rights reserved.

1. Introduction

In recent years, transition metal oxides (TMOs) and carbon composites in core-shell structures have been used in a wide range of fields, including electromagnetic wave absorption [1], sensors [2], supercapacitors [3] and lithium-ion batteries (LIBs) [4,5]. The advantages are the low density and high conductivity of the carbon layer and the large fraction of void space. In a typical synthesis, the metal oxides are fabricated first in a certain morphology and then coated with a carbon layer to form a core-shell structure. The carbon shell can come from various sources: glucose [6], starch [7], polydopamine [8], metal-organic frameworks [9], pyrrole [10], acrylonitrile [11], and pyridine [12]. Among them, starch is very attractive given its wide availability, non-toxicity and low-cost. The large amounts of hydroxyl groups in starch can coordinate well with metal ions, allowing good dispersion and well controlled size and shape of TMO nanoparticles. In order to improve the starch carbon properties further, the doping method play an important role [13–16]. Various doping strategies has been put up by dif-

ferent research groups; this includes doping with metal ions [17–19], B [20], and N [21–24]. Polydopamine [25,26] is a biomimetic adhesive polymer that can easily coat on material surfaces by self-polymerization in aqueous media. Additionally, calcination of polydopamine results in a nitrogen-doped carbon layer with high electrical conductivity [27–30].

For electrode material of LIB, commercial anodes are mainly relying on carbon-based materials, such as graphite, with a theoretical capacity of 372 mAh g^{-1} . There is a potential safety issue when using carbon-based anodes since lithium insertion primarily occurs at a low voltage of about 0.1 V vs. Li/Li^+ [31], which can lead to an internal short circuit due to the formation of lithium dendrites [32]. An alternative anode material is spinel lithium titanate ($\text{Li}_4\text{Ti}_5\text{O}_{12}$, LTO), exhibiting a high insertion potential about 1.55 V vs. Li/Li^+ for charge and discharge [33,34]. However, LTO suffers from a poor electronic conductivity and a limited theoretical capacity of 175 mAh g^{-1} [35].

Zinc vanadium oxide materials are among the most promising anode candidates, possessing a similar insertion potential to spinel LTO and a much higher theoretical capacity over 500 mAh g^{-1} . Zinc vanadate exists in several crystal forms including a spinel-type. It can be converted to composite materi-

* Corresponding authors.

E-mail addresses: hucan@kemi.dtu.dk (H. Cao), smo@kemi.dtu.dk (S. Mossin).

als with both conversion-type (zinc vanadate) and alloying material (Zn). Alloying materials exhibit higher gravimetric capacity compared to conversion-type materials, and suffer from more serious volumetric expansion during Li^+ uptake [36,37]. Therefore, the mixed conversion type and alloying type materials are applied in mixed-valence TMOs to give an excellent electrochemical performance. The complex chemical composition allows interfacial and synergistic effects between the multiple metal species [38]. For example, Yin et al. [39] synthesized hollow $\text{Zn}_3\text{V}_2\text{O}_8$ nanocages by a solvothermal method showing a capacity of 1400 mAh g^{-1} at a current density of 100 mA g^{-1} after 80 cycles. Luo et al. [40] employed electrospinning to fabricate one-dimensional $\text{Zn}_2\text{V}_2\text{O}_7$ nanofibers with a capacity of 700 mAh g^{-1} after 100 cycles at a current density of 50 mA g^{-1} . It is hypothesized that carbon coating is effective to improve the electronic conductivity while maintaining a stable morphology of zinc vanadate.

Similar to some other TMOs, zinc vanadate is expected to be reduced to a lower oxidation state due to the presence of carbon during the calcination process. For example, Wang et al. [41] calcinated porous Mn_2O_3 microspheres coated with polypyrrole and identified the product as MnO/NC by XRD. Similarly, FeOOH nanorods [42], Ni/C composites [43], peapod-like V_2O_3 nanorods [44], and VO_2 -carbon composites [45] with carbon coatings were derived from metal oxide precursors with higher oxidation states. Bimetallic oxides such as core-shell $\text{Zn}_3\text{V}_3\text{O}_8/\text{C}$ composite microspheres [46] were obtained from PVP encapsulated $\text{Zn}_3\text{V}_2\text{O}_7(\text{OH})_2$, where V^{5+} was reduced to V^{4+} and V^{3+} . These examples clearly demonstrate that carbon coating induces reduction of the metal. It is important to understand the chemical composition of the electrode completely, because it will not only help us to estimate the number of electrons that can be transferred, but also to identify the chemical reactions during the charge and discharge process. Analysis of the reduction process is often limited to XRD and XPS, which might not be suitable for nano-scaled samples with broad XRD peaks or on particles encapsulated in thick shells with weak XPS signals. It's noteworthy, but not widely recognized, that the bimetallic oxide zinc vanadate might also experience a zinc to vanadium ratio change during calcination [46].

Herein, we report a facile method to synthesize nitrogen-doped (N-doped) carbon-coated porous flower-like zinc vanadate by a simple direct precipitation at room temperature and calcination in an argon atmosphere. To investigate the effects of the calcination process on the ratio of metal ions and the vanadium oxidation state, ICP-OES, EPR and HAADF-EELS are applied to obtain the concentration of zinc and vanadium in the as-prepared products, and the prevalent oxidation state of vanadium after the coating process. The materials are applied as the anode of LIBs revealing that the core-shell carbon-coated zinc vanadate with a high specific surface area ($115 \text{ m}^2 \text{ g}^{-1}$) exhibits a high stable specific capacity of 404 mAh g^{-1} at 500 mA g^{-1} after 250 cycles. We hypothesize that the porous structure is well suited to accommodate the volume expansion and extraction during the electrochemical process. A three-electrode system is applied to study the contribution of the anode to the impedance of the whole cell.

2. Experimental

2.1. Chemicals

Zinc acetate dihydrate ($\text{Zn}(\text{CH}_3\text{COO})_2 \cdot 2\text{H}_2\text{O}$, 99.0%, CAS:5970-45-6), ammonium metavanadate (NH_4VO_3 , 99.0%, CAS:7803-55-6), and carbon black (99.9%, CAS: 1333-86-4) were bought from Alfa Aesar. Starch ($(\text{C}_6\text{H}_{10}\text{O}_5)_n$, CAS:9005-25-8), poly(vinylidene fluoride) (PVDF, $(\text{CH}_2\text{CF}_2)_n$, average $M_w \sim 534,000$), dopamine hydrochloride (2-(3,4-dihydroxyphenyl)ethylamine hydrochloride, $\text{C}_8\text{H}_{11}\text{NO}_2 \cdot \text{HCl}$), tris base (2-amino-2-hydroxymethyl-1,3-

propanediol, tris(hydroxymethyl)aminomethane, $\text{C}_4\text{H}_{11}\text{NO}_3$, 99.9%) and 1-methyl-2-pyrrolidinone ($\text{C}_5\text{H}_9\text{NO}$, NMP, 99.5%) were purchased from Sigma-Aldrich, Denmark.

2.2. Synthesis of $\text{Zn}_3\text{V}_2\text{O}_8/\text{N}$ -doped carbon flowers

In a typical synthesis, 1 mmol NH_4VO_3 was dissolved in 20 mL Milli-Q water to form solution A at 80°C . 1.5 mmol $\text{Zn}(\text{CH}_3\text{COO})_2 \cdot 2\text{H}_2\text{O}$ and 0.5 g starch were dissolved in 30 mL Milli-Q water to form solution B at room temperature (RT). Solution A was added into solution B and stirred for 1 h at RT to form the precursor in solid form (ZnVS). After filtration and washing with Milli-Q water and ethanol several times, the precursor was stirred in 80 mL tris-buffer with a pH of 8.5 (about 10 mM), into which 45 mg dopamine was added. After stirring overnight, the poly-dopamine (PDA) coated precursor was isolated by filtration and washed with water and ethanol. The PDA coated precursor was calcinated at 550°C for 2 h in Ar atmosphere at a ramping rate of 5°C min^{-1} to obtain ZnVC. For comparison, the pure precursor was also calcined in air (ZnVair) and Ar (ZnVAr) at the same temperature.

2.3. Material characterization

X-ray powder diffraction patterns (XRD) of various samples were recorded using an Image Plate Huber G670 Guinier diffractometer (Cu $\text{K}\alpha 1$ radiation, transmission mode). Field emission scanning electron microscopy (SEM) and energy-dispersive X-ray spectroscopy (EDX) characterizations were carried out on a FEI Quanta FEG 200 ESEM. Transmission electron microscopy (TEM) investigations and selected area electron diffraction (SAED) were studied by a FEI Tenai T20 operated at 200 kV equipped with a CCD camera. The high-angle annular dark-field scanning transmission electron microscopy (HAADF-STEM) images and electron energy loss spectroscopy (EELS) were obtained with a FEI Titan Analytical 80-300ST TEM at 300 kV. X-ray photoelectron spectroscopy (XPS) was tested with a Thermo Scientific K-alpha spectrometer using Al $\text{K}\alpha$ radiation. Electron paramagnetic resonance (EPR) spectra were collected on an EMX X-band continuous-wave (CW) EPR spectrometer with an ER 4102ST cavity at RT. Thermal gravimetric and differential thermal analysis (TGA, DTA) was measured in air with a ramping rate of 5 or $10^\circ\text{C min}^{-1}$ and heated up to 700°C . Textural properties were determined via nitrogen sorption at -200°C using a conventional volumetric technique on an ASAP 2020. The surface area was calculated using the Brunauer-Emmett-Teller (BET) method based on the adsorption branch of nitrogen adsorption/desorption isotherms. The elemental composition of the sample was determined via inductively coupled plasma-optical emission spectroscopy (ICP-OES) analysis on a Perkin Elmer 3000 DV analyzer.

2.4. Electrochemical measurements

The active material, carbon black and poly(vinylidene fluoride) (PVDF) with a weight ratio of 8:1:1 were mixed in 1-methyl-2-pyrrolidinone (NMP) to form a homogenous slurry, which was then coated on a copper foil current collector and dried in a vacuum oven at 120°C for 12 h. The coated copper foil was punched into a circle with a diameter of 15 mm and used as the working electrode. The loading of the active material was determined to be about 1 mg cm^{-2} . Glass microfiber filters dried at 120°C in a vacuum oven overnight were used as the separator. The tested cells were assembled in an argon glove box. A disc of fresh Li foil with a diameter of 15 mm was used as the combined counter/reference electrode, with 1 M LiPF_6 in ethylene carbonate/dimethyl carbonate (EC:DMC = 1:1 by volume) as the electrolyte. Galvanostatic

testing of the cell was evaluated in a voltage range of 0.02–3.00 V at various current densities. Cyclic voltammetry (CV) was measured in the same potential range at a scan rate of 0.1 mV s⁻¹ and electrochemical impedance spectroscopy (EIS) at the open-circuit voltage in a frequency range of 0.1–100 kHz were tested on either a Metrohm Autolab potentiostat or a Biologic Science Instrument VMP3.

3. Results and discussion

3.1. Morphology and structure characterization

The synthesis of N-doped carbon-coated zinc vanadate is illustrated in Fig. 1. The precursor (ZnVS) precipitates directly by mixing solutions of the zinc and vanadium salts at RT in a flower-like morphology. The formation of its morphology is thought to take place through an Ostwald ripening process [47]. PDA coating is performed by simply adding dopamine into the tris-buffer (pH 8.5) suspension of ZnVS, undergoing spontaneous polymerization [48]. Zinc vanadate coated carbon composites (ZnVC) are obtained after the carbonization of PDA coated ZnVS. By calcination the ZnVS in air and Ar, the comparison samples ZnVair and ZnVAr can be obtained, respectively.

The detailed morphology and the structural features of the products were investigated by SEM and XRD. The as-obtained precursor ZnVS is well distributed and exhibits a uniform flower-like structure with an average size of 500 nm, as shown in Figure S1. The higher magnification image (Fig. 1a) shows that the flower is assembled by nanosheets with smooth surfaces. All the peaks of the precursor (ZnVS) can be indexed to $\text{Zn}_3(\text{OH})_2(\text{V}_2\text{O}_7) \cdot 2\text{H}_2\text{O}$ (ICOD: 00-087-0417), in Fig. 1b. A broad peak appears at around 10–20° after PDA coating, indicating that the amorphous polymer dopamine is successfully introduced into the ZnVS.

When as-produced ZnVS is calcinated in air (to ZnVair), the smooth nanosheets of the flower shrink into nanoparticles in the same overall size (about 500 nm) as in ZnVS (Fig. 1d). XRD patterns (Fig. 1g) display the highly crystalline peaks corresponding to the orthorhombic crystal structure of $\text{Zn}_3\text{V}_2\text{O}_8$ (ICOD:00-034-0378). TEM is used at low magnification in order to estimate the average size of the nanoparticles. As shown in Fig. S2a and b, the nanoparticles in ZnVair are well distributed with sizes of about 100–300 nm. The high-resolution TEM (Fig. S2c) recorded on the particles shows clear lattice fringes, and the calculated interplanar spacing is ca. 0.247 nm, assigned to the (311) plane of $\text{Zn}_3\text{V}_2\text{O}_8$.

ZnVAr is a black powder obtained by calcination of ZVS in an Ar atmosphere, the colour indicating carbonization of a remnant of starch in the precursor. ZnVAr maintains the flower morphology (Fig. 2e). The surface of the ZnVAr flower is rougher than that of ZnVS. TEM images show a porous flake structure (Fig. S2d and e), composed of nanoparticles with an average size of 10 nm. The lattice fringes on the nanoparticle (Fig. S2f) indicate good crystallinity of the product. In the corresponding converted fast Fourier transform (FFT) pattern (inset of Fig. S2f), it is determined that the diameter of the spot is ca. 3.96 1/nm, corresponding to an interplanar spacing of 0.253 nm. This is assigned to the (311) plane in the spinel structure of Zn_2VO_4 or ZnV_2O_4 , which contains vanadium in lower oxidation states (V^{4+} or V^{3+}). It indicates that some of the vanadium has been reduced to a lower oxidation state by starch during calcination. Due to the small size of the nanoparticles, there are some broad peaks in the XRD patterns (Fig. 1h). The main diffraction patterns at 30.0°, 35.4°, 56.9°, and 62.5° (2 theta) can be assigned to the (220), (311), (511), and (440) crystal planes of either Zn_2VO_4 (ICOD:01-073-1632) or ZnV_2O_4 (ICOD:01-075-0318). Peaks at 31.7°, 34.4°, and 36.2° correspond to the (010), (002) and (011) crystal planes of ZnO (ICOD: 00-001-1136).

Fig. 1f shows that the ZnVC also maintains the flower structure of the precursor. The XRD result (Fig. 1i) shows that ZnVC and ZnVAr primarily consists of the same crystal phase. A typical STEM image of the ZnVC flowers is given in Fig. 2a, suggesting a uniform distribution of the samples. The carbon layer coats the flake uniformly to form a core-shell structure. The thickness of the layer is ca. 20 nm, with a porous inner core (of ca. 10 nm in diameter, see Fig. 2b). The line scan EDS element analysis by HAADF-STEM in Fig. 2c is used to confirm the core-shell element distribution. Zn, V, and O are the dominant elements at the centre of the flake and are uniformly distributed. The outside shell contains C and N. Thanks to the supporting carbon layer, the flake keeps integrity during the calcination process. The high-resolution TEM image of the ZnVC clearly shows the crystalline structure. By calculating the converted FFT spots (inset of Fig. 2d), the lattice fringes (0.253 nm) again correspond to Zn_2VO_4 or ZnV_2O_4 . Raman spectroscopy (Fig. S3) is applied to investigate the presence of carbon in ZnVAr and ZnVC. There are two peaks in the Raman spectrum at about 1340 and 1600 cm⁻¹, which can be assigned to amorphous carbon (D-band) and graphitic carbon (G-band), respectively [49,50]. This indicates the presence of carbon in both ZnVAr and ZnVC.

3.2. The oxidation state of vanadium

Dopamine, a non-toxic and safe carbon source, can be easily polymerized and coated on the metal oxide surface and forms an N-doped carbon layer upon calcination. Vanadium in the component metal oxides will be reduced from +5 to lower oxidation states during the carbon coating process in an inert atmosphere like what is observed for both Mn-based oxides and Fe-based oxides [51,52]. The oxidation state of V after the calcination process is difficult to predict, in particular as a ternary metal oxide. The oxidation state of V in the spinel structure can not be determined by XRD due to the low crystallinity of the materials. XPS is thus applied to further investigate the products. As shown in Fig. 3a, the precursor ZnVS contains Zn, V, C, and O. C might come from starch or carbon contamination. The sharp peaks at 1020.87 and 1043.67 eV are assigned to Zn 2p_{1/2} and Zn 2p_{3/2} from Zn²⁺ [53], with the small peaks between 527 and 512 eV assigned to V 2p. The same peaks can be observed in ZnVair, ZnVAr and ZnVC. There is an extra tiny peak in ZnVC at 399.37 eV which is assigned to N 1s, due to the dopamine carbon source. In the high-resolution XPS pattern of V 2p in Fig. 3b, the peaks of ZnVAr and ZnVC are redshifted to lower binding energy position, indicating the reduction of vanadium during the calcination process [54]. The peak patterns are analyzed by fitting with Gaussian shapes, as shown in Fig. S4. The main peaks observed for ZnVS at 517.2 and 524.4 eV originate from V⁵⁺ 2p_{3/2} and V⁵⁺ 2p_{1/2} [55]. The sharp peaks in ZnVair are observed at the same position, indicating the presence of V⁵⁺. Peaks assigned to V⁴⁺ can be observed as well at 515.9 and 522.7 eV. ZnVAr and ZnVC both show peaks that can be assigned to V 2p_{3/2} at about 515.8 eV, corresponding to V⁴⁺ and clear shoulders that show the presence of V³⁺. Although XPS is employed successfully in some vanadium-based materials, in this particular case this method seems to be less useful due to the proximity of O1s. Besides, the relevant peak in a V₂O₃/carbon composite might also blue shift compared to the peak in pure V₂O₃. For example, Wu et al. [56] fabricated amorphous V₂O₃/C where the V 2p_{3/2} peak is located at 517.2 eV. We concluded that another approach is needed to confirm unequivocally the oxidation state of vanadium.

Electron energy loss spectroscopy (EELS) is commonly used to identify the oxidation state of transition metals in materials because the near edge features of the element are highly sensitive to the local valence electronic structures [57]. Fig. 3c shows that the vanadium L edge of ZnVC and the L3 energy loss peak is lo-

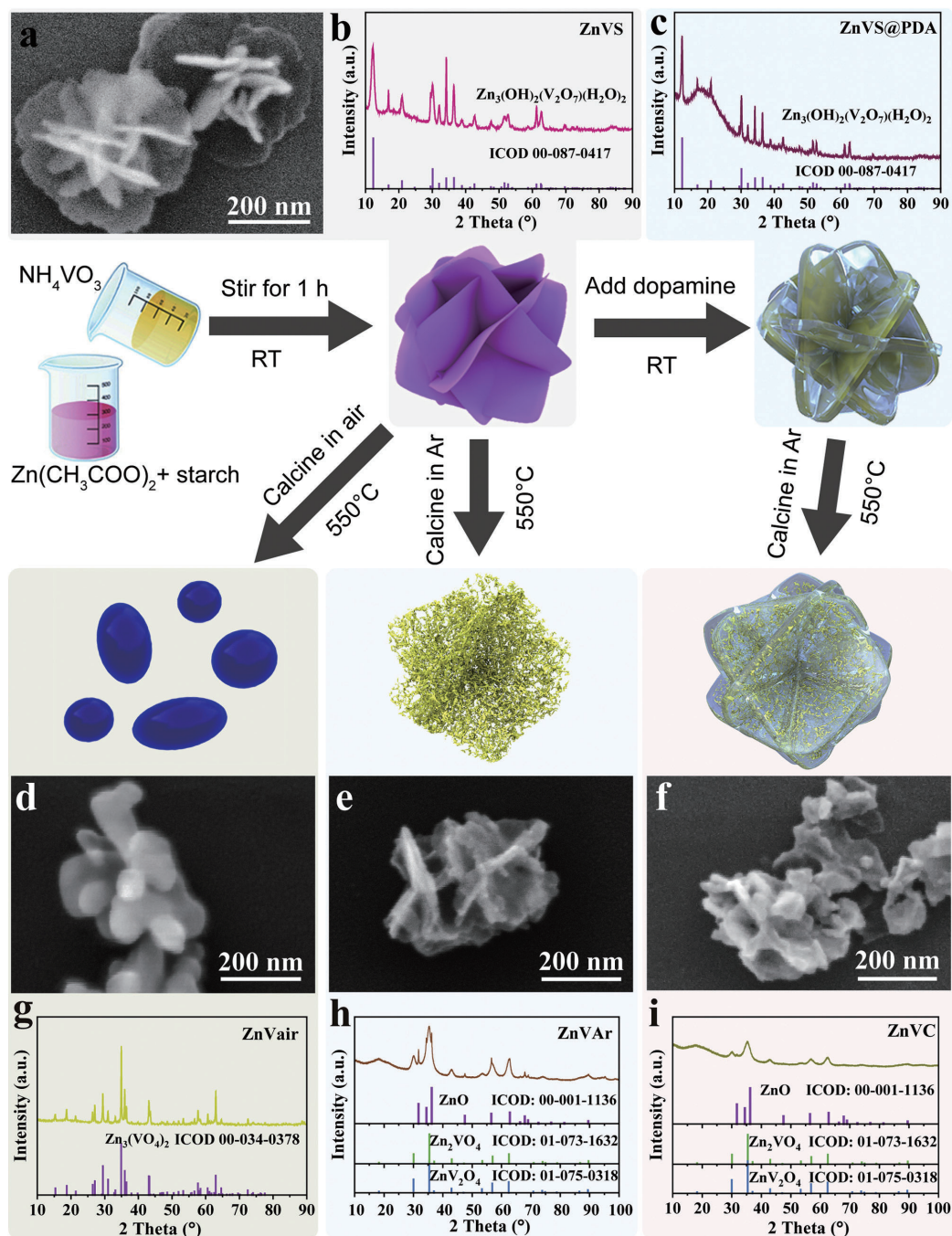


Fig. 1. Schematic illustration of the three types of zinc vanadate synthesis process. SEM image and XRD patterns of precursor ZnVS (a) and (b), XRD pattern from ZnVS coated with dopamine (c); SEM images and XRD patterns of ZnVair (d) and (g), ZnVAr (e) and (h), and ZnVC (f) and (i).

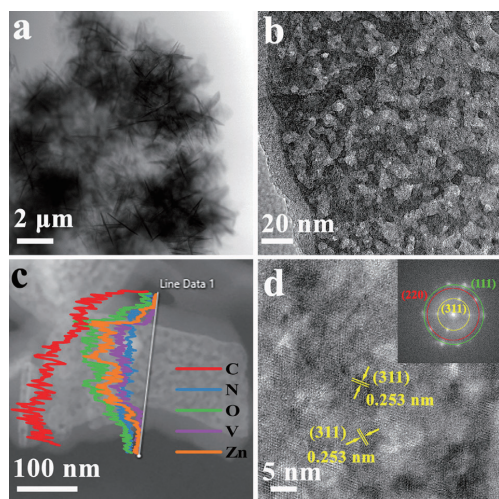


Fig. 2. STEM images at low magnification (a); TEM image of the porous structure (b); HAADF image and linear scan EDS elemental analysis of core-shell ZnVC (c), and HRTEM image of ZnVC (d). Inset of (d) is the corresponding converted FFT spots.

cated at 518.5 eV. It is still difficult to confirm the oxidation state of vanadium due to the use of different standards in various works [58]. Nevertheless, the oxidation state of vanadium in ZnVC could be limited to be either V^{3+} or V^{4+} according to the combination of all of the characterization efforts described above.

EPR spectroscopy is a very powerful method to identify V^{4+} species, due to its 3d ¹ electron configuration with an electron spin $S=1/2$. V^{5+} is diamagnetic and always EPR silent. V^{3+} is an integer spin system ($S=1$) that is not observed at room tempera-

Table 1
Percentage of V^{4+} obtained from EPR

Sample	ZnVS	ZnVair	ZnVAr	ZnVC
Total Mass (ppm)	22.28	23.29	24.95	19.89
V^{4+}	0.056%	0.025%	0.032% ^a	0.167% ^a

^a The majority of the EPR signal in ZnVAr and ZnVC is due to a C-centered radical

ture in X-band EPR spectroscopy due to a high zero-field splitting, but it is possible to detect it by other types of EPR investigations. EPR is applied here to detect and quantify V^{4+} . The EPR spectra of ZnVS, ZnVair, ZnVAr, and ZnVC at RT are given in Fig. 3d, confirming the presence of V^{4+} ions in all samples. It is recognized by the characteristic splitting pattern due to the interaction of the unpaired electron with the ^{51}V nuclei (natural abundance 100%) with a nuclear spin of $I=7/2$. The sharp central peak in ZnVAr and ZnVC confirms the presence of carbon residues and the broadening at the base of the sharp peak in ZnVC indicates the presence of N-doping (^{14}N has $I=1$). To quantify the amount of EPR active V^{4+} ions, the background-corrected spectra are integrated twice and compared to the double integral of reference samples consisting of $\text{VOSO}_4 \cdot 3\text{H}_2\text{O}$ diluted in K_2SO_4 . The results are collected in Table 1. In ZnVS, ZnVair, and ZnVAr, the concentration of V^{4+} correspond to less than 0.06% of the total vanadium content. The integration of ZnVC shows a relatively higher concentration of about 0.167%, but closer analysis of the spectra shows that most of the EPR signal is due to C and N-based radicals in the N-doped carbon shell. The amount of EPR active V^{4+} is comparable to the other samples.

Based on all data presented here, we suggest that the precursor ZnVS mainly contains V^{5+} , unchanged from the NH_4VO_3 starting material. ZnVair is obtained by calcination in air and is also confirmed to contain only V^{5+} . On the other hand, vanadium in ZnVAr and ZnVC is mainly reduced to V^{3+} , in a form of the spinel ZnV_2O_4 . The main crystalline phases in ZnVAr and ZnVC are ZnV_2O_4 and ZnO .

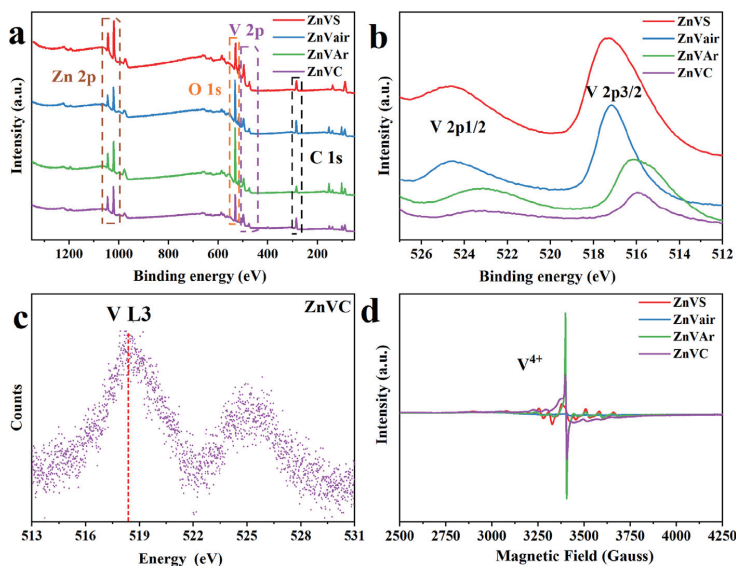


Fig. 3. XPS survey spectra (a), and V 2p (b) of ZnVS, ZnVair, ZnVAr and ZnVC; EELS spectroscopy at vanadium L edge of ZnVC (c); and EPR spectra (d).

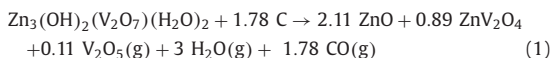
Table 2
Zn and V mass concentration determined by ICP and residual mass after heating in air determined by TGA

Samples	ZnVS	ZnVair	ZnVAr	ZnVC
Zn concentration (w%)	34.26	47.13	46.67	34.87
V concentration (w%)	17.33	23.72	22.54	16.02
Zn/V atom ratio	1.540	1.547	1.613	1.695
Experimental TGA residual mass	68.80%	-	96.25%	71.04%
Residual mass calculated from ICP data	73.58%	101.02%	98.34%	72.02%

3.3. Loss of vanadium during calcination

It was reported in the literature that the ratio of Zn to V may change during synthesis [46,59]. To confirm the composition of the obtained materials, the elemental analysis is performed by ICP analysis. All the samples are dissolved by heating in 70% HNO₃ and then diluted to 3% HNO₃. The corresponding concentrations are calibrated using standard curves (Fig. S5a). The results are collected in the first two rows in Table 2. In the precursor ZnVS, Zn mass concentration is 34.26% and V ion mass concentration is 17.33%, giving a Zn/V ratio of 1.540 in accordance with the crystalline phase Zn₃(OH)₂(V₂O₇)(H₂O)₂ as suggested by XRD. For ZnVair, the calcination process has converted the hydroxide to oxide and removed crystal water. Thus, the Zn and V concentration increases to 47.13% and 23.72%, but the ratio is the same (1.547). The procedure performed during TGA in air will result in the loss of water and carbon (giving a weight loss) and the oxidation of all vanadium to V₂O₅ (giving the possibility of a weight gain). It is almost the same procedure that is performed in order to convert ZnVS to ZnVair. The TGA results for ZnVS, ZnVAr and ZnVC are found in Fig. S5b–d. For ZnVS (Fig. S5b) the residual mass is 68.80%. During the initial drying process, about 4.43% moisture is lost and the more relevant value to compare is 72.0%. A value of 73.58% is calculated from the ICP results under the assumption that the residual mass after the TGA experiment is only due to Zn²⁺, V⁵⁺ and charge compensating O²⁻, see the bottom row of Table 2. The TGA analysis of ZnVAr under air atmosphere (Fig. S5c) shows a weight loss at the beginning due to the loss of absorbed water and the combustion of carbon and weight gain at ca. 300–400 °C, indicative of vanadium in a lower oxidation state in the sample [46]. If we compare ZnVAr with ZnVair, the Zn concentration is about the same, but some V has disappeared during the calcination process to make ZnVAr, leading to a higher Zn/V ratio (1.613). The experimental residual mass by TGA is 96.25%, close to the residual mass calculated from the ICP data of 98.34%. For ZnVC the concentration of both Zn and V is lower (34.87% and 16.02%) due to the presence of a significant amount of carbon, and the Zn/V atom ratio is even higher at 1.695. The weight loss due to absorbed water in the materials is 3.50% (Fig. S5d). The loss of weight during thermal decomposition is about 25.56%, a combined effect of combustion of the carbon to CO₂ and the oxidation of vanadium. The residual mass is 71.04%, very close to the value calculated from ICP data of 72.02%.

Therefore, the ratio of Zn to V increases from 1.54 to 1.695 after the carbon coating process, indicating ca. 9% V loss, which might be caused by the evaporation of V₂O₅(g) at high temperature during the calcination step. The ratio of Zn to V corresponds to a ratio of ZnO to ZnV₂O₄ of 2.39 in porous core-shell ZnVC. There is about 25% carbon in ZnVC from starch in the precursor synthesis and from dopamine in the coating process. Assuming that all vanadium is V³⁺ in the product, the stoichiometry of the calcination to obtain ZnVC corresponds to:



3.4. Determination of porosity

The porosity and surface area are crucial for LIB electrodes. The nitrogen adsorption-desorption isotherms and the corresponding pore size distribution of the ZnVair, ZnVAr and ZnVC are measured to further investigate the porosity of the products. As shown in Fig. 4a, The Brunauer–Emmett–Teller (BET) surface area of the ZnVair nanoparticles is ca. 21 m² g⁻¹. The corresponding Barrett–Joyner–Halenda pore size distribution is displayed in Fig. 4d, with an average pore size of ca. 40 nm and pore volume of 0.12 cm³ g⁻¹. The product ZnVAr (Fig. 4b and e) possesses a very high specific surface area of 117 m² g⁻¹, with many mesopores of up to 50 nm and a high pore volume of 0.29 cm³ g⁻¹. Interestingly, the specific surface area of ZnVC has the same high value of 115 m² g⁻¹ and pore volume of 0.27 cm³ g⁻¹, but contains more mesopores (Fig. 4c and f). Literature values of the BET surface area of vanadium-based metal oxides applied as lithium-ion batteries are collected in Table S1. For example, Xue et al. [60] synthesized hierarchical lychee-like Zn₃V₂O₈@C/rGO nanospheres with a surface area of 20 m² g⁻¹. Balaji et al. [61] fabricated porous Zn₃V₂O₈ sheets with a surface area of 22 m² g⁻¹, with improved diffusion kinetics due to a shorter diffusion pathway. Compared to this, the porous ZnVC material presented here has a significantly higher specific surface area. We suggest that the high specific surface area and the high porosity provide more active sites and facilitate Li-ion diffusion. With the help of the carbon layer, the anode materials can more efficiently accommodate the volume variation during the charge and discharge process.

3.5. Electrochemical performance

The electrochemical performance as LIB anode materials is investigated in various electrochemical tests by using a CR2032 type coin half-cell assembled with Li metal cathode. The typical cyclic voltammogram (CV) curves during the second scan are recorded in a potential range of 0.02–3.0 V at a scan rate of 0.1 mV s⁻¹ (Fig. 5). For pure Zn₃V₂O₈ nanoparticles, the obvious reduction peaks at ca. 0.5 and 0.8 V are attributed to the reduction of V⁵⁺ to V⁴⁺ and V³⁺ along with the reduction of Zn²⁺ to metallic Zn [62]. The irreversible side reaction of solid electrolyte (SEI) interphase formation with metallic Zn further alloyed to form Li-Zn occurs at ca. 0.02 V [63]. For the oxidation process, there are three peaks at ca. 0.3 and 1.4 V, corresponding to the de-lithiation of Li-Zn alloys and the oxidation of Zn⁰ to Zn²⁺, respectively [59,64]. The same peaks are observed for ZnVAr and the capacity is mainly due to faradic capacitance on the material [65]. For ZnVC, the same peaks as for ZnVAr are observed and there is one clear oxidation peak at 2.5 V. The extra peak is assigned to the extraction of Li⁺ from Li_xVO₂. The porous core-shell ZnVC exhibits both double layer capacity from carbon and faradaic capacity from redox reactions.

The charge/discharge profiles of the ZnVair, ZnVAr and ZnVC anode materials for the initial two cycles and the 35th cycle at a current density of 100 mA g⁻¹ are given in Fig. 6a–c. The charge and discharge curves show plateaus at the same potential after the initial cycle. The difference in the initial discharge curve is due to

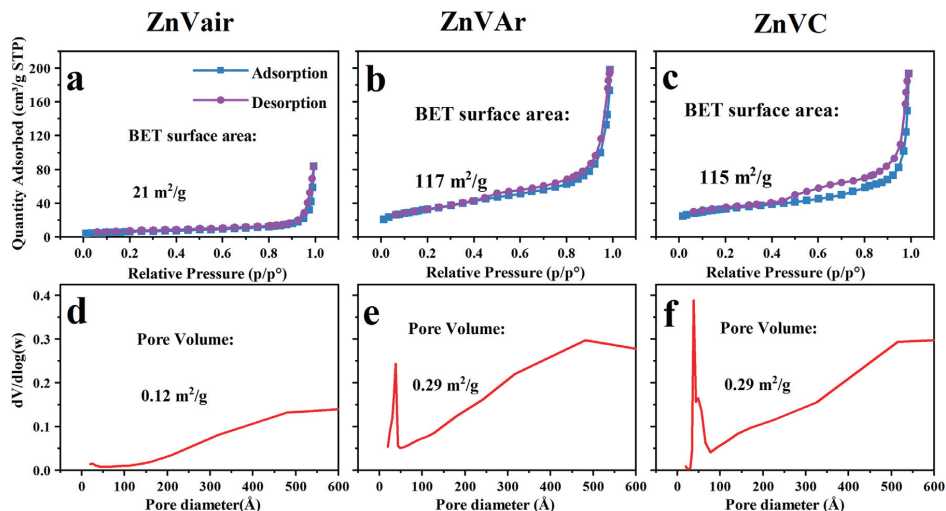


Fig. 4. N_2 adsorption-desorption isotherms of the products and their corresponding pore size distributions: ZnVair (a) and (d); ZnVAr (b) and (e); ZnVC (c) and (f).

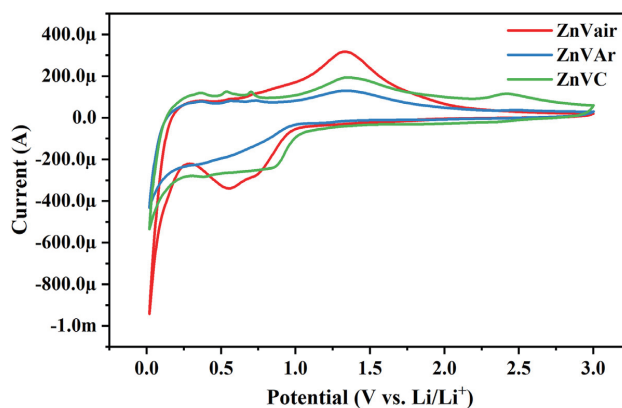


Fig. 5. CV curves of ZnVair, ZnVAr and ZnVC at 0.1 mV s^{-1} .

the different chemical compositions in the as-synthesized materials. In the first discharge curve for ZnVair, a voltage decrease at 1.5 V indicates the decomposition of the active ZnVair into ZnO, along with the formation of $\text{Li}_x\text{V}_2\text{O}_5$; the plateau at 0.8 V can be assigned to the reduction of ZnO into Zn^0 ; The two plateaus at 0.3 and 0.1 V are related to the irreversible reaction of the SEI layer by the formation of Li_2O and Li-Zn alloy [66]. The first charge curve shows a slope from 1.0 to 1.5 V, corresponding to the broad peak in the CV curve Fig. 5. The crystal phase in ZnVair is $\text{Zn}_3\text{V}_2\text{O}_8$ with V^{5+} , which potentially can transfer 15 electrons from 1 mol of $\text{Zn}_3\text{V}_2\text{O}_8$, resulting in a high initial discharge capacity of 1320 mAh g^{-1} . The coulombic efficiency is only 65%, due to side reactions of the SEI layer formation at the surfaces of the nanoparticles. In the following cycles, the plateaus are not obvious, indicating severe polarization, and the capacity decreases seriously to 267 mAh g^{-1} at the 35th cycle. In the initial discharge curve of ZnVAr a decomposition process takes place at 1.5 V, reduction of Zn at 1.0 V, and the formation of Li-Zn alloy at 0.1 V. Since the main crystal phases in ZnVAr are ZnV_2O_4 and ZnO, vanadium is in oxidation state V^{3+} , leading to fewer electrons to trans-

fer compared to ZnVair. Thus the initial discharge capacity is significantly lower (837 mAh g^{-1}). The initial coulombic efficiency is ca. 66% and the reversible capacity after 35 cycles is more stable at a value of 306 mAh g^{-1} . The same crystal phases are present in ZnVAr and ZnVC, and the initial discharge capacity of ZnVC is 860 mAh g^{-1} , close to the value for ZnVAr. The initial discharge curves follow the same trend. The reversible capacity is very stable and the same value of 620 mAh g^{-1} is found after both 2 and after 35 cycles of charging and discharging at 100 mA g^{-1} . The plateaus during charge and discharge of the ZnVC are obvious even after 35 cycles, due to the stability of the material [67]. In order to investigate the stability of the anode materials further, the cycling performance is tested at a high current density of 500 mA g^{-1} after 35 or 50 cycles (Fig. 6d-f). The capacity of ZnVair (Fig. 6d) decreases severely from 1320 to 267 mAh g^{-1} at a current density of 100 mA g^{-1} . At a current density of 500 mA g^{-1} , the capacity is even lower, 70 mAh g^{-1} . After 200 cycles, the capacity gradually climbs to 161 mAh g^{-1} . For ZnVAr (Fig. 6e) the value at cycle 35 is 299 mAh g^{-1} . At a higher current density, the capacity is stable at 225 mAh g^{-1} even after 200 cycles. Very interestingly,

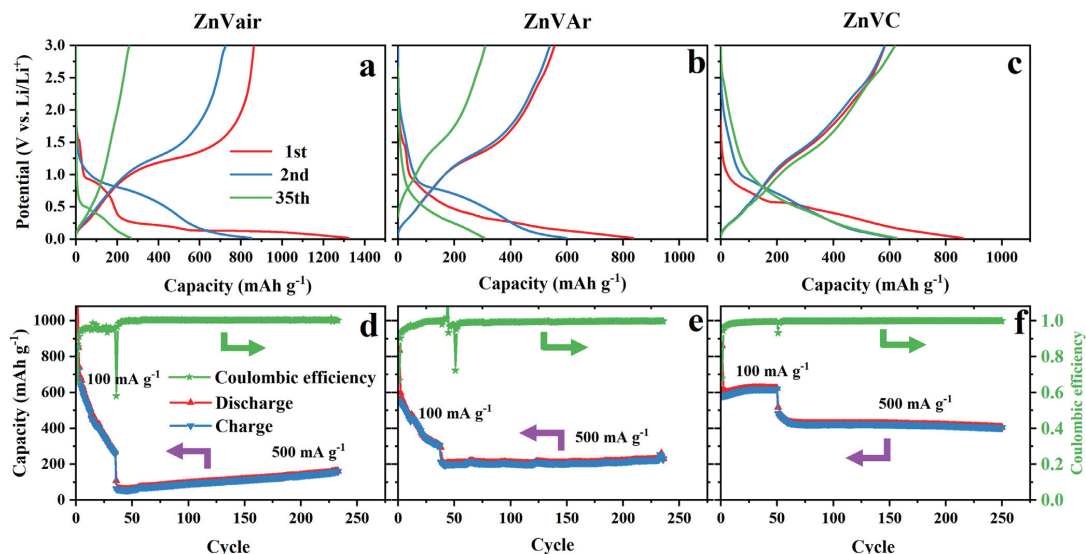
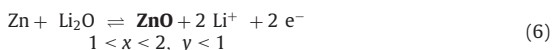
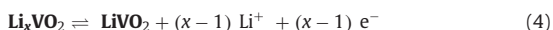
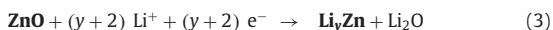
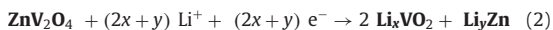


Fig. 6. Galvanostatic discharge/charge curves of the 1st 2nd and 35th cycles of ZnVair (a), ZnVAr (b) and ZnVC (c). Charge-discharge cycling performances and coulombic efficiency of battery anodes based on ZnVair (d), ZnVAr (e) and ZnVC (f).

ZnVC exhibits a super stable capacity of 620 mAh g^{-1} in the initial 50 cycles at a current density of 100 mA g^{-1} , (Fig. 6f) and a reversible capacity of 404 mAh g^{-1} in the following 200 cycles at a high current density of 500 mA g^{-1} . Though ZnVair ($\text{Zn}_3\text{V}_2\text{O}_8$) and ZnVAr ($\text{ZnV}_2\text{O}_4/\text{ZnO}$) are different initially and ZnVair has a much higher theoretical capacity than ZnVAr, the ZnVAr still delivers higher capacity than ZnVair, indicating that the porous structure contributes to a better performance. ZnVAr and ZnVC have the same metal oxide composition and morphology, but ZnVC shows a much more stable electrochemical performance, which is suggested to be the effect of nitrogen-doped carbon coating. According to the CV curves and charge/discharge curves, the reactions during charge and discharge can be summarized as follows [39,68]: Eqs. (2) and (3) (describe the initial discharge, (4–6) are the reversible charge (forward arrow) and discharge (back arrow) reactions. Compounds written in bold are observed by PXRD:



As written above, the ratio of ZnO to ZnV_2O_4 in porous core-shell ZnVC is about 2.39 with a weight percentage of about 25% carbon, indicating 53% ZnO and 22% ZnV_2O_4 . The maximum number of electrons that could be transferred for ZnV_2O_4 would be 5, and for ZnO, there are 2 electrons for the reduction process and 1 electron for the alloying process. Thus the theoretical specific ca-

capacity could be calculated by the formula [69]:

$$C_{th} = \frac{nF}{3.6 M_w} \quad (7)$$

where n is the number of the electrons that the material could transfer, F is Faradays constant (96485 C mol^{-1}) and M_w is the molar mass (g mol^{-1}). Using this, the maximum theoretical capacity of ZnVC is calculated to be 651 mAh g^{-1} disregarding any contribution from the carbon layer to the capacity. The initial discharge capacity of the ZnVC is 860 mAh g^{-1} , and the coulombic efficiency is 72%, due to the irreversible capacity formation of the SEI film and incomplete restoration to original active materials [70]. After the second cycle of the ZnVC, the value is stable at 620 mAh g^{-1} during the following 49 cycles at a current density of 100 mA g^{-1} , very close to the theoretical capacity of this material, indicating the full utilization of the material. The electrochemical performance in terms of capacity and cycling performance of the ZnV_2O_4 is better than most of the reported ZnV_2O_4 materials. For example, ZnV_2O_4 /ordered mesoporous carbon (CMK) nanocomposite obtained by a direct precipitation and calcination process exhibited 575 mAh g^{-1} at a current density of 100 mA g^{-1} after 200 cycles [71]. The porous ZnVC also outperforms LTO and other metal oxides, as shown in Table S2, such as TiO_2 nanoparticles [72], $\text{HfNb}_{24}\text{O}_{62}$ [73], $\text{Nb}_{12}\text{O}_{29}$ [74].

In battery applications, it is generally observed that materials consisting of particles perform worse than porous structures, due to particles aggregating during the charge and discharge process. Therefore, the morphology of the materials is investigated by SEM and TEM after cycling. The ZnVair nanoparticles (Fig. 7a and d) have aggregated to form large particles, but some of the porous ZnVAr flakes and most of the porous ZnVC maintain the morphology. Porous ZnVAr (Fig. 7b and e) breaks into nanoparticles. Interestingly, ZnVC (Fig. 7c and f) still retains the flower morphology with an unchanged size of ca. 500 nm. Moreover, the core-shell structure is easily observed (Fig. S6a). Fig. S6b shows the linear scan EDS element analysis by HAADF-STEM. Zinc and vanadium are present in the centre and carbon at the edges, indicating that

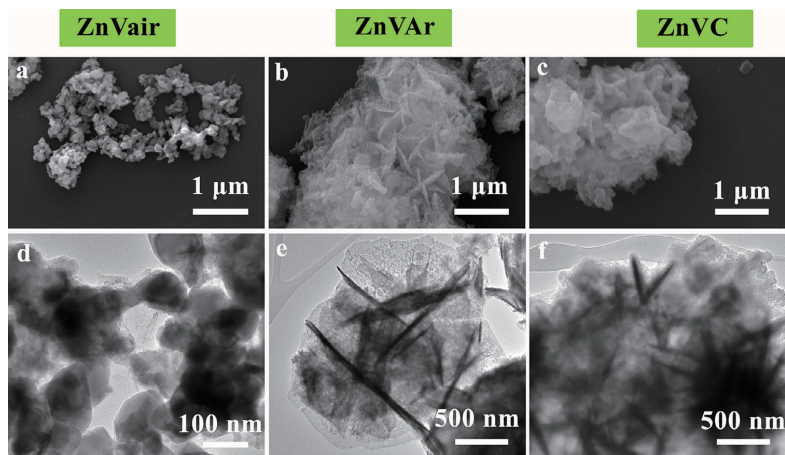


Fig. 7. SEM and TEM images of ZnVair (a, d), ZnVAR (b, e) and ZnVC (c, f) after long-term cycling.

the core-shell structure is stable during the cycling process. XRD is also applied to test the crystalline phases of the materials after extensive cycling. The results after the final discharge process (0.02 V) are shown in Fig. S7a. For ZnVair the peaks in the XRD are very weak after cycling compared to before cycling (Fig. 1g). The XRD peaks observed for ZnVAR and ZnVC after extended cycling are also weak, but there is less change from before the testing of the materials. The peaks can be assigned to $\text{Zn}_{1.98}\text{Li}_{0.02}$ (ICOD:96-153-7986) alloy as well as the spinel phase ZnV_2O_4 (ICOD:01-089-7413), which was present also before testing. The ZnV_2O_4 phase is more apparent in ZnVAR than in ZnVC and the fact that it is still present after discharge could indicate a less sufficient utilization of the material. In the fully charged state (3.0 V), the vanadium is primarily in a LiVO_2 phase (COD: 96-152-9720), and the zinc is in a ZnO phase (ICOD: 00-001-1136), as shown in Fig. S7b. Due to the irreversible reactions in ZnVair, the ZnO phase is hardly observed, comparing to ZnVAR and ZnVC.

The samples are also tested by galvanostatic discharge/charge at different current densities. As shown in Fig. S8, the reversible capacity of the ZnVair nanoparticles exhibits discharge capacities of 400, 243, 147 and 73 mAh g^{-1} at current densities of 100, 200, 400 and 800 mA g^{-1} , respectively. In contrast, the porous ZnVAR and ZnVC exhibit much better rate capacities. For ZnVAR the reversible capacities are 594, 463, 343 and 221 mAh g^{-1} and for ZnVC they are 620, 477, 368, and 259 mAh g^{-1} at these current densities, respectively. The rate performance is also a significant criterion for electrochemical performance. The ZnVAR and ZnVC both exhibit great capacity, benefiting from the porous structure that facilitates the diffusion of Li ions during the fast charge and discharge process. We suggest that the relatively high reversible capacity of the ZnVC material is due to the improved electrical conductivity from the added carbon layer.

The electrochemical properties of all materials were investigated by EIS which is a common method to reveal the electron transfer resistance at the open-circuit voltage and the negative permittivity [75]. In Fig. S9a, the plots reveal semicircles in the high-frequency region and straight line in the low-frequency region. The value of the intercept with the x-axis is the bulk resistance of the cell, reflecting the conductivity of the electrolyte and the separator resistance R_s in the range 10 to 13 Ω . The semicircle in the plot is related to the Faradaic charge transfer resistance and its relative double-layer capacitance, and the linear part is related to a combination of the diffusional effects of Li-ion on the interface be-

tween the active material and electrolyte. According to the diameter of the semicircles, the charge transfer impedance (R_{ct}) can be obtained. A low R_{ct} generally corresponds to fast kinetics of the Faradaic reaction [76,77]. ZnVC (32 Ω) has a lower R_{ct} than those of ZnVAR (139 Ω) and ZnVair (118 Ω) anodes, indicating that the conductivity of the ZnVC anode is superior. The Li^+ diffusion coefficient can be calculated from the following formula [78]:

$$Z' = R_s + R_{ct} + A_w w^{-1/2} \quad (8)$$

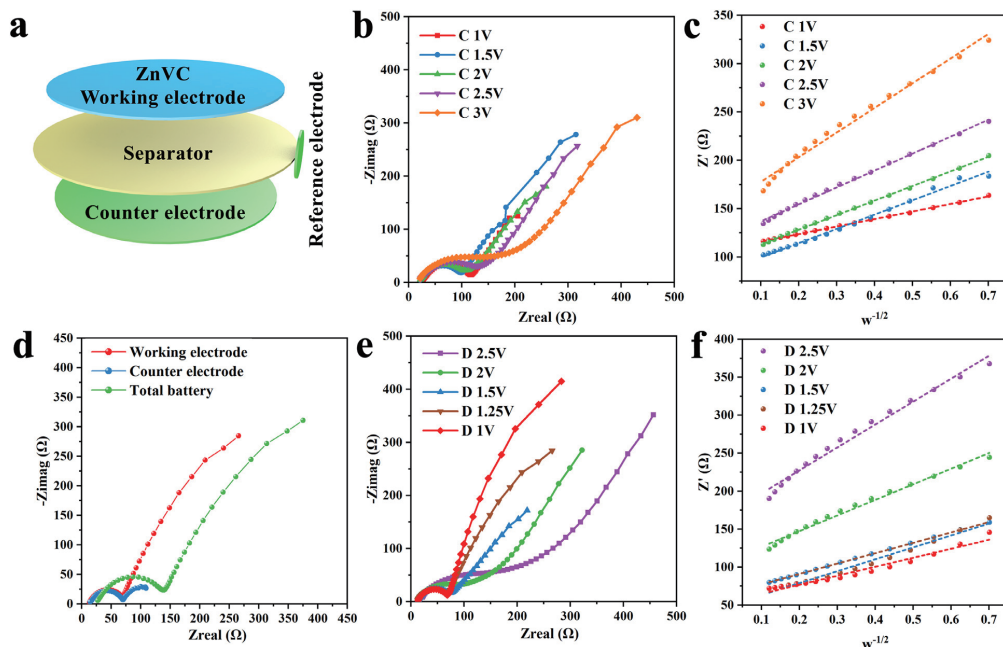
$$D_{\text{Li}^+} = \left[\frac{V_m}{FAA_w} \left(-\frac{dE}{dx} \right) \right]^2 \quad (9)$$

Here Z' is the real impedance collected during the experiment; A_w is the Warburg coefficient, which is the diffusion coefficient of ions in solution; w is angular frequency; V_m is the molar volume of the samples; dE/dx is the slope of the open-circuit voltage proportional to the concentration of Li^+ ; A is the surface area of the electrode; F is the Faraday constant [78]. As shown in Fig. S9 b, the Warburg coefficient A_w is equal to the slope of the Z' vs. $w^{-1/2}$ line at low frequency and can be estimated according to Eq. (8). The EIS parameters are collected in Table 3. Eq. (9) indicates that D_{Li^+} is mainly determined by $(1/A_w)$ [2] and that a small value of A_w implies a high Li^+ diffusion coefficient [79]. As shown in Table 3, the fresh ZnVair nanoparticles have the lowest A_w (52.2 $\Omega \text{ s}^{-1/2}$) compared to fresh ZnVAR (414.5 $\Omega \text{ s}^{-1/2}$) and ZnVC (149.3 $\Omega \text{ s}^{-1/2}$). It is anticipated that ion conductivity in materials consisting of nanoparticles would be found to be higher than for the porous structure-material ZnVC. The same phenomenon has been observed in our previous work [80]. After the cycling test, ZnVC (52 Ω) has the lowest electron transfer resistance R_{ct} compared to ZnVair (653 Ω) and ZnVAR (305 Ω). In addition, the porous ZnVC also has the lowest Warburg coefficient, about 61.9 $\Omega \text{ s}^{-1/2}$. ZnVC shows better ion conductivity than that of ZnVAR and ZnVair nanoparticles because the porous structure buffers the volume change during the cycling process, and the carbon layer helps to maintain the structural integrity.

However, the measured impedance of the cell has contributions from all components, and if the cell is activated, the impedance spectra will become more complicated. It is difficult to single out the contribution of the working electrode because the impedance spectrum in a two-electrode experiment is a combination of the

Table 3
EIS parameters of the anode electrode before and after cycling test.

	Fresh electrode			Electrode after cycling		
	Rs (Ω)	Rct (Ω)	Aw (Ω s ^{-1/2})	Rs (Ω)	Rct (Ω)	Aw (Ω s ^{-1/2})
ZnVair	10	118	52.2	20	653	72.6
ZnVAr	13	139	414.5	52	305	1078.2
ZnVC	13	32	149.3	28	52	61.9

**Fig. 8.** Visualization of the setup of the three-electrode system with ZnVC coated on the working electrode (a); impedance spectra of the working electrode during charging (b) and the corresponding linear fitting of the square root of Warburg impedance with real part Z' obtained for Nyquist plot (c); and the full cell impedance spectra (d); the impedance spectra of the working electrode during discharge process (e) and the corresponding linear fitting (f).

contributions from the positive and negative electrode. Therefore, a three-electrode system (EL-CELL GmbH, Germany) is applied to investigate the contribution of the active material in the second cycle (Fig. 8a). The counter and reference electrodes are both Li metal. In the three-electrode experiment the individual impedances of the electrodes versus the reference electrode is determined giving impedance contributions at the same time: counter and reference, reference and working electrode, and counter and the working electrode (Fig. 8d). To understand the effects on the impedance of the Li-ion insertion and extraction in the working electrode, the cell is charged and discharged to a certain potential and the EIS experiment is performed when the reactions reach equilibrium. Interestingly, the charge transfer impedance R_{ct} (Fig. 8b) gradually increases with more Li-ion extraction from the working electrode. The oblique linear Warburg part is fitted in Fig. S9c, and the Warburg coefficient (A_w) is equal to the slope of the Z' vs. $w^{-1/2}$ line at low frequency. The response is reversible during the discharge process (Fig. 8e and f), indicating the stability of the porous core-shell ZnVC.

4. Conclusions

In conclusion, porous $\text{ZnV}_2\text{O}_4/\text{ZnO@N}$ -doped carbon with a high specific surface area of $115 \text{ m}^2 \text{ g}^{-1}$ has been obtained from flower-

like $\text{Zn}_3(\text{OH})_2(\text{V}_2\text{O}_7)(\text{H}_2\text{O})_2$ coated with polymer dopamine by calcination in Ar. During the calcination process, the ratio of Zn and V is maintained at 1.695 after some loss of vanadium, and the vanadium is reduced from V^{5+} to V^{3+} due to the presence of carbon. When used as an anode electrode of LIBs, $\text{ZnV}_2\text{O}_4/\text{ZnO@N}$ -doped carbon exhibits a very stable specific capacity of 620 mAh g^{-1} at a current density of 100 mA g^{-1} . This excellent performance is caused by the high electronic conductivity and ionic conductivity. In addition, the charge transfer impedance of the $\text{ZnV}_2\text{O}_4/\text{ZnO@N}$ -doped carbon increases at high potential, and the Li-ion diffusion coefficient decreases.

Associated content

Notes

There are no conflicts to declare.

Declaration of Competing Interest

We declare that we have no financial and personal relationships with other people or organizations that can inappropriately influence our work. There is no professional or other personal interest of any nature or kind in any product, service and/or company

that could be construed as influencing the position presented in the manuscript entitled.

Data for reference

Raw data from all measurements are available from the authors.

CRediT authorship contribution statement

Huili Cao: Conceptualization, Methodology, Validation, Formal analysis, Investigation, Resources, Data curation, Writing - original draft, Visualization. **Zhiyong Zheng:** Resources, Validation, Formal analysis. **Jie Meng:** Validation, Formal analysis. **Xinxin Xiao:** Formal analysis, Writing - review & editing. **Poul Norby:** Supervision, Writing - review & editing. **Susanne Mossin:** Formal analysis, Supervision, Writing - review & editing, Project administration.

Acknowledgements

The authors gratefully acknowledge the financial support from the **China Scholarship Council** for a Ph.D. scholarship (No. 201706220078) to H. C. and a H. C. Ørsted COFUND Scholarship to X. X.

Supplementary materials

Supplementary material associated with this article can be found, in the online version, at [doi:10.1016/j.electacta.2020.136791](https://doi.org/10.1016/j.electacta.2020.136791).

References

- [1] K. Wang, Y. Chen, R. Tian, H. Li, Y. Zhou, H. Duan, H. Liu, Porous Co-C core-shell nanocomposites derived from Co-MOF-74 with enhanced electromagnetic wave absorption performance, *ACS Appl. Mater. Interfaces* 10 (2018) 11333–11342.
- [2] Z. Cui, H. Yin, Q. Nie, Controllable preparation of hierarchically core-shell structure NiO/C microspheres for non-enzymatic glucose sensor, *J. Alloy. Compd.* 632 (2015) 402–407.
- [3] E. Lim, C. Jo, H. Kim, M.-H. Kim, Y. Mun, J. Chun, Y. Ye, J. Hwang, K.-S. Ha, K.C. Roh, K. Kang, S. Yoon, J. Lee, Facile synthesis of Nb₂O₅@Carbon core-shell nanocrystals with controlled crystalline structure for high-power anodes in hybrid supercapacitors, *ACS Nano* 9 (2015) 7497–7505.
- [4] B. Sun, Z. Chen, H.-S. Kim, H. Ahn, G. Wang, MnO/C core-shell nanorods as high capacity anode materials for lithium-ion batteries, *J. Power Sources* 196 (2011) 3346–3349.
- [5] S. Wang, Y. Zhu, X. Xu, J. Sunarso, Z. Shao, Adsorption-based synthesis of Co₃O₄/C composite anode for high performance lithium-ion batteries, *Energy* 125 (2017) 569–575.
- [6] X.H. Rui, C. Li, C.H. Chen, Synthesis and characterization of carbon-coated Li₂V₂(PO₄)₃ cathode materials with different carbon sources, *Electrochim. Acta* 54 (2009) 3374–3380.
- [7] Y. Huang, H. Ren, S. Yin, Y. Wang, Z. Peng, Y. Zhou, Synthesis of LiFePO₄/C composite with high-rate performance by starch sol assisted rheological phase method, *J. Power Sources* 195 (2010) 610–613.
- [8] H. Li, L. Shen, K. Yin, J. Ji, J. Wang, X. Wang, X. Zhang, Facile synthesis of N-doped carbon-coated Li₄Ti₅O₁₂ microspheres using polydopamine as a carbon source for high rate lithium ion batteries, *J. Mater. Chem. A* 1 (2013) 7270–7276.
- [9] G. Zou, H. Hou, G. Zhao, P. Ge, D. Yin, X. Ji, N-rich carbon coated CoSnO₃ derived from in situ construction of a Co-MOF with enhanced sodium storage performance, *J. Mater. Chem. A* 6 (2018) 4839–4847.
- [10] G. Lu, S. Qiu, J. Liu, X. Wang, C. He, Y.-J. Bai, Enhanced electrochemical performance of Zn-doped Fe₃O₄ with carbon coating, *Electrochim. Acta* 117 (2014) 230–238.
- [11] G. Lu, S. Qiu, H. Lv, Y. Fu, J. Liu, X. Li, Y.-J. Bai, Li-ion storage performance of MnO nanocrystals coated with nitrogen-doped carbon derived from different carbon sources, *Electrochim. Acta* 146 (2014) 249–256.
- [12] Z. Ding, L. Zhao, L. Suo, Y. Jiao, S. Meng, Y.-S. Hu, Z. Wang, L. Chen, Towards understanding the effects of carbon and nitrogen-doped carbon coating on the electrochemical performance of Li₄Ti₅O₁₂ in lithium ion batteries: a combined experimental and theoretical study, *Phys. Chem. Chem. Phys.* 13 (2011) 15127–15133.
- [13] M. Idrees, S. Batool, J. Kong, Q. Zhuang, H. Liu, Q. Shao, N. Lu, Y. Feng, E.K. Wujcik, Q. Gao, T. Ding, R. Wei, Z. Guo, Polypyrrole/silica derived ceramics - Nitrogen sulfur dual doped graphene nanocomposite anode for enhanced lithium ion batteries, *Electrochim. Acta* 296 (2019) 925–937.
- [14] C. Shi, H. Qi, R. Ma, Z. Sun, L. Xiao, G. Wei, Z. Huang, S. Liu, J. Li, M. Dong, J. Fan, Z. Guo, N,S-self-doped carbon quantum dots from fungus fibers for sensing tetracyclines and for bioimaging cancer cells, *Mater. Sci. Eng. C* 105 (2019) 110132.
- [15] J. Tan, D. Li, Y. Liu, P. Zhang, Z. Qu, Y. Yan, H. Hu, H. Cheng, J. Zhang, M. Dong, C. Wang, J. Fan, Z. Li, Z. Guo, M. Liu, A self-supported 3D aerogel network lithium-sulfur battery cathode: sulfur spheres wrapped with phosphorus doped graphene and bridged with carbon nanofibers, *J. Mater. Chem. A* 8 (2020) 7980–7990.
- [16] X. Zhang, K.S. Ziemer, B.L. Weeks, Combustion synthesis of N-doped three-dimensional graphene networks using graphene oxide-nitrocellulose composites, *Adv. Comp. Hybrid Mater.* 2 (2019) 492–500.
- [17] J. Huang, Y. Li, Y. Cao, F. Peng, Y. Cao, Q. Shao, H. Liu, Z. Guo, Hexavalent chromium removal over magnetic carbon nanoadsorbents: synergistic effect of fluorine and nitrogen co-doping, *J. Mater. Chem. A* 6 (2018) 13062–13074.
- [18] M. Idrees, L. Liu, S. Batool, H. Luo, J. Liang, B. Xu, S. Wang, J. Kong, Cobalt-doping enhancing electrochemical performance of silicon/carbon nanocomposite as highly efficient anode materials in lithium-ion batteries, *Eng. Sci.* 6 (2019) 64–76.
- [19] H. Chen, Q. Luo, T. Liu, M. Tai, J. Lin, V. Murugadoss, H. Lin, J. Wang, Z. Guo, N. Wang, Boosting multiple interfaces by co-doped graphene quantum dots for high efficiency and durability perovskite solar cells, *ACS Appl. Mater. Interfaces* 12 (2020) 13941–13949.
- [20] B. Song, Q. Wang, L. Wang, J. Lin, X. Wei, V. Murugadoss, S. Wu, Z. Guo, T. Ding, S. Wei, Carbon nitride nanoplatelet photocatalysts heterostructured with B-doped carbon nanodots for enhanced photodegradation of organic pollutants, *J. Colloid Interface Sci.* 559 (2020) 124–133.
- [21] H. Yu, L. Yang, D. Cheng, D. Cao, Zeolitic-imidazolate framework (ZIF)/ZnCo-ZIF core-shell template derived Co, N-doped carbon catalysts for oxygen reduction reaction, *Eng. Sci.* 3 (2018) 54–61.
- [22] X. Wu, W. Li, P. Wu, C. Ma, Y. Liu, M. Xu, S. Liu, Long-lived room-temperature phosphorescent nitrogen-doped CQDs/PVA composites: fabrication, characterization and application, *Eng. Sci.* 4 (2018) 111–118.
- [23] H. Dong, Y. Li, H. Chai, Y. Cao, X. Chen, Hydrothermal synthesis of CuCo₂S₄ nano-structure and N-doped graphene for high-performance aqueous asymmetric supercapacitors, *ES Energy Environ.* 4 (2019) 19–26.
- [24] C. Zhang, Y. Xie, H. Deng, C. Zhang, J.-W. Su, J. Lin, Nitrogen doped coal with high electrocatalytic activity for oxygen reduction reaction, *Eng. Sci.* 8 (2019) 39–45.
- [25] H. Zhao, J. Li, H. Wu, T. Dong, Y. Zhang, H. Liu, Dopamine self-polymerization enables an N-doped carbon coating of exfoliated MoS₂ nanoflakes for anodes of lithium-ion batteries, *ChemElectroChem* 5 (2018) 383–390.
- [26] Y. Wang, Q. Qu, G. Li, T. Gao, F. Qian, J. Shao, W. Liu, Q. Shi, H. Zheng, 3D interconnected and multivalued carbon@MoS₂@Carbon hollow nanocubes as outstanding anodes for Na-ion batteries, *Small* 12 (2016) 6033–6041.
- [27] Y. Lv, L. Zhu, H. Xu, L. Zhang, Z. Liu, D. Cheng, X. Cao, J. Yun, D. Cao, Core/shell template-derived Co, N-doped carbon bifunctional electrocatalysts for rechargeable Zn-air battery, *Eng. Sci.* 7 (2019) 26–37.
- [28] Y. Zhai, J. Wang, Q. Gao, Y. Fan, C. Hou, Y. Hou, H. Liu, Q. Shao, S. Wu, L. Zhao, T. Ding, F. Dang, Z. Guo, Highly efficient cobalt nanoparticles anchored porous N-doped carbon nanosheets electrocatalysts for Li-O₂ batteries, *J. Catal.* 377 (2019) 534–542.
- [29] X. Wang, X. Zeng, D. Cao, Biomass-derived Nitrogen-doped Porous Carbons (NPC) and NPC/ polyaniline composites as high performance supercapacitor materials, *Eng. Sci.* 1 (2018) 55–63.
- [30] J. Chen, X. Wang, Y. Huang, S. Lv, X. Cao, J. Yun, D. Cao, Adsorption removal of pollutant dyes in wastewater by nitrogen-doped porous carbons derived from natural leaves, *Eng. Sci.* 5 (2018) 30–38.
- [31] X. Xue, H. Yan, Y. Fu, Preparation of pure and metal-doped Li₄Ti₅O₁₂ composites and their lithium-storage performances for lithium-ion batteries, *Solid State Ion.* 335 (2019) 1–6.
- [32] N. Zhu, W. Liu, M. Xue, Z. Xie, D. Zhao, M. Zhang, J. Chen, T. Cao, Graphene as a conductive additive to enhance the high-rate capabilities of electrosynthesized Li₄Ti₅O₁₂ for lithium-ion batteries, *Electrochim. Acta* 55 (2010) 5813–5818.
- [33] H. Iuchi, T. Horikawa, K.-I. Sotowa, Synthesis and electrochemical performance of a nanocrystalline Li₄Ti₅O₁₂/C composite for lithium-ion batteries prepared using resorcinol-formaldehyde resins, *Electrochim. Acta* 295 (2019) 540–549.
- [34] B. Zhao, R. Ran, M. Liu, Z. Shao, A comprehensive review of Li₄Ti₅O₁₂-based electrodes for lithium-ion batteries: The latest advancements and future perspectives, *Mater. Sci. Eng. R* 98 (2015) 1–71.
- [35] L. Sun, J. Wang, K. Jiang, S. Fan, Mesoporous Li₄Ti₅O₁₂ nanoclusters as high performance negative electrodes for lithium ion batteries, *J. Power Sources* 248 (2014) 265–272.
- [36] M. He, M. Walter, K.V. Kravchyk, R. Erni, R. Widmer, M.V. Kovalenko, Monodisperse SnSb nanocrystals for Li-ion and Na-ion battery anodes: synergy and dissonance between Sn and Sb, *Nanoscale* 7 (2015) 455–459.
- [37] D. Bresser, S. Passerini, B. Scrosati, Leveraging valuable synergies by combining alloying and conversion for lithium-ion anodes, *Energy Environ. Sci.* 9 (2016) 3348–3367.
- [38] Y. Lu, L. Yu, X.W. Lou, Nanostructured conversion-type anode materials for advanced lithium-ion batteries, *Chemistry* 4 (2018) 972–996.
- [39] Z. Yin, J. Qin, W. Wang, M. Cao, Rationally designed hollow precursor-derived Zn₃V₂O₈ nanocages as a high-performance anode material for lithium-ion batteries, *Nano Energy* 31 (2017) 367–376.
- [40] L. Luo, Y. Fei, K. Chen, D. Li, X. Wang, Q. Wang, Q. Wei, H. Qiao, Facile synthesis of one-dimensional zinc vanadate nanofibers for high lithium storage anode material, *J. Alloy. Compd.* 649 (2015) 1019–1024.

- [41] X. Wang, S. Qiu, G. Lu, C. He, J. Liu, L. Luan, W. Liu, Fabrication of porous MnO microspheres with carbon coating for lithium ion battery application, *CrysTengComm* 16 (2014) 1802–1809.
- [42] T. Zhu, J.S. Chen, X.W. Lou, Glucose-assisted one-pot synthesis of FeOOH nanorods and their transformation to Fe₃O₄@Carbon nanorods for application in lithium ion batteries, *J. Phys. Chem. C* 115 (2011) 9814–9820.
- [43] K. Tao, P. Li, L. Kang, X. Li, Q. Zhou, L. Dong, W. Liang, Facile and low-cost combustion-synthesized amorphous mesoporous NiO/carbon as high mass-loading pseudocapacitor materials, *J. Power Sources* 293 (2015) 23–32.
- [44] X. Li, J. Fu, Z. Pan, J. Su, J. Xu, B. Gao, X. Peng, L. Wang, X. Zhang, P.K. Chu, Peapod-like V₂O₃ nanorods encapsulated into carbon as binder-free and flexible electrodes in lithium-ion batteries, *J. Power Sources* 331 (2016) 58–66.
- [45] J.M. Won, Y.N. Ko, J.-K. Lee, Y.C. Kang, Superior electrochemical properties of rutile VO₂-carbon composite microspheres as a promising anode material for lithium ion batteries, *Electrochim. Acta* 156 (2015) 179–187.
- [46] C. Bie, J. Pei, G. Chen, Q. Zhang, J. Sun, Y. Yu, D. Chen, Hierarchical Zn₃V₂O₈/C composite microspheres assembled from unique porous hollow nanoplates with superior lithium storage capability, *J. Mater. Chem. A* 4 (2016) 17063–17072.
- [47] H. Yan, Y. Luo, X. Xu, L. He, J. Tan, Z. Li, X. Hong, P. He, L. Mai, Facile and scalable synthesis of Zn₃V₂O₇(OH)₂·2H₂O microflowers as a high-performance anode for lithium-ion batteries, *ACS Appl. Mater. Interfaces* 9 (2017) 27707–27714.
- [48] Q. Wei, F. Zhang, J. Li, B. Li, C. Zhao, Oxidant-induced dopamine polymerization for multifunctional coatings, *Polym. Chem.* 1 (2010) 1430–1433.
- [49] J.-W. Oh, J. Heo, T.H. Kim, An electrochemically modulated single-walled carbon nanotube network for the development of a transparent flexible sensor for dopamine, *Sens. Actuators B* 267 (2018) 438–447.
- [50] C. Srinivas, M. Sudharsan, G.R.K. Reddy, P.S. Kumar, A.J. Amali, D. Suresh, Co/Co-N@Nanoporous carbon derived from ZIF-67: a highly sensitive and selective electrochemical dopamine sensor, *Electroanalysis* 30 (2018) 2475–2482.
- [51] S. Wang, Y. Xing, C. Xiao, H. Xu, S. Zhang, A peapod-inspired MnO@C core-shell design for lithium ion batteries, *J. Power Sources* 307 (2016) 11–16.
- [52] N. Wu, C. Liu, D. Xu, J. Liu, W. Liu, Q. Shao, Z. Guo, Enhanced electromagnetic wave absorption of three-dimensional porous Fe₃O₄/C composite flowers, *ACS Sustain. Chem. Eng.* 6 (2018) 12471–12480.
- [53] Y. Tian, Y. An, C. Wei, B. Xi, S. Xiong, J. Feng, Y. Qian, Flexible and free-standing Ti₃C₂T_x MXene@Zn paper for dendrite-free aqueous zinc metal batteries and nonaqueous lithium metal batteries, *ACS Nano* 13 (2019) 11676–11685.
- [54] D. Chao, C. Zhu, M. Song, P. Liang, X. Zhang, N.H. Tiep, H. Zhao, J. Wang, R. Wang, H. Zhang, H.J. Fan, A high-rate and stable quasi-solid-state zinc-ion battery with novel 2D layered zinc orthovanadate array, *Adv. Mater.* 30 (2018) 1803181.
- [55] Y. Tian, Y. An, H. Wei, C. Wei, Y. Tao, Y. Li, B. Xi, S. Xiong, J. Feng, Y. Qian, Micron-sized nanoporous vanadium pentoxide arrays for high-performance gel zinc-ion batteries and potassium batteries, *Chem. Mater.* 32 (2020) 4054–4064.
- [56] H. Wu, Z. Zhang, M. Qin, Q. Wang, Z. Cao, Y. Yu, B. Jia, X. Qu, Solution combustion synthesis of crystalline V₂O₃ and amorphous V₂O₃/C as anode for lithium-ion battery, *J. Am. Ceram. Soc.* 103 (2020) 2643–2652.
- [57] G. Habererflehner, A. Orthacker, M. Albu, J. Li, G. Kothleitner, Nanoscale voxel spectroscopy by simultaneous EELS and EDS tomography, *Nanoscale* 6 (2014) 14563–14569.
- [58] H.-T. Zhang, L. Zhang, D. Mukherjee, Y.-X. Zheng, R.C. Haislmaier, N. Alem, R. Engel-Herbert, Wafer-scale growth of VO₂ thin films using a combinatorial approach, *Nat. Commun.* 6 (2015) 8475.
- [59] R. Nie, G. Fang, J. Zhou, J. Guo, Y. Tang, S. Liu, Y. Cai, P. Hao, S. Liang, Three-dimensional Zn₃V₂O₈/carbon fiber cloth composites as binder-free anode for lithium-ion batteries, *Electrochim. Acta* 246 (2017) 97–105.
- [60] H. Xue, Y. Fang, L. Zeng, X. He, F. Luo, R. Liu, J. Liu, Q. Chen, M. Wei, Q. Qian, Facile synthesis of hierarchical lychee-like Zn₃V₂O₈/C/rGO nanospheres as high-performance anodes for lithium ion batteries, *J. Colloid Interface Sci.* 533 (2019) 627–635.
- [61] B. Sambandam, V. Soundharajan, J. Song, S. Kim, J. Jo, D.T. Pham, S. Kim, V. Mathew, J. Kim, Zn₃V₂O₈ porous morphology derived through a facile and green approach as an excellent anode for high-energy lithium ion batteries, *Chem. Eng. J.* 328 (2017) 454–463.
- [62] C. Bie, J. Pei, J. Wang, K. Hua, D. Chen, G. Chen, Graphite nanoplates firmly anchored with well-dispersed porous Zn₃V₂O₈ nanospheres: rational fabrication and enhanced lithium storage capability, *Electrochim. Acta* 248 (2017) 140–149.
- [63] Y. An, Y. Tian, C. Wei, H. Jiang, B. Xi, S. Xiong, J. Feng, Y. Qian, Scalable and physical synthesis of 2D silicon from bulk layered alloy for lithium-ion batteries and lithium metal batteries, *ACS Nano* 13 (2019) 13690–13701.
- [64] J. Zhou, B. Zhao, J. Bai, Z. Fang, K. Li, H. Ma, J. Dai, X. Zhu, Y. Sun, Three-dimensional porous Zn₃VO₄/ZnO/C thin film anode materials for high-performance Li-ion batteries, *Scr. Mater.* 166 (2019) 87–91.
- [65] B. Zhang, Q.B. Zheng, Z.D. Huang, S.W. Oh, J.K. Kim, SnO₂-graphene-carbon nanotube mixture for anode material with improved rate capacities, *Carbon* 49 (2011) 4524–4534.
- [66] Y. Sharma, N. Sharma, G.V. Subba Rao, B.V.R. Chowdari, Nanophase ZnCo₂O₄ as a high performance anode material for Li-ion batteries, *Adv. Funct. Mater.* 17 (2007) 2855–2861.
- [67] L. Zhou, K. Zhang, Z. Hu, Z. Tao, L. Mai, Y.-M. Kang, S.-L. Chou, J. Chen, Recent developments on and prospects for electrode materials with hierarchical structures for lithium-ion batteries, *Adv. Energy Mater.* 8 (2018) 1701415.
- [68] Y. Zhang, Y. Lu, S. Feng, D. Liu, Z. Ma, S. Wang, On-site evolution of ultra-fine ZnO nanoparticles from hollow metal-organic frameworks for advanced lithium ion battery anodes, *J. Mater. Chem. A* 5 (2017) 22512–22518.
- [69] Q. Zhao, Y. Lu, J. Chen, Advanced organic electrode materials for rechargeable sodium-ion batteries, *Adv. Energy Mater.* 7 (2017) 1601792.
- [70] G.-L. Xu, Y. Li, T. Ma, Y. Ren, H.-H. Wang, L. Wang, J. Wen, D. Miller, K. Amine, Z. Chen, PEDOT-PSS coated ZnO/C hierarchical porous nanorods as ultra-long-life anode material for lithium ion batteries, *Nano Energy* 18 (2015) 253–264.
- [71] L. Zeng, F. Xiao, J. Wang, S. Gao, X. Ding, M. Wei, ZnV₂O₄-CMK nanocomposite as an anode material for rechargeable lithium-ion batteries, *J. Mater. Chem.* 22 (2012) 14284–14288.
- [72] X.-C. Zhao, P. Yang, L.-J. Yang, Y. Cheng, H.-Y. Chen, H. Liu, G. Wang, V. Murugadoss, S. Angaiah, Z. Guo, Enhanced electrochemical performance of Cu²⁺ doped TiO₂ nanoparticles for lithium-ion battery, *ES Mater. Manuf.* 1 (2018) 67–71.
- [73] Q. Fu, H. Cao, G. Liang, L. Luo, Y. Chen, V. Murugadoss, S. Wu, T. Ding, C. Lin, Z. Guo, A highly Li⁺-conductive HfNb₂₄O₆₂ anode material for superior Li⁺ storage, *Chem. Commun.* 56 (2020) 619–622.
- [74] R. Li, X. Zhu, Q. Fu, G. Liang, Y. Chen, L. Luo, M. Dong, Q. Shao, C. Lin, R. Wei, Z. Guo, Nanosheet-based Nb₁₂O₂₉ hierarchical microspheres for enhanced lithium storage, *Chem. Commun.* 55 (2019) 2493–2496.
- [75] P. Xie, Y. Li, Q. Hou, K. Sui, C. Liu, X. Fu, J. Zhang, V. Murugadoss, J. Fan, Y. Wang, R. Fan, Z. Guo, Tunneling-induced negative permittivity in Ni/MnO nanocomposites by a bio-gel derived strategy, *J. Mater. Chem. C* 8 (2020) 3029–3039.
- [76] S.S. Zhang, K. Xu, T.R. Jow, Electrochemical impedance study on the low temperature of Li-ion batteries, *Electrochim. Acta* 49 (2004) 1057–1061.
- [77] G. Liang, X. Sun, J. Lai, C. Wei, Y. Huang, H. Hu, J. Zou, Y. Xu, Asphalt-decomposed carbon-coated SnO₂ as an anode for lithium ion batteries, *J. Electron. Mater.* 48 (2019) 3324–3329.
- [78] T.-G. Kim, E. Samuel, B. Joshi, C.-W. Park, M.-W. Kim, M.T. Swihart, W.Y. Yoon, S.S. Yoon, Supersonically sprayed rGO–Zn₂SnO₄ composites as flexible, binder-free, scalable, and high-capacity lithium ion battery anodes, *J. Alloy. Compd.* 766 (2018) 331–340.
- [79] J. Huang, J. Wang, H. Zhong, L. Zhang, N-cyanoethyl polyethylenimine as a water-soluble binder for LiFePO₄ cathode in lithium-ion batteries, *J. Mater. Sci.* 53 (2018) 9690–9700.
- [80] H. Cao, X. Xiao, X. Wang, J. Liu, P. Si, Morphology engineering of self-assembled porous zinc manganese hexagons for lithium ion storage, *Electrochim. Acta* 330 (2020) 135260.

Supporting Information for

Examining the Effects of Nitrogen-doped Carbon Coating on Zinc Vanadate Nanoflowers Towards High Performance Lithium Anode

Huili Cao^{a}, Zhiyong Zheng^a, Jie Meng^a, Xinxin Xiao^a, Poul Norby^b and Susanne Mossin^{a*}*

^aDepartment of Chemistry, Technical University of Denmark, 2800 Kgs. Lyngby, Denmark

*^bDepartment of Energy Conversion and Storage, Technical University of Denmark, 2800
Kgs. Lyngby, Denmark*

Corresponding authors: hucao@kemi.dtu.dk (Huili Cao); slmo@kemi.dtu.dk (Susanne Mossin)

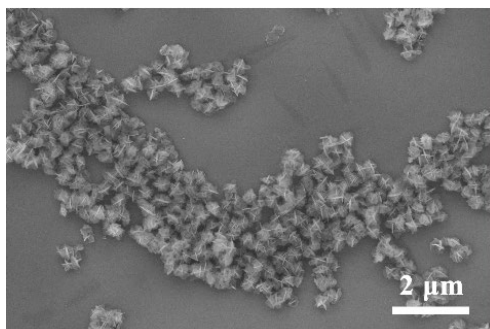


Fig. S1 SEM image of the precursor ZnVS.

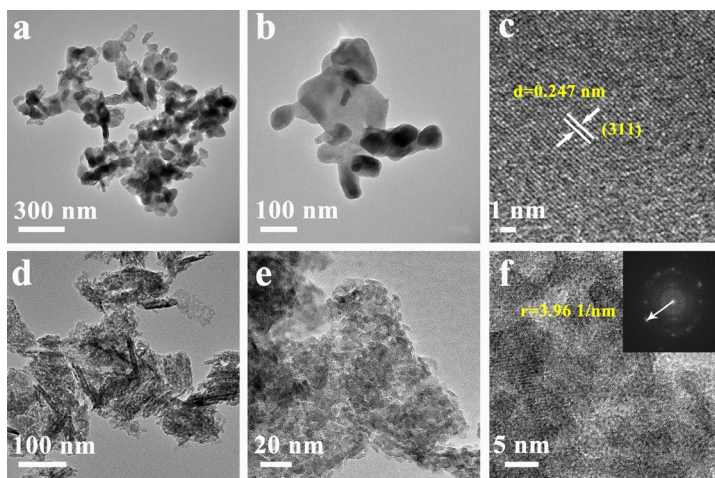


Fig. S2 TEM images of ZnVair (a-c) and ZnVAr (d-f) at different magnifications. Inset of (f) is the corresponding converted FFT patterns.

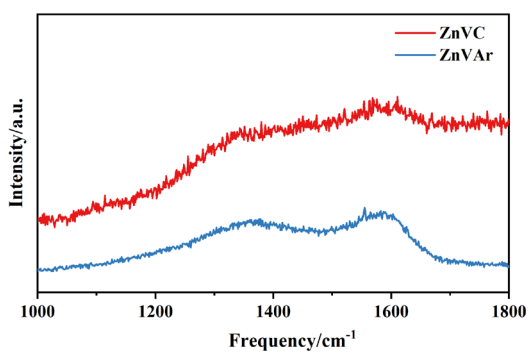


Fig. S3 Raman spectra of ZnVAr and ZnVC.

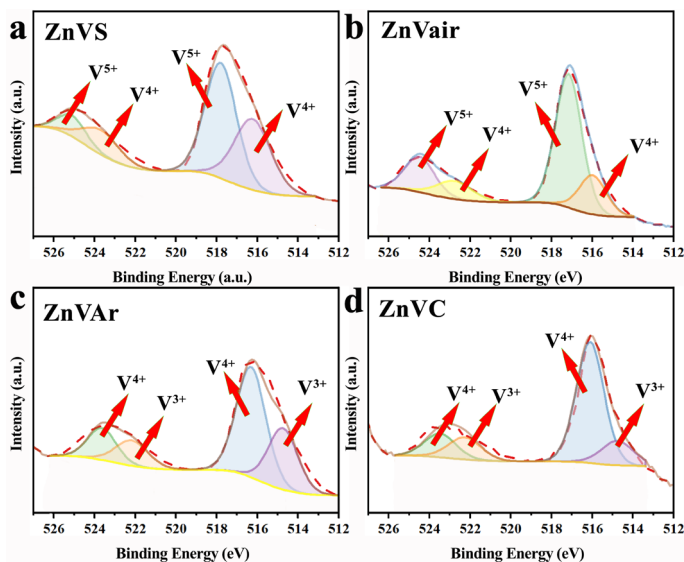


Fig. S4 V 2p spectra of the ZnVS (a), ZnVair (b), ZnVAr (c), and ZnVC (d).

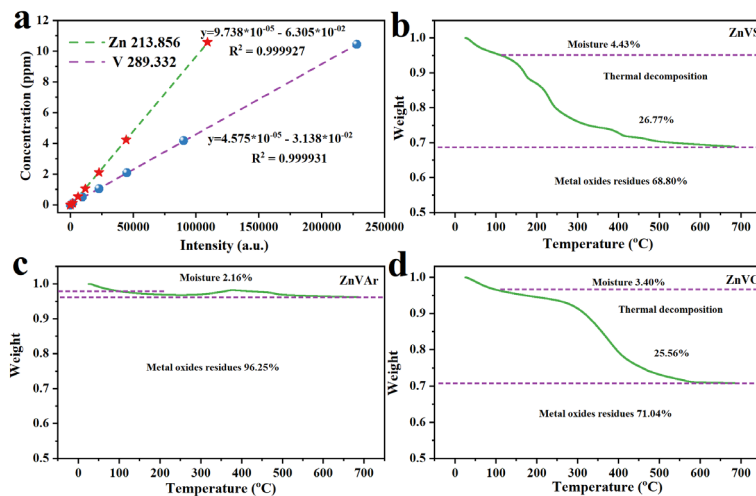


Fig. S5 Standard ICP curve (a); TGA curves of ZnVS (b), ZnVAr (c) and ZnVC (d) from R.T. to 700 °C at 10 °C min⁻¹ in air.

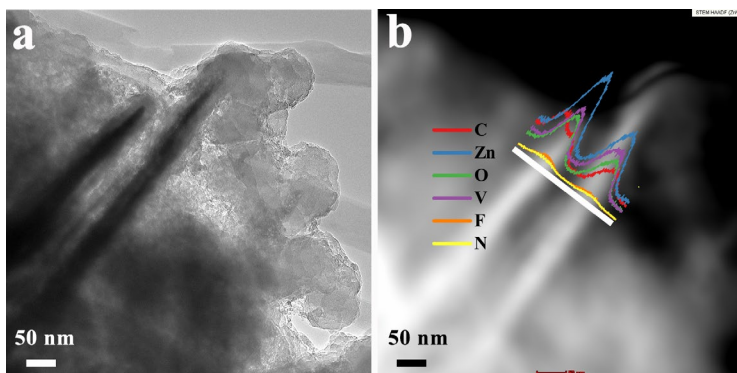


Fig. S6 TEM image (a) and line scan of EDS element analysis (b) of core-shell ZnVC after cycling.

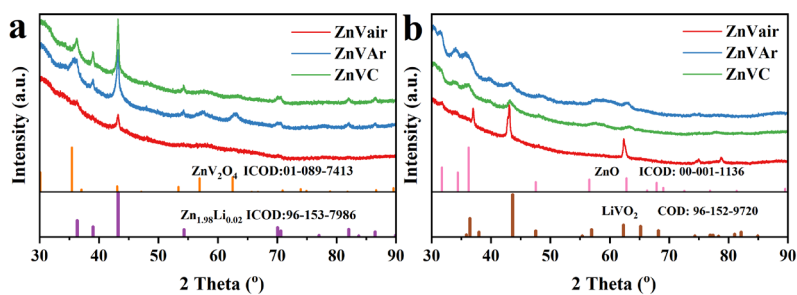


Fig. S7 XRD patterns of the ZnVair, ZnVAr and ZnVC in the discharge state (0.02 V) (a) and charge state (3.0 V) (b) after cycling.

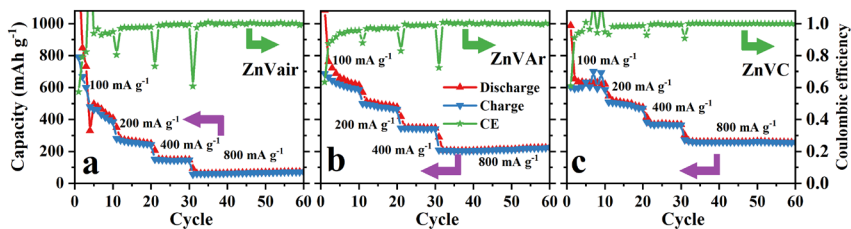


Fig. S8 Rate performance of ZnVair (a), ZnVAr (b) and ZnVC (c) at various current densities of 100, 200, 400, and 800 mA g⁻¹.

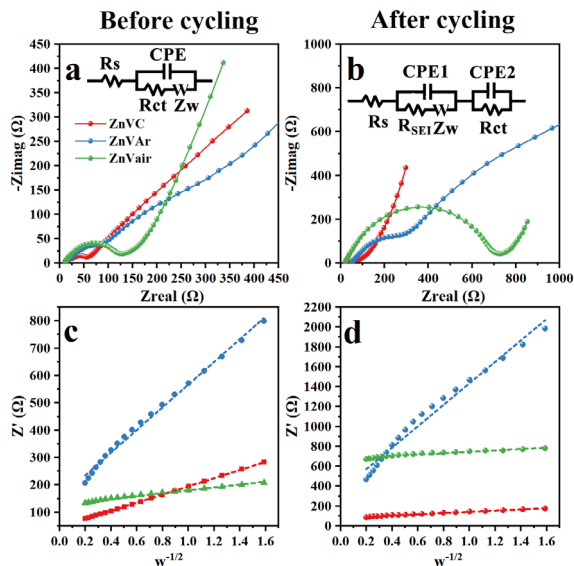


Fig. S9 Nyquist plots of ZnVair, ZnVAr and ZnVC before (a) and after (c) cycling testing. Associated linear fitting of the square root of Warburg impedance with real part Z' before (b) and after (d) cycling. Inset of (a) and (b) are the equivalent circuits.

Table S1 Comparison of specific surface area of the proposed vanadium-based metal oxides.

Materials	BET surface area ($\text{m}^2 \text{g}^{-1}$)	Reference
$\text{Zn}_3\text{V}_3\text{O}_8@\text{C}/\text{rGO}$ nanospheres	20	[1]
Porous $\text{Zn}_3\text{V}_2\text{O}_8$ sheets	22	[2]
$\text{Zn}_3\text{V}_2\text{O}_8/\text{Graphite}$ nanoplates	34	[3]
$\text{Zn}_3\text{V}_2\text{O}_7$ nanoplates/Graphene	10	[4]
$\text{Co}_3\text{V}_2\text{O}_8$ sponge network	8.0	[5]
$\text{Zn}_3\text{V}_2\text{O}_8$ nanocages	13	[6]
SbVO_4 nanospheres	22	[7]
ZnVair nanoparticles	21	This work
Porous $\text{ZnV}_2\text{O}_4@\text{NC}$	117	This work
Porous $\text{ZnV}_2\text{O}_4@\text{NC}$	115	This work

Table S2 Comparison of the reversible capacity of published ZnV_2O_4 and other metal oxides.

Morphologies	Capacity (mAh g^{-1})	Current density (mA g^{-1})	Cycles	Reference
$\text{ZnV}_2\text{O}_4\text{-CMK}$	575	100	200	[8]
Clewlike ZnV_2O_4 hollow spheres	524	50	50	[9]
Nanophase ZnV_2O_4	181	500	12	[10]
Porous ZnV_2O_4 nanowire	460	1000	100	[11]
ZnV_2O_4 microspheres	460	100	50	[12]
TiO_2 nanoparticles	67.5	1675	100	[13]
$\text{HfNb}_{24}\text{O}_{62}$ nanocubes	182	400	100	[14]
$\text{Nb}_{12}\text{O}_{29}$ hierarchical microspheres	297	1860	500	[15]
$\text{Si}@\text{C}$ nanospheres	868	100	500	[16]

MoO ₂ -Mo ₂ C/C	845.2	100	200	[17]
Si/C composites	883	400	500	[18]
Li ₄ Ti ₅ O ₁₂ @carbon cloth	150	200	300	[19]
Li ₄ Ti ₅ O ₁₂ /Graphene	193.4	100	40	[20]
Porous Zn ₃ V ₃ O ₈	541.2	120	200	[21]
Zn ₃ V ₂ O ₈ nanoplates	270	100	40	[22]
CuV ₂ O ₆ /PEDOT:PSS nanobelts	536.6	50	100	[23]
AlV ₃ O ₉ microspheres	373.5	100	100	[24]
Porous ZnO nanosheets	400	500	100	[25]
Porous ZnV ₂ O ₄ /ZnO@NC	620	100	50	This work
Porous ZnV ₂ O ₄ /ZnO@NC	404	500	250	This work

References

- [1] Xue H., Fang Y., Zeng L., He X., Luo F., Liu R., Liu J., Chen Q., Wei M., Qian Q., Facile synthesis of hierarchical lychee-like $\text{Zn}_3\text{V}_3\text{O}_8@\text{C/rGO}$ nanospheres as high-performance anodes for lithium ion batteries. *J. Colloid Interface Sci.* **2019**, *533*, 627-635.
- [2] Sambandam B., Soundharrajan V., Song J., Kim S., Jo J., Pham D. T., Kim S., Mathew V., Kim J., $\text{Zn}_3\text{V}_2\text{O}_8$ porous morphology derived through a facile and green approach as an excellent anode for high-energy lithium ion batteries. *Chem. Eng. J.* **2017**, *328*, 454-463.
- [3] Bie C., Pei J., Wang J., Hua K., Chen D., Chen G., Graphite Nanoplates Firmly Anchored with Well-dispersed Porous $\text{Zn}_3\text{V}_2\text{O}_8$ Nanospheres: Rational Fabrication and Enhanced Lithium Storage Capability. *Electrochim. Acta* **2017**, *248*, 140-149.
- [4] Yu Y., Niu C., Han C., Zhao K., Meng J., Xu X., Zhang P., Wang L., Wu Y., Mai L., Zinc Pyrovanadate Nanoplates Embedded in Graphene Networks with Enhanced Electrochemical Performance. *Ind. Eng. Chem. Res.* **2016**, *55* (11), 2992-2999.
- [5] Soundharrajan V., Sambandam B., Song J., Kim S., Jo J., Kim S., Lee S., Mathew V., Kim J., $\text{Co}_3\text{V}_2\text{O}_8$ Sponge Network Morphology Derived from Metal–Organic Framework as an Excellent Lithium Storage Anode Material. *ACS Appl. Mater. Interfaces* **2016**, *8* (13), 8546-8553.
- [6] Yin Z., Qin J., Wang W., Cao M., Rationally designed hollow precursor-derived $\text{Zn}_3\text{V}_2\text{O}_8$ nanocages as a high-performance anode material for lithium-ion batteries. *Nano Energy* **2017**, *31*, 367-376.
- [7] Yang H., Wang P., Zhang J., Zhang L., Yan J., Microwave hydrothermal synthesis of SbVO_4 nanospheres as anode materials for sodium ion batteries. *Ionics* **2020**, *26*, 1267–1273.
- [8] Zeng L., Xiao F., Wang J., Gao S., Ding X., Wei M., ZnV_2O_4 –CMK nanocomposite as an anode material for rechargeable lithium-ion batteries. *J. Mater. Chem.* **2012**, *22* (28), 14284-14288.
- [9] Xiao L., Zhao Y., Yin J., Zhang L., Clewlike ZnV_2O_4 Hollow Spheres: Nonaqueous Sol–Gel Synthesis, Formation Mechanism, and Lithium Storage Properties. *Chemistry – A European Journal* **2009**, *15* (37), 9442-9450.

- [10] Zhu X., Jiang X., Xiao L., Ai X., Yang H., Cao Y., Nanophase ZnV_2O_4 as stable and high capacity Li insertion electrode for Li-ion battery. *Current Applied Physics* **2015**, *15* (4), 435-440.
- [11] De Juan-Corpuz L. M. Z., Nguyen M. T., Corpuz R. D., Yonezawa T., Rosero-Navarro N. C., Tadanaga K., Tokunaga T., Kheawhom S., Porous ZnV_2O_4 Nanowire for Stable and High-Rate Lithium-Ion Battery Anodes. *ACS Applied Nano Materials* **2019**, *2* (7), 4247-4256.
- [12] Zheng C., Zeng L., Wang M., Zheng H., Wei M., Synthesis of hierarchical ZnV_2O_4 microspheres and its electrochemical properties. *CrystEngComm* **2014**, *16* (44), 10309-10313.
- [13] Zhao X.-C., Yang P., Yang L.-J., Cheng Y., Chen H.-Y., Liu H., Wang G., Murugadoss V., Angaiah S., Guo Z., Enhanced Electrochemical Performance of Cu^{2+} doped TiO_2 Nanoparticles for Lithium-ion Battery. *ES Materials & Manufacturing* **2018**, *1*, 67-71.
- [14] Fu Q., Cao H., Liang G., Luo L., Chen Y., Murugadoss V., Wu S., Ding T., Lin C., Guo Z., A highly Li^+ -conductive $\text{HfNb}_{24}\text{O}_{62}$ anode material for superior Li^+ storage. *Chem. Commun.* **2020**, *56* (4), 619-622.
- [15] Li R., Zhu X., Fu Q., Liang G., Chen Y., Luo L., Dong M., Shao Q., Lin C., Wei R., Guo Z., Nanosheet-based $\text{Nb}_{12}\text{O}_{29}$ hierarchical microspheres for enhanced lithium storage. *Chem. Commun.* **2019**, *55* (17), 2493-2496.
- [16] Batool S., Idrees M., Kong J., Zhang J., Kong S., Dong M., Hou H., Fan J., Wei H., Guo Z., Assessment of the electrochemical behaviour of silicon@carbon nanocomposite anode for lithium-ion batteries. *J. Alloys Compd.* **2020**, *832*, 154644.
- [17] Hou C., Wang J., Du W., Wang J., Du Y., Liu C., Zhang J., Hou H., Dang F., Zhao L., Guo Z., One-pot synthesized molybdenum dioxide–molybdenum carbide heterostructures coupled with 3D holey carbon nanosheets for highly efficient and ultrastable cycling lithium-ion storage. *J. Mater. Chem. A* **2019**, *7* (22), 13460-13472.
- [18] Idrees M., Batool S., Zhuang Q., Kong J., Seok I., Zhang J., Liu H., Murugadoss V., Gao Q., Guo Z., Achieving carbon-rich silicon-containing ceramic anode for advanced lithium ion battery. *Ceram. Int.* **2019**, *45* (8), 10572-10580.

-
- [19] Jiang C., Ye Z., Ye H., Zou Z., $\text{Li}_4\text{Ti}_5\text{O}_{12}$ @carbon cloth composite with improved mass loading achieved by a hierarchical polypyrrole interlayer assisted hydrothermal process for robust free-standing sodium storage. *Appl. Surf. Sci.* **2020**, *504*, 144464.
- [20] Zhang F., Yi F., Gao A., Shu D., Sun Z., Mao J., Zhou X., Zhu Z., Sun Y., Interfacial electrostatic self-assembly in water-in-oil microemulsion assisted synthesis of $\text{Li}_4\text{Ti}_5\text{O}_{12}$ /Graphene for lithium-ion-batteries. *J. Alloys Compd.* **2020**, *819*, 153018.
- [21] Tang J., Ni S., Zhou B., Chao D., Li T., Yang X., Theoretical calculation and experimental verification of $\text{Zn}_3\text{V}_3\text{O}_8$ as an insertion type anode for LIBs. *J. Alloys Compd.* **2018**, *730*, 228-233.
- [22] Vijayakumar S., Lee S.-H., Ryu K.-S., Synthesis of $\text{Zn}_3\text{V}_2\text{O}_8$ nanoplatelets for lithium-ion battery and supercapacitor applications. *RSC Adv.* **2015**, *5* (111), 91822-91828.
- [23] Zhang S., Hu R., Synthesis and electrochemical performance of CuV_2O_6 /PEDOT:PSS composite nanobelts as anode materials for lithium-ion batteries. *Mater. Lett.* **2016**, *176*, 131-134.
- [24] Yang G., Song H., Yang G., Wu M., Wang C., 3D hierarchical AlV_3O_9 microspheres: First synthesis, excellent lithium ion cathode properties, and investigation of electrochemical mechanism. *Nano Energy* **2015**, *15*, 281-292.
- [25] Huang X. H., Xia X. H., Yuan Y. F., Zhou F., Porous ZnO nanosheets grown on copper substrates as anodes for lithium ion batteries. *Electrochim. Acta* **2011**, *56* (14), 4960-4965.

Chapter 6

Zinc vanadate cathode applied in zinc-ion batteries

Zinc vanadate which can crystallize in various crystal structure types is also envisioned to be applied as an excellent cathode material for zinc ion batteries. With the large amount of morphologies being put forward, fancy and complex morphologies have become an aim in itself during the exploration of electrode materials. On the basis of the investigation presented in Chapter 5, the carbon coating of zinc vanadate with 3-D porous structures and high specific surface area which was applied in Li^+ ion storage, the ionic and electronic conductivities can be effectively improved and furthermore a stable electrochemical performance can be achieved in a simple way I concluded that it would also be expected to exhibit an excellent Zn^{2+} ion storage performance. The carbon coated zinc vanadate only delivers about 50 mAh g^{-1} , however, and have a poor stability, see Appendix I. Therefore, this chapter, which is presented as a submitted manuscript, Paper II, focus on exploring the factors influencing the Zn^{2+} ion energy storage materials. Solid-state nuclear magnetic resonance (ss-NMR) was performed during my external stay at the University of Southern Denmark under the supervision of Professor Ulla Gro Nielsen and Mr. Christian B. Jørgensen and they helped me to conduct the experiments and to analyse the results. Density functional theory investigations was performed under the supervision of Chao Peng. The design and performance of all other experiments, the analysis and writing of the paper were performed by me with suggestions and proof-reading by the other co-authors.

This chapter is a submitted article of “New Insight into the Effect of the Orientation of zinc vanadate on Zinc Ion Storage Performance” on *Electrochemical Acta* by Huili Cao, Chao Peng, Zhiyong Zheng, Zhenyun Lan, Qinying Pan, Ulla Gro Nielsen, Poul Norby, Xinxin Xiao, Susanne Mossin.

The article is given below:

New Insight into the Orientation Effect of Zinc Vanadate on Zinc Ion Storage Performance

Huili Cao,^{a,1,*} Chao Peng,^{b,1} Zhiyong Zheng,^a Zhenyun Lan,^c Qinying Pan,^a Ulla Gro Nielsen,^d Poul

Norby,^c Xinxin Xiao^{a,*} and Susanne Mossir^{a,*}

^a*Department of Chemistry, Technical University of Denmark, 2800 Kgs. Lyngby,
Denmark*

^b*School of Engineering, University of Southampton, Southampton SO17 1BJ, UK*

^c*Department of Energy Conversion and Storage, Technical University of Denmark,
2800 Kgs. Lyngby, Denmark*

^d*Department of Physics, Chemistry and Pharmacy, University of Southern
Denmark, Campusvej 55, 5230 Odense M, Denmark*

¹*These authors contributed equally to this work*

Corresponding authors: hucao@kemi.dtu.dk (H. Cao); xixiao@kemi.dtu.dk (X. Xiao); slmo@kemi.dtu.dk (S. Mossin).

Abstract: Rechargeable aqueous zinc-ion battery (ZIB) is considered as a promising energy storage device due to the low cost, high obtainable output voltage, non-toxicity, and environmental friendliness. To achieve an excellent energy storage performance, morphology engineering of cathode materials for aqueous ZIBs has been widely reported as an important strategy. The impacts of dimension and orientation of the cathode material on the electrochemical performance are, however, less studied. Herein, we compare two types of zinc pyrovanadate ($\text{Zn}_3\text{V}_2\text{O}_7(\text{OH})_2 \cdot 2\text{H}_2\text{O}$, ZnVO) in nanowires and nanoflakes with the same crystal type but different orientations. ZnVO nanowires expose mostly the (001) plane lattice, in contrast to (020) and (110) lattice for ZnVO flakes. Interestingly, nanowires exhibit an excellent specific discharge capacity of 108 mAh g^{-1} after 700 cycles at 2 A g^{-1} , contributed from Faradic and diffusion-controlled capacity. In a distinctive comparison, nanoflakes deliver a very poor capacity of 2.2 mAh g^{-1} after 50 cycles at 0.1 A g^{-1} with only diffusion-controlled capacity. Density functional theory (DFT) reveals significantly different Zn^{2+} ion diffusion rates in ZnVO along different orientations.

Keywords: zinc vanadate; orientation; density functional theory; cathode; zinc-ion battery

1. Introduction

The rapid development of electric vehicles and portable electronics pose a great demand for energy storage devices.[1-4] Lithium-ion batteries (LIBs) have excellent energy density and have long battery life. They are applied in a wide range of commercial applications.[5-7] Battery safety,[8-10] the environmental concerns connected with the use of toxic organic electrolytes, as well as the high cost of the lithium metal and recycling, however, hinder their application and further development towards use in power grid energy storage.[11, 12] Accordingly, aqueous rechargeable multivalent-ions batteries have been put forward. These include ZIBs[13] and aluminium-ion batteries (AIBs). Aqueous electrolytes possess higher ionic conductivity (10^{-1} - 6 S cm^{-1}) than the organic counterparts (10^{-3} - $10^{-2} \text{ S cm}^{-1}$).[14] Besides, multivalent ions can, in principle, enable a very high specific capacity due to the multiple electrons involved.[15] Among these, the aluminium ion can only be operated in acid solutions ($\text{pH} < 4$) due to precipitation of Al_2O_3 at neutral pH. ZIBs can operate with pH-neutral electrolytes and hold a tremendous promise as cheap and safe alternatives for grid-scale energy storage.[16]

The metallic zinc anode of ZIBs possesses a relatively low redox potential of -0.762 V vs. standard hydrogen electrode and a high theoretical specific capacity of 820 mAh g^{-1} . Currently, the main challenges remain at the cathode materials that host Zn^{2+} . The radius of Zn^{2+} is about 0.75 \AA , close to lithium ion (0.76 \AA), but rises sharply to 4.3 \AA in the hydrated form.[17] Two classes of cathode materials, including i) tunnel-type with a tunnel diameter above 3.0 \AA and ii) layered-type with a large layer spacing (beyond 4.3 \AA), have been developed.[18] Tunnel-type materials suffer from a low reversible capacity and a disappointing cycling performance. This is likely due to the narrow interlayer distance that undergoes a significant structure expansion upon Zn^{2+} insertion.[18] In comparison, layered-type materials with a sufficiently large layer spacing to accommodate Zn^{2+} are promising. Vanadium-based materials, including zinc pyrovanadate ($\text{Zn}_3\text{V}_2\text{O}_7(\text{OH})_2 \cdot 2\text{H}_2\text{O}$, ZnVO), with integrated molecular water in the crystal structure represent a classic layered-type material and enjoy significantly high electronic and ionic conductivity.[19]

Morphology engineering of cathode materials has been regarded as an important strategy for better ZIB. Specifically, Muhammad et al.[20] fabricated layer-type $\delta\text{-MnO}_2$ nanoflakes, delivering a ZIB capacity of 122 mAh g^{-1} at a current density of 83 mA g^{-1} .

Meanwhile, Guo et al.[21] synthesized δ - MnO_2 microspheres with the same crystal phase, exhibiting a similar capacity of 120 mAh g^{-1} at 100 mA g^{-1} . This suggests that the morphology may be not the most governing factor for ZIB capacity. Rather than morphology, the orientation effect in ZIBs is rarely investigated.

In this work, we pursue the influence of the predominant crystal planes and facets in ZIBs by rational design of two types of ZnVO materials. The different materials are fabricated via facile reactions of direct precipitation and microwave-assistant growth, respectively. Both types of ZnVO materials have been characterized by solid-state NMR, XRD and TEM, providing conclusive evidence that the materials possess the same crystal phase but have different preferred orientations. When used as the cathode material of ZIBs, the ZnVO material with the highly preferred (001) facet orientation exhibits capacitive properties, whose capacities are an order of magnitude better than a material where the same type of crystal phase exists in a morphology where (020) and (110) plane lattices are preferred.

2. Experimental

2.1 Chemicals

Zinc acetate dihydrate ($\text{Zn}(\text{CH}_3\text{COO})_2 \cdot 2\text{H}_2\text{O}$), ammonium metavanadate (NH_4VO_3), and carbon black were bought from Alfa Aesar. Steel meshes were purchased from Lizhiyuan Co., Ltd, China. Poly(vinylidene fluoride) (PVDF, $(\text{CH}_2\text{CF}_2)_n$, average MW $\sim 534,000$), zinc nitrate hexahydrate ($\text{Zn}(\text{NO}_3)_2 \cdot 6\text{H}_2\text{O}$), glycine ($\text{C}_2\text{H}_5\text{NO}_2$), zinc trifluoromethanesulfonate ($\text{Zn}(\text{CF}_3\text{SO}_3)_2$), 1-methyl-2-pyrrolidinone ($\text{C}_5\text{H}_8\text{NO}$, NMP) and zinc foils (thickness: 0.25 mm) were obtained from Sigma-Aldrich, Denmark.

2.2 Synthesis of 2D $\text{Zn}_3(\text{OH})_2(\text{V}_2\text{O}_7) \cdot 2\text{H}_2\text{O}$ nanosheets in flower morphology, ZnVF

In a typical synthesis, 1 mmol NH_4VO_3 and 1.5 mmol $\text{Zn}(\text{CH}_3\text{COO})_2 \cdot 2\text{H}_2\text{O}$ were dissolved in 20 and 30 mL Milli-Q water, respectively, to form clear solutions. The two solutions were mixed and stirred for 1 h . The resulting precipitates, $2\text{D } \text{Zn}_3(\text{OH})_2(\text{V}_2\text{O}_7) \cdot 2\text{H}_2\text{O}$ nanosheets, were collected by centrifugation and subsequently dried in an oven at 50°C overnight.

2.3 Synthesis of 1D $\text{Zn}_3(\text{OH})_2(\text{V}_2\text{O}_7)\cdot 2\text{H}_2\text{O}$ nanowires, ZnVW

1D $\text{Zn}_3(\text{OH})_2(\text{V}_2\text{O}_7)\cdot 2\text{H}_2\text{O}$ nanowires were synthesized by a simple microwave method. First, 1 mmol NH_4VO_3 was dissolved in 10 mL Milli-Q water at 80 °C; 1.5 mmol $\text{Zn}(\text{NO}_3)_2\cdot 6\text{H}_2\text{O}$ and glycine were dissolved in 10 mL Milli-Q water. When the two solutions were clear, they were blended at room temperature and stirred for 10 minutes. The aged solution was then sealed in a microwave vessel with 20 mL volume and heated at 100 °C for 6 h. The resulting brown precipitates were centrifuged and washed several times with a few mL of Milli-Q and ethanol, subsequently, allowed to dry in an oven at 50 °C to obtain the final product.

2.4 Material characterization

XRD patterns were measured by an Image Plate Huber G670 Guinier diffractometer with Cu K α 1 radiation in a transmission mode. Scanning electron microscopy (SEM) images were obtained using an AFEG 250 Analytical ESEM under a high vacuum atmosphere. Transmission electron microscopy (TEM) images were recorded by a FEI Tenai T20 operated at 200 kV equipped with a TVIPS XF416 CCD camera. The specific surface area and pore diameter distributions were studied by the Brunauer-Emmett-Teller (BET) method using a Micromeritics ASAP 2020. The thermal gravimetric and differential thermal analysis (TGA) was measured in air with a ramping rate of 5 °C min⁻¹ and heating up to 700 °C.

¹H and ⁵¹V MAS NMR spectra were recorded at 14.1 T on an Agilent 600 MHz NMR spectrometer using a 3.2 mm HXY MAS NMR probe tuned to ¹H and ⁵¹V in double resonance mode. ⁵¹V MAS NMR spectra were recorded using a short (0.1 μ s, ca 10°) pulse, with 1 s relaxation delay and 833 kHz spectral width. Two or more spinning speeds in the range of 15-20 kHz were used for ⁵¹V. Single-pulse (90° excitation pulse) and a rotor synchronized Hahn echo (90°- τ -180°- τ -acquisition, τ = 1 rotor period) were used. ¹H MAS NMR spectra were recorded with 20 kHz spinning speed. The magic-angle was set by minimizing the linewidth of the spinning sidebands in the ²³Na MAS NMR spectrum of sodium nitrate. ⁵¹V MAS NMR spectra were referenced relative to neat VOCl_3 (0 ppm) using vanadium pentoxide as a secondary reference. The ¹H MAS NMR spectra were referenced against water ($\delta(^1\text{H})$ = 4.6 ppm) as a secondary reference.

2.5 Electrochemical measurements

The cathode electrode was fabricated by coating a mixture of active material (70%), carbon black (20%), and poly(vinylidene fluoride) (PVDF, 10%) on a stainless-steel mesh followed by drying in a vacuum oven at 120 °C for 12 h. The loading of the active materials was about 1.3 mg cm⁻². The coin cells are assembled to CR2032 type with the Zn metal foil as the anode, glass microfiber filters as the separator, and 3 M Zn(CF₃SO₃)₂ as the electrolyte. Cell performance was tested on a Metrohm Autolab potentiostat. The galvanostatic testing of the cell was evaluated in a voltage range of 0.2-1.6 V at various current densities. Cyclic voltammetry (CV) was measured in the same potential range at various scan rates ranging from 0.1 to 0.8 mV s⁻¹ and electrochemical impedance spectroscopy (EIS) was recorded at the open-circuit voltage in a frequency range of 0.1 to 100k Hz.

2.6 Density functional theory (DFT) calculations

Spin-polarized DFT calculations were performed by using the Vienna Ab-Initio Simulation Package (VASP). The Perdew-Burke-Ernzerhof (PBE) functional within the generalized gradient approximation were used in this work.[22-24] We applied the projector-augmented wave method to represent the core electrons.[25, 26] The valence electronic states were expanded in plane-wave basis sets with cutoff energies of 450 eV. For the ion migration, the climbing-image nudged elastic band (CI-NEB) method was employed to search for the transition states with three images inserted between the initial state and the final state.[27, 28] The force convergence criterion is 0.05 eV/Å for structural optimization. A k-mesh of (3×3×2) was used for geometry optimization of ZnVF supercell ($a=b=12.10$ Å, $c=14.39$ Å; $\alpha=\beta=90^\circ$, $\gamma=120^\circ$). The DFT-D3 method was employed to describe dispersion interactions.[29, 30] The GGA+*U* approach was applied to correct V 3*d* orbitals with $U_{\text{eff}}=3.2$ eV.[31]

3. Results and discussion

3.1 Morphology and structure characterization

The ZnVO materials in this work are fabricated via direct precipitation for flower-shaped nanosheets (ZnVF), and microwave-assistant growth for the nanowires (ZnVW), respectively. The crystalline features were investigated by XRD (Fig. 1a-b). The sharp

diffraction peaks of the ZnVF (Fig. 1a) suggest good crystallinity, which are well-indexed to the hexagonal ZnVO (ICOD: 01-087-0417). No other crystal phases appear in the XRD patterns, indicating phase-pure materials. The identical peaks can be observed for ZnVW (Fig. 1b), confirming the same layer-type crystal structure. The structure consists of ZnO_6 octahedra forming layers with V-O-V columns of the V_2O_7 group in the middle of a sandwich-like structure (Fig. 1c). The crystal water is located between the layers. It is noteworthy that the relative peak intensities are different for ZnVF and ZnVW, revealing that the predominant crystal planes are not the same.

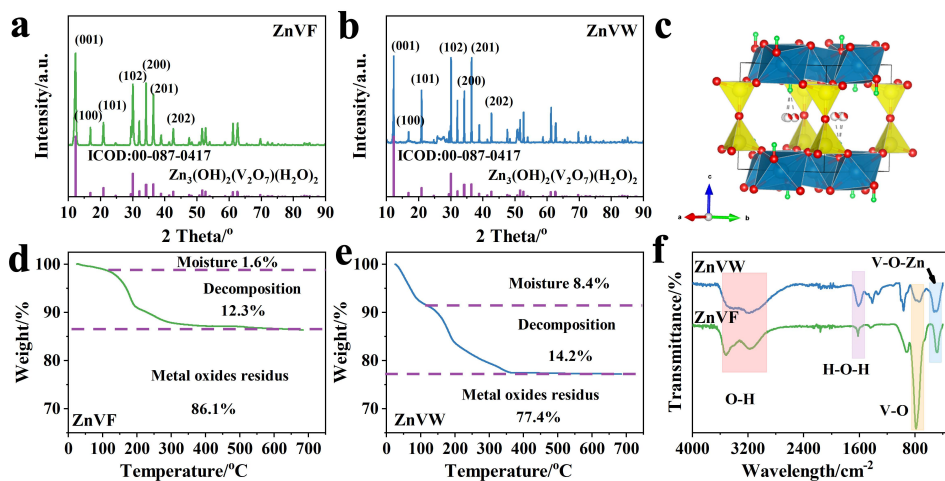


Fig. 1 XRD patterns of ZnVF (a), ZnVW (b) and corresponding crystal structure of ZnVO (c); TGA curves of ZnVF (d) and ZnVW (e); FT-IR spectra of ZnVF and ZnVW (f).

The thermal decomposition processes of both samples were investigated by thermogravimetric analysis (TGA) in air at a ramping rate of $5\text{ }^{\circ}\text{C min}^{-1}$ (Fig. 1d). There are three stages for the weight loss of ZnVF. The weight loss of about 1.6% in 30-100 $^{\circ}\text{C}$ is attributed to the evaporation of physically absorbed water. The mass loss of ca. 12.3 % in the temperature range 100-380 $^{\circ}\text{C}$ is assigned to the loss of crystal water and decomposition of hydroxides, along with a phase transition from hexagonal ZnVO to orthorhombic $\text{Zn}_3(\text{VO}_4)_2$. The same procedure applied to ZnVW reveals an approximately four times higher amount of physically absorbed water on the surface of ZnVW (8.4%, Fig. 1e).

The FTIR spectra of ZnVF and ZnVW (Fig. 1f) confirm the expected stretching and bending modes from the functional groups. The IR band at about 480 cm^{-1} is assigned to

symmetric V-O-Zn stretch.[32] The appearance of a peak at about 780 cm^{-1} is due to the bond shared by corner atoms of a (VO_4) tetrahedral structure.[33] The vibration at about 840 cm^{-1} is attributed to the tetrahedral rocking vibration modes of VO_4 . [34] The peaks located at $3000\text{-}3600$ and 1620 cm^{-1} are assigned to symmetric stretch and bend vibrations of H_2O , respectively.[35] Though the intensities of the bands in the spectra of ZnVF and ZnVW are different, the peak positions are the same. Furthermore, the presence of the peaks confirms that only zinc and vanadium metal oxides are present in the as-prepared samples. It also indicates that the ZnVF and ZnVW share the same local environment of vanadate and are nearly phase pure, but with slightly different amount of moisture and crystal water.

The ZnVW was dried under vacuum at $200\text{ }^\circ\text{C}$ for 2 h before remeasuring the TGA and XRD (Fig. S1a). The moisture and decomposition weight loss approximately decrease to the same value of ZnVF. This weight loss is due to the removal of the physically absorbed water and some of the crystal water. The XRD patterns indicate that the drying process does not change the crystal phase, which remains as hexagonal ZnVO (Fig. S1b).

^1H MAS NMR spectroscopy was applied to probe the speciation of hydrogen and vanadium in ZnVF and ZnVW. ^1H MAS NMR spectra can be used to confirm the presence of the hydroxide and water molecules inside of the framework, and the physically absorbed surface moisture. Both single-pulse (sp) and Hahn Echo (echo) ^1H MAS NMR spectra were recorded on both ZnVF and ZnVW (Fig. S2). The spectra reveal several resonances. It is noted that the crystal structure of ZnVO contains 6 crystallographic inequivalent H, 4 and 2 of which originate from interlayer water and hydroxide, respectively.[36] The obtained spectra were deconvoluted with a minimum number of resonances. ^1H MAS NMR spectra of ZnVF and ZnVW are both fitted with 5 resonances. Taking the single pulse ^1H MAS NMR spectra as an example, the resonances are at $\delta_{\text{iso}}(^1\text{H}) = 3.7, 5.0, 6.2, 7.3$ and 8.2 ppm , where three resonances are from interlayer water, one from physisorbed water and one from hydroxyl groups bonding to the ZnO_6 octahedron, respectively. The intensity of the resonances has been listed in Table S1. There is a significant difference in the central part of the resonances (around 5 ppm) between the ^1H MAS NMR spectra recorded with a single pulse and with a rotor synchronized echo. This intensity loss in the echo experiment is most likely due to the motion of the water molecules on the time scale of the spinning speed (kHz range).

The ^{51}V MAS NMR spectra of both samples contained an intense central transition with a center of gravity at -557.7 ppm and several spinning sidebands from the satellite transitions. The spectrum is characteristic of an orthovanadate influenced by small chemical shift anisotropy and moderate quadrupole interaction,[37] as illustrated in Fig. S3. Both ZnVF and ZnVW have a small shoulder at -579.3 ppm of ca 9.4 % intensity as compared to the main resonance. The resonance does not match previously reported values for $\text{Zn}_3(\text{VO}_4)_2$ (-522 ppm),[38] ZnV_2O_6 (-494 ppm)[39], or $\text{Zn}_2\text{V}_2\text{O}_7$ (-616 ppm)[40] due to the different binding geometries in the various zinc vanadates. This suggests that it is not due to a small impurity of a different zinc vanadate phase in the samples. The presence of the hydroxide bond and the water molecules inside the framework leads to distorted octahedral V-O environments.[41] Thus, according to the ^{51}V MAS NMR analysis, both ZnVF and ZnVW have the same local environment of the vanadate and the samples are nearly phase-pure.

To ascertain the elemental composition, XPS analysis has been conducted for both ZnVF and ZnVW. The XPS survey spectra in Fig. S4 show that both samples are composed of Zn, V, and O. In the Zn 2p spectra, the two obvious peaks at 1022 and 1405 eV correspond to Zn 2p_{3/2} and Zn 2p_{1/2} from Zn^{2+} , respectively.[42] The high-resolution V 2p spectra show two strong peaks at 524 and 517 eV from V 2p_{3/2} and V 2p $\frac{1}{2}$, respectively, indicating that vanadium is in oxidation state +5 in both ZnVF and ZnVW.[43] Due to the broad peak, a small amount of V^{4+} can be observed as well. The O 1s peak is split into various peaks due to the presence of M-O, O-H, and C-O.[44, 45] The M-O bonds in ZnVO includes both V-O and Zn-O; the C-O is from carbon-containing surface contamination and O-H is from the physically absorbed H_2O , crystal H_2O , and also hydroxide in the structure, corresponding well with the solid state NMR results.

The morphology and orientation of the zinc vanadate products are examined by SEM and TEM. The SEM image indicates that the synthesized ZnVF has a flower-like structure. Each flower with a size of 1 μm is assembled by individual nanoflakes (Fig. 2a). The TEM image shows the detailed nanostructure of the ZnVF (Fig. 2b). The thin flakes are of even thickness and 200-500 nm in diameter. The lattice fringes can be observed in high-resolution TEM images (inset of Fig. 2b). One lattice fringe with a d spacing of 0.26 nm corresponds to the (020) plane of the ZnVO phase, and the other plane (110) having 30° angles to the (020) plane has a 0.30 nm d spacing, in consistent to the XRD results. Combining the SAED image (Fig. 2c) with the information from high resolution-TEM and

XRD, the axis zone of the structures in ZnVF is [001]. A view from the top is shown in Fig. 2d.

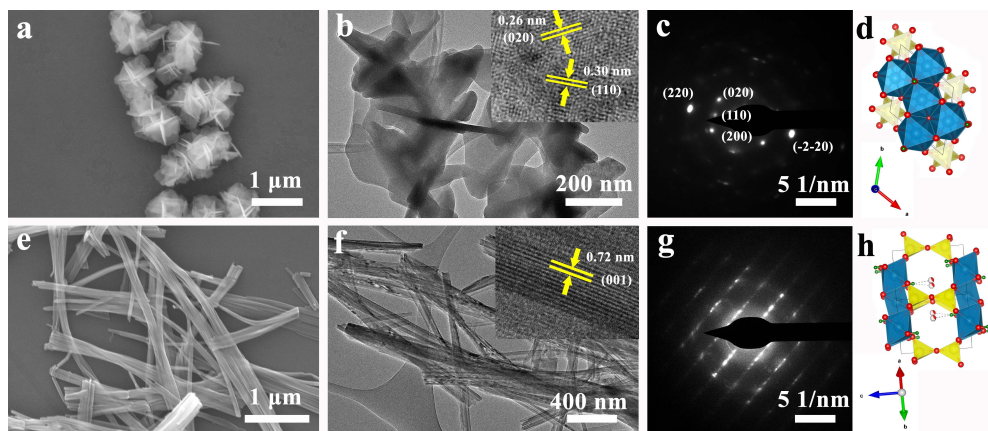


Fig. 2 SEM image, TEM image, SAED, and top-view crystal structure of ZnVF (a-d) and ZnVW (e-h).

In contrast to the dominating planar structure of ZnVF, ZnVW displays a nanowire structure. The lengths of 1D wires are at micrometer-scale (Fig. 2e). The distribution of nanowires is uniform with diameters of ca. 40 nm. The exposed lattice of the nanowire is the (001) plane lattice, with a d spacing of 0.72 nm (inset of Fig. 2f). The SAED image also confirm the layer structure of ZnVW (Fig. 2g). Fig. 2h shows the orientation of the structure in top-view. The BET surface area analyses of ZnVF and ZnVW were performed by N_2 adsorption-desorption (Fig. S5). It is found that the ZnVW nanowire structure exhibits a much larger specific surface area of $66.6 \text{ m}^2 \text{ g}^{-1}$, exceeding ZnVF flower structure ($15.6 \text{ m}^2 \text{ g}^{-1}$). The pore size distributions of ZnVF and ZnVW indicate there are no pores on the surface, in agreement with the observations from TEM.

3.2 Electrochemical performance

The electrochemical performance of both ZnVF and ZnVW was investigated in coin cells. The cycling performance of ZnVF at 100 mA g^{-1} is shown in Fig. 3a. It delivers a very poor capacity of about 3 mAh g^{-1} in the third cycle. The electrochemical profile of ZnVF provides evidence on the Zn^{2+} insertion and extraction process during charge and discharge. It is noted that the curves for ZnVF at 100 mA g^{-1} initially shows charge and discharge plateaus at 1.2 and 0.8 V (Fig. 3b), which, however, disappear fast, suggesting the poor reversibility of ZnVF. The morphology after cycling remains the flower morphology (Fig.

3c and Fig. S6). Furthermore, the high-resolution TEM image obtained after cycling show that the interplanar spacing of 0.26 nm for (020) is maintained.

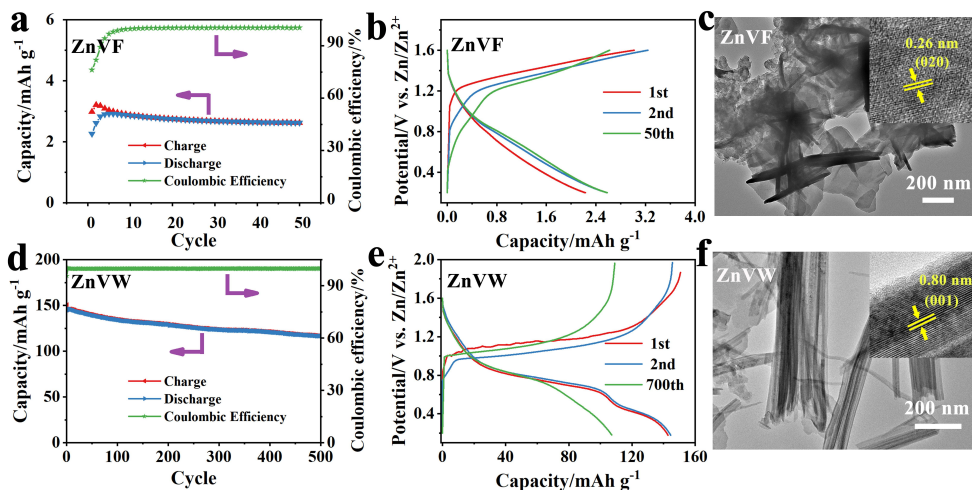


Fig. 3 Charge-discharge cycling profile and coulombic efficiency of cathode electrode; galvanostatic discharge/charge curves of the 1st, 2nd, and 50th or 700th cycle of ZnVF at the current density of 100 mA g⁻¹ (a-b) and ZnVW at a current density of 2A g⁻¹ (d-e); TEM images of ZnVF (c) and ZnVW (f) after cycling (insets are high-resolution TEM images).

In contrast, ZnVW initially delivers about 140 mAh g⁻¹ at a high current density of 2A g⁻¹ (Fig. 3d), about 50 times higher than that of ZnVF. After 700 cycles, the capacity is well retained at 108 mAh g⁻¹, suggesting a high cycling stability. The initial coulombic efficiency is 95%, outperforming ZnVF (76%). The galvanostatic discharge/charge curves of ZnVW in Fig. 3e shows that there are two obvious plateau regions at 1.0/1.2 V, and 0.8/0.5 V, respectively, indicating more storage of the Zn²⁺ ions compared to ZnVF. After 700 cycles, one pair of plateaus (0.8-1.2 V) still exists without shift. The stable structure is further verified by TEM and SEM. Interestingly, the interplanar spacing of the exposed (001) plane spacing increases from the initial value of 0.72 nm to 0.80 nm. This proves the Zn²⁺ ion insertion into the (001) plane lattice, with the crystalline phase maintained, as evidenced by XRD (Fig. S7). The large amount of Zn²⁺ ions insertion also causes the reduction of vanadium (Fig. S8). The as-fabricated ZnVW material was tested by galvanostatic charge/discharge (Fig. S9), exhibiting reversible capacities of 227, 198, 166, 118, 86, and 64 mAh g⁻¹ at current densities of 100, 200, 400, 800, 1600, and 3200 mA g⁻¹, respectively. The electrochemical performance of the ZnVW in terms of capacity and cycling performance is also better than other layer-type cathode materials. For example,

Xia et al.[46] synthesized a porous framework ZnVO material delivering a capacity of 101 mAh g⁻¹ at 200 mA g⁻¹ after 300 cycles. Li et al.[47] fabricated a layer-type Na₃V₂(PO₄)₂F₃ cathode material and obtained a capacity of 50 mAh g⁻¹ at 0.2 A g⁻¹ after 600 cycles.

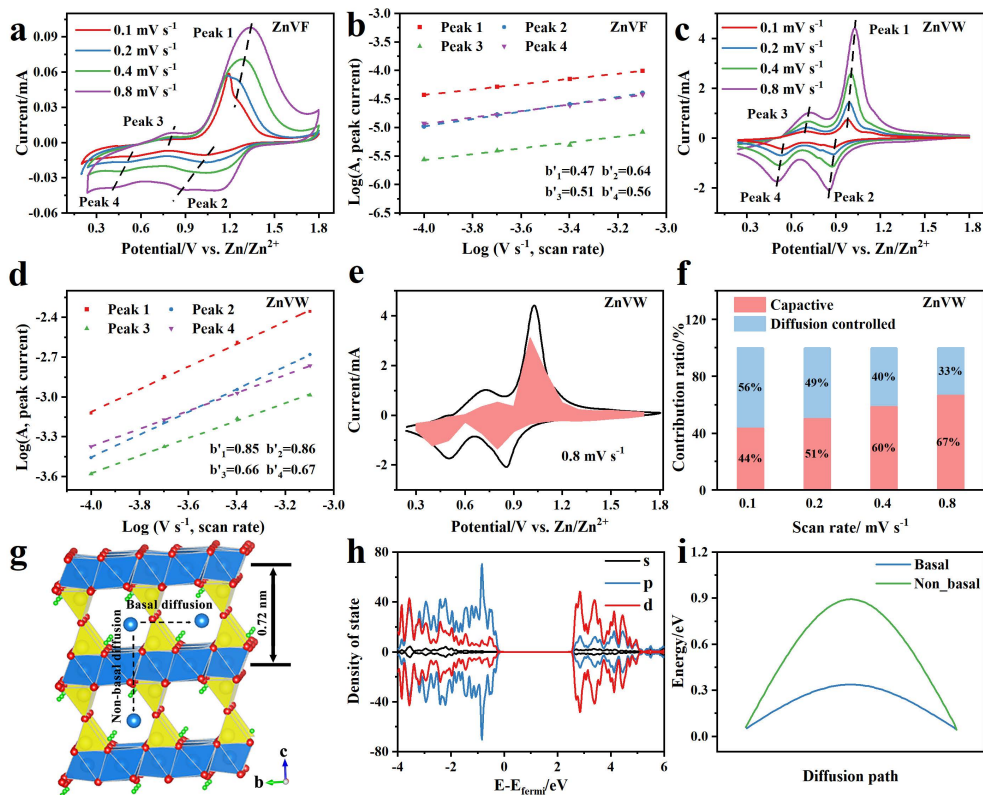


Fig. 4 CV curves and the dependence of the peak currents at various scan rates from 0.1 to 0.8 mV s⁻¹ of ZnVF (a, b) and ZnVW (c, d); Capacitive contribution (pink part) and diffusion contribution (void part) at 0.8 mV s⁻¹ (e); Normalized contribution ratio of the capacitive capacity at different scan rates (f); The possible diffusion pathways of Zn²⁺ ion in the crystal structures (g); Projected density of state (pDOS) of the Zn₃V₂O₇(OH)₂ bulk structure (h) and the corresponding diffusion energy in two directions (i).

In general, the energy storage mechanism is a combination of Faradic capacitive behavior and diffusion-controlled behavior. Cyclic voltammetry (CV) was performed to distinguish the two types of charge storage mechanisms in both ZnVF and ZnVW. The CV curves of ZnVF were measured in a potential range of 0.2 to 1.8 V (vs. Zn/Zn²⁺), with minimal hydrogen or oxygen evolution reactions, and at different scan rates ranging from 0.1 to 0.8 mV s⁻¹ (Fig. 4a). The CV curves exhibit different peaks at a low scan rate, because the low ion diffusion coefficient leads to an irreversible insertion and extraction of the Zn²⁺

ion in the crystal structure at a high scan rate. ZnVW exhibits two distinct pairs of peaks at around 1.0/0.9 V (peak1/peak2) and 0.75/0.5 V (peak 3/peak 4), assigned to Zn^{2+} intercalation and extraction in a two-step process (Fig. 4c). Based on the previous reports and power law principles, the relationship between peak current and scan rate is $i = a'v^{b'}$ (a' and b' are variable values), details given in the supporting information.[18, 48] The b' values of ZnVW are 0.85, 0.86, 0.66, and 0.67 during charging and discharging process, as compared to 0.47, 0.64, 0.51, and 0.56 of ZnVF, indicating complete diffusion-controlled kinetics in ZnVF and a partial capacitive contribution in ZnVW. For example, 67% of the current can be assigned to the capacitive response at 0.8 mV s^{-1} (calculation is given in supporting information and Fig. S10), see Fig. 4e. With decreasing scan rate, the diffusion-controlled contribution increases, consistent to previously reported materials undergoing an intercalation mechanism.[49]

3.3 DFT calculation

Zn ion diffusion pathway in the crystal structure is proposed to be the main reason for the significant difference, of nearly 50 folds, in the capacity of ZnVF and ZnVW. The difference of the surface area by a factor of 4.3 is unlikely the governing factor (Fig. S5). The possible diffusion pathways of Zn^{2+} in the crystal structures in $\text{Zn}_3\text{V}_2\text{O}_7(\text{OH})_2$ are given in Fig. 4g. The projected density of state (pDOS) of the $\text{Zn}_3\text{V}_2\text{O}_7(\text{OH})_2$ bulk structure is shown in Fig. 4h. 2D flakes of ZnVF expose mainly the (001) basal plane, consisting of compact layers of ZnO_6 octahedras (blue colour in Fig. 4g). Zn^{2+} intercalating in that direction has to go through the small lattice spacing between ZnO_6 octahedras with large hinderance. In contrast, the ZnVW exposes the (010) non-basal plane (or (001) plane lattice), comprising the ZnO_6 octahedron layers connecting with each other through an oxygen bridge. The much larger interlayer spacing of 0.72 nm is identified between the ZnO_6 layers, allowing facile Zn^{2+} diffusion.

DFT calculations were carried out to investigate the migration barrier of Zn^{2+} though each of those two planes. As shown in Fig. 4i, Zn^{2+} intercalation from the compact ZnO_6 octahedrons layer in ZnVF is regarded as the non-basal diffusion, while Zn^{2+} migration in between the ZnO_6 layers in ZnVW is described as the basal diffusion (along the basal plane). The climbing-image nudged elastic band (CI-NEB) calculations shows that the basal diffusion of Zn^{2+} in the ZnVW structure has a much lower energy barrier of 0.31 eV, compared to the non-basal diffusion in the ZnVF of 0.89 eV. We compare the diffusion

rates of Zn^{2+} in the two systems further by using transition-state theory which can be expressed as follows: [50]

$$r = v e^{\left(-\frac{E_a}{kT}\right)} \quad (1)$$

where v , E_a , k and T are pre-exponential factor, diffusion barrier, Boltzmann constant (8.617×10^{-5} eV/K) and temperature (298 K), respectively. Zn^{2+} diffusion in the b direction (non-basal diffusion) is around a factor of 10^9 faster than that in the c direction. It reveals that ZnVO exposing a large enough lattice spacing can easily accommodate the intercalation of Zn^{2+} . In addition, electrochemical spectroscopy (EIS) (Fig. S11) reveals that the electrical resistance of the ZnVW is about 9 times lower than that of ZnVF, leading to a more efficient Zn^{2+} transportation. Furthermore, the Zn^{2+} diffusion coefficient in ZnVW is determined to be in a range of 10^{-11} - 10^{-10} $\text{cm}^2 \text{ s}^{-1}$ using the galvanostatic intermittent titration technique (GITT)[51] (Fig. S12-S13).

4. Conclusions

In conclusion, we have observed that ZnVF and ZnVW, in the same crystal phase and chemical environment, show vastly different performance as the ZIB cathode material. Using TEM and ss-NMR, we identify the differences between the as-prepared samples in morphology, dimension, and crystal orientation. When used as the cathode electrode of ZIBs, ZnVW exhibits lower polarization, higher electrochemical activity, higher electrical conductivity, and faster ion diffusion capability than ZnVF. In addition, ZnVW has a combined contribution of diffusion-controlled and Faradic capacitive behavior, leading to the great Zn^{2+} storage performance. The knowledge about the critical requirement for the crystalline orientation is highly valuable for next-generation cathode materials.

Associated content

Supporting Information

Additional information and figures include TGA curve and XRD pattern of ZnVW dried under vacuum; ^1H ss-NMR spectra, XPS spectra, N_2 adsorption-desorption isotherms, SEM images, XRD patterns and XPS spectra of the charge and discharge states, EIS spectra of the ZnVF and ZnVW. Rate performance, plots of $v^{-1/2}$ vs. $i/v^{-1/2}$ at different potential states, GITT of ZnVW.

Notes

There are no conflicts to declare.

Acknowledgements

This article is dedicated to Professor Jens Ulstrup on the occasion of his 80th birthday. The authors gratefully acknowledge the financial support from the China Scholarship Council for a Ph.D. scholarship (No. 201706220078) to H. C. and a VILLUM Experiment (grant No. 35844) to X. X.. C. P. thanks for the Natural Science Foundation of Hunan Province (2019JJ50526). Mr. Christian B Jørgensen is thanked for assistance with the NMR experiments. U. G. N. acknowledges funding from the Danish Council for Independent Research (DFF-7014-00198). The 600 MHz NMR spectrometer is part of the Villum center for bioanalytical analyses.

Data availability

Raw data from all measurements are available from the authors.

References

- [1] P. Hu, T. Zhu, X. Wang, X. Wei, M. Yan, J. Li, W. Luo, W. Yang, W. Zhang, L. Zhou, Z. Zhou, L. Mai, Highly Durable $\text{Na}_2\text{V}_6\text{O}_{16} \cdot 1.63\text{H}_2\text{O}$ Nanowire Cathode for Aqueous Zinc-Ion Battery, *Nano Lett.* 18(3) (2018) 1758-1763.
- [2] Y. Zhang, Y. An, L. Wu, H. Chen, Z. Li, H. Dou, V. Murugadoss, J. Fan, X. Zhang, X. Mai, Z. Guo, Metal-free energy storage systems: combining batteries with capacitors based on a methylene blue functionalized graphene cathode, *J. Mater. Chem. A* 7(34) (2019) 19668-19675.
- [3] B. Kirubasankar, V. Murugadoss, J. Lin, T. Ding, M. Dong, H. Liu, J. Zhang, T. Li, N. Wang, Z. Guo, S. Angaiah, In situ grown nickel selenide on graphene nanohybrid electrodes for high energy density asymmetric supercapacitors, *Nanoscale* 10(43) (2018) 20414-20425.
- [4] H. Lyu, P. Li, J. Liu, S. Mahurin, J. Chen, D.K. Hensley, G.M. Veith, Z. Guo, S. Dai, X.-G. Sun, Aromatic Polyimide/Graphene Composite Organic Cathodes for Fast and Sustainable Lithium-Ion Batteries, *ChemSusChem* 11(4) (2018) 763-772.
- [5] Y. Tian, Y. An, C. Wei, B. Xi, S. Xiong, J. Feng, Y. Qian, Flexible and Free-Standing $\text{Ti}_3\text{C}_2\text{T}_x$ MXene@Zn Paper for Dendrite-Free Aqueous Zinc Metal Batteries and Nonaqueous Lithium Metal Batteries, *ACS Nano* 13(10) (2019) 11676-11685.
- [6] X. Lou, C. Lin, Q. Luo, J. Zhao, B. Wang, J. Li, Q. Shao, X. Guo, N. Wang, Z. Guo, Crystal Structure Modification Enhanced $\text{FeNb}_{11}\text{O}_{29}$ Anodes for Lithium-Ion Batteries, *ChemElectroChem* 4(12) (2017) 3171-3180.
- [7] J. Guan, Y. Li, Y. Guo, R. Su, G. Gao, H. Song, H. Yuan, B. Liang, Z. Guo, Mechanochemical Process Enhanced Cobalt and Lithium Recycling from Wasted Lithium-Ion Batteries, *ACS Sustain. Chem. Eng.* 5(1) (2017) 1026-1032.
- [8] H. Lyu, C.J. Jafta, I. Popovs, H.M. Meyer, J.A. Hachtel, J. Huang, B.G. Sumpter, S. Dai, X.-G. Sun, A dicyanobenzoquinone based cathode material for rechargeable lithium and sodium ion batteries, *J. Mater. Chem. A* 7(30) (2019) 17888-17895.
- [9] H. Lyu, Y. Li, C.J. Jafta, C.A. Bridges, H.M. Meyer, A. Borisevich, M.P. Paranthaman, S. Dai, X.-G. Sun, Bis(trimethylsilyl) 2-fluoromalonate derivatives as electrolyte additives for high voltage lithium ion batteries, *J. Power Sources* 412 (2019) 527-535.

-
- [10] H. Lyu, J. Liu, S. Qiu, Y. Cao, C. Hu, S. Guo, Z. Guo, Carbon composite spun fibers with in situ formed multicomponent nanoparticles for a lithium-ion battery anode with enhanced performance, *J. Mater. Chem. A* 4(25) (2016) 9881-9889.
- [11] X. Wang, B. Xi, Z. Feng, W. Chen, H. Li, Y. Jia, J. Feng, Y. Qian, S. Xiong, Layered $(\text{NH}_4)_2\text{V}_6\text{O}_{16} \cdot 1.5\text{H}_2\text{O}$ nanobelts as a high-performance cathode for aqueous zinc-ion batteries, *J. Mater. Chem. A* 7(32) (2019) 19130-19139.
- [12] P. Tan, B. Chen, H. Xu, H. Zhang, W. Cai, M. Ni, M. Liu, Z. Shao, Flexible Zn- and Li-air batteries: recent advances, challenges, and future perspectives, *Energ. Environ. Sci.* 10(10) (2017) 2056-2080.
- [13] X. Wang, B. Xi, X. Ma, Z. Feng, Y. Jia, J. Feng, Y. Qian, S. Xiong, Boosting Zinc-Ion Storage Capability by Effectively Suppressing Vanadium Dissolution Based on Robust Layered Barium Vanadate, *Nano Lett.* 20(4) (2020) 2899-2906.
- [14] B. Tang, L. Shan, S. Liang, J. Zhou, Issues and opportunities facing aqueous zinc-ion batteries, *Energ. Environ. Sci.* 12(11) (2019) 3288-3304.
- [15] G. Fang, J. Zhou, A. Pan, S. Liang, Recent Advances in Aqueous Zinc-Ion Batteries, *ACS Energy Lett.* 3(10) (2018) 2480-2501.
- [16] Y. Zhong, X. Xu, J.-P. Veder, Z. Shao, Self-Recovery Chemistry and Cobalt-Catalyzed Electrochemical Deposition of Cathode for Boosting Performance of Aqueous Zinc-Ion Batteries, *iScience* 23(3) (2020) 100943.
- [17] Y. Tian, G.-D. Li, J.-S. Chen, Chemical Formation of Mononuclear Univalent Zinc in a Microporous Crystalline Silicoaluminophosphate, *J. Am. Chem. Soc.* 125(22) (2003) 6622-6623.
- [18] Y. Yang, Y. Tang, G. Fang, L. Shan, J. Guo, W. Zhang, C. Wang, L. Wang, J. Zhou, S. Liang, Li^+ intercalated $\text{V}_2\text{O}_5 \cdot n\text{H}_2\text{O}$ with enlarged layer spacing and fast ion diffusion as an aqueous zinc-ion battery cathode, *Energ. Environ. Sci.* 11(11) (2018) 3157-3162.
- [19] Y. Yang, Y. Tang, S. Liang, Z. Wu, G. Fang, X. Cao, C. Wang, T. Lin, A. Pan, J. Zhou, Transition metal ion-preintercalated V_2O_5 as high-performance aqueous zinc-ion battery cathode with broad temperature adaptability, *Nano Energy* 61 (2019) 617-625.
- [20] M.H. Alfuruqi, J. Gim, S. Kim, J. Song, D.T. Pham, J. Jo, Z. Xiu, V. Mathew, J. Kim, A layered $\delta\text{-MnO}_2$ nanoflake cathode with high zinc-storage capacities for eco-friendly battery applications, *Electrochem. Commun.* 60 (2015) 121-125.

- [21] C. Guo, Q. Zhou, H. Liu, S. Tian, B. Chen, J. Zhao, J. Li, A case study of β - and δ - MnO_2 with different crystallographic forms on ion-storage in rechargeable aqueous zinc ion battery, *Electrochim. Acta* 324 (2019) 134867.
- [22] J.P. Perdew, K. Burke, M. Ernzerhof, Generalized Gradient Approximation Made Simple, *Phys. Rev. Lett.* 77(18) (1996) 3865-3868.
- [23] G. Kresse, J. Furthmüller, Efficiency of ab-initio total energy calculations for metals and semiconductors using a plane-wave basis set, *Comput. Mater. Sci.* 6(1) (1996) 15-50.
- [24] G. Kresse, J. Hafner, Ab initio molecular-dynamics simulation of the liquid-metal–amorphous-semiconductor transition in germanium, *Phys. Rev. B* 49(20) (1994) 14251-14269.
- [25] G. Kresse, D. Joubert, From ultrasoft pseudopotentials to the projector augmented-wave method, *Phys. Rev. B* 59(3) (1999) 1758-1775.
- [26] P.E. Blöchl, O. Jepsen, O.K. Andersen, Improved tetrahedron method for Brillouin-zone integrations, *Phys. Rev. B* 49(23) (1994) 16223-16233.
- [27] G. Henkelman, H. Jónsson, Improved tangent estimate in the nudged elastic band method for finding minimum energy paths and saddle points, *J. Chem. Phys.* 113(22) (2000) 9978-9985.
- [28] G. Henkelman, B.P. Uberuaga, H. Jónsson, A climbing image nudged elastic band method for finding saddle points and minimum energy paths, *J. Chem. Phys.* 113(22) (2000) 9901-9904.
- [29] S. Grimme, S. Ehrlich, L. Goerigk, Effect of the damping function in dispersion corrected density functional theory, *J. Comput. Chem.* 32(7) (2011) 1456-1465.
- [30] S. Grimme, J. Antony, S. Ehrlich, H. Krieg, A consistent and accurate ab initio parametrization of density functional dispersion correction (DFT-D) for the 94 elements H-Pu, *J. Chem. Phys.* 132(15) (2010) 154104.
- [31] L. Ma, N. Li, C. Long, B. Dong, D. Fang, Z. Liu, Y. Zhao, X. Li, J. Fan, S. Chen, Achieving Both High Voltage and High Capacity in Aqueous Zinc-Ion Battery for Record High Energy Density, *Adv. Funct. Mater.* 29(46) (2019) 1906142.
- [32] M.M. Sajid, N.A. Shad, S.B. Khan, Z. Zhang, N. Amin, Facile synthesis of Zinc vanadate $\text{Zn}_3(\text{VO}_4)_2$ for highly efficient visible light assisted photocatalytic activity, *J. Alloys Compd.* 775 (2019) 281-289.
- [33] S.A. Mahmoud, S.H. Bendary, A.A. Salem, O.A. Fouad, Facile synthesis of high yield two dimensional zinc vanadate nanoflakes, *SN Applied Sciences* 1(5) (2019) 497.

-
- [34] S. Ezhil Arasi, P. Devendran, R. Ranjithkumar, S. Arunpandiyam, A. Arivarasan, Electrochemical property analysis of zinc vanadate nanostructure for efficient supercapacitors, *Mater. Sci. Semicond. Process.* 106 (2020) 104785.
- [35] Y.E. Bhoge, V.J. Patil, T.D. Deshpande, R.D. Kulkarni, Synthesis and anticorrosive performance evaluation of zinc vanadate pigment, *Vacuum* 145 (2017) 290-294.
- [36] N.D. Jensen, N.T. Duong, R. Bolanz, Y. Nishiyama, C.A. Rasmussen, J. Gottlicher, R. Steininger, V. Prevot, U.G. Nielsen, Synthesis and Structural Characterization of a Pure $\text{ZnAl}_4(\text{OH})_{12}(\text{SO}_4) \cdot 2.6\text{H}_2\text{O}$ Layered Double Hydroxide, *Inorg. Chem.* 58(9) (2019) 6114-6122.
- [37] U.G. Nielsen, A. Boisen, M. Brorson, C.J.H. Jacobsen, H.J. Jakobsen, J. Skibsted, Aluminum Orthovanadate (AlVO_4): Synthesis and Characterization by ^{27}Al and ^{51}V MAS and MQMAS NMR Spectroscopy, *Inorg. Chem.* 41(24) (2002) 6432-6439.
- [38] J. Skibsted, C.J.H. Jacobsen, H.J. Jakobsen, ^{51}V Chemical Shielding and Quadrupole Coupling in Ortho- and Metavanadates from ^{51}V MAS NMR Spectroscopy, *Inorg. Chem.* 37(12) (1998) 3083-3092.
- [39] U.G. Nielsen, H.J. Jakobsen, J. Skibsted, Characterization of Divalent Metal Metavanadates by ^{51}V Magic-Angle Spinning NMR Spectroscopy of the Central and Satellite Transitions, *Inorg. Chem.* 39(10) (2000) 2135-2145.
- [40] U.G. Nielsen, H.J. Jakobsen, J. Skibsted, ^{51}V MAS NMR Investigation of ^{51}V Quadrupole Coupling and Chemical Shift Anisotropy in Divalent Metal Pyrovanadates, *J. Phys. Chem. B* 105(2) (2001) 420-429.
- [41] N.R. Jaegers, C. Wan, M.Y. Hu, M. Vasiliu, D.A. Dixon, E. Walter, I.E. Wachs, Y. Wang, J.Z. Hu, Investigation of Silica-Supported Vanadium Oxide Catalysts by High-Field ^{51}V Magic-Angle Spinning NMR, *J. Phys. Chem C* 121(11) (2017) 6246-6254.
- [42] Y. Zhu, Y. Zhong, G. Chen, X. Deng, R. Cai, L. Li, Z. Shao, A hierarchical $\text{Zn}_2\text{Mo}_3\text{O}_8$ nanodots-porous carbon composite as a superior anode for lithium-ion batteries, *Chem. Commun.* 52(60) (2016) 9402-9405.
- [43] X. Chen, B. Zhao, Y. Cai, M.O. Tadé, Z. Shao, Amorphous V-O-C composite nanofibers electrospun from solution precursors as binder- and conductive additive-free electrodes for supercapacitors with outstanding performance, *Nanoscale* 5(24) (2013) 12589-12597.

- [44] H. Lyu, J. Li, T. Wang, B.P. Thapaliya, S. Men, C.J. Jafta, R. Tao, X.-G. Sun, S. Dai, Carbon Coated Porous Titanium Niobium Oxides as Anode Materials of Lithium-Ion Batteries for Extreme Fast Charge Applications, *ACS Appl. Energy Mater.* 3(6) (2020) 5657-5665.
- [45] J.-L. Qin, H.-L. Zhu, N. Lun, Y.-X. Qi, Y.-J. Bai, $\text{Li}_2\text{ZnTi}_3\text{O}_8/\text{C}$ anode with high initial Coulombic efficiency, long cyclic life and outstanding rate properties enabled by fulvic acid, *Carbon* 163 (2020) 297-307.
- [46] C. Xia, J. Guo, Y. Lei, H. Liang, C. Zhao, H.N. Alshareef, Rechargeable Aqueous Zinc-Ion Battery Based on Porous Framework Zinc Pyrovanadate Intercalation Cathode, *Adv. Mater.* 30(5) (2018) 1705580.
- [47] W. Li, K. Wang, S. Cheng, K. Jiang, A long-life aqueous Zn-ion battery based on $\text{Na}_3\text{V}_2(\text{PO}_4)_2\text{F}_3$ cathode, *Energy Storage Mater.* 15 (2018) 14-21.
- [48] V. Augustyn, J. Come, M.A. Lowe, J.W. Kim, P.-L. Taberna, S.H. Tolbert, H.D. Abruña, P. Simon, B. Dunn, High-rate electrochemical energy storage through Li^+ intercalation pseudocapacitance, *Nat. Mater.* 12(6) (2013) 518-522.
- [49] G. Fang, C. Zhu, M. Chen, J. Zhou, B. Tang, X. Cao, X. Zheng, A. Pan, S. Liang, Suppressing Manganese Dissolution in Potassium Manganate with Rich Oxygen Defects Engaged High-Energy-Density and Durable Aqueous Zinc-Ion Battery, *Adv. Funct. Mater.* 29(15) (2019) 1808375.
- [50] M.H. Dahan, A. Baranovskiy, Y. Natanzon, Y. Amouyal, A first-principles study of the temperature-dependent diffusion coefficients of silver in the thermoelectric compound PbTe, *Acta Mater.* 202 (2021) 243-254.
- [51] W. Shi, B. Yin, Y. Yang, M.B. Sullivan, J. Wang, Y.-W. Zhang, Z.G. Yu, W.S.V. Lee, J. Xue, Unravelling V_6O_{13} Diffusion Pathways via CO_2 Modification for High-Performance Zinc Ion Battery Cathode, *ACS Nano* (2021).

Supporting Information for

New Insight into the Orientation Effect of Zinc Vanadate on Zinc Ion Storage Performance

Huili Cao,^{a,1,*} Chao Peng,^{b,1} Zhiyong Zheng,^a Zhenyun Lan,^c Qinying Pan,^a Ulla Gro Nielsen,^d Poul
Norby,^c Xinxin Xiao^{a,*} and Susanne Mossin^{a,*}

^aDepartment of Chemistry, Technical University of Denmark, 2800 Kgs. Lyngby, Denmark

^bSchool of Engineering, University of Southampton, Southampton SO17 1BJ, UK

^cDepartment of Energy Conversion and Storage, Technical University of Denmark, 2800
Kgs. Lyngby, Denmark

^dDepartment of Physics, Chemistry and Pharmacy, University of Southern Denmark,
Campusvej 55, 5230 Odense M, Denmark

¹These authors contributed equally to this work

Corresponding authors: hucao@kemi.dtu.dk (H. Cao); xixiao@kemi.dtu.dk (X. Xiao);
slmo@kemi.dtu.dk (S. Mossin).

Supporting Figures and table

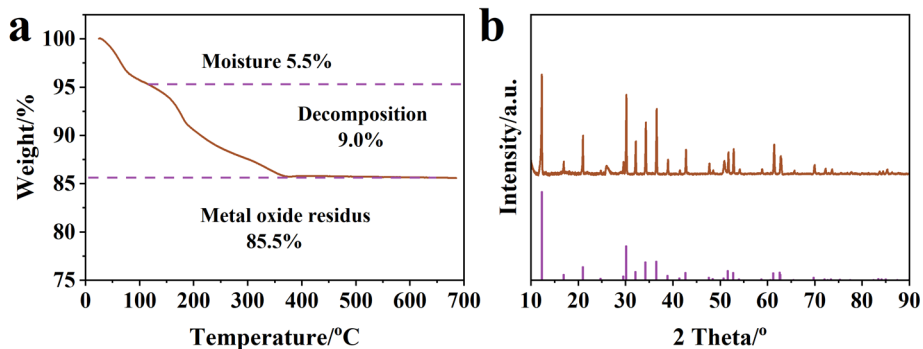


Fig. S1 Data for vacuum dried ZnVW. TGA curve (a) and XRD patterns (b) of ZnVW dried under vacuum at 200 °C.

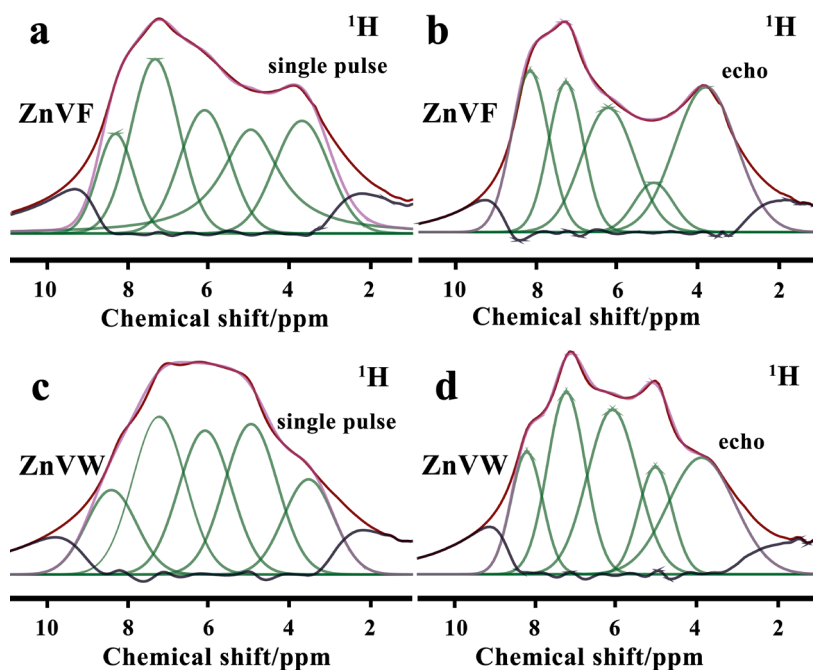


Fig. S2 ^1H solid state-NMR. NMR spectra and Gaussian deconvolution with the minimum number of peaks to reproduce the overall line width for the spectra of both ZnVF and ZnVW obtained by single pulse and by echo.

Table S1 $\delta_{\text{iso}}(^1\text{H})$ and relative intensity (I) of the different ^1H resonances obtained from deconvolution of the single pulse (sp) and echo ^1H MAS NMR spectra of ZnVF and ZnVW.

$\delta_{\text{iso}}(^1\text{H})$ (ppm)	ZnVF sp I (%)	ZnVW sp I (%)	ZnVF echo I (%)	ZnVW echo I (%)
3.7	18	14	31	25
5.0	27	24	7	11
6.2	19	23	23	29
7.3	25	25	18	22
8.2	11	14	21	13

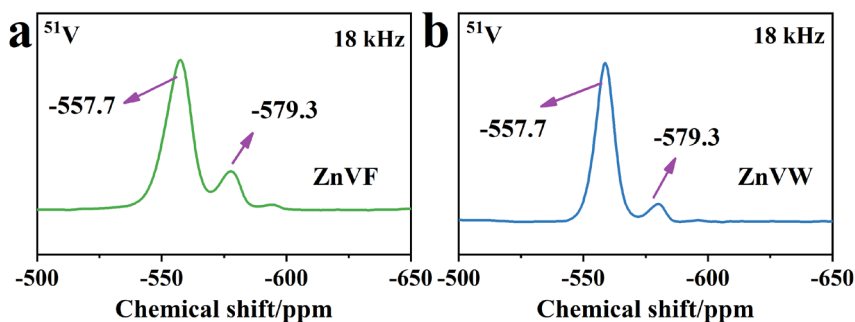


Fig. S3 ^{51}V solid state-NMR. NMR spectra of ZnVF (a) and ZnVW (b) in a 18 kHz spinning speed.

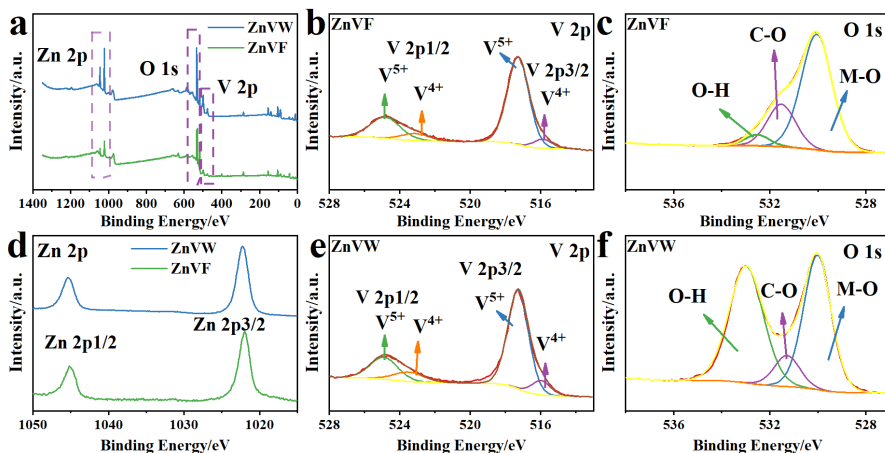


Fig. S4 XPS spectra. Survey spectra of ZnVF and ZnVW (a), spectra for ZnVF at V 2p (b), and O 1s (c), spectra for Zn 2p of ZnVF and ZnVW (d), spectra for ZnVW for V2p (e), and O1s (f).

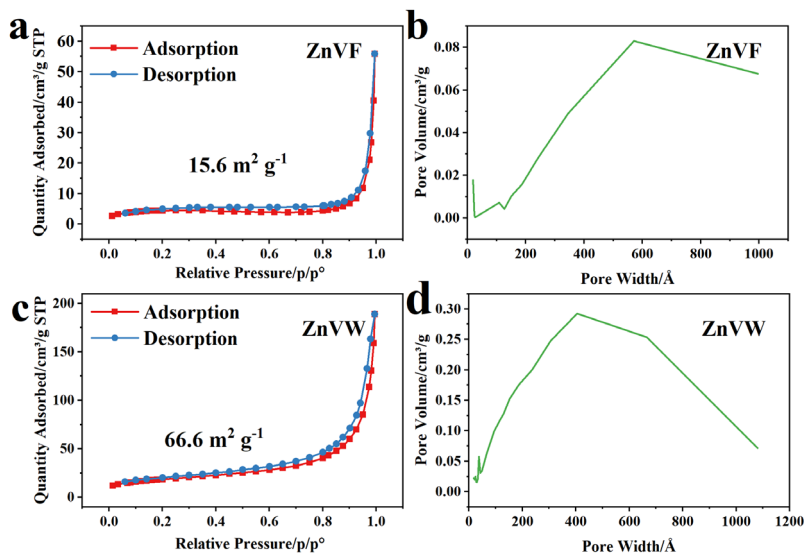


Fig. S5 BET data. N₂ adsorption-desorption isotherms (a and c) and their corresponding pore size distributions (b and d) for both ZnVF and ZnVW.

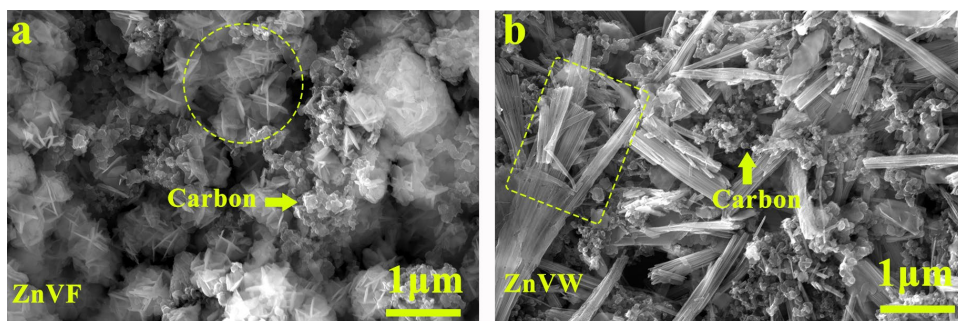


Fig. S6 SEM. Images of ZnVF (a) and ZnVW (b) after cycling.

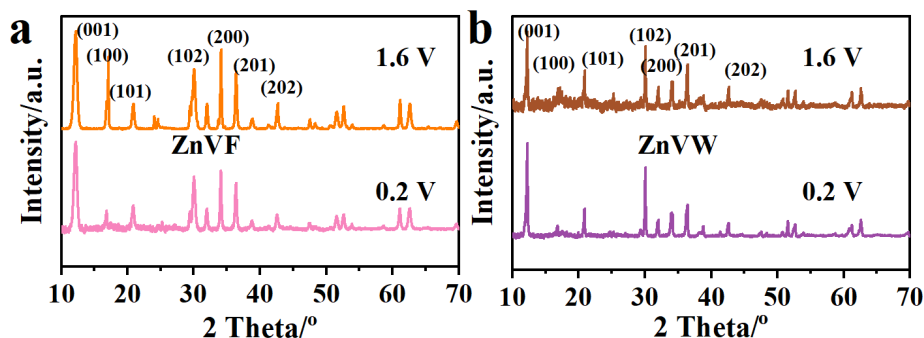


Fig. S7 XRD of cathode materials. Comparison of XRD patterns of ZnVF (a) and ZnVW (b) in the charged (at 1.6 V) and discharged (at 0.2 V) state.

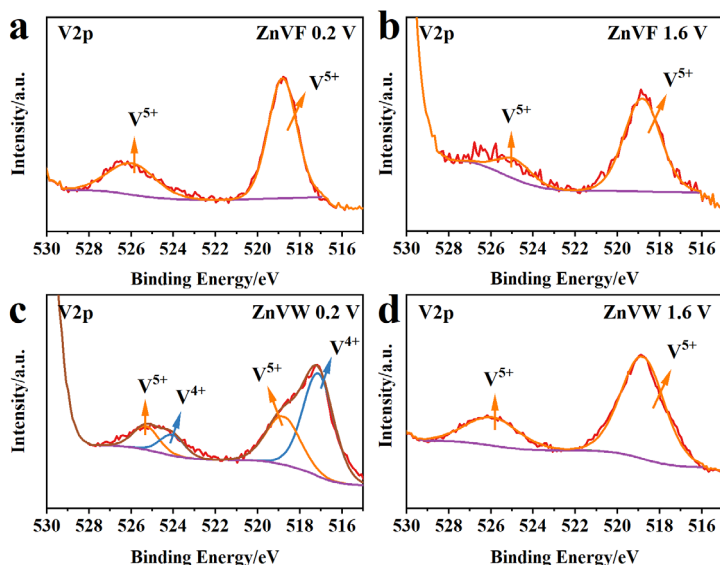


Fig. S8 XPS spectra of cathode materials. High resolution XPS spectra of the V 2p region of ZnVF and ZnVW in the discharged (0.2 V) and charged (1.6 V) state.

Note: XRD and XPS were employed to provide more insight into the structure evolution and change of the oxidation state of vanadium during electrochemical cycling. The XRD patterns show that the ZnVF maintains the hexagonal ZnVO (ICOD: 01-087-0417) phase during the energy storage process and that only the intensity of the (100) plane changes, see Fig. S7. In comparison, the crystal phase of ZnVW is unchanged between the fully charged discharged stages, without the appearance of new peaks, indicating the intercalation mechanism for the Zn^{2+} ion storage process in ZnVO. Further insight is

disclosed by XPS (Fig. S8). In the V 2p region of the spectra from the ZnVF cathode, there is only one peak assigned to the V 2p_{2/3} component (518.5 eV) from the original V site in ZnVO (V⁵⁺), even at a fully discharged stage (0.2 V). For the ZnVW cathode, there is an obvious red shift of the V 2p_{2/3} peak from the V⁵⁺ to V⁴⁺ component during discharge. This difference between the ZnVF and ZnVW implies the different amounts of Zn²⁺ ions inserted into the host cathode materials.

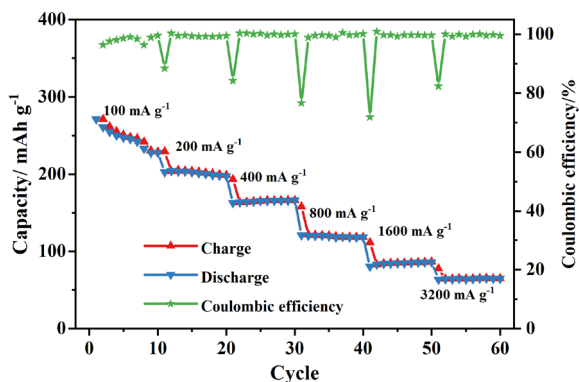


Fig. S9 Electrochemical performance. Rate performance of ZnVW applied as the cathode material when assembled into a coin cell at various current densities of 100, 200, 400, 800, 1600 and 3200 mA g⁻¹.

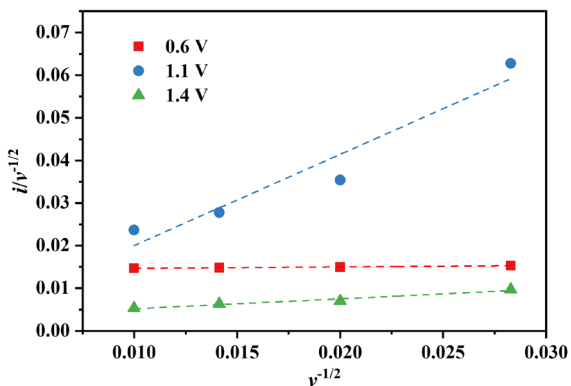


Fig. S10 Determination of contribution to the capacity. Plots of $v^{-1/2}$ vs. $i/v^{-1/2}$ for the ZnVW cathode material at potentials of 0.6, 1.1 and 1.4 V; the scan rate ranges from 0.1 to 0.8 mV s⁻¹ (Current data is from the CV curves).

Note: In CV curves, the peak current (i) is managed by both diffusion-controlled and capacitive contributions. They can be described by a power-law:[1]

$$i = a' v^{b'} \quad (1)$$

where a' and b' are adjustable parameters; v is scan rate. A b' value of 0.5 indicates that the reaction is controlled by a semi-infinite diffusion process, while a b' value of 1.0 indicates that it is dominated by a capacitive behavior. For ZnVF, the four peaks have fitted values of 0.47, 0.64, 0.51, and 0.56, respectively, reflecting that they follow diffusion-controlled kinetics. In contrast, the peaks for ZnVW are fitted to values of 0.85, 0.86, 0.66, and 0.67, indicating a contribution from both storage mechanisms. The following equation is used to quantitatively separate the contributions:[2]

$$i = k_1 v + k_2 v^{-1/2} \quad (2)$$

To estimate the k_1 and k_2 values, the points are taken for every 0.1 V. k_1 , the capacitive contribution factor, can be obtained as the slope of the linear relationship between $i/v^{-1/2}$ and $v^{-1/2}$ (Fig. S10).

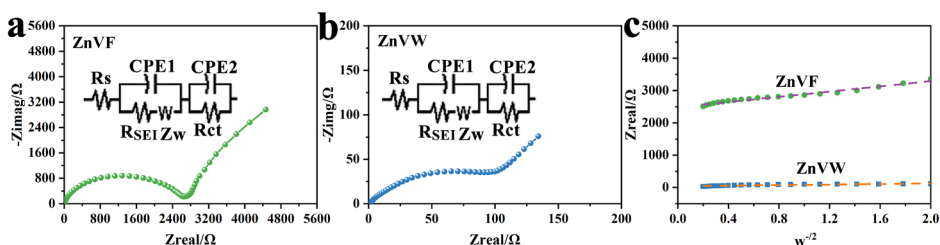


Fig. S11 EIS data. Nyquist plots for ZnVF (a) and ZnVW (b); Associated linear fitting of the square root of the Warburg impedance with real part Z (c). Inset of (a) and (b) are the equivalent circuits used in the data collection.

Note: EIS is performed at the open-circuit potential to study the faradic electron transfer resistance and the diffusion coefficient of ZnVF and ZnVW. The Nyquist plots consist of two regions: i) a semicircle in the high-frequency region, reflecting the cell component resistance and Faradic charge transfer resistance, and ii) a linear part in the low-frequency region, reflecting the resistance of the ion diffusion on the surface of the electrode, see Fig. S11. It can be observed that the resistance R_s of the cell component of the ZnVF and ZnVW are both around 10 Ω from the intercept with the x-axis. The charge transfer impedances (Rct), however, are about 2800 Ω and 100 Ω, respectively, suggesting fast kinetics of the Faradic reactions in ZnVW. The diffusion coefficient of the Zn^{2+} ion can be calculated by the following equations: [3]

$$Z_{\text{real}} = R_s + R_{\text{ct}} + A_w w^{-\frac{1}{2}} \quad (3)$$

where Z_{real} is the impedance collected during the experiment; A_w is the Warburg coefficient; w is the angular frequency; A is the surface area; V_m is the molar volume of the samples and dE/dx is the slope of the potential proportional to the concentration of ions. Therefore, the slope of the Z_{real} and $w^{-1/2}$ line reflects the ion diffusion coefficient A_w . ZnVW has a A_w of $42 \Omega \text{ s}^{-1/2}$; about 9 times lower than the value for ZnVF of $400 \Omega \text{ s}^{-1/2}$. Clearly, ZnVW exhibits a greatly increased ion conductivity during cycling.

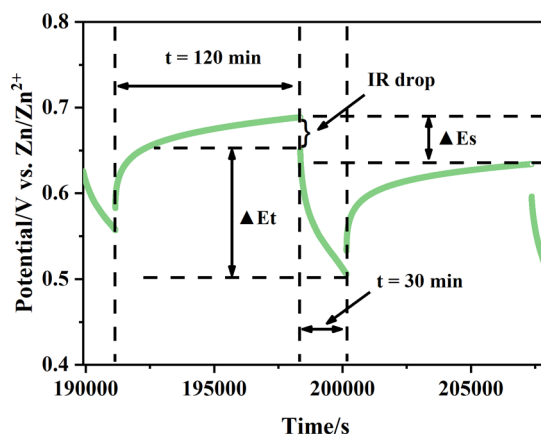


Fig. S12 GITT analysis. Measured potential response for ZnVW for a single step of a GITT experiment at a current density of 50 mA g^{-1} . (Ohmic voltage drop: IR drop)

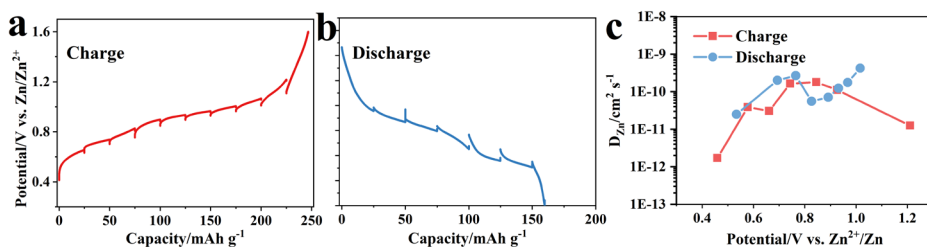


Fig. S13 GITT results. GITT curves and the calculated chemical diffusivity coefficient (D) versus the specific capacity for Zn^{2+} in ZnVW electrode.

Note: The specific Zn^{2+} ion diffusion coefficient value (D) is calculated from the galvanostatic intermittent titration technique (GITT), see Fig. S12. The analysis is based on the following equation:

$$D = \frac{4L^2}{\pi t} \left(\frac{\Delta E_s}{\Delta E_t} \right)^2 \quad (4)$$

where ‘L’ is the thickness of the mess loading on steel mesh; ‘t’ denotes the constant current pulse time; ‘ ΔE_s ’ is the change of the voltage during a single-step GITT experiment, and ‘ ΔE_t ’ is the voltage change during a constant pulse t. It is noted that the average D values at charge and discharge are in the range 10^{-11} - 10^{-10} cm² s⁻¹ (Fig. S13). This high value is ascribed to the exposed large lattice offering effective Zn²⁺ diffusion channels, suggesting a low Faradic electron transfer resistance and fast Zn²⁺ ion diffusion during the reactions.

References

- [1] H. Lindström, S. Södergren, A. Solbrand, H. Rensmo, J. Hjelm, A. Hagfeldt, S.-E. Lindquist, Li⁺ Ion Insertion in TiO₂ (Anatase). 2. Voltammetry on Nanoporous Films, *J. Phys. Chem. B* 101(39) (1997) 7717-7722.
- [2] V. Augustyn, J. Come, M.A. Lowe, J.W. Kim, P.-L. Taberna, S.H. Tolbert, H.D. Abruña, P. Simon, B. Dunn, High-rate electrochemical energy storage through Li⁺ intercalation pseudocapacitance, *Nat. Mater.* 12(6) (2013) 518-522.
- [3] J.G. Kim, S.H. Lee, Y. Kim, W.B. Kim, Fabrication of Free-Standing ZnMn₂O₄ Mesoscale Tubular Arrays for Lithium-Ion Anodes with Highly Reversible Lithium Storage Properties, *ACS Appl. Mater. Interfaces* 5(21) (2013) 11321-11328.

Chapter 7

$\text{V}_3\text{O}_7 \cdot \text{H}_2\text{O}$ nanobelts/rGO cathode for zinc-ion batteries

Chapter 6 describe the discovery of the decisive effect of the orientation on the Zn^{2+} ion storage properties: The electrode material which expose the large lattice spacings will exhibit a higher capacity than the one exposing small lattice spacings. Chapter 5 describes the discovery of how the carbon additive effectively improve the electrochemical performance. This knowledge is combined in this chapter, paper III, which describes the design of a layered-type vanadium oxide with large lattice spacings exposed on the surface, and reduced graphene oxide additive to improve the ionic and electronic conductivities. The capacity of the resulting material is superior to most of the published articles at high current density. More interestingly, a phase transition process is discovered and investigated. This provides a new insight into the energy storage mechanism of the vanadium oxides. All of the experiments, the analysis and writing of the manuscript were conducted by myself. The other co-authors provided suggestions and proof-read the manuscript.

This chapter is presented as a submitted manuscript titled “Electrochemically induced phase transition in $\text{V}_3\text{O}_7 \cdot \text{H}_2\text{O}$ nanowires/reduced graphene oxide composites for aqueous zinc-ion batteries” by Huili Cao, Zhiyong Zheng, Poul Norby, Xinxin Xiao, Susanne Mossin, which is currently under consideration for publication in the journal *Small* published by Wiley.

The article is given below:

Electrochemically induced phase transition in $V_3O_7 \cdot H_2O$ nanobelts/reduced graphene oxide composites for aqueous zinc-ion batteries

Huili Cao,^{a*} Dr. Zhiyong Zheng,^a Prof. Poul Norby,^b Dr. Xinxin Xiao,^{a*} and Prof. Susanne Mossin^{a*}

^aDepartment of Chemistry, Technical University of Denmark, 2800 Kgs. Lyngby, Denmark

^bDepartment of Energy Conversion and Storage, Technical University of Denmark, 2800 Kgs. Lyngby, Denmark

Email: hucao@kemi.dtu.dk (Huili Cao); xixiao@kemi.dtu.dk (Xinxin Xiao); slmo@kemi.dtu.dk (Susanne Mossin)

Keywords: Microwave-assisted; $V_3O_7 \cdot H_2O$ nanobelt; reduced graphene oxide; phase transition; zinc-ion battery.

$V_3O_7 \cdot H_2O$ nanobelts/reduced graphene oxide (rGO) composites (weight ratio: 86%/14%) are synthesized by a microwave approach with a high yield (85%) through controlling pH utilizing acids. The growth mechanisms of the highly crystalline nanobelts (average diameter: 25 nm; length: ca. 20 μm ; oriented along the [101] direction) have been thoroughly investigated, with the governing role of the acid upon the morphology and oxidation state of vanadium disclosed. When used as the ZIB cathode, the composite can deliver a high specific capacity of 410.7 and 385.7 mAh g⁻¹ at the current density of 0.5 and 4 A g⁻¹, respectively, with a high retention of the capacity of 93%. The capacity of the composite is greater than those of $V_3O_7 \cdot H_2O$, V_2O_5 nanobelts, and $V_5O_{12} \cdot 6H_2O$ film. Zinc ion storage in $V_3O_7 \cdot H_2O$ /rGO is mainly a pseudocapacitive behavior rather than ion diffusion. The presence of rGO enables outstanding cycling stability up to 1000 cycles with a capacity retention of 99.6%. Extended cycling shows a gradual phase transition, *i.e.*, from the original orthorhombic $V_3O_7 \cdot H_2O$ to a stable hexagonal $Zn_3(VO_4)_2(H_2O)_{2.93}$ phase, which is a new electrochemical route found in V_3O_7 materials. This phase transition process provides new insight into the reactions of aqueous ZIBs.

1. Introduction

Lithium-ion batteries (LIBs) are commercially successful due to the high energy density and low self-discharge. However, lithium dendrite formation, high activity of the metallic lithium and the toxicity of the organic electrolytes cause safety and environmental concerns.[1] Alternatively, rechargeable multivalent ion batteries with earth-abundant elements (Mg, Al, Zn, etc.) are emerging. Among them, zinc-ion batteries (ZIBs) exhibit unique advantages: i) the aqueous electrolyte is either pH neutral or mildly acidic with a high ionic conductivity; ii) the zinc anode has a quite negative redox potential (-0.78 V vs. standard hydrogen electrode), leading to a high battery voltage ($0.7\text{-}2.0 \text{ V}$)[2] and a considerable theoretical specific capacity of 820 mA g^{-1} . [3] However, hydrated Zn^{2+} cation has a large radius of 0.43 nm and exhibits sluggish transport kinetics in the active cathode materials, resulting in insufficient rate performance and low coulombic efficiency.[4] It is thus an urgent task to find a suitable cathode material with favourable capacity and stable structure during Zn^{2+} insertion and desertion. To date, the cathode materials of ZIBs can be divided into two categories: tunnel-type and layer-type structure.[5]

Multivalent manganese- and vanadium-based materials are promising cathode candidates.[6] A range of oxidation states of the metal are involved. The well-characterized MnO_2 undergoes stepwise reduction in battery reactions (*i.e.*, $2\text{Mn(IV)O}_2 + \text{Zn}^{2+} + 2\text{e}^- \rightleftharpoons \text{ZnMn(III)}_2\text{O}_4$; $\text{ZnMn(III)}_2\text{O}_4 + \text{Zn}^{2+} + 2\text{e}^- \rightleftharpoons 2\text{ZnMn(II)O}_2$).[7] The stepwise reduction is accompanied with phase transition. Tunnel-type MnO_2 (α - MnO_2 , β - MnO_2 , and γ - MnO_2) transforms into layered Zn-birnessite (Zn_xMnO_2) upon Zn^{2+} insertion. Layered-type δ - MnO_2 and spinel MnO_2 retain the same crystal structure during the insertion process. In comparison to MnO_2 , vanadium-based materials have more oxidation states and crystal types, thus the insertion processes are even more complicated. Taking V_2O_5 as an example, the cathode reactions can be summarized as: $\text{V(V)}_2\text{O}_5 + \text{Zn}^{2+} + 2\text{e}^- \rightleftharpoons \text{ZnV(IV)}_2\text{O}_5$ or $\text{V(V)}_2\text{O}_5 + 2\text{Zn}^{2+} + 4\text{e}^- \rightleftharpoons \text{Zn}_2\text{V(III)}_2\text{O}_5$, [7] corresponding to different theoretical capacities. To date, there are only a few reports disclosing phase transformation in V-based ZIB cathodes: Yang et al.[8] observed the formation of hexagonal $\text{Zn}_3(\text{OH})_2\text{V}_2\text{O}_7 \cdot 2\text{H}_2\text{O}$ among the orthorhombic V_2O_5 phase in the initial discharging cycle. The transformation was irreversible and barely contributed to the capacity in the following cycles. Recent reports only investigated the gradual phase change of V-based ZIB cathode for the initial several charge/discharge cycles,[9] using either *in situ* or *ex situ* characterizations. The gradual changes in the crystal phase during

long-term cycles have not been investigated throughout, which are possibly responsible for the poor cycling performance of the cathode materials. It's proposed that i) the development of stable vanadium oxide based ZIB cathodes that can withstand long-term operation and ii) the detailed investigations of the phase transition during extended cycling which is one of key for making a significant progress for ZIB.

$V_3O_7 \cdot H_2O$ has a two-dimension crystal structure and a high capacity, and thus is a good candidate for the investigation. It is composed of layers of corner-sharing VO_6 octahedra and VO_5 square pyramids, where the layers interact through hydrogen bonding to the crystal water molecule, providing the position for the insertion and desorption of Zn^{2+} . [10] Furthermore, the presence of two oxidation states of vanadium (V^{4+}/V^{5+}) in $V_3O_7 \cdot H_2O$ improves the electronic conductivity compared to vanadium oxides with only one oxidation state, [11] due to the narrower bandgap (e.g. 2.0 eV for V_2O_5 ; 1.0 eV for V_3O_7). Most of the reported $V_3O_7 \cdot H_2O$ materials rely on a time-consuming hydrothermal process taking days, [12] posing the demand for more efficient fabrication methods.

A fast and energy-efficient synthesis allows the scale-up of production. Microwave-assisted heating is considered to be very efficient and energy-saving compared to traditional hydrothermal methods. [13] Herein, a high-yield one-step synthesis of $V_3O_7 \cdot H_2O$ and $V_3O_7 \cdot H_2O$ nanobelts/rGO composites by a microwave-assisted method is presented. *Ex situ* investigations are applied to monitor the morphological evolution with time. $V_3O_7 \cdot H_2O$ nanobelts/rGO composite exhibited an ultra-long cycle life (99.6% capacity retention after 1000 cycles) in a potential range of 0.2-1.6 V vs. Zn^{2+}/Zn , making it possible to investigate the phase transition systematically. Cyclic voltammetry (CV), *ex situ* x-ray diffraction (XRD) and X-ray photoelectron spectroscopy (XPS) characterization have been applied towards this purpose.

2. Results and discussion

2.1. Characterizations of $V_3O_7 \cdot H_2O$ nanobelts and $V_3O_7 \cdot H_2O$ /rGO composites

The $V_3O_7 \cdot H_2O$ nanobelts and $V_3O_7 \cdot H_2O$ /rGO composites are synthesized through a microwave-assisted hydrothermal method by controlling pH with added acid (Figure S1). The reaction is maintained at 180 °C (Figure S1a). The morphology of the as-prepared products has been investigated by scanning electron microscope (SEM), atomic force microscope (AFM), and transmission electron microscope (TEM), see Figure 1. The as-prepared pure vanadium oxide exhibits a uniform nanobelt structure with a length of up

to 20 μm in the SEM image (Figure 1a), and the mean width of the nanobelts is determined to be about 35 nm by TEM (Figure 1b). The strands are well-dispersed from each other. The typical thickness of the nanobelts is 20 nm measured by AFM (Figure 1c). The high resolution TEM (HR-TEM) image reveals the detail of the nanostructure. The nanobelts are highly crystalline, displaying lattice fringes with an interplanar spacing of ~ 0.36 nm corresponding to the (230) lattice planes of $V_3O_7 \cdot H_2O$ (Figure 1d) (ICOD: 00-028-1433).

During the fabrication process, graphene oxide (GO) is introduced to obtain a composite of vanadium oxide/reduced GO (rGO). The vanadium oxide is anchored on the surface of the rGO while retains the nanobelt morphology and the same dimensional features (Figure 1e). The HR-TEM image shows two interplanar spacings with an angle of $\sim 70^\circ$ with respect to each other (Figure 1f). The smaller interplanar spacing (0.36 nm) is indexed to be (230) and the other (0.85 nm) is (020), suggesting that the nanobelts are oriented along the [101] direction (*b*-axis oriented).

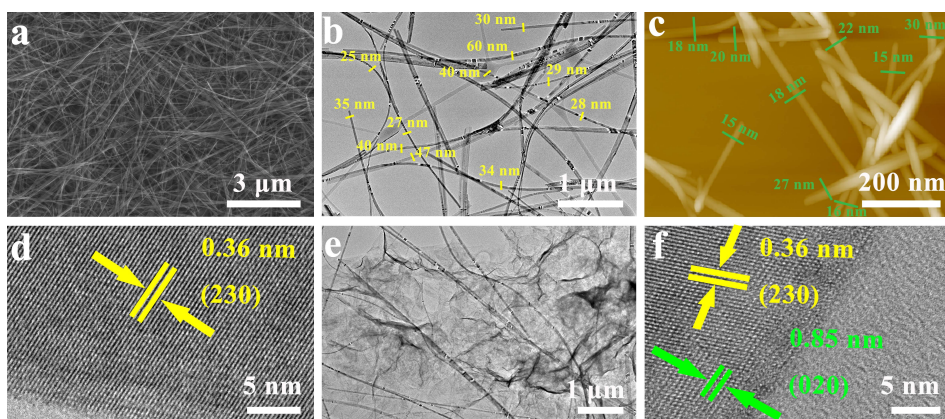


Figure 1 SEM (a), TEM (b), AFM (c), and HR-TEM images (d) of $V_3O_7 \cdot H_2O$ nanobelts. TEM (e) and HR-TEM (f) image of $V_3O_7 \cdot H_2O$ /rGO composite.

The typical XRD patterns of the $V_3O_7 \cdot H_2O$ nanobelts and $V_3O_7 \cdot H_2O$ /rGO have been characterized (Figure S2a). The pure nanobelts sample exhibits sharp peaks demonstrating high crystallinity, in consistency with the HR-TEM observation in Figure 1d. All peaks are in good agreement with the orthorhombic structure of $V_3O_7 \cdot H_2O$ (ICOD: 00-028-1433, $a = 9.34$ Å, $b = 17.00$ Å, $c = 3.62$ Å, $\alpha = \beta = \gamma = 90^\circ$). The peak at $2\theta = 24.7^\circ$ is assigned to (230) planes, as also observed in HR-TEM. $V_3O_7 \cdot H_2O$ /rGO presents all the characteristic peaks of the $V_3O_7 \cdot H_2O$ phase and an additional peak at $20-25^\circ$

corresponding to the (002) plane of disordered rGO nanosheets,[14] confirming again the successful preparation of the designed composite.

Thermogravimetric analysis (TGA) is performed to determine the weight ratio of rGO in the composites by increasing the temperature from 25 to 600 °C in a flow of air (Figure S2b and c). The TGA curve of $V_3O_7 \cdot H_2O$ shows a slight weight loss of ca. 2.5% at below 200 °C (Figure S2b), assigned to the release of adsorbed H_2O . [15] The weight loss of about 4.0% between 200 and 400 °C is due to the joint consequence of the crystal water loss in the $V_3O_7 \cdot H_2O$ precursor and the weight gain due to the oxidation from V_3O_7 to V_2O_5 . $V_3O_7 \cdot H_2O/rGO$ exhibits a relative weight loss of 24% between 200 and 400 °C, with ca. 14% of the rGO decomposition, which is in consistency with the feed ratio for the synthesis.

As another important benchmark material, V_2O_5 is obtained by calcining $V_3O_7 \cdot H_2O$ nanobelts in air using a temperature ramp of 5 °C min⁻¹ to 500 °C and maintaining 2 h at 500 °C. The nanobelts expand so that the diameter increases to 50-200 nm due to calcination-induced ripening, see Figure S3a. HR-TEM presents a typical lattice fringe spacing of around 0.58 nm, corresponding to the (020) crystal plane of V_2O_5 (Figure S3b). XRD further confirms the phase purity of orthorhombic V_2O_5 (Figure S3c) (COD: 01-085-0601).

2.2. Mechanism of the $V_3O_7 \cdot H_2O$ nanobelt formation

The $V_3O_7 \cdot H_2O$ nanobelts are produced via a facile one-step microwave treatment of $VOSO_4 \cdot xH_2O$ at acidic conditions. To investigate the governing factors for the formation of nanobelt morphology, control experiments have been carried out by varying the time and the identity of the acid used for the synthesis. First, the evolution in morphology with time is examined. As shown in Figure 2a, the product obtained after 10 min microwave reaction shows a cubic structure consisting of sheets with an average size of 1 μm . The HR-TEM image shows sheets of uniform thickness with edges gradually rolling into nanobelts with poor crystallinity (Figure S4). The interplanar spacing of sheets is determined to be 0.36 nm corresponding to the (230) planes of the $V_3O_7 \cdot H_2O$ (Figure S4a). After 60 min of reaction (Figure 2b), the cubic structure is stretched into sheets and the nanobelts become more obvious. HR-TEM further confirms that the $V_3O_7 \cdot H_2O$ nanobelts grow along the b-axis. Extending the reaction time to 80 min, more nanobelts are formed and the boundaries of the sheet are shrinking into a needle-like morphology (Figure 2c).

The final products, i.e., $\text{V}_3\text{O}_7 \cdot \text{H}_2\text{O}$ nanobelts with a length of 20 μm , are obtained after 120 min of reaction (Figure 1b).

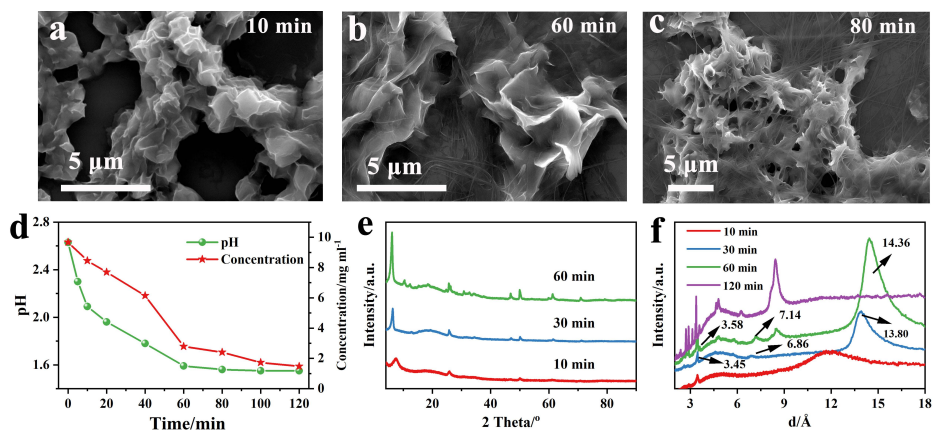
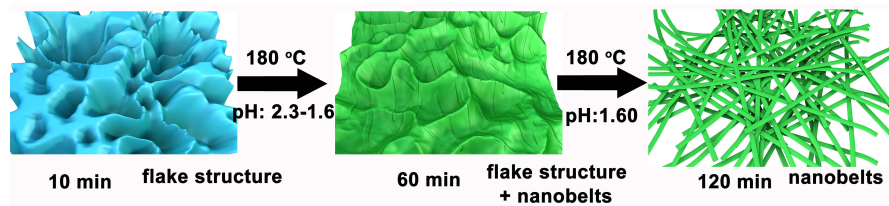


Figure 2 SEM images of $\text{V}_3\text{O}_7 \cdot \text{H}_2\text{O}$ obtained at 10 (a), 60 (b) and 80 min (c); time profiles (d) of the corresponding VO_2^+ concentration and pH; XRD patterns (e) of the product at 30 and 60 min and (f) converted XRD patterns obtained from Fullprof software.

Using *ex-situ* UV-Vis spectroscopy of the supernatant, it is straightforward to monitor the reaction due to the prominent d-d transitions of oxidovanadium(IV), VO^{2+} in the 760–780 nm range (Figure S5).^[16] The absorbance of VO^{2+} decreases as the reaction proceeded (Figure S5a). The initial 40 min shows a consumption rate of VO^{2+} of about 0.08 mg min^{-1} , as referred to the standard calibration curve in Figure S5c. The reaction rate is doubled in the following 20 min, whereas the final 60 min shows a rather slow reaction with $[\text{VO}^{2+}]$ concentration being almost constant. The pH decreases steadily and stabilized at 1.60 in the final stage (Figure 2d). Up to 85% of the initially fed vanadium is converted into the final product, implying that the microwave-assisted synthesis is a high yield method.

XRD is applied to investigate the phase transition (Figure 2e). The crystallinity increases with the reaction time. Most of the prominent peaks can be assigned to $\text{V}_3\text{O}_7 \cdot \text{H}_2\text{O}$ (ICOD: 00-028-1433). To precisely identify the $\text{V}_3\text{O}_7 \cdot \text{H}_2\text{O}$ phase, converted XRD patterns associated with lattice space are obtained using Fullprof software (Figure 2f).^[17] The analysis shows that the peaks at 3.45, 6.86 and 13.80 nm in the sample obtained at 30 min are due to the layer structure. After 60 min of reaction, the $\text{V}_3\text{O}_7 \cdot \text{H}_2\text{O}$ phase is dominant and the interlayer spacing increased to 3.58, 7.14 and 14.36 nm. After 2 h of reaction, the peaks due to the layer structure disappeared. Scheme 1 illustrates the suggest nanobelt formation mechanism, where 2D sheets are obtained in the beginning,

forming nanobelts while growing. As the reaction proceeds, the vanadium in solution is nearly depleted, and pH drops and stabilizes at about 1.60. The suggested formation process of the $V_3O_7 \cdot H_2O$ nanobelt morphology is illustrated in Scheme 1.



Scheme 1 Diagram illustrating the formation process of $V_3O_7 \cdot H_2O$ nanobelts.

Based on the above *ex situ* investigation, the mechanism of $V_3O_7 \cdot H_2O$ nanobelt formation *via* microwave treatment can be summarized as:



VO^{2+} is oxidized by O_2 in the atmosphere at high temperature, which produces H^+ and thus reduces pH. The presence of O_2 during the hydrothermal reaction is often necessary to obtain metal oxides with high oxidation states.[18] This assumption is validated by the control experiment showing that the reaction is hindered without O_2 (Figure S6). It is also hindered when the initial pH is lower than 1.8, regardless of the atmosphere (Figure S7).

The identity of the acid is also a key factor. Control experiments (Figure S8) with the addition of HCl, CH_3COOH (HAc) and H_2SO_4 resulted in dark cyan suspensions, while the addition of HNO_3 leads to a dark brown suspension. The sample fabricated without the addition of any acids (initial pH = 3.0) presents nanobelt morphology, but with a wide range of diameter distribution and large particles with a size of 10 μm . When the pH is controlled by HAc and HCl, more uniform and longer nanobelts are obtained (Figure S9b and c). In comparison, the use of HNO_3 results in a pure film structure (Figure S9d).

XPS analysis of different acid-derived samples is applied for a detailed understand the effect of acid on the chemical composition and oxidation state of vanadium. The survey spectra of all the samples found three main elements (V, O, and C) present (Figure 3a). The high-resolution spectra of V2p and O1s show that the samples obtained with HAc, H_2SO_4 , HCl have similar V2p peaks (Figure 3b). Taking H_2SO_4 as a representative, the peaks at 517.2 and 525.0 eV are assigned to V2p_{2/3} and V2p_{1/3} from V^{5+} , with a peak separation of about 7.8 eV.[19] The peaks at 515.7 and 523.5 eV are assigned to V^{4+}

(Figure 3c).[20] In contrast, the HNO_3 derived sample and V_2O_5 (Figure 3b) both display strong peaks at 517.2 and 525.0 eV assigned to V^{5+} and only very weak peaks assigned to V^{4+} , suggesting the majority of the vanadium are in the oxidation state +5.[21]

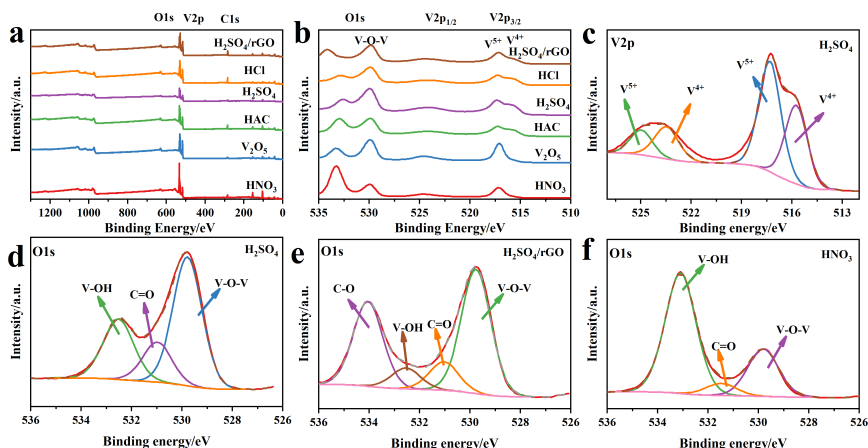


Figure 3 XPS survey spectra (a), O1s, and V2p spectra (b) of all samples; high-resolution V2p spectrum (c) and (d) O1s spectrum of the H_2SO_4 derived sample. O1s spectrum of the $V_3O_7 \cdot H_2O$ /rGO composite (e) and the HNO_3 derived sample (f).

Based on the O1s spectra, the samples can be divided into three categories. The samples obtained with strong acids, HCl, and H_2SO_4 , presents peaks at 529.8, 531.0 and 532.5 eV after deconvolution corresponding to V-O-V, C=O and V-OH, respectively.[22] The C=O peak might originate from CO_2 , and V-OH is from the crystal water in the product and from moisture. For the $V_3O_7 \cdot H_2O$ /rGO composite (Figure 3e), there is an additional peak at 534.0 eV,[23] which is assigned to C-O. The weak acid HAC leads to the sample with a stronger O1s peak from V-OH compared to the strong acid-derived samples (Figure 3b and f). For the samples derived from V_2O_5 or HNO_3 , the V-OH peak shifts to a higher binding energy, *i.e.*, from 532.5 to 533.1 eV. This observation might be related to the crystal water, especially in the film structure present in the HNO_3 derived sample. The presence of a strong hydroxyl signal in the product is also reported in other film structure materials.[24]

X-ray diffraction is applied to identify the crystal structure and phase purity of the as-prepared samples. All peaks of the samples derived from H_2SO_4 , HAC, or HCl are indexed to be $V_3O_7 \cdot H_2O$ (ICOD: 00-028-1433) (Figure S10a). In contrast, the diffraction patterns of the HNO_3 derived product are indexed to be the monoclinic phase of $V_5O_{12} \cdot 6H_2O$ (JCPDS 45-1401) with C2/m(12) space group (Figure S10b). The strongest peak is at $2\theta =$

7.5°, corresponding to the (001) plane. $V_5O_{12} \cdot 6H_2O$ has 4 out of 5 vanadium in oxidation state +5, suggesting that the oxidizing property of HNO_3 affects the vanadium oxidation states and thus the phase formation.

2.3. Electrochemical performance of $V_3O_7 \cdot H_2O$ /rGO and $V_3O_7 \cdot H_2O$ nanobelt

The electrochemical properties of the as-prepared $V_3O_7 \cdot H_2O$ and $V_3O_7 \cdot H_2O$ /rGO nanobelts are investigated by cyclic voltammetry (CV) at a scan rate of 0.1 mV s^{-1} in a voltage window of 0.2-1.6 V. The first cycle of $V_3O_7 \cdot H_2O$ shows much broad peaks, which gradually disappears in the following cycle. It might be due to either an initial activation process of the fresh electrolyte or a phase transition similar to that found in LIBs (Figure 4a and S11). [25] To explore the reactions in pure $V_3O_7 \cdot H_2O$, a narrow potential range of 0.4-1.1 V is used for following test, see Figure S11c. There are two main pairs of redox peaks (0.76/0.87 V and 0.51/0.61 V) for $V_3O_7 \cdot H_2O$, demonstrating a multi-step insertion/desertion mechanism. [26] The curves also confirms that the voltage window of 0.4-1.1 V (vs. Zn/Zn^{2+}) for $V_3O_7 \cdot H_2O$ nanobelts is suitable. In sharp comparison, the initial cycle of $V_3O_7 \cdot H_2O$ /rGO, however, well overlaps with the subsequent cycles. Additional peaks can be observed at 0.96/1.04 V, 0.88/0.98 V, 0.72/0.81 V and 0.35/0.58 V in $V_3O_7 \cdot H_2O$ /rGO. These peaks are well known in pure V_2O_5 and VO_2 structures. [8, 27] In comparison to $V_3O_7 \cdot H_2O$, $V_3O_7 \cdot H_2O$ /rGO composites exhibit more peaks, which are indicative of the importance of rGO for attracting more Zn^{2+} ions to (de)insertion in the host structure.

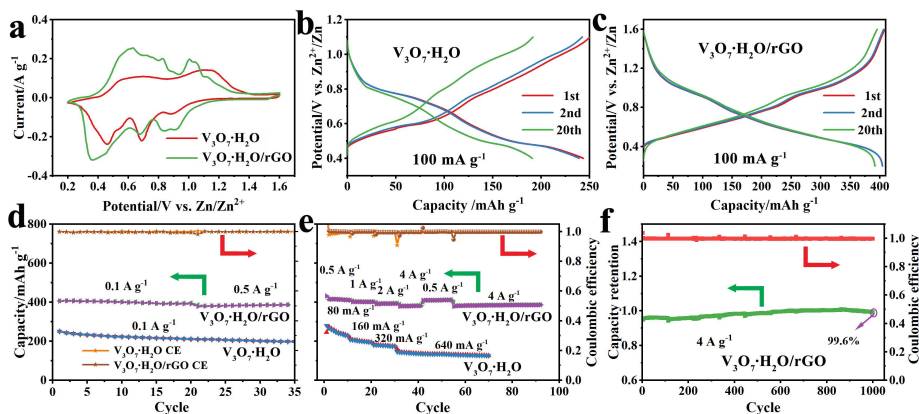


Figure 4 Initial CV curves (a) of $V_3O_7 \cdot H_2O$ and $V_3O_7 \cdot H_2O$ /rGO at a scan rate of 0.1 mV s^{-1} ; galvanostatic charge/discharge profiles of $V_3O_7 \cdot H_2O$ (b), and $V_3O_7 \cdot H_2O$ /rGO (c) at a current density of 100 mA g^{-1} ; cycling performance (d) and rate capability (e) of the $V_3O_7 \cdot H_2O$ and $V_3O_7 \cdot H_2O$ /rGO; long-term cycling performance (f) of the $V_3O_7 \cdot H_2O$ /rGO at a current density of 4 A g^{-1} .

To investigate the electrochemical stability and capacity retention, the performance and coulombic efficiency of $\text{V}_3\text{O}_7 \cdot \text{H}_2\text{O}$ and $\text{V}_3\text{O}_7 \cdot \text{H}_2\text{O}/\text{rGO}$ are tested during extended cycling. $\text{V}_3\text{O}_7 \cdot \text{H}_2\text{O}$ shows an initial discharge capacity of 243.6 mAh g^{-1} with a coulombic efficiency of 97.2%. Two obvious repeatable voltage plateaus are found in the potential range of 0.9–0.7 V and 0.4–0.6 V, corresponding to the redox peaks of the CV curves (Figure 4a). The specific capacity of $\text{V}_3\text{O}_7 \cdot \text{H}_2\text{O}$ decreases to 210.9 mAh g^{-1} after 20 cycles at 100 mA g^{-1} (86.6% retention), which further gradually decreases to 198.8 mAh g^{-1} at 35 cycles (Figure 4d). The degradation of capacity is likely due to the structure change upon Zn^{2+} insertion and consequent lattice distortion and loss of active sites.[28] In comparison, $\text{V}_3\text{O}_7 \cdot \text{H}_2\text{O}/\text{rGO}$ exhibits a much higher initial capacity of 404.7 mAh g^{-1} with a coulombic efficiency of 99.0% (Figure 4c). In the subsequent cycles, the charge-discharge profiles are almost identical, with a specific capacity of 391.9 mAh g^{-1} (96.8% retention) after 20 cycles. At a high current density of 500 mA g^{-1} (Figure 4d), $\text{V}_3\text{O}_7 \cdot \text{H}_2\text{O}/\text{rGO}$ still delivers a high specific capacity of 386 mAh g^{-1} with a retention ratio of 95.3% of the initial capacity, indicating excellent structural stability of the composite material. Additionally, the coulombic efficiency of both $\text{V}_3\text{O}_7 \cdot \text{H}_2\text{O}$ and $\text{V}_3\text{O}_7 \cdot \text{H}_2\text{O}/\text{rGO}$ are stabilized at approximately 100% during the cycling testing, suggesting a highly reversible reaction process. When applied $\text{V}_3\text{O}_7 \cdot \text{H}_2\text{O}$ cathode in the wide potential range of 0.2–1.6 V, the voltage plateaus disappear, and it only delivers ca. 100 mAh g^{-1} , compared to over 400 mAh g^{-1} with clear plateaus of $\text{V}_3\text{O}_7 \cdot \text{H}_2\text{O}/\text{rGO}$ (Figure S11d and e). After 20 cycles, the capacity decreases to a level of lower than 100 mAh g^{-1} .

The rate performance is given in Figure 4e. The discharge capacities of $\text{V}_3\text{O}_7 \cdot \text{H}_2\text{O}$ nanobelts are 227.3, 194.1, 173.9, and 126.1 mAh g^{-1} at current densities of 80, 160, 320, and 640 mA g^{-1} , respectively. The specific capacity shows a downward trend, and the capacity at 640 mA g^{-1} is only about 55% of that at 80 mA g^{-1} . Distinguishably, $\text{V}_3\text{O}_7 \cdot \text{H}_2\text{O}/\text{rGO}$ exhibits reversible capacities of 410.7, 401.1, 391.7, and 380.4 mAh g^{-1} at much higher current densities of 0.5, 1, 2, and 4 A g^{-1} , respectively. Impressively, the capacity is 411.5 mAh g^{-1} when the current density is returned to 0.5 A g^{-1} . Even upon a current density of 4 A g^{-1} , a considerable capacity of 385.7 mAh g^{-1} is registered. The retained capacity ratio is 94% when increasing the current density from 0.5 to 4 A g^{-1} . It is concluded that $\text{V}_3\text{O}_7 \cdot \text{H}_2\text{O}/\text{rGO}$ composites exhibit a highly stable structure during the significant current fluctuation, leading to a very stable performance during long-term

cycling (Figure 4f). The V₃O₇-H₂O/rGO composite shows a retained capacity of 99.6% and a coulombic efficiency at nearly 100% upon 1000 cycles at 4 A g⁻¹.

The electron transfer resistance of the active material interfaces is investigated by electrochemical impedance spectroscopy (EIS) at the open-circuit voltage before and after cycling testing (Figure S12). The Nyquist plots display two small semicircles in the high-frequency region and a straight line in the low-frequency region. The diameter of the semicircle reveals the charge-transfer impedance (R_{ct}) from anode and cathode, while the straight line at the low-frequency region is related to the Zn²⁺ diffusion process in the electrolyte. Before cycling, the R_{ct} of V₃O₇-H₂O is about 529 Ω, twice that of V₃O₇-H₂O/rGO. After cycling, V₃O₇-H₂O/rGO shows R_{ct} = 21.6 Ω, which is only ~10 % of that of V₃O₇-H₂O (206.3 Ω). The linear fitting of the Warburg impedance with the real part Z' shows that V₃O₇-H₂O/rGO has a small slope of the line before and after cycling, suggesting a low Warburg coefficient and a fast metal ion diffusion coefficient. Based on the Warburg coefficient, the zinc ion diffusion coefficient in the interfacial region, D, can be calculated using the following equations:[29]

$$D = \frac{R^2 T^2}{2(A n^2 F^2 C_{Zn} \sigma)^2} \quad (2)$$

$$Z_{re} = R_{ct} + R_s + \sigma \omega^{-0.5} \quad (3)$$

where R is the gas constant (8.314 J mol K⁻¹), T the temperature (298 K), A the surface area of the electrode (1.77 cm²), F the Faraday constant (96500 C mol⁻¹), C_{zn} the concentration of zinc ion (0.003 mol cm⁻³), and σ the Warburg factor obtained from Figure S12b. Thus, the zinc ion diffusion coefficient for V₃O₇-H₂O/rGO composite after cycling is calculated to be ca. 6.5×10⁻¹¹ cm² s⁻¹, about 100 times higher than that of pure V₃O₇-H₂O. It suggests that rGO can effectively enhance the kinetics of the electron transfer in electrodes and facilitate electrolytic infiltration and diffusion of Zn²⁺.

For comparison, the other as-prepared vanadium oxides (V₂O₅ nanobelts and V₅O₁₂·6H₂O film), as well as pure rGO, are investigated as ZIB cathodes (Figure S13). CV curves of V₂O₅ show multiple redox peaks, which become intensified after the initial cycle due to the trapped Zn²⁺ ions acting as interlayer pillars.[30] This matches well with the galvanostatic charge/discharge curves with increased capacity upon cycling. Specifically, the discharge capacity of the V₂O₅ nanobelts climbs from 36 to 286 mAh g⁻¹ after 30 cycles at 100 mA g⁻¹, implying that an activation process occurred during the first several

cycles.[31] The rate performance is poor with only 31% capacity retention when amplifying the current density from 100 to 800 mA g^{-1} . The coulombic efficiency is approximately 86% at 800 mA g^{-1} . The discharge voltage plateaus of the $\text{V}_5\text{O}_{12} \cdot 6\text{H}_2\text{O}$ film during the charge and discharge process are ca. 0.95 V and 0.42 V, corresponding well with the redox peaks in the CV curve (Figure S14a and b). Even after 20 cycles, the voltage plateaus are still obvious, revealing a high reversibility during the reaction process.[32] In the 50th cycle, the specific capacity at a current density of 100 mA g^{-1} is 46.3 mAh g^{-1} . The pure rGO material is obtained by the same microwave method, but without introducing VOSO_4 . There is no obvious voltage plateau in the charge-discharge curves, neither peak, in the CV curve (Figure S14d and e), suggesting that the dominant contribution to the capacity is from the electrochemical double layer. The specific capacity of pure rGO reaches 62.8 mAh g^{-1} (Figure S14f), 6.5 times lower than that of $\text{V}_3\text{O}_7 \cdot \text{H}_2\text{O}$ /rGO. These control experiments indicate that the mixed oxidation state of vanadium can help to overcome the sluggish Zn^{2+} diffusion kinetics and lead to a high coulombic efficiency. The electrochemical behaviors of the cathode are also possibly affected by the morphology and the amount of crystal water.[33]

$\text{V}_3\text{O}_7 \cdot \text{H}_2\text{O}$ /rGO also outperforms most reported vanadium oxide materials, see Table S1. Benchmark materials such as hollandite-type Al-doped $\text{VO}_{1.52}(\text{OH})_{0.77}$ obtained by solvothermal synthesis delivered 105 mAh g^{-1} at a current density of 0.015 A g^{-1} . [34] Freestanding graphene/ VO_2 composites, fabricated *via* freeze-drying, high-temperature reduction and subsequent mechanical compression, had a reversible capacity of 240 mAh g^{-1} at a current density of 4 A g^{-1} . [27] Ultrafine nanogrid-shaped layered $\text{V}_3\text{O}_7 \cdot \text{H}_2\text{O}$ arched on carbon synthesized by *in situ* electrochemical oxidation delivered 481.3 mAh g^{-1} at a current density of 0.1 A g^{-1} . The reversible capacity, however, decreased to 171.6 mAh g^{-1} at a high current density of 5 A g^{-1} . [35] In brief, the $\text{V}_3\text{O}_7 \cdot \text{H}_2\text{O}$ nanobelt/rGO composites are a promising high-performance ZIB cathode candidate, featuring fast electron transfer in the materials at high current densities.

2.4. Investigation of the reaction mechanism of $\text{V}_3\text{O}_7 \cdot \text{H}_2\text{O}$ /rGO cathode

The multiple redox reactions of vanadium with more feasible Zn^{2+} ion insertion is believed to be the reason for the considerable specific capacity. To distinguish the capacity current distribution from either diffusion or pseudocapacitance, CV is conducted at various scan rates from 0.1 to 0.8 mV s^{-1} (Figure 5a). It is noted that with increasing scan rate, the CV curves feature broader peaks but still maintain the similar shape. The relationship

between the peak current (i) and the scan rate (v) can be described by the following equation:

$$i = av^b \quad (4)$$

where 'b' is a parameter between 0.5 and 1. When the results are fitted using this equation and the resulting fitted 'b' parameter is close to 0.5, it is an indication that the process is dominated by ion diffusion; when 'b' approaches 1, the reaction is best characterized as a pseudocapacitance response.[36] Based on the fitting of $\log i$ vs $\log v$, the values of 'b' for the four main peaks can be calculated to be 0.99, 0.94, 0.88 and 0.86, respectively (Figure 5b). In addition, the reversible capacity contribution of the $V_3O_7 \cdot H_2O/rGO$ composite is further quantitatively evaluated according to the following equation:[37]

$$i = k_1 v + k_2 v^{1/2} \quad (5)$$

where 'k₁' and 'k₂' are constants, associated with the surface capacity contribution and diffusion faradic contribution, respectively. The capacity contribution gradually increases from 90% to 99% with scan rate in a range of 0.1-0.8 mV s⁻¹ (Figure S15), suggesting the dominant capacitive effect. The capacitive contribution of $V_3O_7 \cdot H_2O/rGO$ composite is much higher in comparison to other reported layered V-based cathodes, such as V_2O_5 /polyaniline,[38] $Mn_{0.15}V_2O_5 \cdot nH_2O$,[39] $(NH_4)_2V_4O_9$,[40] which might be due to the low electron transfer resistant and the fast diffusion coefficient in the electrode.

Very interestingly, it is found that the 11th CV curve shape obtained at 0.8 mV s⁻¹ differs from the previous cycles, seeing that the major cathodic peak shifts from 0.57 to 0.67 V and the minor peak at ca. 1.1 V disappear (Figure S16). The same changes are also visible at 0.1 mV s⁻¹. In addition, the shape of the forward scan (1.6 to 0.2 V) in the first cycle differed from the following scans and also from the one found in the literature for $V_3O_7 \cdot H_2O/rGO$. It can be concluded that, unlike the reported insertion mechanism for vanadium oxides,[41] a phase transition during operation is the most likely explanation for the observed CV characteristics of the $V_3O_7 \cdot H_2O/rGO$ electrode.

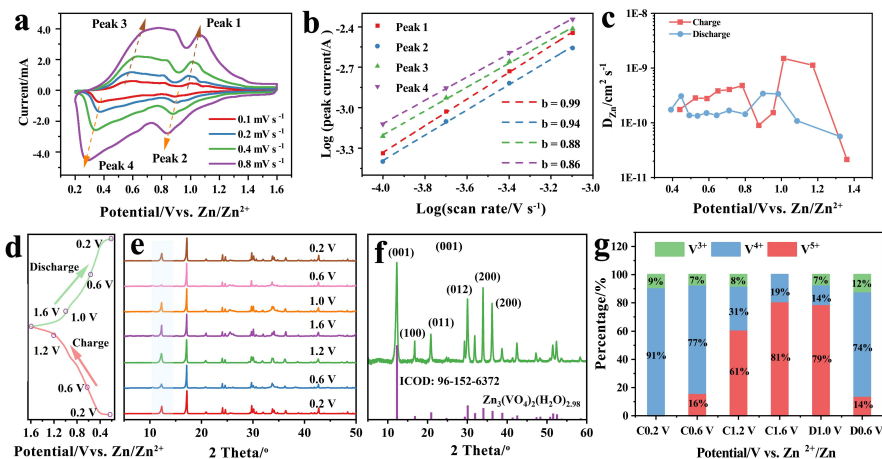


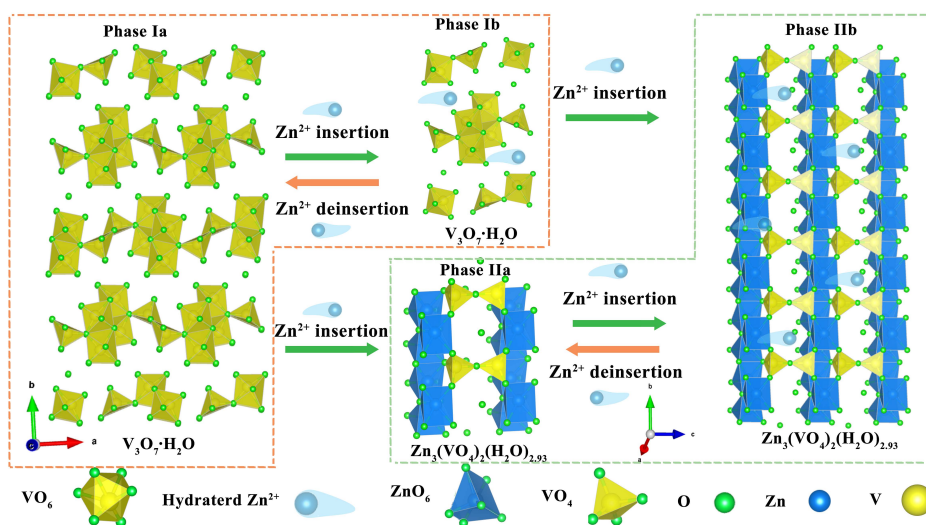
Figure 5 CVs of $\text{V}_3\text{O}_7 \cdot \text{H}_2\text{O}/\text{rGO}$ at different scan rates from 0.1 to 0.8 mV s^{-1} (a); $\log i$ vs. $\log v$ plots of the oxidation and reduction peaks of the electrode (b); Zn^{2+} coefficient of the $\text{V}_3\text{O}_7 \cdot \text{H}_2\text{O}/\text{rGO}$ cathode as a function of working potential during CD testing (c). ex situ XRD patterns of $\text{V}_3\text{O}_7 \cdot \text{H}_2\text{O}/\text{rGO}$ at different charge/discharge states of the 11th cycle (d, e); XRD patterns of $\text{V}_3\text{O}_7 \cdot \text{H}_2\text{O}/\text{rGO}$ after 1000 cycles (f). Oxidation state of vanadium in $\text{V}_3\text{O}_7 \cdot \text{H}_2\text{O}/\text{rGO}$ during the charge (C) and discharge process (D) at different voltages calculated from the V2p peak of the XPS spectra (g).

Ex situ XRD and XPS are employed to investigate this hypothesis further in Figure S17 and 18. For this investigation, a thin layer of 0.5 mg cm^{-2} of the active materials has been applied on the electrode to guarantee a full utilization. In comparison, 1.3 mg cm^{-2} is used for routine investigations. XRD patterns of $\text{V}_3\text{O}_7 \cdot \text{H}_2\text{O}/\text{rGO}$ are obtained at different discharge stages (1.0, 0.6 and 0.4 V) of the initial cathodic scan at 0.1 mV s^{-1} . Overall, the XRD peaks of $\text{V}_3\text{O}_7 \cdot \text{H}_2\text{O}$ transform from being sharp to broad, due to the collapse of the original structure and the formation of a new phase. Upon initial discharge to 1.0 V, the main peak at 10.4° , belonging to (020), disappears. Further discharging to 0.4 V, it results in the appearance of new peaks at 12.3° , 30.1° , and 36.5° corresponding to (001), (012), and (021) of hexagonal $\text{Zn}_3(\text{VO}_4)_2(\text{H}_2\text{O})_{2.93}$ ($a = b = 6.05 \text{ \AA}$, $c = 7.195 \text{ \AA}$, $\alpha = \beta = 90^\circ$, $\gamma = 120^\circ$, ICOD:96-152-6372). Those results confirm the phase transition during Zn^{2+} discharge/insertion. The associated XPS V2p spectrum shows that at 1.0 V, +5 is the dominant oxidation state of vanadium, see Figure S17a. Upon further discharged to lower potentials (0.6 and 0.4 V), the amount of V^{4+} and V^{3+} increases (Figure S18b and c), verifying the change in vanadium oxidation state in $\text{V}_3\text{O}_7 \cdot \text{H}_2\text{O}/\text{rGO}$ alongside the phase transition. The quantitative peak-fitting analysis of the V2p spectra from XPS show that the dominant V^{5+} decreases from 53% to 5% under a backward scan (from 1.0 to 0.4 V), corresponding to the insertion of about 0.5 mol Zn^{2+} into 1 mol $\text{V}_3\text{O}_7 \cdot \text{H}_2\text{O}$. The galvanostatic intermittent

titration technique (GITT, the detailed measurements are shown in SI, Figure S20) is also employed to calculate the Zn^{2+} ion diffusion coefficient in $\text{V}_3\text{O}_7\cdot\text{H}_2\text{O}/\text{rGO}$ composite (Figure 5c). It is noted that the diffusion coefficient of Zn^{2+} ion in the active material during the entire insertion and desertion process is in the range of 10^{-10} - 10^{-9} $\text{cm}^2 \text{s}^{-1}$, which is higher than the Zn^{2+} diffusion in other vanadium-based cathode materials.[42]

To understand the different CV features of the 11th charge/discharge cycle, *ex situ* XRD and XPS are applied. To obtain better XRD signals, an increased mass loading of the active materials (1.3 mg cm^{-2}) is employed at a current density of 50 mA g^{-1} . The 11th charge/discharge cycle is not connected, and an obvious shift of the XRD peaks at different charge/discharge status is observed, whereas the peak intensity at 12.3° corresponding to the (001) plane becomes stronger under the charging process. The latter is associated with insertion of Zn^{2+} (Figure 5e). The evolution in the oxidation state of vanadium during the charge and discharge process is also studied by *ex situ* XPS (Figure S19). In the Zn 2p region, the Zn 2p_{1/2} and Zn 2p_{3/2} peaks in the discharge state (0.2 V) are obvious, due to Zn^{2+} insertion. Upon charging, however, these two peaks are still present but with lower intensity, suggesting that residual zinc ions are present even after Zn^{2+} extraction. The V2p spectra at the fully discharged state (0.2 V) display a strong V^{4+} peak and a weak V^{3+} peak, suggesting a significant reduction of V_3O_7 . Upon recharge, the V^{5+} peaks appear and becomes gradually stronger, corresponding to the extraction of Zn^{2+} . The discharge process, on the other hand, shows the opposite trend, indicating that Zn^{2+} insertion and desertion in V_3O_7 are close to being reversible. The amount of vanadium in different oxidation states during the charge and discharge process is quantified by analyzing the V2p spectra (Figure 5g). By calculating the amount of Zn^{2+} ions inserted, there is about 1.4 mmol Zn^{2+} for each mol of $\text{V}_3\text{O}_7\cdot\text{H}_2\text{O}$ participating in the redox reactions. This corresponds to a high specific capacity of 265 mAh g^{-1} by only considering the contribution from the faradic capacity. It further confirms that the $\text{V}_3\text{O}_7\cdot\text{H}_2\text{O}/\text{rGO}$ for Zn^{2+} storage process is dominated by pseudocapacitive behavior rather than ion diffusion and the new phase of $\text{Zn}_3(\text{VO}_4)_2(\text{H}_2\text{O})_{2.93}$. It is likely due to the activation of the active materials and the reversible phase transition. The composition of crystalline phases in $\text{V}_3\text{O}_7\cdot\text{H}_2\text{O}/\text{rGO}$ is investigated after 1000 cycles. The initial orthorhombic $\text{V}_3\text{O}_7\cdot\text{H}_2\text{O}$ phase is transformed completely to a phase-pure hexagonal $\text{Zn}_3(\text{VO}_4)_2(\text{H}_2\text{O})_{2.93}$ (Figure 5f). This development is attributed to the presence of rGO, which enables a highly stable cycling performance.

Both of $\text{V}_3\text{O}_7 \cdot \text{H}_2\text{O}$ (phase I) before phase transition and $\text{Zn}_3(\text{VO}_4)_2(\text{H}_2\text{O})_{2.93}$ (phase II) after phase transition undergo the Zn^{2+} insertion mechanism without changing the crystal structure. A hypothesis for the Zn^{2+} insertion and desertion process in the host vanadium oxide cathode, which is in agreement with all results, are summarized in Scheme 2. In the initial discharge process, hydrated Zn^{2+} ions intercalate into the $\text{V}_3\text{O}_7 \cdot \text{H}_2\text{O}$ (phase Ia) structure layers forming phase Ib, and further discharge leads to a partial phase transition to $\text{Zn}_3(\text{VO}_4)_2(\text{H}_2\text{O})_{2.93}$ (phase IIa and b). During the initial charge process, reversible Zn^{2+} desertion takes place converting the phase Ib to phase Ia, and phase IIb is transformed back into the phase IIa. With extended cycling, more of the phase II forms, until the cycles are ultimately dominated by the reversible transition between the phase IIa and phase IIb. Such a new discovery of phase transition is unique, which promotes the understanding of underling mechanism of layered $\text{V}_3\text{O}_7 \cdot \text{H}_2\text{O}$ for long-term and stable cycling.



Scheme 2 Illustration of the phase transition during Zn^{2+} ion insertion and desertion. The conversion in the pink and green dash box governs the initial cycles and long-term cycling, respectively.

3. Conclusion

In summary, the combination of $\text{V}_3\text{O}_7 \cdot \text{H}_2\text{O}$ and rGO has been achieved by a facile microwave-assisted approach. For the preparation of $\text{V}_3\text{O}_7 \cdot \text{H}_2\text{O}$ nanobelts material, it is found that two-dimensional layered flakes form initially, which stretch into films and finally into nanobelts. This process is independent of the choice of acid for pH control as

long as the acid is not oxidizing. When applied as the cathode electrode of zinc-ion batteries, the $V_3O_7 \cdot H_2O$ /rGO composite exhibits a much better retention of capacity and rate performance, compared to pure $V_3O_7 \cdot H_2O$ nanobelts, V_2O_5 nanobelts, and $V_5O_{12} \cdot 6H_2O$ films. This is mainly due to the presence of rGO, which improves the electron transfer kinetics. The combination with rGO makes it possible to extend the cycling performance of $V_3O_7 \cdot H_2O$ up to 1000 cycles, leading to the identification of the gradual phase transition: from orthorhombic $V_3O_7 \cdot H_2O$ to hexagonal $Zn_3(VO_4)_2(H_2O)_{2.93}$. The final reversible phase transition between an intermediate phase and hexagonal $Zn_3(VO_4)_2(H_2O)_{2.93}$ paves the way for screening highly stable zinc vanadate ($Zn_3(VO_4)_2$).

4. Experimental Section

Chemicals: Potassium persulfate ($K_2S_2O_8$, 99%) was bought from Ferak. Graphite, phosphorous pentoxide (P_2O_5 , 98%), sulfuric acid (H_2SO_4 , 95%-97%), concentrated hydrochloric acid (HCl, 37% w/w, diluted to 1.0 M), 1-methyl-2-pyrrolidinone (C_5H_8NO , NMP, 99.5%), poly(vinylidene fluoride) (PVDF, $(CH_2CF_2)_n$, average MW $\sim 534,000$), vanadium oxide sulfate hydrate ($VOSO_4 \cdot xH_2O$, 97%), nitric acid, zinc trifluoromethanesulfonate ($Zn(CF_3SO_3)_2$, 98%), and zinc foil (thickness: 0.25 mm, 99.9%) were purchased from Sigma-Aldrich, Denmark. Potassium permanganate ($KMnO_4$, 99.9%) and hydrogen peroxide (H_2O_2 , 30 wt%) were bought from Merck. Potassium hydrogenphosphate (K_2HPO_4 , 99.99%) and carbon black (99.9%) were from Fluka. Steel meshes were obtained from Lizhiyuan Co., Ltd, China.

Synthesis of $V_3O_7 \cdot H_2O$ nanobelts/reduced GO: 0.5 mmol $VOSO_4 \cdot xH_2O$ was dissolved into 10 mL Milli-Q to form a clear blue solution, into which 0.1 M H_2SO_4 was added to adjust the pH to 2.6-2.7. After stirring for 2 h, 1 mL as-prepared GO solution (see supporting information) was added into the solution, which was sealed in a 35 mL microwave tube and heated up to 180 °C for 2 h in a Biotage® microwave reactor. The reaction parameters were monitored during the reaction. The as-synthesized product was collected by filtering and washed with Milli-Q water. For comparison, the pure vanadium oxide product was obtained using the same procedure without addition of GO. Besides H_2SO_4 , various acids including HCl, HAc, and HNO_3 were utilized during fabrication to investigate the effect of the added acid on the morphology of final product.

Characterization: The morphology of the materials was investigated by field emission scanning electron microscopy (FE-SEM) using a Quanta FEG 250 Analytical ESEM,

transmission electron microscopy (TEM, Tecnai T20 G2, 200 kV), and a 5500 atomic-force microscopy (AFM) system (Alignment Technology). The X-ray powder diffraction (XRD) patterns were obtained using a Huber instrument with a monochromatized Cu K α radiation of $\lambda=1.5406 \text{ \AA}$. Thermogravimetric analysis (TGA) was performed using a Thermogravimetric Analyzer (Mettler Toledo) to examine the weight percentage of rGO in the composite under an air atmosphere from room temperature to 700 °C with a ramping rate of 10 °C min⁻¹. UV-vis spectra were recorded on an Agilent 8453 (Santa Clara, CA) and X-ray photoelectron spectrometry (XPS) results were collected with a Thermo Scientific K-alpha spectrometer using Al K α radiation.

Electrochemical measurements: To prepare the working electrode, the steel mesh was coated by a homogenous slurry containing active material, carbon black, and PVDF in a weight ratio of 7:2:1. After that, the coated steel mesh was dried in a vacuum oven at 120 °C for 12 h. The zinc ion coin cells were assembled using active materials as the cathode, metallic zinc foil as the anode, 3 M $\text{Zn}(\text{CF}_3\text{SO}_3)_2$ as the electrolyte and glass microfiber filters as the separator. The mass loading (composite weight for the $\text{V}_3\text{O}_7 \cdot \text{H}_2\text{O}$ /rGO cathode) during the testing was in a range of 0.5-1.3 mg cm⁻². Electrochemical performance of the cell was evaluated *via* an Autolab potentiostat, including galvanostatic performance at various current densities, electrochemical impedance spectroscopy (EIS) at the open-circuit voltage in a frequency range of 0.01 Hz-100 kHz, and cyclic voltammetry (CV) in a potential range of 0.2-1.6 V at a scan rate of 0.1 mV s⁻¹.

Supporting Information

Supporting Information is available from the Wiley Online Library or from the author.

Acknowledgements

The financial support from the China Scholarship Council for a Ph.D. scholarship (No. 201706220078) to H. C. and a VILLUM Experiment (grant No. 35844) to X. X. is greatly acknowledged.

Received: ((will be filled in by the editorial staff))

Revised: ((will be filled in by the editorial staff))

Published online: ((will be filled in by the editorial staff))

References

-
1. J. Huang; Z. Wang; M. Hou; X. Dong; Y. Liu; Y. Wang; Y. Xia, *Nat. Commun.* **2018**, *9* (1), 2906.
 2. G. Fang; J. Zhou; A. Pan; S. Liang, *ACS Energy Lett.* **2018**, *3* (10), 2480-2501.
 3. K. Zhao; C. Wang; Y. Yu; M. Yan; Q. Wei; P. He; Y. Dong; Z. Zhang; X. Wang; L. Mai, *Adv. Mater. Interfaces* **2018**, *5* (16), 1800848.
 4. T. Wei; Q. Li; G. Yang; C. Wang, *J. Mater. Chem. A* **2018**, *6* (41), 20402-20410.
 5. a) K. Lu; B. Song; Y. Zhang; H. Ma; J. Zhang, *J. Mater. Chem. A* **2017**, *5* (45), 23628-23633; b) H. Qin; Z. Yang; L. Chen; X. Chen; L. Wang, *J. Mater. Chem. A* **2018**, *6* (46), 23757-23765.
 6. Y. Yang; Y. Tang; G. Fang; L. Shan; J. Guo; W. Zhang; C. Wang; L. Wang; J. Zhou; S. Liang, *Energy Environ. Sci.* **2018**, *11* (11), 3157-3162.
 7. J. Ming; J. Guo; C. Xia; W. Wang; H. N. Alshareef, *Mater. Sci. Eng. R Rep* **2019**, *135*, 58-84.
 8. Y. Yang; Y. Tang; S. Liang; Z. Wu; G. Fang; X. Cao; C. Wang; T. Lin; A. Pan; J. Zhou, *Nano Energy* **2019**, *61*, 617-625.
 9. a) P. Jing; W. Wei; W. Luo; X. Li; F. Xu; H. Li; M. Wei; D. Yu; Q. Zhu; G. Liu, *Inorg. Chem. Commun.* **2020**, *117*, 107953; b) H. Yan; Q. Ru; P. Gao; Z. Shi; Y. Gao; F. Chen; F. Chi-Chun Ling; L. Wei, *Appl. Surf. Sci.* **2020**, *534*, 147608; c) H. Chen; L. Chen; J. Meng; Z. Yang; J. Wu; Y. Rong; L. Deng; Y. Shi, *J. Power Sources* **2020**, *474*, 228569.
 10. H. Li; T. Zhai; P. He; Y. Wang; E. Hosono; H. Zhou, *J. Mater. Chem.* **2011**, *21* (6), 1780-1787.
 11. W. Duan; M. Zhao; Y. Li; N. u. R. Lashari; T. Xu; F. Wang; X. Song, *Energy Fuels* **2020**, *34* (3), 3877-3886.
 12. S. Gao; Z. Chen; M. Wei; K. Wei; H. Zhou, *Electrochim. Acta* **2009**, *54* (3), 1115-1118.
 13. W. Huang; X. Zheng; H. Shangguan; X. Xiao; J. Tang; H. Sun; K. Mølhave; L. Ci; P. Si; J. Zhang, *Appl. Surf. Sci.* **2020**, *525*, 146513.
 14. a) J. Zhong; F. Yi; A. Gao; D. Shu; Y. Huang; Z. Li; W. Zhu; C. He; T. Meng; S. Zhao, *ChemElectroChem* **2017**, *4* (5), 1088-1094; b) Z.-J. Zhang; Y.-X. Wang; S.-L. Chou; H.-J.

- Li; H.-K. Liu; J.-Z. Wang, *J. Power Sources* **2015**, *280*, 107-113; c) M. Darvishi; F. Jamali-Paghaleh; M. Jamali-Paghaleh; J. Seyed-Yazdi, *Surf. Interfaces* **2017**, *9*, 167-172.
15. C. M. Gilmour; C. D. K. Herd; P. Beck, *Meteorit. Planet. Sci.* **2019**, *54* (9), 1951-1972.
16. a) R. Gryboś; J. Szklarzewicz; A. Jurowska; M. Hodorowicz, *J. Mol. Struct.* **2018**, *1171*, 880-887; b) M. Le; O. Rathje; A. Levina; P. A. Lay, *JBIC J. Biol. Inorg. Chem.* **2017**, *22* (5), 663-672.
17. I. Kokal; M. Somer; P. H. L. Notten; H. T. Hintzen, *Solid State Ionics* **2011**, *185* (1), 42-46.
18. H. Cao; X. Wang; H. Gu; J. Liu; L. Luan; W. Liu; Y. Wang; Z. Guo, *RSC Adv.* **2015**, *5* (44), 34566-34571.
19. a) P. Vishnuprakash; C. Nithya; M. Premalatha, *Electrochim. Acta* **2019**, *309*, 234-241; b) G. Silversmit; D. Depla; H. Poelman; G. B. Marin; R. De Gryse, *J. Electron Spectrosc. Relat. Phenom.* **2004**, *135* (2), 167-175.
20. N. Alov; D. Kutsko; I. Spirovová; Z. Bastl, *Surf. Sci.* **2006**, *600* (8), 1628-1631.
21. C. Y. Foo; A. Sumboja; D. J. H. Tan; J. Wang; P. S. Lee, *Adv. Energy Mater.* **2014**, *4* (12), 1400236.
22. D. J. Ahirrao; K. Mohanapriya; N. Jha, *Mater. Res. Bull.* **2018**, *108*, 73-82.
23. D. Pham-Cong; K. Ahn; S. W. Hong; S. Y. Jeong; J. H. Choi; C. H. Doh; J. S. Jin; E. D. Jeong; C. R. Cho, *Curr. Appl. Phys.* **2014**, *14* (2), 215-221.
24. a) J. Lv; Q. Zhu; Z. Zeng; M. Zhang; J. Yang; M. Zhao; W. Wang; Y. Cheng; G. He; Z. Sun, *J. Phys. Chem. Solids* **2017**, *111*, 104-109; b) M. S. Abdel-wahab; A. Jilani; I. S. Yahia; A. A. Al-Ghamdi, *Superlattices Microstruct.* **2016**, *94*, 108-118.
25. T. Liu; W. Wang; M. Yi; Q. Chen; C. Xu; D. Cai; H. Zhan, *Chem. Eng. J.* **2018**, *354*, 454-462.
26. a) J. Ding; Z. Du; L. Gu; B. Li; L. Wang; S. Wang; Y. Gong; S. Yang, *Adv. Mater.* **2018**, *30* (26), 1800762; b) P. He; Y. Quan; X. Xu; M. Yan; W. Yang; Q. An; L. He; L. Mai, *Small* **2017**, *13* (47), 1702551.
27. X. Dai; F. Wan; L. Zhang; H. Cao; Z. Niu, *Energy Storage Mater.* **2019**, *17*, 143-150.

-
28. G. Li; Z. Yang; Y. Jiang; C. Jin; W. Huang; X. Ding; Y. Huang, *Nano Energy* **2016**, *25*, 211-217.
29. a) P. Yang; C. Feng; Y. Liu; T. Cheng; X. Yang; H. Liu; K. Liu; H. J. Fan, *Adv. Energy Mater.* **2020**, *10* (48), 2002898; b) Y. Cai; R. Chua; S. Huang; H. Ren; M. Srinivasan, *Chem. Eng. J.* **2020**, *396*, 125221; c) T. Sun; Q. Nian; S. Zheng; J. Shi; Z. Tao, *Small* **2020**, *16* (17), 2000597.
30. J. Zhou; L. Shan; Z. Wu; X. Guo; G. Fang; S. Liang, *Chem. Commun. (Cambridge, U. K.)* **2018**, *54* (35), 4457-4460.
31. H. Qin; L. Chen; L. Wang; X. Chen; Z. Yang, *Electrochim. Acta* **2019**, *306*, 307-316.
32. H. Yan; Q. Ru; P. Gao; S. Cheng; F. Chen; F. C.-C. Ling; L. Wei, *Energy Technol.* **2020**, *8* (3), 1901105.
33. J. Lai; H. Zhu; X. Zhu; H. Koritala; Y. Wang, *ACS Appl. Energy Mater.* **2019**, *2* (3), 1988-1996.
34. J. H. Jo; Y.-K. Sun; S.-T. Myung, *J. Mater. Chem. A* **2017**, *5* (18), 8367-8375.
35. Q. Pang; C. Sun; Y. Yu; K. Zhao; Z. Zhang; P. M. Voyles; G. Chen; Y. Wei; X. Wang, *Adv. Energy Mater.* **2018**, *8* (19), 1800144.
36. H.-S. Kim; J. B. Cook; H. Lin; Jesse S. Ko; Sarah H. Tolbert; V. Ozolins; B. Dunn, *Nat. Mater.* **2017**, *16* (4), 454-460.
37. Y. Liu; Z. Pan; D. Tian; T. Hu; H. Jiang; J. Yang; J. Sun; J. Zheng; C. Meng; Y. Zhang, *Chem. Eng. J.* **2020**, *399*, 125842.
38. a) S. Liu; H. Zhu; B. Zhang; G. Li; H. Zhu; Y. Ren; H. Geng; Y. Yang; Q. Liu; C. C. Li, *Adv. Mater.* **2020**, *32* (26), 2001113; b) S. Chen; K. Li; K. S. Hui; J. Zhang, *Adv. Funct. Mater.* **2020**, *30* (43), 2003890.
39. H. Geng; M. Cheng; B. Wang; Y. Yang; Y. Zhang; C. C. Li, *Adv. Funct. Mater.* **2020**, *30* (6), 1907684.
40. Y. Zhang; H. Jiang; L. Xu; Z. Gao; C. Meng, *ACS Appl. Energy Mater.* **2019**, *2* (11), 7861-7869.

41. a) C. Shen; X. Li; N. Li; K. Xie; J.-g. Wang; X. Liu; B. Wei, *ACS Appl. Mater. Interfaces* **2018**, *10* (30), 25446-25453; b) D. Chen; X. Rui; Q. Zhang; H. Geng; L. Gan; W. Zhang; C. Li; S. Huang; Y. Yu, *Nano Energy* **2019**, *60*, 171-178.

42. a) P. Hu; T. Zhu; X. Wang; X. Wei; M. Yan; J. Li; W. Luo; W. Yang; W. Zhang; L. Zhou; Z. Zhou; L. Mai, *Nano Lett.* **2018**, *18* (3), 1758-1763; b) Y. Liu; Q. Li; K. Ma; G. Yang; C. Wang, *ACS Nano* **2019**, *13* (10), 12081-12089.

Electrochemically induced phase transition in $V_3O_7 \cdot H_2O$ nanobelts/reduced graphene oxide composites for aqueous zinc-ion batteries

Huili Cao,^{a} Dr. Zhiyong Zheng,^a Prof. Poul Norby,^b Dr. Xinxin Xiao,^{a*} and Prof. Susanne Mossin^{a*}*

^aDepartment of Chemistry, Technical University of Denmark, 2800 Kgs. Lyngby, Denmark

^bDepartment of Energy Conversion and Storage, Technical University of Denmark, 2800 Kgs. Lyngby, Denmark

Email: hucan@kemi.dtu.dk (Huili Cao); xixiao@kemi.dtu.dk (Xinxin Xiao); slmo@kemi.dtu.dk (Susanne Mossin)

I Experimental Section**Synthesis of graphene oxide (GO)**

GO was obtained by a modified Hummers method.[1] 2.5 g $\text{K}_2\text{S}_2\text{O}_8$ was added to 5.0 mL of concentrated H_2SO_4 while stirring, into which 2.5 g P_2O_5 was added and dissolved. 5.0 g graphite was added into the solution together with more concentrated H_2SO_4 until the suspension turned to be non-sticky. The mixture was heated in an oil bath at 80 °C for 180 min. After the reaction, the pre-oxidized graphite was diluted by Milli-Q water and then filtered, with further washing using Milli-Q water until pH of the washing water tested to be neutral. 1.0 g pre-oxidized graphite and 3.0 g KMnO_4 were slowly added into 23 mL H_2SO_4 in an ice bath. After 5 min reaction, the ice bath was changed to an oil bath and the mixture was heated to 35 °C for 2 h. 46 mL Milli-Q was added slowly and left to react for 15 min. Then, 140 mL Milli-Q water was added, followed by dropwise addition of 2.0 mL H_2O_2 until no further bubble generation. Finally, the product was washed with 1.0 M HCl and filtered. The collected GO was redispersed in Milli-Q water with a concentration of ca. 7.2 mg mL^{-1} .

II Supporting data

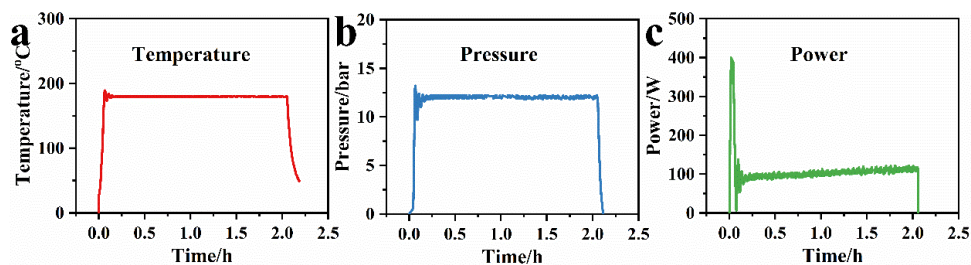


Figure S1 Microwave parameters, including temperature (a), pressure (b) and power (c), during the microwave-assisted hydrothermal process.

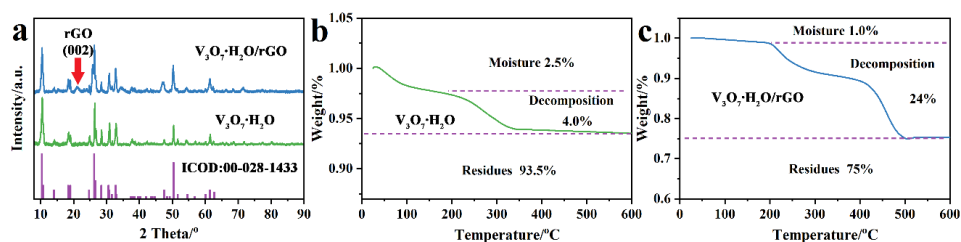


Figure S2 XRD patterns (a), TGA curves of the as-prepared $V_3O_7 \cdot H_2O$ nanobelts (b) and $V_3O_7 \cdot H_2O/rGO$ (c).

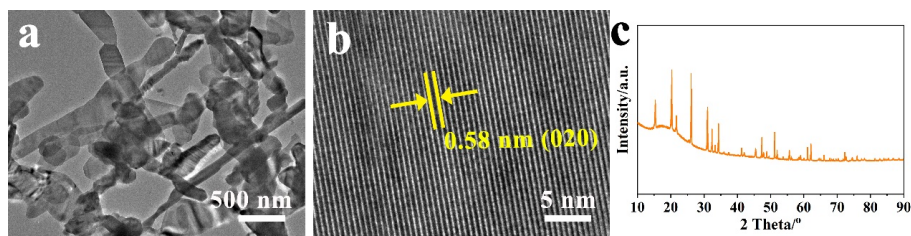


Figure S3 TEM images (a-b), and XRD patterns (c) of the V_2O_5 nanobelts obtained by annealing $V_3O_7 \cdot H_2O$ in air.

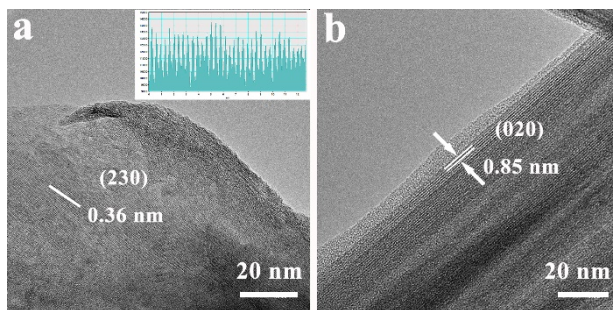


Figure S4 TEM images of $V_3O_7 \cdot H_2O$ obtained at 10 min (a), and 60 min (b) during the microwave-assisted hydrothermal process.

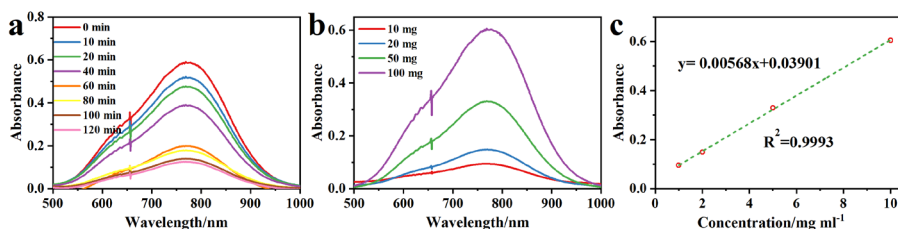


Figure S5 *Ex situ* UV-vis curves (a) of the supernatant during the reaction (a); UV-vis curves of standard $VOSO_4$ solution in different concentrations (b); Correlation between the absorbance at 773 nm and the concentration of $VOSO_4$ (c).

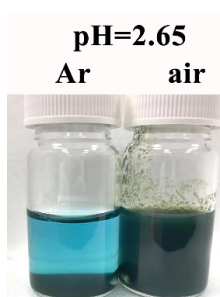


Figure S6 Digital photo of the samples obtained without pH adjustment by acid addition.

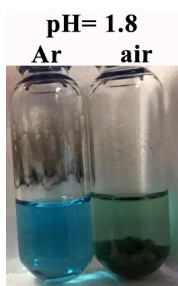


Figure S7 Digital photo of the samples obtained at pH 1.8 by adding H_2SO_4 .

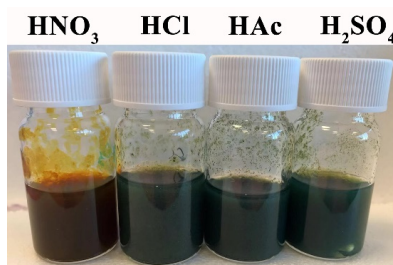


Figure S8 Digital photo of the samples obtained at pH 2.6-2.7 by adding HNO_3 , HCl , HAc , and H_2SO_4 , respectively.

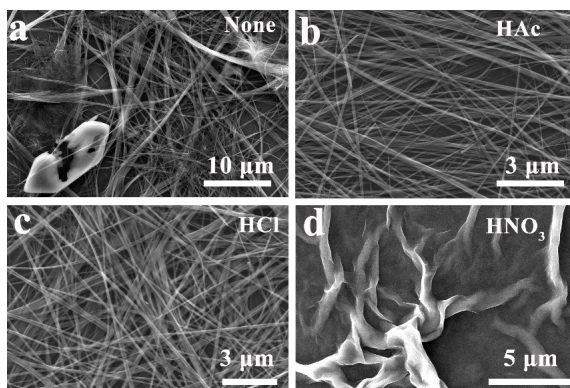


Figure S9 SEM images of the samples obtained without addition of acid (a) and with additions of HAc (b), HCl (c), and HNO_3 (d), respectively.

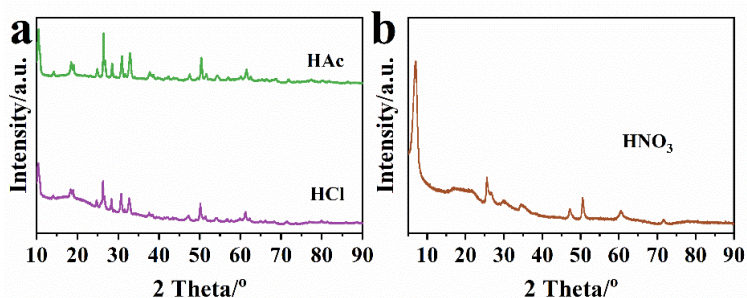


Figure S10 XRD patterns of the product obtained by adding HAc , HCl (a), and HNO_3 (b), respectively.

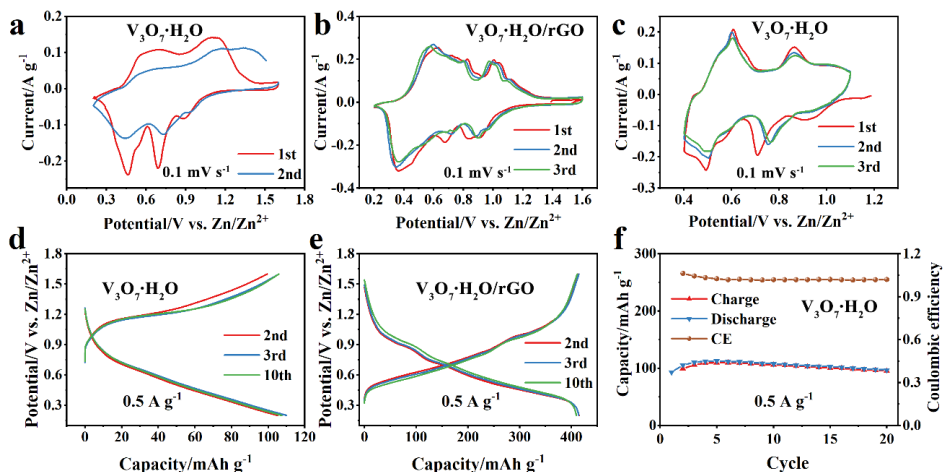


Figure S11 CVs of $\text{V}_3\text{O}_7 \cdot \text{H}_2\text{O}$ (a) and $\text{V}_3\text{O}_7 \cdot \text{H}_2\text{O}/\text{rGO}$ (b) in potential range of 0.2–1.6 V; (c) CV curves of $\text{V}_3\text{O}_7 \cdot \text{H}_2\text{O}$ in potential range of 0.4–1.1 V at a scan rate of 0.1 mV s⁻¹; galvanostatic charge/discharge profiles of $\text{V}_3\text{O}_7 \cdot \text{H}_2\text{O}$ (d), and $\text{V}_3\text{O}_7 \cdot \text{H}_2\text{O}/\text{rGO}$ (e); cycling performance of $\text{V}_3\text{O}_7 \cdot \text{H}_2\text{O}$ at current density 0.5 A g⁻¹.

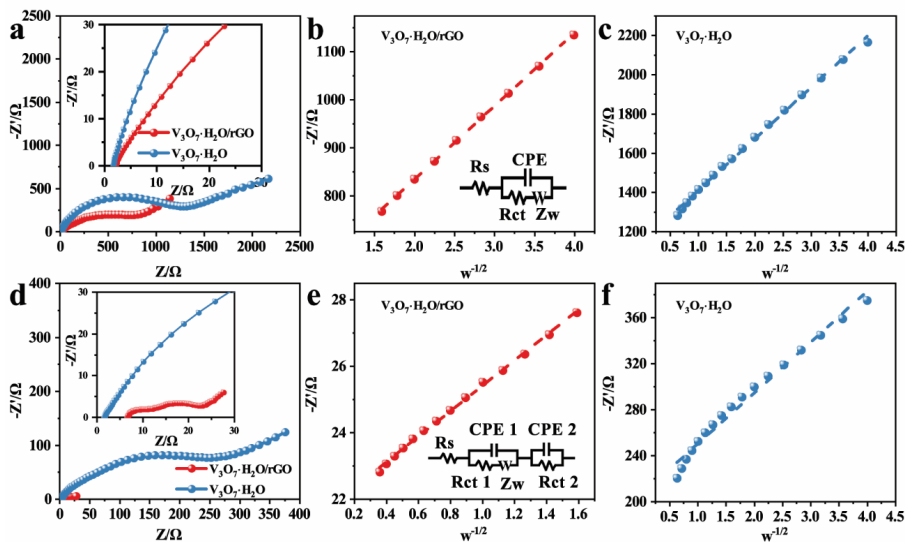


Figure S12 Nyquist plot of $\text{V}_3\text{O}_7 \cdot \text{H}_2\text{O}/\text{rGO}$ composite and $\text{V}_3\text{O}_7 \cdot \text{H}_2\text{O}$ before (a) and after (d) cycling testing; linear fitting of the square root of Warburg impedance with real part Z' obtained for the Nyquist plot before and after cycling of $\text{V}_3\text{O}_7 \cdot \text{H}_2\text{O}/\text{rGO}$ composite (b and e), and $\text{V}_3\text{O}_7 \cdot \text{H}_2\text{O}$ (c and f). Insets of (b) and (e) are the equivalent circuits.

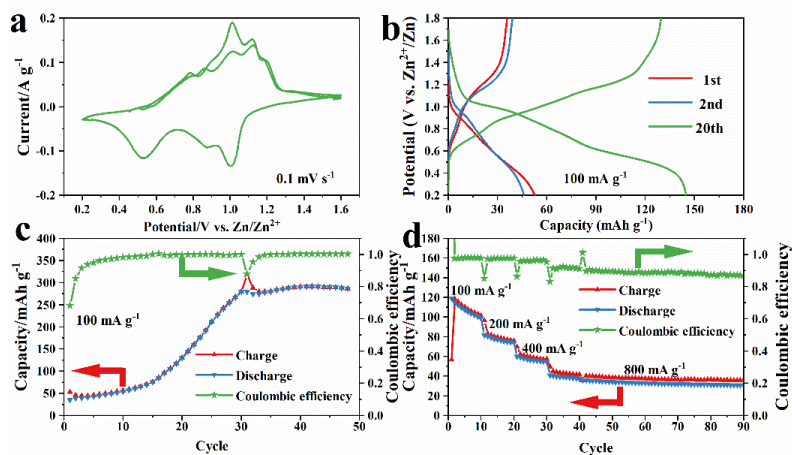


Figure S13 CVs at a scan rate of 0.1 mV s^{-1} (a), cyclic performance (b); galvanostatic charge/discharge profiles (c), and rate capability (d) of V_2O_5 nanobelts.

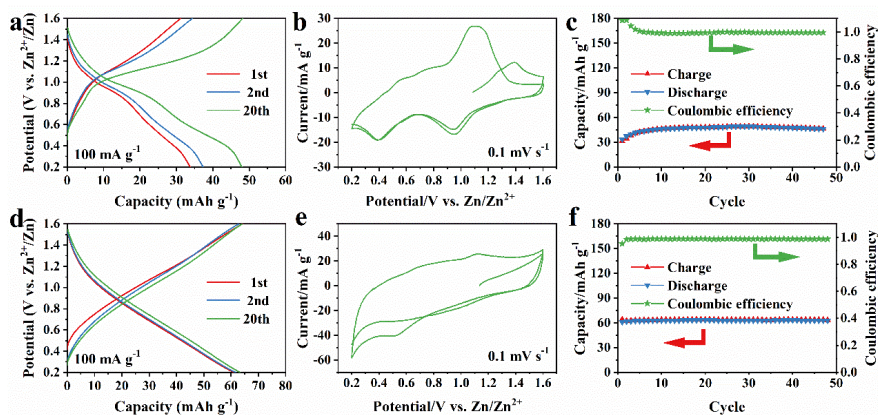


Figure S14 Galvanostatic charge and discharge curves(a) at a current density of 100 mA g^{-1} , CV curves at a scan rate of 0.1 mV s^{-1} (b) and cycling performance of $\text{V}_3\text{O}_{12} \cdot 6\text{H}_2\text{O}$ (c) and rGO (f).

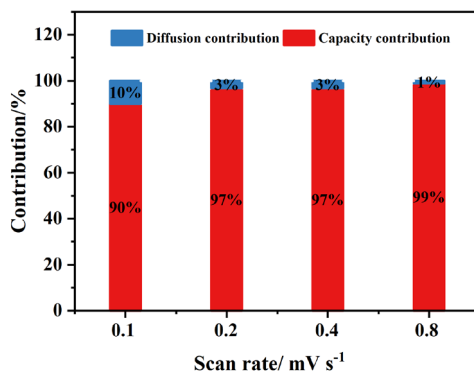


Figure S15 Contribution of capacitance and diffusion-dominated contributions at various scan rates of the $\text{V}_3\text{O}_7 \cdot \text{H}_2\text{O}$ /rGO composite.

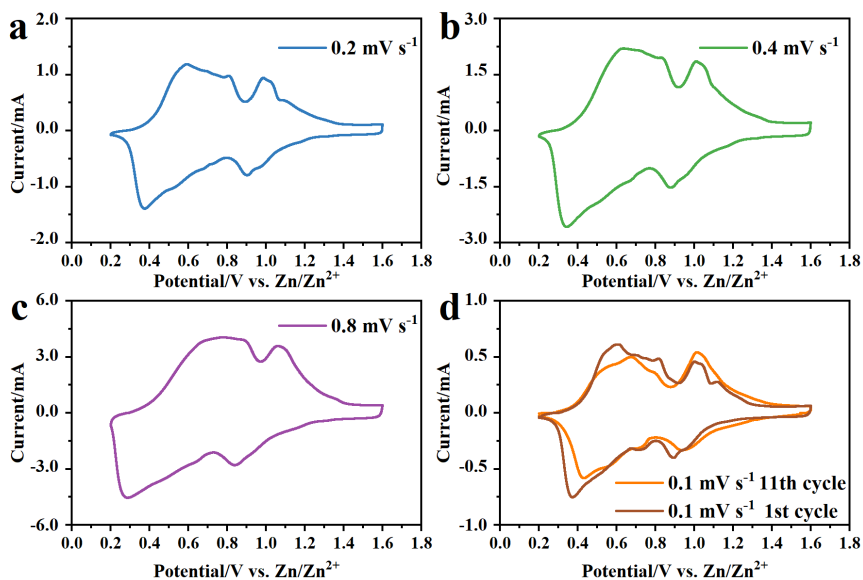


Figure S16 CVs of $\text{V}_3\text{O}_7 \cdot \text{H}_2\text{O}$ /rGO at the scan rate at 0.2 (a), 0.4 (b), 0.8 mV s^{-1} (c); and 0.1 mV s^{-1} in the 1st and 11th cycle (d).

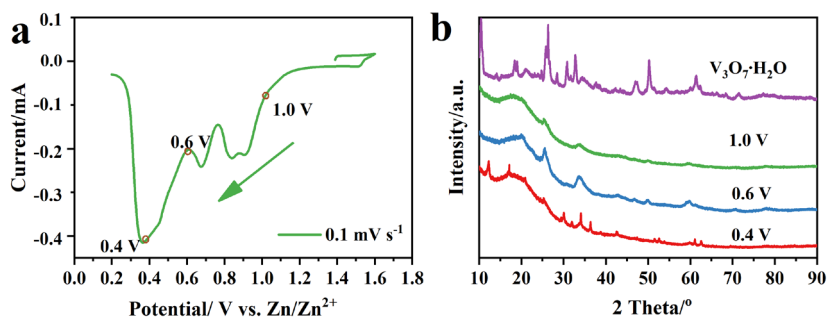


Figure S17 Linear scan voltammetry of $\text{V}_3\text{O}_7\cdot\text{H}_2\text{O}/\text{rGO}$ in the 1st cycle (a); corresponding XRD patterns of the $\text{V}_3\text{O}_7\cdot\text{H}_2\text{O}/\text{rGO}$ at 0.4, 0.6 and 1.0 V (b).

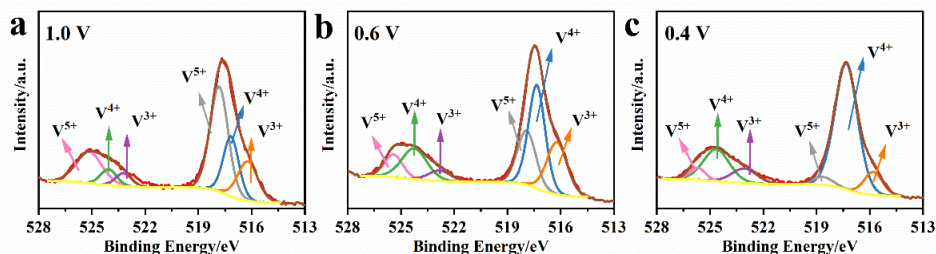


Figure S18 $\text{V}2\text{p}$ spectra of the $\text{V}_3\text{O}_7\cdot\text{H}_2\text{O}/\text{rGO}$ electrode at 1.0 (a), 0.6 (b) and 0.4 V(c).

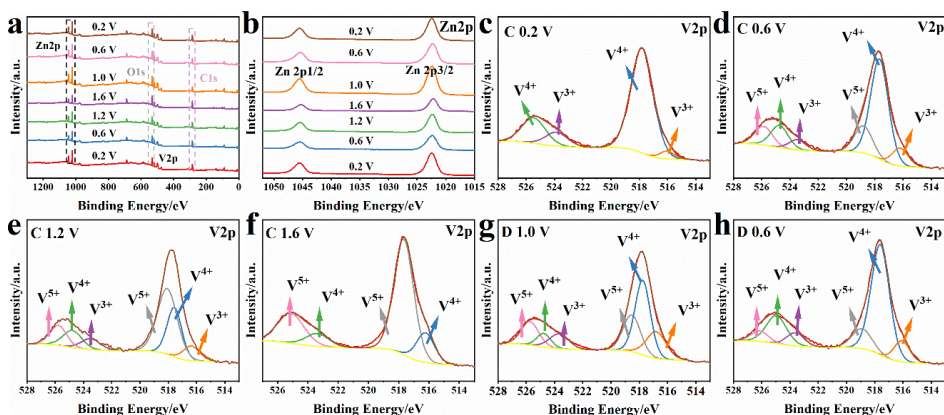


Figure S19 XPS survey (a) and $\text{Zn}2\text{p}$ spectra (b) at various charge and discharge states; $\text{V}2\text{p}$ spectra of $\text{V}_3\text{O}_7\cdot\text{H}_2\text{O}/\text{rGO}$ electrode at charge states of 0.2 V (c), 0.6 V (d), 1.2 V(e), 1.6 V (f), and discharge states of 1.0 V (g), and 0.6 V (h). C and D in (c) to (d) indicate charge and discharge states, respectively.

III Supplementary discussions

Galvanostatic intermittent titration technique (GITT)

GITT measurements were performed on an Autolab potentiostat at current density of 60 mA g^{-1} for 30 min and a relaxation duration of 120 min. Zn^{2+} diffusion coefficient (D , $\text{cm}^2 \text{ s}^{-1}$) can be obtained via: [2]

$$D = \frac{4L^2}{\pi t} \left(\frac{\Delta E_s}{\Delta E_t} \right)^2 \quad (\text{S1})$$

where ‘ t ’ is the time (s) for an applied galvanostatic current; ‘ L ’ is the diffusion length of Zn^{2+} (cm), calculated by the electrode thickness of the coating layer; ‘ ΔE_s ’ and ‘ ΔE_t ’ are the quasi-equilibrium potential and the change of cell potential during the current pulse, respectively (Fig. S20).

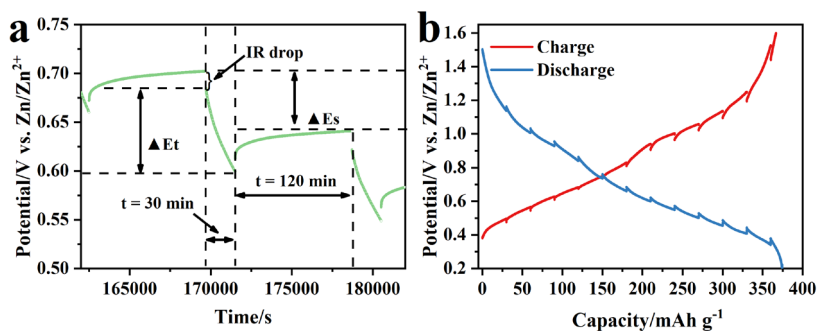


Figure S20 Definition of ΔE_t , ΔE_s and IR drop (a) for a single GITT during discharge process; Charge-discharge GITT curves (b) for the $V_3O_7 \cdot H_2O$ /rGO cathode at a current density of 60 mA g^{-1} .

IV Supplementary table

Table S1 Specific capacity of vanadium oxides applied as zinc-ion battery cathode electrodes.

Materials	Current density A g^{-1}	Specific Capacity mAh g^{-1}	References
Al-doped $\text{VO}_{1.52}(\text{OH})_{0.77}$	0.015	105	[3]
VO_2 hollow nanospheres	0.1	408	[4]
Graphene/ VO_2 composite	4	240	[5]
$\text{H}_2\text{V}_3\text{O}_8$ Nanobelt	0.1	423.8	[6]
$\text{H}_2\text{V}_3\text{O}_8$ nanobelt/Graphene	0.1/6	394/270	[7]
Nanogrid-shaped $\text{V}_3\text{O}_7 \cdot \text{H}_2\text{O}/\text{C}$ composites	0.1/5	481.3/171.6	[8]
$\text{V}_3\text{O}_7 \cdot \text{H}_2\text{O}/\text{rGO}$ composite	0.3/0.6/1.5/3	267/240/218/185	[9]
$\text{V}_5\text{O}_{12} \cdot 6\text{H}_2\text{O}$ Nanobelts	0.05/1	328/146	[10]
Porous V_2O_5 microspheres	0.1	401	[11]
Porous V_2O_5 nanoplates	0.1	300	[12]
rGO	0.1	62.8	This work
$\text{V}_5\text{O}_{12} \cdot 6\text{H}_2\text{O}$ film	0.1	46.3	This work
V_2O_5 nanobelts	0.1/0.2/0.4/0.8	101.2/74.1/54.8/30.9	This work
$\text{V}_3\text{O}_7 \cdot \text{H}_2\text{O}$ nanobelts	0.08/0.16/0.32/0.64	227.3/194.1/173.9/126.1	This work
$\text{V}_3\text{O}_7 \cdot \text{H}_2\text{O}/\text{rGO}$ composites	0.5/1/2/4	410.7/401.1/391.7/380.4	This work

References

1. M. Zhang; C. Hou; A. Halder; J. Ulstrup; Q. Chi, *Biosens. Bioelectron.*, **2017**, *89*, 570-577.
2. H. Chen; L. Chen; J. Meng; Z. Yang; J. Wu; Y. Rong; L. Deng; Y. Shi, *J. Power Sources*, **2020**, *474*, 228569.
3. J. H. Jo; Y.-K. Sun; S.-T. Myung, *J. Mater. Chem. A*, **2017**, *5*, 8367-8375.
4. L. Chen; Z. Yang; Y. Huang, *Nanoscale*, **2019**, *11*, 13032-13039.
5. X. Dai; F. Wan; L. Zhang; H. Cao; Z. Niu, *Energy Storage Mater.*, **2019**, *17*, 143-150.
6. P. He; Y. Quan; X. Xu; M. Yan; W. Yang; Q. An; L. He; L. Mai, *Small*, **2017**, *13*, 1702551.
7. Q. Pang; C. Sun; Y. Yu; K. Zhao; Z. Zhang; P. M. Voyles; G. Chen; Y. Wei; X. Wang, *Adv. Energy Mater.*, **2018**, *8*, 1800144.
8. Z. Cao; H. Chu; H. Zhang; Y. Ge; R. Clemente; P. Dong; L. Wang; J. Shen; M. Ye; P. M. Ajayan, *J. Mater. Chem. A*, **2019**, *7*, 25262-25267.
9. C. Shen; X. Li; N. Li; K. Xie; J.-g. Wang; X. Liu; B. Wei, *ACS Appl. Mater. Interfaces*, **2018**, *10*, 25446-25453.
10. H. Yan; Q. Ru; P. Gao; S. Cheng; F. Chen; F. C.-C. Ling; L. Wei, *Energy Technol.*, **2020**, *8*, 1901105.
11. P. Hu; T. Zhu; J. Ma; C. Cai; G. Hu; X. Wang; Z. Liu; L. Zhou; L. Mai, *Chem. Commun. (Cambridge, U. K.)*, **2019**, *55*, 8486-8489.
12. Y. Ding; Y. Peng; W. Chen; Y. Niu; S. Wu; X. Zhang; L. Hu, *Appl. Surf. Sci.*, **2019**, *493*, 368-374.

Chapter 8

Conclusion and perspectives

Batteries are excellent energy storage systems and have been considered as an important part of the solution for the increasing energy demand due to the sustained power delivery and the capability of fast response. The design of electrode material with high-performance and the reaction mechanisms exploration for batteries are important for the society and have been the target for intense scientific research resulting in important progress in recent decades. In this Ph.D. project, several types of vanadium-based nanomaterials have been investigated in great detail from material fabrication mechanism to energy storage mechanism, including different types of zinc vanadates and vanadium oxides.

In terms of the electrode material formation process, three simple routes are put forward: direct precipitation, calcination and highly-yield microwave methods, resulting in different morphologies. To ascertain the chemical component and certain morphology fabrication mechanism, some advanced techniques are applied, like high-angle annular dark-field scanning transmission electron microscopy, electron energy loss spectroscopy and electron paramagnetic resonance, combined with some *ex situ* studies. During the carbon coating process for fabricating carbon coated zinc vanadate, the vanadium in zinc vanadate is reduced to low oxidation state, accompanied with an interesting vanadium loss. It gives a new insight into the understanding of the lower initial specific capacity than the carbon-free zinc vanadate.

The vanadium oxide nanobelts fabricated by microwave method is proved to be a pH derived mechanism. By applying *ex situ* techniques, the nanowire formation mechanism is confirmed from nanosheet stretching into nanobelts affected by pH. Furthermore, the oxidizing acid and non-oxidizing acid also have a big difference on the morphology formation process. By making full use of the two fabrication skills, two types of zinc vanadate were fabricated with the same crystal structures but different orientations. In solid state nuclear magnetic resonance (ss-NMR) results, it confirms the vanadium phase

is the same in the two samples, however, the protons show a subtle difference in the predominant type due to the amount mobility of water molecules in the structures. This technique, to the best of my knowledge, is first applied on investigating on this type of zinc vanadate ($\text{Zn}_3\text{V}_2\text{O}_7(\text{OH})_2 \cdot 2\text{H}_2\text{O}$), which might give some new ideas for the other zinc vanadate.

Used as electrode materials, carbon coated zinc vanadate exhibits a high and stable capacity after a long cycling in Li^+ ion storage. This excellent performance is attributed to the carbon layer providing stable structures and high electronic conductivities, as well as the porous structure with amount of active sites. Though the initial capacity is lower than other zinc vanadate due to the low oxidation state of vanadium, the stability is superior. Using three-electrode technique reveals the high reversibility of the anode material during Li^+ ion intercalation process, which can help to accurately evaluate the energy storage performance of the material.

However, when used as cathode electrode in ZIB, carbon coated zinc vanadate exhibits a poor cycling performance. By further investigation, the orientation of the crystal structure is confirmed as an important factor to affect the ZIB performance. The zinc vanadate exposing the large lattice spacing exhibit a high capacity by contributing from Faradic (redox reactions) and diffusion (double layer capacity contribution) capacities, which is much better than the one exposing planes perpendicular to the large lattice spacing with only double layer capacity. This difference is due to the different energy barrier when the Zn^{2+} ion diffusion in different directions. Compared to the carbon-free cathode exposing narrow planes on the surface, carbon coated zinc vanadate with the same orientation exhibits a better electrochemical performance. It is suggesting the carbon additive and orientations are both important factors for energy storage process.

Therefore, the vanadium oxide exposing large spacing lattice on the surface and compositing with reduced graphene oxide (rGO) exhibits a very fast Zn^{2+} ion diffusion coefficient and high capacity. The large lattice provides a fast path for Zn^{2+} diffusing into the active material to achieve the rich redox reactions for the vanadium from V^{5+} to V^{3+} with a high Faradic capacity contribution. Compared to the pure vanadium oxides, the composite electrode also shows a large potential window with low polarization. Additionally, a graduate phase transition mechanism is firstly observed in this type of vanadium oxide ($\text{V}_3\text{O}_7 \cdot \text{H}_2\text{O}$), which will give a new insight into aqueous ZIB reactions.

Though the research on electrode materials has been a very hot topic in recent years, and a large amount of new electrode materials with high capacity are put forward, there are still some issues remaining to be figured out. Here, based on my best knowledge and understanding, I will propose some perspectives to the development of the battery.

Firstly, the fabrication process for materials with attractive structural properties and morphologies is generally complicated and inefficient. And the recycling of electrode material and dealing with the toxic electrolyte are still insufficient. It is not following the movement towards a more sustainable production as formulated in the 17 UN Sustainable Development Goals. Some strategies may be able to solve the above issues: i) choosing abundant and non-toxic material as electrode; ii) proposing one step synthesis method with low requirements, like ball milling or calcination process; iii) promoting hybrid solid state electrolyte.

Secondly, though the 3-dimensional porous morphologies have been confirmed to provide more active reaction sites than other morphologies, the formation mechanism is still ambiguous. More *ex situ* and *in situ* techniques need to be developed to monitor the reactions. Based on the investigations, controllable structures can be easily designed, like designing crystals growing in a certain direction.

Thirdly, the combination between the experiment and theoretical calculation needs to be strengthened. For example, designing defects in materials is a common tool to obtain a high-performance electrode material. Variety of investigations focus on designing the oxygen hole or other element holes to decrease the internal resistance, and further achieving an excellent energy storage performance. The effects of the defect concentration, however, are often ignored. By combining experimental and calculation means, designing optimal defects concentration in electrode materials should be a useful way.

Finally, the fundamental investigations on the reaction mechanisms and the factors of the battery potential decay are still lacking. It is my suggestion to perform more in-depth studies of prepared electrode materials in order to achieve a deeper understanding of the decisive factors behind the successful materials and even the reasons for the failure of the electrode materials.

Appendix

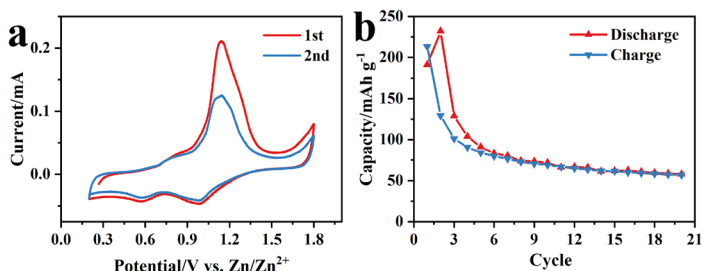


Fig. 1 CV curves at 0.1 mV s⁻¹ (a) and cycling performance at a current density of 100 mA g⁻¹ (b) of the nitrogen-doped carbon coated zinc vanadate applied as zinc ion battery cathode.

Note: The zinc-ion storage performance of the N-doped carbon coated zinc vanadate (ZnVC, in Chapter 5) is also investigated. Fig. 1a shows the CV curves at a scan rate of 0.1 mV s⁻¹, where two pairs of peaks appear during the Zn²⁺ ion intercalation process. It is similar to the zinc vanadate cathode in Chapter 6. In cycling testing (Fig. 1b), the initial capacity can reach about 200 mAh g⁻¹. After only 20 cycles, it drops to 50 mAh g⁻¹ due to the irreversible Zn²⁺ ion intercalation, which is lower than that of zinc vanadate nanowires (ZnVW, in Chapter 6), but much better than zinc vanadate flowers (ZnVF, in Chapter 6). Therefore, besides the orientation effects, the carbon additive also can improve Zn²⁺ ion storage for the cathode electrode.